Bulletin of Pure & Applied Sci. VOL. 32 D 2013

132146

2

Print Version ISSN 0970 6569
Online Version ISSN 2320 3218

BPAS Research

Bulletin of Pure & Applied Sciences

Volume 32 D (Physics)

No. 1 (Jan. - June)

2013

www.bpas.in

Bulletin of Pure and Applied Sciences

Volume 32-D- Physics
Issue No.1 (January-June)
2013

A Peer Reviewed Journal

.Sha
132146

पुस्तकालय
132146
गुरुकुल कांगड़ी विश्वविद्यालय

This publication is included in Abstracted/Indexed coverage of ProQuest , EBSCOhost , Indian Science Abstract, Indian citation index. etc

Url : www.bpas.in

Bulletin of Pure and Applied Sciences

Volume 32 D (Physics), Issue (No.1) January-June, 2013

EDITORIAL BOARD

Convenor (Hon.) : Prof. Durga P. Ojha, *FRSC (UK)*
*Professor,*School of Physics, Sambalpur University, Jyoti Vihar-768 019,Sambalpur, Orissa, India
E-mail: durga_ojha@hotmail.com

MEMBERS

Prof. R. N. P. Choudhary Dept. of Physics IIT Kharagpur(WB) (INDIA)	Prof. Florentin Smarandache University of New Mexico Gallup NM 87301 USA	Prof. A. K. Deb Dept. of Physics University of Chittagong Chittagong Bangladesh
Prof. V. R. K. Murthy Dept. of Physics IIT Chennai (INDIA)	Prof. Dmitri Rabounski Sirenevi boulevard 69–1–65, Moscow 105484, Russia.	Prof. Sarabettin EREL Dept. of Physics University of Kirikale (INDIA)
Prof. Madan jee Dept of Physics B.R.A. Bihar University Muzaffarpur (Bihar) (INDIA)	Prof. H.O. Boyo Dept. of Applied Physics Fukuoka University Nanakuma, Joham-ku Fukuoka Japan	Prof. M.C.Rao Dept. of Physics Andhra Loyola College Vijayawada (A.P.) 520 008 (INDIA)
Prof. B. Hanumanaiah Dept. of Physics IIT Bangalore (INDIA)	Prof. A. O. Boyo, Dept. of Physics, Lagos State University Ojo Lagos State Nigeria	Dr. D. K. Dwivedi Reader in Physics Dept of Applied Sciences M.M.M. Engineering College Gorakhpur
Prof. Rajnikant Head P.G. Dept of Physics University of Jammu Jammu Tawi (J & K)	Prof. C. Y. Lo Applied and Pure Research Institute Nashua NH 03060,USA	Prof. R.Jeevan Kumar Dept. of Physics S.K. University Anantapur (A.P.) (INDIA)
Prof. S.H. Pawar Dept. of Physics Shivaji University Kolhapur (INDIA)	Prof. Bekir GURBULAK Ataturk University Fizik Bolumu, 25240 ERZYRUM TURKEY	Prof. Lalan Jha Dept. of Physics L.N. Mithila University Darbhanga (INDIA)
Prof. S.C. Mehrotra Dept. of Physics Dr. B.A.M. University Aurangabad (INDIA)	Prof. S. Umapathy School of Physics Madurai Kamaraj University, Madurai (INDIA)	Prof. S.K. Narayandass Dept. of Physics Bharathiar University Coimbatore (INDIA)

(Research papers may be submitted through the above Professors)

Bulletin of Pure & Applied Sciences is devoted to the international advancement of organized knowledge on all aspects of Science. It provides a forum for comments by publishing original research contributions, scientific survey, case studies, book review and letter to the Editor-in-Chief.

Bulletin of Pure & Applied Sciences is issued six monthly, i.e. June and December of every year. The Editor-in-Chief/Managing Editor/Editorial Board etc. assumes no responsibility for the statements and opinions advanced by the contributors. The editorial staff in its work of examining papers, received for possible publication is assisted, in an honorary capacity, by a large number of distinguished scientist working in various parts of the world.

Bulletin of Pure & Applied Science is copy-righted. Manuscripts published in the Bulletin should not be reproduced without the written permission of the Editor-in-Chief.

Annual Subscription Rate

Print version INDIA) Rs. 1000 U.S. $ 60 U.K. £ 30 (www.bpas.in)
Online version (contact www.indianjournals.com)

Bulletin of Pure and Applied Science

Vol.32D- Physics (No.1) January- June 2013

Contents

Central Library
Gurukul Kangri University
Haridwar

Reza Javadi
APPLICATION OF ORGANIC FIELD-EFFECT TRANSISTORS IN ELECTRONIC CHARGE TRANSPORT. **P.1-14**

Aparajita, Rakesh Kumar Singh, Kalpana Kumari Singh, Tapaswi Prasad Singh and Bhagwan Prasad
FABRICATION OF TRIANGULAR LATTICE OF PARALLEL GOLD AND SILVER NANOWIRES OF HIGH OPTICAL QUALITY. **P.15-17**

P.K.Verma, C.S.Thakur and Harsha Vardhan
SCATTERING OF POSITRON BY ATOMS IN SMALL ANGULAR RANGE OF SCATTERING. **P.19-22**

Raj Kumar Tiwari, Sachin Kumar and G. R. Mishra
A MODIFIED APPROACH TO NOISE ANALYSIS IN CCII. **P.23-35**

Seema Priyadarshini, Rajiv Mishra, Kumari Ruchi, Shashi Shekhar, Sanjay Kumar Singh and Gyandeo Prasad Tiwari
TROTTER DECOMPOSITION AND A SERIES EXPANSION OF THE PARTITION FUNCTION FOR HUND'S EXCHANGE COUPLING IN A QUANTUM MONTE CARLO ALGORITHM. **P.37-41**

K. K. Karun, G. Chandra and B. K. Singh
ELECTRONIC SPECTRA AND STRUCTURE OF CARBON DIOXIDE AND NITROUS OXIDE BY RINDO-CI METHOD. **P.43-50**

Meghdad Khademian, Ali Alizde, Hamidreza Baharvandi and Hasan Majidi
COMPARISON OF PROPERTIES AND MICROSTRUCTURE OF A356 - B4C NANO COMPOSITES, PRODUCED BY TWO METHODS OF CASTING VORTEX AND SEMI-SOLID CASTING. **P.51-58**

Address for communication :

Dr. A. K. Sharma , *Editor –in-chief* ,
115-RPS- DDA Flats, Mansarover Park,
Post Box No.-9043,Shahdara, Delhi- 110032, India
(Phone : 011-22138726, Mobile-9212200909
Emails : editorbulletin@yahoo.co.in, editorbulletin8@gmail.com, ajay_shrm@yahoo.com , editordrsharma@rediffmail.com

Website : www.bpas.in

INSTRUCTIONS TO CONTRIBUTORS

BPAS/Bulletin of Pure and applied Sciences invites original, research-based papers, articles, cases & book reviews on topics of current concern in all areas of Pure & Applied Sciences. While sending contributions the following guidelines must be strictly followed. Contributions that do not adhere to the guidelines will not be considered.

1. Papers should be reader friendly & written in clear, straightforward language, avoiding too many jargons & technical terms.
2. The selection of papers for publication will be based on their relevance, clarity, topicality and originality; the extent to which they advance knowledge, understanding and application; and their likely contribution towards inspiring further development and research.
3. The style of paper/manuscript should be lucid but concise. The text should be preceded by s short descriptive **TITLE** of the paper, Author/s' /Contributor/s' names, designations, official addresses with Pin code/Zip code, Mobile/phone/fax numbers, and e-mail IDs ; an informative **ABSTRACT** ; 5 10 **Key words** and subject classification if any. The main Body should be divided into numbered sections with appropriate Headings. Figures and tables should be incorporated in the text of paper at suitable places.
4. The articles should be in clear, coherent and concise English. Author/s should also send a copy of the contribution in MS word2003, in Verdana/Times New Roman font, by e-mail to: editorbulletin8@gmailcom, editorbulletin@yahoo.co.in, ajay_shrm@yahoo.com. The hard copy and electronic files must match exactly. Author/s should also certify that the paper has not been published or submitted for publication elsewhere.
5. The contributions received will be acknowledged immediately by e-mail. All correspondence with contributors will only be through e-mail. All papers submitted for publication will be reviewed by following the `double blind' system. Only those contributions, which comply with the "Guidelines for Contributors" will be processed for publication.
6. Manuscripts not considered or not accepted for publication will not be sent back. Contributors whose contributions are accepted or rejected will be informed by e-mail only.
7. References should be complete in all respects and arranged in alphabetical order.

   (a) Journal references should be listed as follows:

   Lo, C.Y. and Wang, S.(2010). On experimental verifications of the Einstein equation and consequences of the charge-mass repulsive force. *Bulletin of Pure and Applied Sciences, Vol.* 30 D(2):177-194

   (b) Books should be referred to as follows:

   Pozar, David M. Microwave Engineering.Third ed.(International edition),2005,John Wiley,pp.35-39
8. **Copyright:** Wherever copyrighted material is used, the authors should be accurate in reproduction and obtain permission from copyright holders, if necessary. Papers published in Bulletin of Pure and applied Sciences /BPAS Research should not be reproduced or reprinted in any form, either in full or in part, without prior written permission from the Editor-in-chief.
9. **Review Process:** Two or more referees review all contributions by following the `double blind' system. The review process usually takes about 30-60 days. ***BPAS Research / Bulletin of Pure and applied Sciences*** reserves the right of making editorial amendments in the final draft of the manuscript to suit the journal's requirements and exclusive copy right after publication .

Dr. A.K. Sharma, ***Editor in chief***
115 RPS DDA Flat, M.S. Park,Post Box 9043, Shahdara, Delhi-110032 (India)
Contact No. +91 11 2213 8726; Mobile: 0 92122 00909
Url: www.bpas.in
Emails: editorbulletin@yahoo.co.in,ajay_shrm@yahoo.com

Bulletin of Pure and Applied Science

Vol.32D- Physics (No.2) July-December 2013

Contents

Sudhanshu Srivastava and K. K. Verma
FABRICATION AND ANALYSIS OF ELECTRICAL BEHAVIOUR OF CARBON NANOWIRES BY FOCUSED ION BEAM INDUCED DEPOSITION TECHNIQUE. P.59-65

Morteza Alipanah and Ali Zahmatkesh
AN EXPERIMENTAL AND NUMERICAL STUDY OF VORTEX GENERATORS ON THE FLOW PATTERN AND THE AERODYNAMIC COEFFICIENTS. P.67-80

Padmaja P Natarajan and Dr. V. Geetha
COMPUTER SIMULATION OF SEM STRUCTURES OF THIN FILMS. P.81-94

Aparajita, Amita Sharma and Sippy Kumari
TRANSPOT COEFFICIENT OF SILICON BASED QUANTUM WELL AND CALCULATION OF ENERGY LOSS RATE. P.95-98

B. Prasad, B.N. Mahto and Archana
DESIGN OF MULTIPURPOSE SOLAR COLLECTORS FOR DOMESTIC USE.. P.99-103

Ahmad Afsari and Mohammad Vahdani
ERROR MODELING ON CNC MACHINE TOOL FOR GEOMETRIC, THERMAL AND LOAD ERRORS. P.105-125

Ravi Anjan,Rekha Singh,Kumari Ruchi,Satyendra Kumar Singh,Shashi Sekhar and Rakesh Kumar Ranjan
TRANSMISSION OF HOLES BY A MULTIBAND-MULTICHANNEL MODEL. P.127-130

Ashok Kumar
SCATTERING OF ELECTROMAGNETIC WAVE FROM SPHERICAL ROUGH SURFACE. P.131-139

Vrishali Joshi
A FIRST PRINCIPLE STUDY OF ELECTRONIC AND STRUCTURAL PROPERTIES OF INDIUM ARSENIDE(INAS). P.141-146

Mojgan Eivazzadeh Kalejahi
WIRELESS SENSOR NETWORK SIMULATOR TO STUDY ROUTING PROTOCOLS. P.147-157

Shiv Ranjan Kumar
PHOTONIC CRYSTAL IN ELECTRICAL ENGINEERING. P.159-164

H T Ananda, Thejas Urs G, M B Nanda Prakash and R Somashekar
CHARACTERIZATION OF HPMC/GLY: NA_2SO_4 POLYMER COMPOSITE USING X-RAY TECHNIQUE P.165-173

Address for communication :

Dr. A. K. Sharma , *Editor –in-chief* ,
115-RPS- DDA Flats, Mansarover Park, Post Box No.-9043,Shahdara,
Delhi- 110032, India (Phone : 011-22138726, Mobile-9212200909
Emails : editorbulletin@yahoo.co.in, editorbulletin8@gmail.com, ajay_shrm@yahoo.com ,
Website : www.bpas.in

INSTRUCTIONS TO CONTRIBUTORS

BPAS/Bulletin of Pure and applied Sciences invites original, research-based papers, articles, cases & book reviews on topics of current concern in all areas of Pure & Applied Sciences. While sending contributions the following guidelines must be **strictly** followed. Contributions that do not adhere to the guidelines will not be considered.

1. Papers should be reader friendly & written in clear, straightforward language, avoiding too many jargons & technical terms.
2. The selection of papers for publication will be based on their relevance, clarity, topicality and originality; the extent to which they advance knowledge, understanding and application; and their likely contribution towards inspiring further development and research.
3. The style of paper/manuscript should be lucid but concise. The text should be preceded by s short descriptive **TITLE** of the paper, Author/s' /Contributor/s' names, designations, official addresses with Pin code/Zip code, Mobile/phone/fax numbers, and e-mail IDs ; an informative **ABSTRACT** ; 5 10 **Key words** and subject classification if any. The main Body should be divided into numbered sections with appropriate Headings. Figures and tables should be incorporated in the text of paper at suitable places.
4. The articles should be in clear, coherent and concise English. Author/s should also send a copy of the contribution in MS word2003, in Verdana/Times New Roman font, by e-mail to: editorbulletin8@gmailcom, editorbulletin@yahoo.co.in, ajay_shrm@yahoo.com. The hard copy and electronic files must match exactly. Author/s should also certify that the paper has not been published or submitted for publication elsewhere.
5. The contributions received will be acknowledged immediately by e-mail. All correspondence with contributors will only be through e-mail. All papers submitted for publication will be reviewed by following the `double blind' system. Only those contributions, which comply with the "Guidelines for Contributors" will be processed for publication.
6. Manuscripts not considered or not accepted for publication will not be sent back. Contributors whose contributions are accepted or rejected will be informed by e-mail only.
7. References should be complete in all respects and arranged in alphabetical order.

   (a) Journal references should be listed as follows:

   Lo, C.Y. and Wang, S.(2010). On experimental verifications of the Einstein equation and consequences of the charge-mass repulsive force. *Bulletin of Pure and Applied Sciences, Vol.* 30 D(2):177-194

   (b) Books should be referred to as follows:

   Pozar, David M. Microwave Engineering.Third ed.(International edition),2005,John Wiley,pp.35-39
8. **Copyright:** Wherever copyrighted material is used, the authors should be accurate in reproduction and obtain permission from copyright holders, if necessary. Papers published in Bulletin of Pure and applied Sciences /BPAS Research should not be reproduced or reprinted in any form, either in full or in part, without prior written permission from the Editor-in-chief.
9. **Review Process:** Two or more referees review all contributions by following the `double blind' system. The review process usually takes about 30-60 days. **BPAS Research / *Bulletin of Pure and applied Sciences*** reserves the right of making editorial amendments in the final draft of the manuscript to suit the journal's requirements and exclusive copy right after publication .

Dr. A.K. Sharma, *Editor in chief*
115 RPS DDA Flat, M.S. Park,Post Box 9043, Shahdara, Delhi-110032 (India)
Contact No. +91 11 2213 8726; Mobile: 0 92122 00909
Url: www.bpas.in
Emails: editorbulletin@yahoo.co.in,ajay_shrm@yahoo.com

Bulletin of Pure and Applied Sciences
Vol. 32 D (Physics) Issue (No.1) 2013:P.1-14
www.bpas.in

APPLICATION OF ORGANIC FIELD-EFFECT TRANSISTORS IN ELECTRONIC CHARGE TRANSPORT

Reza Javadi
Electrical Engineering and Computer Science Department,
Sungkyunkwan University, South Korea
Email: rezajavadi906@yahoo.com

Received on 30 April 2013: Accepted on 30 May 2013

ABSTRACT

Organic field-effect transistors (FETs) and light emitting diodes have attracted much interest based on possible inexpensive and flexible alternatives. However, a better understanding of the nature of charge transport in these devices and the physics of contacts is crucial for further development. While it is known that the charge-carrier mobility in organic semiconductors is only weakly dependent on the electric field at low fields, the experimental mobility in organic field-effect transistors using silylethynyl-substituted pentacene is found to be surprisingly field dependent at low source-drain fields. This research investigates about understanding and characterizing the transport mechanisms of charge carriers in solution processed poly (3-hexylthiophene) field-effect devices. Charge transport from different source/drain electrodes such as Au, Cu and Cr was examined over a broad temperature range. The results show chemically increasing the injecting electrode work function significantly improves hole injection relative to untreated Au electrodes.

Keywords: Organic, field-effect transistors, Electronic charge, Transport

1-INTRODUCTION

Organic semiconducting materials have been synthesized and studied for over 5 decades (Horowitz, 2004). In the 1950s, drift mobility measurements and the photoconductivity (PC) response of small molecules such as anthracene were examined (Pasveer, 2004) and although these materials showed semiconducting properties, their performance and stability were poor. However, with drastic improvements in synthesis and processing of new classes of molecules such as conjugated polythiophenes in the past two decades, the prospects of commercially using organic semiconductors (OSCs) in applications such as organic light-emitting diodes (OLEDs), field-effect transistors (OFETs) and the solar cells is now greater than ever. In fact, in 2002 Philips introduced the Sensotec Philishave as the first product in the market featuring a display panel based on OLED technology, and following suit, Kodak has introduced the Kodak EasyShare LS633 digital zoom camera with an award-winning OLED display technology (Fig. 1). Simplicity in manufacturing and lower costs of organic electronic devices have been cited as the primary reasons for drive towards commercialization of these devices.

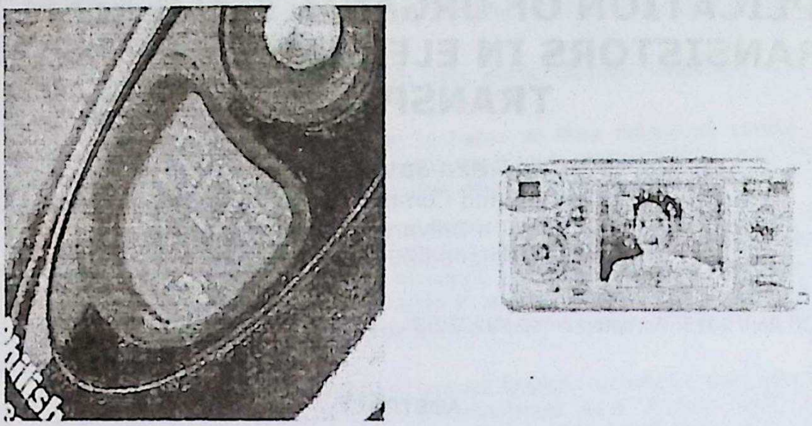

Figure 1: Two examples of use of OLEDs in commercial products. The image on the left shows a new Philips shaver (Sensotec Philishave) that was introduced to the market in 2002. It uses PolyLED technology for its display panel and was featured in the James Bond movie, Die Another Day. The image on the right shows the display of Kodak LS633 digital zoom camera driven by OLED technology. It allows for crisp and clear on-camera viewing of the images. Images taken from Ref. (Gutmann and Lyons, 1967)

Today, conjugated materials are the most important class of organic semiconductors and can be categorized into two main groups (Anthopoulos *et al.*, 2006) of conjugated polymers and conjugated oligomers. Polymers, such as polythiophenes consist of many identical units bonded together in a long chain, and are macromolecular in nature, whereas oligomers like oligothiophenes consist of only a few units. In these materials, carbon pz orbitals overlap and the π electrons become delocalized on the molecule, forming the so-called π-conjugated system (Garnier, 2007). The alternating single and double bonds in polymer drawings represent these π electrons. There are other classes of π-conjugated OSCs, such as pentacene, fullerenes and etc. which have demonstrated good semiconducting properties. Fig. 2 shows some important organic semiconductors.

An important conjugated polymer, which has been our material of choice for all the experiments and analysis presented in this paper, is regioregular poly (3-hexylthiophene). Fig. 3 shows a sketch of this molecule. Regioregular means that each 3-hexylthiophene unit in the chain is oriented so that the residue group C_6H_{13} is either head to head or head to tail. This property gives the polymer, upon deposition, better self-organization and order, therefore, increasing substantially the device mobility.

Mobility, μ, which is usually reported in units of cm2/V.s, is an intrinsic property of the material and is an indicator of how readily charge is transported within the semiconducting polymer upon application of an external electric field.

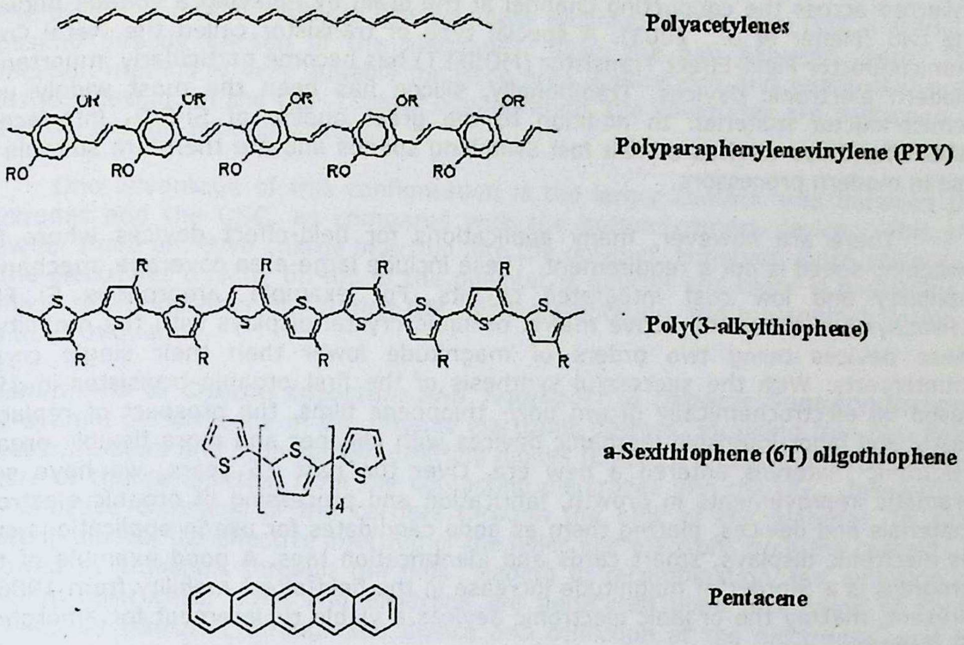
Polyacetylenes
OR
RO
Polyparaphenylenevinylene (PPV)
R
S
Poly(3-alkylthiophene)
S
4
a-Sexithiophene (6T) oligothiophene
Pentacene

Figure 2: A few organic semiconductors

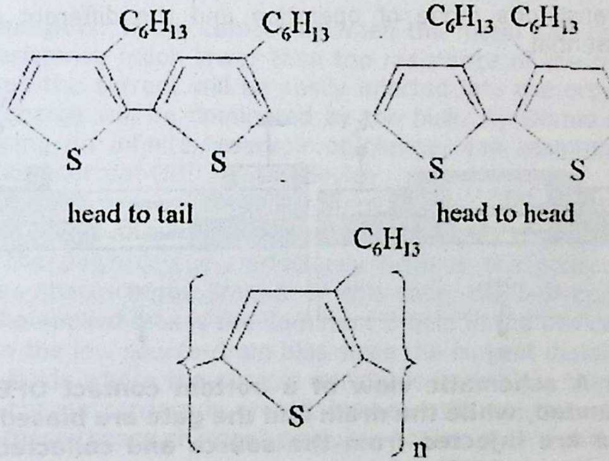
C_6H_{13}
S
head to tail
head to head
n

Figure 3: Poly (3-hexylthiophene) is an important OSC which is solution-processable and has demonstrated good semiconducting properties. P3HT has been the material of choice for the experiments outlined.

Organic Field-Effect Transistors: A field-effect transistor is a 3-terminal device configured like a parallel-plate capacitor. Fig. 4 shows a schematic view of a transistor. By controlling the voltage on one plate (the gate), a charge can be induced on the other. These charges are injected from the source electrode and collected across the conducting channel at the drain by applying a voltage between the two (Meijer *et al.*, 2003). A special type of transistor called the Metal Oxide Semiconductor Field-Effect Transistor (MOSFET) has become particularly important in modern electronic devices. Traditionally, silicon has been the most widely used semiconductor material. In addition to the great quality of Si-SiO_2 interface in MOSFETs, these devices exhibit fast switching speeds and are therefore suitable for use in modern processors.

There are however, many applications for field-effect devices where fast switching speed is not a requirement. These include large-area coverage, mechanical flexibility and low cost integrated circuits. For example, amorphous Si FETs nowadays constitute the active matrix of liquid crystal displays with the mobility in these devices being two orders of magnitude lower than their single crystal counterparts. With the successful synthesis of the first organic transistor in 1986 based on electrochemically grown poly- thiophene films, the prospect of replacing costly and labor-intensive inorganic devices with cheaper and more flexible organic electronic materials entered a new era. Over the past 15 years, we have seen dramatic improvements in growth, fabrication and processing of organic electronic materials and devices, placing them as good candidates for use in applications such as electronic displays, smart cards and identification tags. A good example of this progress is a 5-order of magnitude increase in the field-effect mobility from 1986 to present, making the organic electronic devices a viable replacement for amorphous Si devices.

Despite considerable improvements in fabrication and characterization of thin-film organic field-effect transistors, the physics of charge injection and transport in these devices is not well understood. Before we discuss these issues in detail, a basic review of the transistor's mode of operation and the different charge injection mechanisms is essential.

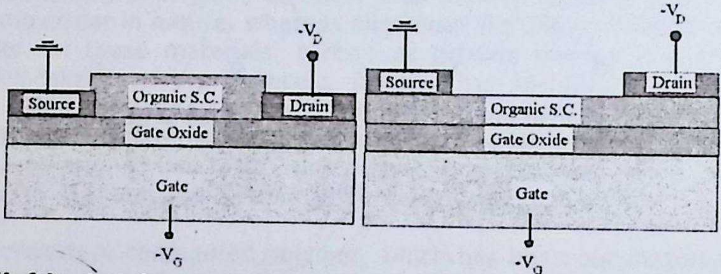

Figure 4: (left): A schematic view of a bottom contact OFET. The source electrode is grounded, while the drain and the gate are biased negatively. In this mode, holes are injected from the source and collected at the drain. (right): A top contact OFET with the electrodes patterned on top of the organic polymer.

OFETs are generally prepared in two configurations: The bottom-contact and the top- contact. In the bottom-contact configuration shown in Fig. 4, first the gate electrode (a conductor) is prepared on a substrate. On top of the gate, a thin layer of a gate insulator, usually an oxide such as SiO_2, is grown followed by the deposition of the metal source and drain electrodes. These electrodes are pre-fabricated on top of the oxide using lithography or shadow-mask techniques. Then the OSC material is deposited directly on top of the electrodes, filling the gap between them. This fabrication method is very suitable for large-area applications and nanometer-scale transistor design. In the top- contact configuration, the electrodes are patterned on top of the organic semiconductor.

One advantage of this configuration is the larger contact area between the electrodes and the OSC, as compared with the bottom-contact devices. This can allow for more effective charge injection into the polymer. However, since patterning of the electrodes directly on top of the polymer is difficult and there is possibility of damage to the polymer film during the metal evaporation, the top-contact design is not used frequently.

Mechanisms of Charge Injection and Transport in Organic Semiconductors: The optimal performance of the organic electronic devices, including thin film field-effect transistors and organic light emitting diodes (OLEDs), critically depends on the nature of charge injection from the contacting electrodes into the OSC, followed by the effective transport of the carriers through the bulk of the material. In light emitting diodes, the effective injection of the holes and electrons from the contacts is followed by transport through the bulk, leading to recombination and emission of light. In solar cells, holes and electrons are generated upon absorption of light, followed by transport through the device and collection at the electrodes, and in FETs, charge injection at the source is followed by transport through the channel and collection at the drain. Since the underlying principle of operation in all these devices is similar, we will review the different mechanisms of charge injection and transport in the following sections.

Bulk-limited transport: If the contact between the metal and the OSC is Ohmic, with a contact resistance much lower than the resistance of the bulk material (see next section), then the current will be easily injected into the organic material and the transport of charge will be dominated by the bulk. By Ohmic contact we mean the electrode, being an infinite reservoir of charge, can maintain a steady state space-charge limited current (SCL) in the device.

In the case where the injected charge dramatically changes the electric field configuration in the polymer (i.e., effectively screens the source-drain field) the transport becomes space-charge limited. In this case, the I–V curves look linear if the field due to the applied bias is the dominant E-field in the device. The conduction is usually linear in the low source-drain bias since the current density in the polymer is low. At higher fields where the current density is very high, there is a significant concentration of charge carriers in transit between the source and the drain. The screening due to these "space charges" produces nonlinear I–V characteristics.

It is important to note that space-charge effects are more readily maintained in materials such as organic semiconductors where the mobility is poor. The low mobility greatly restrains the collection of the carriers at the drain or the recombination of opposite charges. In addition to these effects, OSCs are known to have large concentration of highly localized states (i.e., traps, defects etc.) that trap mobile charges temporarily or permanently (immobile charges). All these factors make organic semiconductors the perfect breeding ground for space-charge transport.

2- LITERATURE REVIEW

As we discussed in the previous section, field-effect mobility in OFETs is an important parameter in describing charge motion within the conducting channel. In disordered polymer semiconductors this mobility, μ, is strongly temperature dependent near room temperature, consistent with thermally assisted hopping between localized states dispersed throughout the polymer film. These localized states are likely to be polaronic. Several different models for hopping transport in these materials have been used to interpret experimental data from 200 K to room temperature, including simple thermal activation, 2d variable range hopping (VRH), and percolative VRH with an exponential density of states. While some models work better with some specific samples, generally distinguishing between them is difficult. The situation is complicated by the fact that the effective mobilities inferred in this manner depend on T, gated charge density, source-drain bias, and contact effects. Parasitic contact resistances in particular can be important. Experiments in several OSC/electrode combinations have shown that contact resistances can be a significant fraction of the total source-drain resistance in the linear regime in short-channel devices. Data in this shallow channel limit must be corrected accordingly for this parasitic series resistance, Rs, to find the true mobility within the semiconductor. We will come back to this issue at great lengths.

As with μ, one must bear in mind that Rs typically depends on temperature, gate voltage, and local electric field. When examining transport properties of organic FETs, it is imperative to determine whether the devices are dominated by the bulk (channel) or the contacts.

This section investigates nonlinear transport measurements in field-effect devices made from high quality, solution cast, regioregular poly(3-hexylthiophene) (P3HT), with channel lengths from 3 μm to 200 nm and aspect ratios (W/L) of 10. Higher temperature properties at low source-drain fields are consistent with those observed by other investigators. From 200 K to 10 K, we observe gate-modulated nonlinear IV characteristics. To understand the effects of contacts in our series of devices, we examined both the devices described above, and an additional series of fixed-width FETs to obtain the channel and contact resistances as a function of temperature. These data demonstrate that (a) the fixed-aspect-ratio devices are bulk (not contact) limited at high temperatures; and (b) the contribution of contacts relative to the channel actually decreases as the temperature is lowered, so that bulk-limited devices tend to remain so as T is decreased. Since the nonlinearities in the IV curves become more pronounced at low temperatures and in wider devices (for which contact resistance are proportionately less important), it is unlikely that these nonlinearities are due to contact effects in these geometries. We find that the nonlinear data are consistent with a model of Poole-Frenkel (PF) type conduction in the space-charge limited (SCL) regime. Within this framework, the strong gate and temperature dependence of this conduction are consistent with a density of localized valence states that varies approximately exponentially in energy. Still within this model, at temperatures below 30 K there appears to be a crossover from thermally assisted hop- ping to a non-thermal mechanism. These nonlinear data over a broad temperature range constrain any other models of transport in such devices. Studying FETs in this nonlinear regime allows comparisons between models not readily performed with linear transport data.

4- MATERIAL AND METHODS

In this section, we investigate at length the issue of contact resistances between the OSC (P3HT) and different metal electrodes. These contact resistances play a dominant role in electronic charge injection properties of OFETs, and therefore cannot be easily ignored when examining intrinsic properties such as mobility and its dependence on the temperature or the gate voltage. This section primarily examines how using various metals as the contacting electrodes affect the charge injection into OSCs. We divide this topic into linear vs. nonlinear charge injection. Linear contact resistances are seen in P3HT devices with a high metal work function, where the HOMO lies energetically close to the Fermi level of the injecting electrode. On the other hand, if there is a significant energy barrier between the two, nonlinear injection is observed.

The physics of charge injection at the metal/OSC contact in field-effect devices remains poorly understood. Contacts in OFETs (extremely restricted contact geometry, essentially undoped OSCs and large current densities due to the very thin channel thickness) are distinct from those in, for example, OLEDs (large contact areas, highly doped OSCs and smaller current densities). Different approaches have been developed to differentiate between contact and channel resistances, including analyses of single device characteristics, scanning potentiometry, gated four-probe measurements and scaling of total resistance with channel length in a series of devices.

Several of these experiments have already shown that the parasitic series resistance, Rs, between the OSC and the metal electrodes can easily dominate the intrinsic channel resistance, Rch, in short channel (few microns and below) OFETs and that Rs correlates inversely with mobility in polymer OFETs at room temperature.

As we discussed modeling of charge injection at the metal/OSC interfaces is a subject of much discussion. Commonly used models include Schottky contacts and antiparallel Schottky diodes in parallel with a resistance. More sophisticated treatments include the fact that conduction in disordered OSCs is by hop- ping, image charge effects, and account for charge recombination at the metal-OSC interface. This last model has received recent experimental support in studies that examine scaling of the contact resistivity with mobility.

Here, first we examine the results of our transport measurements in a set of OFETs with Au electrodes and P3HT as the active semiconducting polymer, with channel lengths from 400 nm to 45 μm. We determine the parasitic series contact resistance, Rs, and the true channel resistance, Rch, from the dependence of the total source-drain resistance, Ron, on the channel length, L. Both Rs and Rch increase as temperature is decreased, with Rch varying more rapidly. The result is that the ratio Rs/Rch actually decreases as T is lowered; relative to the mobility, the contacts actually improve as T is decreased. More generally, we found that Rs correlates inversely with mobility over four decades, over a broad range of temperatures and gate voltages. We compare this data with the predictions of a recent theory (Vissenberg and Matters, 1988) of OSC/metal contacts incorporating a thermionic emission model with diffusion-limited injection currents and accounting for the backflow of charge at the interface. Such a model predicts an inverse relationship between the mobility and the contact resistivity, provided that the

Schottky barrier between Au and P3HT is low. This is expected to be the case since the HOMO of P3HT is estimated to lie between 5.1 and 5.2 eV, close to the work function of Au (5.2 eV).

In the case of lower work function metals such as Cr and Cu, a significant Schottky energy barrier, Δ, for holes is expected to exist at the metal/OSC interface. For a channel mobility, μ, that is thermally activated with characteristic energy EA, typically<~ 0.1 eV, the same model predicts a temperature dependence of the contact resistance, Rs / exp ([EA + Δ]/kBT). For Δ ~ 0.3 eV, the temperature dependence of Rs is therefore predicted to be much stronger than the Au electrode case. However, in recent studies of charge injection in both bottom-contact P3HT FETs (Scott, 2003) and hole injection from a Ag electrode into poly-dialkoxy-p-phenylene vinylene (Murgatroyd, 1970), only a weak T dependence of contact resistance or injecting current was observed. These results imply that the diffusion-limited thermionic emission model is inadequate.

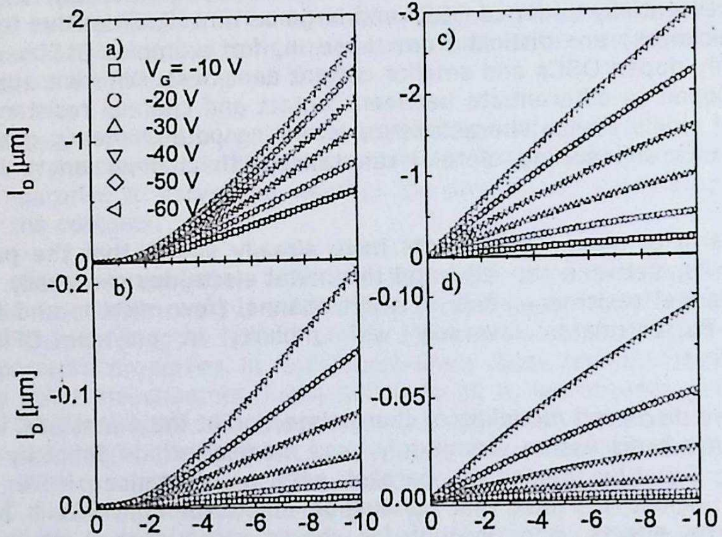

Figure 5: a) Transport characteristics (ID . VD) of a P3HT OFET with Cr source and drain electrodes, with L = 25 ìm, W = 200 ìm at 300 K for several gate voltages. b) Same device at 160 K. c) Analogous plot for a sample with Au electrodes of the same geometry, at 300 K and d) at 160 K.

Work function differences may not be the only parameter determining the validity of thermionic emission models. However, experiments with systematic studies of similarly prepared devices made with identical OSCs and varying metals (Gill, 1972) imply that ¢ is highly relevant to this question. In general, a simple thermionic or thermionic-diffusion model is not a realistic description of the injection process in these systems. The charge in these organic semiconductors is injected into and transported via a density of localized states that is strongly dependent on energy. The simple model of an activated over-barrier hop from the metal into a state in the semiconductor is inadequate, and the detailed energetics of the contact region must be considered. Only recently have the full temperature and field dependence of the injection process been examined experimentally.

With the presence of a significant Schottky injection barrier for holes in P3HT OFETs, the transport characteristics shows nonlinear behavior. Figs. 5(a) and (b) show ID−VD of a P3HT OFET with Cr source and drain electrodes, with L = 25 μm, W=200 μm at 300 and 160 K for several gate voltages. These plots are compared with linear transport in Au OFETs of the same geometry, in (c) and (d). The method of extracting Rs works well in devices where the OSC and the contacting metal electrodes form a linear Ohmic contact as seen in Au devices. In the case of nonlinear charge injection, one must consider the details of the relation between the injecting current and the contact voltage. To differentiate between the IV characteristics of the channel and the contacts, we examine the scaling of device current with channel length, employ the gradual channel approximation [14], and divide the total source-drain voltage VD into a channel component and a voltage dropped at the contacts, VC . We assume, as supported by scanning potentiometry (Emtage and O'Dwyer, 2006), that VC is dominantly dropped at the injecting contact for metals with a significant ¢.

We use ID−VD data from a given series of devices of varying channel length, L, and fixed width, W, to extract both μ and ID −VC for this metal/OSC interface. As expected, the ID−VC characteristics of a specific interface are unique at a given T and VG, independent of L. We analyze the field and temperature dependence of the injected current through a recent analytical model of charge injection from a metallic electrode into a random hopping system. With reasonable fit parameters, this model agrees well with the observed temperature and field dependence of the injected current. We also discuss the distance scale over which VC is dropped, and further experimental avenues to explore.

5- RESULT AND DISCUSSION

As usual, devices are made in the bottom contact configuration on a degenerately doped p+ silicon substrate used as a gate. The gate dielectric is 200 nm of thermal SiO_2. Source and drain electrodes are patterned using electron beam lithography in two different designs: One pattern is a series of L-shaped electrodes, with a fixed W and varying inter-electrode spacing (L), each separated from its neighbors by a distance of about one hundred microns. A second design is an interdigitated set of electrodes with a systematic increase in the distance between each pair. After a few months of experiments with the first design, we started to fabricate the subsequent samples in the interdigitated form. This pattern is more compact and allows for more device packing per chip. In addition, it is easier to get uniform P3HT films across the interdigitated set, and therefore there are fewer fluctuations in performance from device to device. Three different kinds of metallic electrodes (Au, Cr, Cu) were then deposited by electron beam evaporation followed by lift off. (25 nm of each, preceded by 2.5 nm of Ti adhesion layer; no Ti layer for Cr samples). This thickness of metal is sufficient to guarantee film continuity and good metallic conduction, while attempting to minimize disruptions of the surface topography that could adversely affect polymer morphology. The P3HT solution was prepared and solution cast in the exact same manner as described in the previous section. Samples were all tested in vacuum, with HP4145B used for measurements.

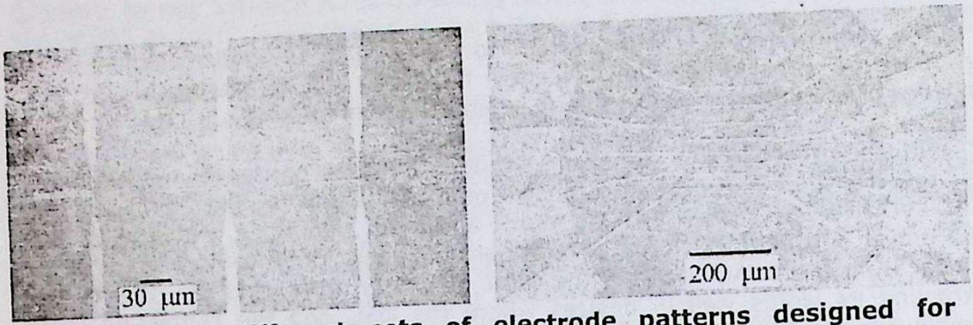

Figure 6: Two different sets of electrode patterns designed for the experiment. In both cases, the distance between each electrode increases systematically, while the channel width is kept fixed for all devices.

We found sample cleanliness to be of crucial importance to achieving devices with high quality, reproducible characteristics. Au electrodes were cleaned for one minute in a 1:1 solution of NH_4OH: H_2O_2 (30%), rinsed in de-ionized water, and exposed for about 1 min to oxygen plasma. The purpose of the oxygen plasma was to remove any remaining organic residue from the lithographic process.

The Cr samples were cleaned in the same manner followed by a last step dipping in a buffered HF solution for under 10 seconds. The HF is believed to etch the native SiO_2 oxide, exposing a fresh layer of dielectric. Given the reactivity of Cr, it is natural to consider the importance of electrode oxidation. As was previously concluded by others, thin oxides appear not to affect transport significantly. For example, Cr electrode devices prepared by lift-off/O2 plasma/HF dipping/P3HT deposition show transport properties very similar to those prepared by lift-off/HF dipping/O2 plasma/P3HT deposition. This supports the conclusion that any small native oxide resulting from brief O2 plasma exposure does not strongly influence device properties.

Table 1: Parameters describing ensembles of devices analyzed in this study. Mobility values are obtained from ID . VD data using Eq. (3.3.1). Contact resistivity values are computed by extrapolating Ron back to L = 0.

Ensemble width [μm]	min. L [μm]	max. L [μm]	μ_{FE} (300 K, $V_G = -90$ V) [cm^2/Vs]	R_sW (300 K, $V_G = -90$ V) [Ω-cm]
5	0.4	5	0.73	1.1×10^3
30*	2	30	0.16	9.6×10^3
100	5	40	0.13	1.1×10^4
200*	5	45	0.11	1.79×10^4

*Data for the 30 and 200 μm wide devices were at $V_G = -70$ V rather than -90 V.

Cu electrodes were more problematic, and were only exposed to less than 25 seconds of O_2 plasma to clean the organic residue from the lift off. We found that Cu samples exposed to any cleaning procedure except for short O_2 plasma generally exhibited very poor transport properties. Without O_2 plasma exposure, mobilities were poor and contact resistances were higher, presumably due to remaining organic contaminants on the electrodes and the dielectric surface. Longer exposures to O_2

plasmas (greater than one minute) clearly resulted in the formation of a significant oxide layer, as indicated by discoloration of the electrodes. Exposure of Cu electrodes to HF never produced improved performance, and often resulted in poor transport (significantly reduced mobilities) compared to no-HF devices.

Here, we first discuss our findings in the case of linear charge injection in devices made from Au electrodes. We have observed that there are also several other metals that make Ohmic contacts to P3HT, such as platinum (Pt) and indium tin oxide (ITO).

However, we analyze the Au/P3HT results only. We report data for four arrays, each with at least eight FET devices, with parameters as described in Table 1. For brevity, most of the data in subsequent figures are drawn from the W = 5 µm ensemble, and are representative of the other channel widths. For each device at each gate voltage, the linear portion of ID−VD is used to find Ron ∂ID/∂VD, the total source-drain resistance.

The values of Ron are then plotted as a function of channel length for the ensemble of OFETs. The slope of such a plot describes Rch per unit channel length. The intercept (the extrapolated resistance of a device of zero channel length) gives Rs, the total parasitic series resistance of the source and drain contacts. The true field-effect mobility, µFE, may be inferred from the gate voltage dependence of Ron:

$$\frac{\partial\left[\left(\frac{\partial R_{on}}{\partial L}\right)^{-1}\right]}{\partial V_G} = \mu_{FE}(V_G,T)WC_i$$

Where Ci is the capacitance per unit area of the gate oxide. Mobilities inferred from the saturation regime (uncorrected for contact effects) are systematically lower than corrected µFE values, and are comparatively independent of L. Device IV characteristics are stable with thermal cycling, and samples stored in vacuum for two months exhibit undegraded performance.

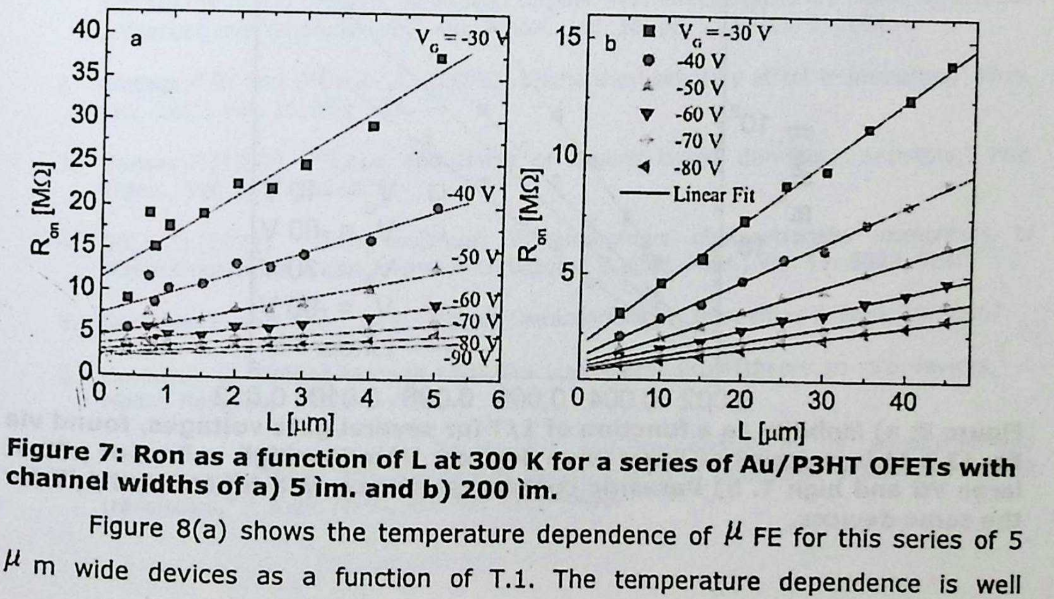

Figure 7: Ron as a function of L at 300 K for a series of Au/P3HT OFETs with channel widths of a) 5 ìm. and b) 200 ìm.

Figure 8(a) shows the temperature dependence of μ FE for this series of 5 μ m wide devices as a function of T.1. The temperature dependence is well approximated as thermal activation, with the activation energy, EA, weakly dependent on gate voltage.

For VG = .90 V, EA ≈ 67.7 meV; for VG = .30 V, EA ≈ 117 meV. The temperature dependence of the parasitic contact resistance for the same devices is shown in Figure (b). The contact resistance increases significantly as T is decreased, again in an activated fashion. The activation energies are very similar to those for μ FE, strongly suggesting that the same physics couples both these parameters. The activation energies inferred for Rs are systematically below those inferred for μ FE for all gate voltages by a few meV (â 4 meV for the 5 μ m ensemble of devices).

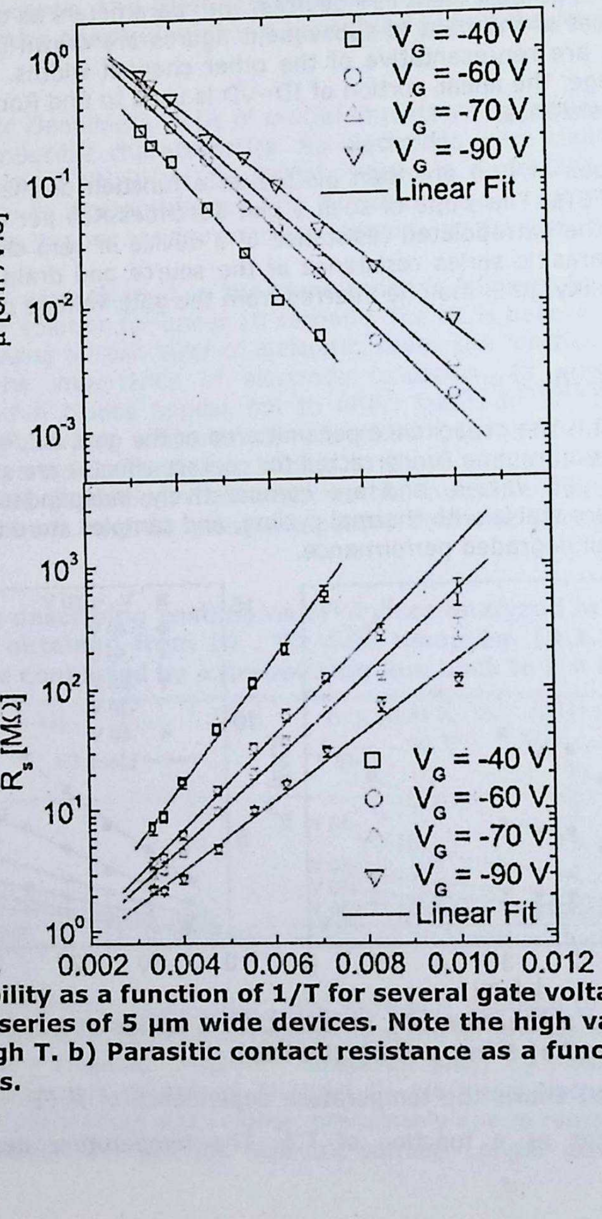

Figure 8: a) Mobility as a function of 1/T for several gate voltages, found via Eq. (3.3.1) in a series of 5 μm wide devices. Note the high values of μFE at large VG and high T. b) Parasitic contact resistance as a function of 1/T for the same devices.

6- CONCLUSION

Transport properties of a series of organic field-effect transistors with P3HT as the active polymer layer and Cr, Cu and Au as the source/drain electrodes were examined over a temperature range. In Au/P3HT devices where linear transport is observed, we used the length dependence of the channel resistance to extract the intrinsic mobility and parasitic contact resistance as a function of temperature and gate voltage for several series of OFETs. Our data were consistent with a mobility-dependent charge injection model accounting the backflow of charge at the interface. We find that the ratio of contact to channel resistance actually decreases slightly as T is reduced, making the devices channel-limited at lower temperatures. Once parasitic contact resistances are taken into account, the mobility of solution-cast P3HT can approach 1 cm2/Vs at room temperature, nearly an order of magnitude larger than uncorrected mobilities. These results indicate that performance of P3HT-based OFETs can be limited more by contact physics than by the intrinsic transport physics in the polymer itself. For the case of nonlinear charge injection from Cr and Cu electrodes, a general approach, incorporating the graduate channel approximation and scaling with length of the conductance, was used to extract the contact current-voltage characteristics of the different devices, with the assumption that the injection barrier primarily applies to holes being injected from the source. This procedure was checked for consistency using devices with electrodes of alternating metal composition. The data confirm that the weak temperature dependence of the injected current cannot be simply explained using the general diffusion-thermionic emission models. With reasonable values of parameters, a more sophisticated model of hopping injection into a disordered density of localized states, with emphasis on the primary injection event, is consistent with the field and the temperature dependence of the data over a broad range of temperatures and gate voltages.

REFERENCES

1. Anthopoulos,T., Tanase,C., Setayesh,S., Meijer,E.J., Hummelen,J.C., .Blom,P.W.M. and Leeuw,D.M.D.(2004). "Ambipolar organic field-effect transistors based on solution processed methanofullerene," *Adv. Mater.*, vol. 16, pp. 2174–2179, 2004.

2. Emtage,P.R. and O'Dwyer,J.J,(2006). "Richardson-schottky effect in insulators," *Phys. Rev. Lett.*, Vol. 16:356–358.

3. Garnier,F.(1997). "Scope and limits of organic-based thin-film transistors," *Phil. Trans.*, Vol. 355: 815–827.

4. Gill,W.D.(1972). "Drift mobilities in amorphous charge-transfer complexes of trinitrofluorenone and poly-n-vinylcarbazole," *J. Appl. Phys.*, Vol. 43: 5033–5040.

5. Gutmann,F. and Lyons,L. E. Organic Semiconductors. John Wiley & Sons, Inc, 1967.

6. Horowitz, G. (2004)."Organic thin film transistors: From theory to real devices," *J. Mater. Res.*, Vol. 19:1946–1962.

7. Meijer,E.J., Detcheverry, C., Baesjou,P.J., van Veenendaal, E., de Leeuw,D.M. and Klapwijk,T.M.(2003). "Dopant density determination in disordered organic field-effect transistors," *J. Appl. Phys.*, Vol. 93: 4831–4835.

8. Murgatroyd,P.N.(1970). "Theory of space-charge-limited current enhanced by frenkel effect," *J. Phys.* D., Vol. 3:151–156.

9. Pasveer,W.F. Charge and Energy Transport in Disordered π-conjugated Systems. PhD thesis, Technische Universiteit Eindhoven, 2004.

10. ScottJ.C.(2003). "Metal-organic interface and charge injection in organic electronic devices," *J. Vac. Sci. Technol.* A., Vol. 21:521–531.

11. Vissenberg, M.C.J.M. and Matters, M.(1998)."Theory of the field-effect mobility in amorphous organic transistors," *Phys. Rev. B.*, Vol. 57: 12964–12967, 1998.

Bulletin of Pure and Applied Sciences
Vol. 32 D (Physics) Issue (No.1) 2013:P.15-17
www.bpas.in

FABRICATION OF TRIANGULAR LATTICE OF PARALLEL GOLD AND SILVER NANOWIRES OF HIGH OPTICAL QUALITY

Aparajita
University Deptt. of Physics, B.R.A. Bihar University, Muzaffarpur, (Bihar), India.

Sippy Kumari
University Department of Physics, B.R.A.B.University, Muzaffarpur, (Bihar), India.

Rakesh Kumar Singh,
Kalpana Kumari Singh,
Tapaswi Prasad Singh
University Deptt. of Physics, J.P.University, Chapra, Saran (Bihar).

Bhagwan Prasad
University Deptt. of Physics B.R.A.B.University, Muzaffarpur, (Bihar), India.

Received on 25 April 2013: Accepted on 20 May 2013

ABSTRACT

We have studied and found that high quality nanowires are produced by pumping molten metal into the hollow channels of silica glass photonic crystal fibers. For this purpose pressurized filling technique have been used. The possible nanowire diameters are 200nm. A shift of surface plasma resonances is found towards lower wave light sides. A triangular array of parallel gold or silver nanowires are fitted around a central missing nanowire. In this study we have found that creation of nanoscale metallic structures reduce the high optical absorption in metals. Due to this there are advantages of strong metal light interactions.

Key words: High quality nanowires , pumping molten metal ,silica glass photonic crystal fibers.

INTRODUCTION

Pelton *et al* (2006) reported surface plasmon resonances at visible wavelength in chemically grown gold nanorods with diameters of nearly 20 nm. Rybczynski *et al* (2007) studied that propagation distances nearly 50 μm were found in nanoscopic coaxial cables made from a central carbon nanotube, an alumina filling and a Cr outer sheath. Schider *et al* (2003) reported that planar nanowire arrays are produced by lithography techniques. Elser *et al* (2006) and shverts *et al* (2007) suggested that arrays of parallel nanowire are means of suitable structures of sub wavelength of imaging. Ozbay (2006) and Maiyer (2006) investigated that surface Plasmon resonance have the potential to which allows very large scale integration of photonic devices at high packing densities. In our study we have fabricated triangular lattices of parallel gold and silver nanowires of high optical activity.

METHODS AND MATERIALS

The nanowires were supported by a Silica glass matrix and were disposed around a central solid glass core. A triangular array of parallel gold or Silver nanowires were arranged around a central missing nanowire which acted as a wave guide. The arrays were made by pumping molten gold and silver into the narrow hollow channels of holely photonic crystal fibres which were made by silica glass. The tree different diameters of holes were 550, 980 and 1520 nanometers were asked. Single and multiwire structures were fabricated by using fusing sheet all but selected holes. Electrical conductivity of fibres with a single nanowire confirmed that the gold nano wires were the continuous over the entire length of the filled section and the reverse in the silver nanowires.

RESULTS AND DISCUSSION

Different hole diameters of 550nm, 980nm and 1520nm were used for constant inter hole spacing of ≈ 2.9 μm. Single and multiwire structures were fabricated by fusing shut all but selected holes at the photonic crystal fiber end face before pumping in the liquid metal. Silver and gold were melt at temperatures below the softening point of the glass silver wires showed cracks a few tens of micrometer wide, spaced nearly 100 μm apart. These cracks proved to be no significant effect on either the loss characteristics. Graph (1) shows that in the absence of any surface-plasmon resonance the nanowire strongly reject light, which is unable to propagate through the bulk metal and light is guided in the core. At certain frequencies surface-plasmon resonances phase match to the guided mode and light leaks away. It is seen from graph that results show an over all decrease in transmission at longer wavelengths, caused by the intrinsic absorption of the metal.

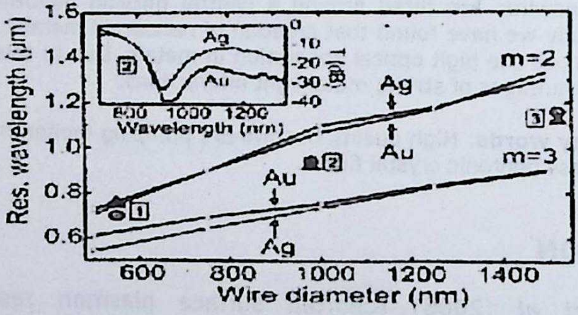

Graph : 1 - SPR wavelength as a function of nanowire diameter.

Additional losses arise because of the finite extent of the nanowire array, which permits light to tunnel through to the outer silica cladding via evanescent fields. The discrepancy between obtained and simulated data improves for narrower wires because the gap size is smaller as shown in graph (1). From graph (2) it is clear that as the nanowire thickness increases at fixed pitch, the transmission loss rises because of the larger light-metal overlap, and the coupling between surface-plasmon resonances also increases, causing the pass bands and the transmission dips to widen as we move from point 1 to 3. The resulting spectra for different gold and silver arrays are shown in graph (2) the transmission loss in the visible which in very high was obtained by successive cutbacks of the metal filled photonic crystal fiber section. In the nanowire array, passbands from around the dispersion curve for single nanowire, their width being proportional to the interwire coupling strength. As the surface Plasmon resonances approach and cross the silica line from higher effective indices, their fields spread out, the nanowires couple more strongly and the pass bands widen.

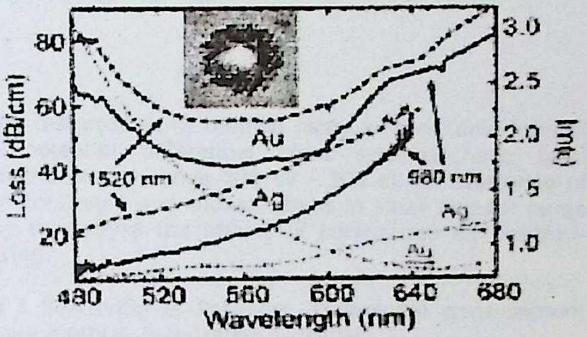

Graph : 2 - Loss spectra in the visible for two different PCFs (hole diameters of 980 and 1520nm) filled with gold and silver.

ÇONCLUSION

The fabrication of triangular lattices of parallel gold and silver nanowires of high optical quality were made. Nanowires were supported by a silica glass matrix. High quality nanowires are produced by pumping molten metal in to the hollow channel of silica glass. It was found that minimum loss wavelength in the gold filled photonic crystal fibers shifted nearly 100nm to shorter wavelengths compared to bulk metal. The guidance loss in a silver array can be reduced to 0.17 dB/mm by this technique. The gap widths of 4,7, and 11 nm for gold wires, 550, 980 and 1520 nm in diameter and 20% for silver are found as shown in graph (1).

REFERENCES

1. Elser J. *et al* (2006), *Appl. Phys. Lett.* 89, 261102
2. Maier S.A., (2006) IEEE, J Sel. Top. Quantum Electron, 12, 1671.
3. Ozbay E. (2006), *Science* 311, 189
4. Pelton. M. *et al* (2006), *Phys. Rev.* B, 73, 155419.
5. Rybczynski. J. *et al* (2007), *Appl., Phys. Lett*, 90, 021104
6. Schider. G. *et al* (2003), *Phys, Rev.* B. 68, 155427
7. Shverts. G. *et al* (2007), *Phys. Rev. Lett.* 99, 053903

Bulletin of Pure and Applied Sciences
Vol. 32 D (Physics) Issue (No.1) 2013:P.19-22
www.bpas.in

SCATTERING OF POSITRON BY ATOMS IN SMALL ANGULAR RANGE OF SCATTERING

P.K.Verma*, C.S.Thakur and Harsha Vardhan
* University Department of Physics,
B.R.Ambedkar Bihar University,
Muzaffarpur - 842001, Bihar, India
E-mail : vermapkv.1@gmail.com

Received on 30 April 2013: Accepted on 29 May 2013

ABSTRACT

By employing distorted wave method along with suitable form of polarization potential differential cross sections have been calculated in the energy range 100 eV - 300 eV for scattering of positrons by potassium and sodium atoms in small angular range of scattering to analyse the impact of polarization on positron-atom scattering.

Key-words : Scattering of Positrons, Differential cross-section, Distorted wave method, Polarization potential.

PACS Nos. : 34.80 BM, 25.30 HM, 34.80 Dp, 34.40

INTRODUCTION

In intermediate energy range a large number of channels including continuum are open, so, it is essential to develop distorted wave method that accounts for the effect of higher excited states and continuum to predict the cross-sections for positron-atom scattering.

In present method a part of Coulomb potential has been included in continuum wave function in the initial channel.

Both potassium and sodium atom have very high dipole polarizability, so, a suitable form of polarization potential has been included. By including polarization potential few excited states are partially included. Moreover, effective Z(atomic number) has been calculated to suit the physical situation, using method proposed by Junker(1975).

The polarization potential is the most effective near forward direction of differential cross sections. This is the reason that differential cross sections have been calculated for positron-atom scattering in small angular range of scattering.

THEORY

The Hamiltonian H for positron-alkali atom can be expressed as follows :-

$$H=\left[-\frac{1}{2}\nabla_{r_1}^2-\frac{1}{2}\nabla_{r_2}^2-\frac{1}{r_1}\right]+\left(\frac{1}{r_2}-\frac{1}{r_{12}}\right)\ldots\ldots\ldots\ldots\ldots\ldots \quad (1)$$

In centre of mass reference frame $\bar{r}_1$ and $\bar{r}_2$ are the position vectors of atomic electron and incident positron with respect to the screened nucleus of target atom. $\nabla_{r_1}^2$ and $\nabla_{r_2}^2$ are kinetic energy operators. Atomic units have been used throughout.

T-matrix element is expressed as

$$T_{i\to f}=\left\langle \Phi_f \middle| V \middle| \chi_i^{(+1)} \right\rangle \ldots\ldots\ldots\ldots\ldots\ldots\ldots\ldots\ldots\ldots \quad (2)$$

with

$$V=\frac{1}{r_2}-\frac{1}{r_{12}} \ldots\ldots\ldots\ldots\ldots\ldots\ldots\ldots\ldots\ldots \quad (3)$$

In atomic unit, differential cross section is expressed as

$$\frac{d\sigma}{d\Omega}=\frac{\mu^2}{4\pi^2}\frac{K_f}{K_i}|T|^2 \ldots\ldots\ldots\ldots\ldots\ldots\ldots\ldots\ldots\ldots \quad (4)$$

The radial part of wave functions for potassium atom and sodium atom are expressed as follows

$$\varphi_{40}(r)=\sum_{i=1}^{2}a_i r\exp(-b_i r)+\sum_{i=2}^{4}a_i r^2\exp(-b_i r)+\sum_{i=5}^{6}a_i r^3\exp(-b_i r)\ \ldots\ldots(5)$$

$$\varphi_{30}(r)=\sum_{i=1}^{2}a_i r\exp(-b_i r)+\sum_{i=3}^{i=4}a_i r^2\exp(-b_i r)+\sum_{i=4}^{7}a_i r^3\exp(-b_i r)\quad \ldots\ldots \quad (6)$$

(in ground state)

The wave functions which represent the positron-atom without distortion and with distortion have following forms :

$$\varphi_r=\exp\left(i\bar{k}.\bar{r}_2\right)\varphi_{nlm}\left(\bar{r}_1\right)\ldots\ldots\ldots\ldots\ldots\ldots\ldots\ldots\ldots\ldots \quad (7)$$

$$\chi_r=\gamma(1+ia)\exp\left(i\bar{k}.\bar{r}_2-\pi/2\right){}_1F_1\left(-ia;1;ikr_2-i\bar{k}.\bar{r}_2\right)\varphi_{nlm}\left(\bar{r}_1\right)\ldots\ldots \quad (8)$$

Here, $\bar{k}$ is the momentum for the direct channel, in which distortion is introduced. The screening parameter δ is evaluated following the method of Junker(1975).

In present case the form of polarization potential $Vp=\left(-\frac{\alpha}{2r^4}\right)$ with α, the dipole polarizability. It is in asymptotic form.

Table- 1: Positron-Potassium Atom Scattering

Energy	**100 eV**	**200 eV**		**300 eV**	
Angle	**DCS**	**DCS**	**DCS (Kh-V)**	**DCS**	**DCS (Kh-V)**
5^0	8.77 (2)	2.09 (2)	2.01 (2)	8.93 (1)	9.21 (1)
10^0	3.39 (1)	6.28 (0)	6.21 (0)	2.16 (0)	2.36 (0)
15^0	1.87 (0)	8.07 (-2)		4.72 (-3)	
20^0	3.67 (-2)	2.26 (-1)		2.41 (-1)	
30^0	1.60 (0)	9.54 (-1)		6.46 (-1)	
40^0	2.56 (0)	1.22 (0)		7.52 (-1)	
60^0	3.07 (0)	1.23 (0)	1.22 (0)	6.75 (-1)	6.74 (-1)

DCS are values of DCS evaluated by Khare and Vijayshri (1988)(Kh-V)

Table-2: Positron-Sodium Atom Scattering

Energy	100 eV	200 eV	300 eV
Angle	DCS	DCS	DCS
5^0	1.12 (-1)	1.02 (-2)	1.01 (-3)
10^0	1.89 (-2)	5.30 (-2)	2.50 (-2)
15^0	4.50 (-2)	1.11 (-1)	4.38 (-2)
20^0	6.42 (-2)	1.41 (-1)	5.08 (-2)
30^0	8.66 (-2)	1.62 (-1)	5.48 (-2)
40^0	9.66 (-2)	1.68 (-1)	5.53 (-2)
60^0	1.02 (-1)	1.69 (-1)	5.63 (-2)

पुस्तकालय
132146
गुरुकुल कांगड़ी विश्वविद्यालय

RESULTS AND DISCUSSION

As literatures reveal, the positronium formation cross section decreases rapidly with enhancement in energy, so, its effect on direct channel is expected to be negligible.

In case of first atomic target, potassium, present differential cross section (DCS) attains minimum value at nearly 20^0, scattering angle at 100 eV whereas at 300 eV, this minimum shifts to angle of scattering nearly 10^0.

In case of second atomic target, sodium, differential cross section is observed to be minimum at angle of scattering 10^0 at 100 eV whereas at 300 eV, this minimum shifts to angle of scattering 5^0.

It is observed that with increase in energy of incident positron, the position of minimum DCS shifts towards forward angles.

In both cases DCS is sensitive to polarization potential which is most effective near forward direction of differential cross section.

The polarization potential is attractive whereas the static potential is repulsive. Their cancellation gives rise to the minimum value of DCS near forward direction.

At 200 eV and 300 eV the present values of DCS for positron-potassium atom scattering show good agreement with values of DCS presented by Khare and Vijayshri (1988) at angle of scattering 5^0, 10^0 and 60^0. This establishes the validity of our present approach.

All the dynamics of system cannot be accommodated in a single distorted wave method but the present method is observed to be suitable for analysis of positron-atom scattering with due success.

REFERENCES

1. Junker,B.R.(1975). *Phys. Rev.* A2 1552 (1975).
2. Khare,S.P. and Vijayshri, (1988).*Ind. J. Phys.* 62B 483 (1988).
3. Nordsieck,A.(1954). *Phys. Rev.* A93 785 (1954).

Bulletin of Pure and Applied Sciences
Vol. 32 D (Physics) Issue (No.1) 2013:P. 23-35
www.bpas.in

A MODIFIED APPROACH TO NOISE ANALYSIS IN CCII

Raj Kumar Tiwari[1], **Sachin Kumar**[1] **and G. R. Mishra**[2]
[1]Circuit Design and Simulation Lab., Department of Physics and Electronics,
Dr. R.M.L. Avadh University, Faizabad (U.P), India

[2]Department of Electronics, Amity University, Lucknow Campus

Email: rktiwari2323@yahoo.co.in, sachin.amitylko@yahoo.com,
gr_mishra@rediffmail.com

Received on 27 April 2013: Accepted on 30 May 2013

ABSTRACT

Noise has continually been a concern in circuit and system design as noise poses a lower limit that a signal can be accurately sensed. Sources of noise come from a variety of places and each source of noise has to be investigated and handled separately as they often come from different mechanisms. Current conveyers are unity gain active element exhibiting wide dynamic range, high linearity and high frequency performance than there voltage counterparts. The Paper presents a different approach to noise analysis on CCII topology, based firstly on the noise determination of each block and then on the analysis of CCII overall noise, considering the connections as shown in different sub blocks of CCII

Keywords : Current Conveyer, Noise, OTA, Inverter.

1.INTRODUCTION

Analog signal processing circuits and conditioning circuits are constantly demanding higher bandwidths and noise performance. With the request of a large number of elements on a single chip, has led to an improved interest in analog circuit design, especially for integrated circuits (Allen and Holberg 1987, 2002,Thoumazou *et al* , Sedra and Smith 1970). Recent trend towards miniaturized circuits has given a strong and decisive boost towards the design of low voltage low power analog integrated circuits with reduced interference levels and noise, they are widely utilized in portable system applications. The more gates integrated, the more important it is to reduce the power consumption and noise. Electronic noise and in particular 1/*f* noise has been a fundamental limit to engineers who attempt to measure and control increasingly smaller currents and voltages. Noise has continually been a concern in circuit and system design as noise poses a lower limit that a signal can be accurately sensed. Sources of noise come from a variety of places and each source of noise has to be investigated and handled separately as they often come from different mechanisms. Noise sources can from physical phenomena in the transistor. Other sources of noise may be the result of the operation of the circuit and the position of components. Power supply noise is one such noise source and is generally the result from ground loops which cause spurious signals to appear on the ground or supply planes that are then coupled into the transistors that are performing the sensing operations (Sedra and Smith 1970 Sedra *et al* 1990, Serdijin *et al* 1995).

With the demand for decreased power supply voltages for low-power applications and the shrinking of transistor dimensions for higher integration, noise presents a bigger challenge for analog circuit designers. In general the noise of the system becomes more difficult to mitigate as supply voltages decrease, bandwidth requirements increase, and especially when the signal of interest is small. Shrinking supply voltages poses a constraint because more and more of the available voltage is consumed by noise. High bandwidth systems will innately have noise due to the fact that in most cases the root-mean squared (RMS) of the noise is proportional to the square root of the bandwidth. When a signal is large compared to the system noise, then noise poses little problem; however, as the signal of interest becomes comparable to the noise it is increasingly difficult to distinguish between the signal and the noise and the noise in the system becomes a strict design criteria. An important metric of a circuit's small signal performance is the Signal-to-Noise Ratio (SNR) (Serdijin *et al* 1995, Hoog 1994, Van Vilet 1958,Kwok *et al* 1990,Arbel 1995).

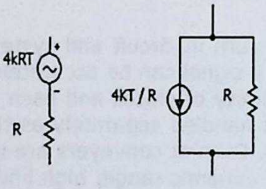

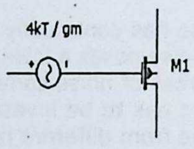

Fig 1a: Noisy Resistance equivalent **Fig1b:** Noisy Model for MOS

2. SEMICONDCTOR NOISE

Noise in electronics has been a concern for design engineers and a research interest since the conception of electrical systems. Noise in electronics is a voltage or current variation about some mean value. Thermal, shot, 1/*f*, and generation-recombination (GR) noise appear with a Gaussian distribution while random-telegraph noise (RTS) noise is found to be Non-Gaussian. Physical device noise is generated through processes such as the random motion, trapping, or random arrival of charge carriers. What makes understanding noise so important is that noise sets a lower limit on the capability of any particular device or circuit to reliably detect small signals (Sedra *et al* 1990, Honge 1994, Van Vilet 1958, Kwok *et al* 1990).

Most often a Gaussian noise source is one that is generalized by a single parameter with no frequency dependence. Another term that can be used to qualify this type of noise is to say that it is "white" noise. White noise is characterized by the standard deviation that is in the strictest sense constant across all frequencies. The amplitude distribution of such a noise source will have a normal probability distribution. MOSFET devices serve as the work horse for most all modern electronic devices in manufacture today. The devices are used in both digital and analog systems and it is the analog domain where noise is of utmost concern. There are four noise sources that are important in semiconductors (Allen and Holberg 1887). These noise sources are thermal, shot, GR, and 1/*f* noise. In order to develop good analog circuits, a basic understanding of the noise sources and analysis is required. Noise takes into account the unwanted and unpredictable voltage and current fluctuations in devices and networks. It is given by two kinds of contributions: external interference (coming from supply, wires, electromagnetic, etc), which can be reduced by accurate wiring and layout; internal noise (thermal, shot and flicker), due to physical fluctuations inherent to devices, which is more predictable and can be reduced by a proper design of transistor sizes (Serdijin *et al* 1995, Hooge 1994,Van Vliet 1958,Kwok *et al* 1990,Arbel 1995,Ferri *et al* 1999).

3.NOISE MODEL FOR MOS

In MOS transistors, the main noise contributions are given by thermal and flicker noise. The first is also called "White" noise, because its spectral density is constant over a given frequency. The flicker noise is also known as 1/f noise, because its spectral density is inversely proportional to frequency, so it is dominant at low frequencies. The intersection between flicker and white noise is called 1/f noise corner. In MOS devices, the thermal noise is inversely proportional to its transconductance and consequently, to its aspect ratio W/L while flicker is inversely proportional to WL product, as a consequence, the choice of the transistor sizes is important to minimize noise and has to be done according to the working frequency of the circuit. The thermal motion of electrons is reputed to be the source of what is called "thermal noise". From a classical point of view, a noisy resistor R can be modelled as an ideal resistance and an equivalent noise source as shown in fig.1a. (Allen and Holberg 2002, Thoumazou *et al* 1993, Sedra and Smith 1970) . The noise expressions are given both in terms of voltage and current spectral density as follows:

$$\overline{V_n^2} = 4KTR\left(\frac{V^2}{Hz}\right) \;;\; \overline{i_n^2} = 4KTR\left(\frac{A^2}{Hz}\right)$$

K is Boltzmann constant and T absolute temperature, expressed n Kelvin degrees. A MOS transistor can be regarded as a voltage controlled resistance, so its noisy model could be an ideal MOS having in parallel a current noise source dependent on channel conductance (g_{DO})

$$\overline{i_n^2} = 4KT\gamma g_{DO}$$

From above equation, γ has a value dependent on the operating region of the transistor. Its value is 1 for a transistor in saturation, and 2/3 when its drain source voltage approaches zero. In the saturation region above equation becomes

$$\overline{i_n^2} = 4KT\gamma g_m$$

Obviously, the equivalent noise source can be considered at the input gate terminal, dividing it by g_m^2, as a voltage spectral density as shown in fig 1b. Shot noise has been observed in all those situations where a current is controlled by a voltage, as, for example, the gate of MOS transistors. Its formula is:

$$\overline{i_S^2} = 2qI_G$$

Where q is the electronic charge of the electron and I_G the gate current (Sedra *et al* 1990, Serdijin *et al* 1995, Hooge 1994, Ferri *et al* 2001). As consequence, MOS devices, where the gate current is extremely low, shot noise contribution can be easily neglected in a first order evaluation. Several electronic devices show a noise component strongly affected by frequency. It has been proved, for example that in some situations noise shows a component inversely proportional to the frequency that is its level increases when frequency is lowered: this kind of noise has been named "flicker noise" or "1/f noise". In a MOS transistor, 1/f noise can be modelled by a noise current generator named $i_f^2 = A_f / f$, placed in parallel with the drain source impedance. Alternatively, it can be taken into account by a series voltage generator connected to gate terminal, named $V_f^2 = K_f/f$, K_f and A_f values depend numerically on the technology employed. The small signal model of MOS with noise effects included is shown in fig1c, this was done by adding noise generators, where different noise generators were modelled as current generators placed at input and output terminals of the MOS transistor (Hooge 1994,Van Vliet 1958 , Piovaccari *et al* 1995,Ferri and Guerrini 2001,Ferri *et al* 2001, Ferri *et al* 2001,Kurashina *et al* 1998, Bruun 1997).

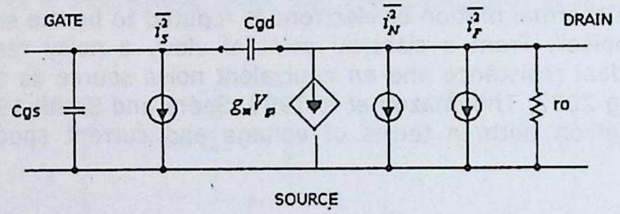

Fig 1c: Small signal noisy model of MOS transistor

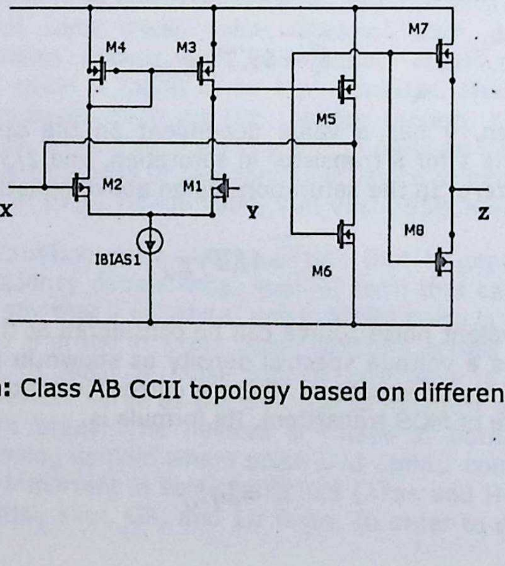

Fig 2a: Class AB CCII topology based on differential pair.

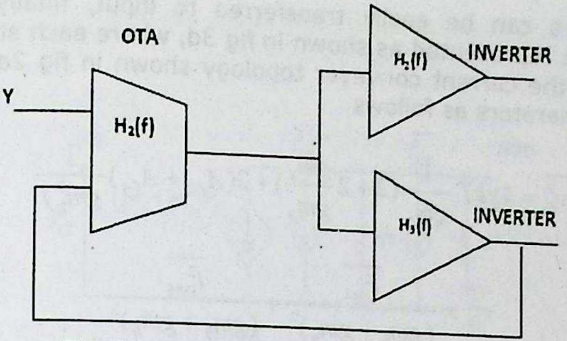

Fig 2b: OTA based CCII block diagram

4.NOISE EVALUATION IN CC II

Evaluation of the noise is more important at reduced supplies, where signals have reduced amplitudes. Current conveyer topology shown in fig 2a, and all its improvements later on, follow, basically, the block scheme reported in fig 2b, where each block has been characterized by its transfer function H(f). For the current conveyer shown in fig 2b, we have a differential pair that may be thought as OTA, followed by two inverting stages. The output of one of these inverters is connected in feedback to one OTA input terminal, so to perform the low impedance X node, while the other inverter is used to obtain the high impedance output node named Z. The first block represented by the input differential pair given in figure 3a posses all related current noise generators. The equivalent output noise current generator, considering all sources as uncorrelated, is given as:

$$\overline{i_{out}^2} = \overline{i_{DS1}^2} + \overline{i_{DS2}^2} + \overline{i_{DS3}^2} + \overline{i_{DS4}^2}$$

$$= 4\gamma kT(gm_1 + gm_2 + gm_3 + gm_4) + (A_{f1} + A_{f2} + A_{f3} + A_{f4})\frac{1}{f}$$

Moreover, considering the fact that M1-M2 and M3-M4 can be considered matched, therefore we can write

$$\overline{i_{out}^2} = 4\gamma kT(2gm_2 + 2gm_4) + 2(A_{f2} + A_{f4})\frac{1}{f}$$

Dividing by gm_2^2, to obtain the equivalent input noise voltage generator, we get

$$\overline{V_{I1}^2} = \frac{\overline{i_{out}^2}}{gm_2^2} = 4\gamma kT\frac{1}{gm_2}(2 + 2\frac{gm_4}{gm_2}) + 2(A_{f2} + A_{f4})\frac{1}{gm_2^2 f}$$

From the noise analysis, an equivalent model for noisy OTA is obtained, as shown in fig 3b, formed by a noise generator and noise free OTA. The small signal equivalent circuit, with noise generators is shown in fig 3c, where

$$\overline{i_{DS1}^2} = 4\gamma kTgm_1 + A_{f1}\frac{1}{f}\ ,\ \overline{i_{DS2}^2} = 4\gamma kTgm_2 + A_{f2}\frac{1}{f}$$

The noise generators can be easily transferred to input, finally the CCII noisy equivalent circuit can represented as shown in fig 3d, where each stage is considered now noise free. For the current conveyer topology shown in fig 2a, it is possible to summarize noise generators as follows

$$\overline{v_{I1}^2} = 4\gamma kT\frac{1}{gm_2}(2+2\frac{gm_4}{gm_2}) + 2(A_{f2}+A_{f4})\frac{1}{gm_2^2 f}$$

$$\overline{v_{I2}^2} = \frac{\overline{i_{DS5}^2}}{(gm_5+gm_6)^2} + \frac{\overline{i_{DS6}^2}}{(gm_5+gm_6)^2}$$

$$\overline{v_{I3}^2} = \frac{\overline{i_{DS7}^2}}{(gm_7+gm_8)^2} + \frac{\overline{i_{DS8}^2}}{(gm_7+gm_8)^2}$$

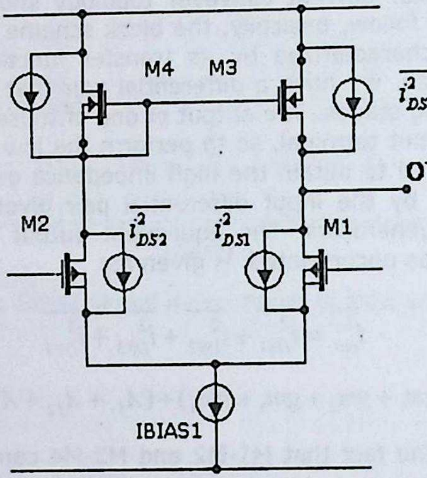
M4
M3
$\overline{i_{DS4}^2}$
$\overline{i_{DS3}^2}$
OUT
M2
$\overline{i_{DS2}^2}$
$\overline{i_{DS1}^2}$
M1
IBIAS1

Fig 3a: Simple OTA with noise generators

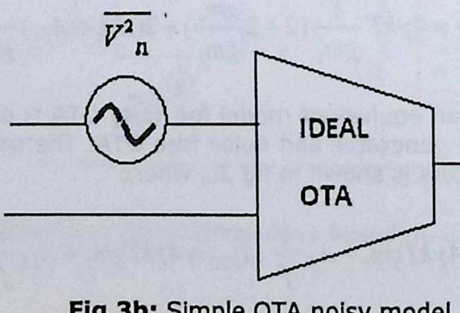
$\overline{V^2}_{I1}$
IDEAL
OTA

Fig 3b: Simple OTA noisy model

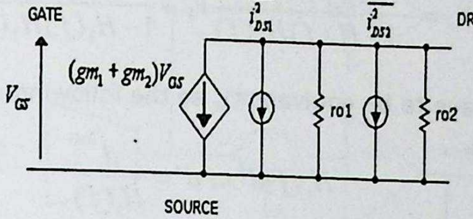

Fig 3c: CMOS inverter small signal equivalent circuit with noise generators

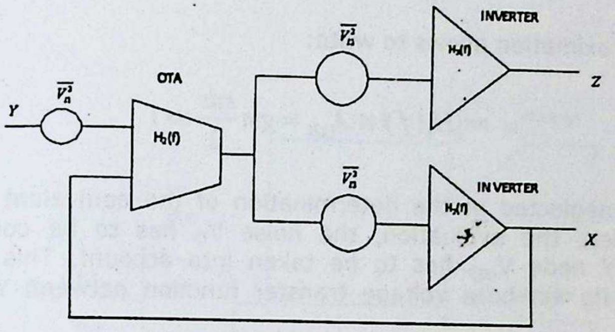

Fig 3d: CCII equivalent circuit with noise generators

In order to obtain a useful model for CCII noise and especially to simplify the analysis, all the noise generators have to be referred to Y and X nodes. In the proposed example, we obtain three equivalent input generators (v_{eq1}, v_{eq2}, and v_{eq3}) from three equivalent noise sources (v_{eq1}, v_{eq2}, and v_{eq3}), for what concerns the first noise generators, it is obvious

$$\overline{V^2_{eq1}} = \overline{V^2_{I1}} .$$

Then, in order to simplify the evaluation of the equivalent Y node noise due to V_{eq2}, related to the first inverter, the CCII block scheme has been modified, as shown in fig4a. In detail, the OTA has been replaced by a subtracting node and a block having a transfer function equal to $H_1(f)$. The equivalent input noise of the inverter related to X node has been considered as an additive quantity, named d. In this condition, the transfer function between X and Y is:

$$V_x = -\frac{H_1(f)H_2(f)}{1-H_1(f)H_2(f)}V_Y + \frac{H_2(f)}{1-H_1(f)H_2(f)}d$$

The noise generator at inverter input can be transferred to CCII input, as in fig 4b. The equivalent noise at Y is now evaluated, considering an additive disturbs d' at Y node and imposing that it gives the same output result. The transfer function between Y and X node is obtained as follows:

$$V_x = -\frac{H_1(f)H_2(f)}{1-H_1(f)H_2(f)}V_Y + \frac{H_2(f)}{1-H_1(f)H_2(f)}d'$$

The two situations have to be equivalent\, so the following relationships have to be verified

$$H_1(f)d' \Rightarrow d' = \frac{d}{H_1(f)}$$

$$\sqrt{\overline{V_{eq2}^2}} = \frac{\sqrt{\overline{V_{I1}^2}}}{H_1(f)} \Rightarrow \overline{V_{eq2}^2} = \frac{\overline{V_{I1}^2}}{(H_1(f))^2}$$

A first order approximation allows to write:

$$|H_1(f)| \approx A_{VO1} = gm\frac{rds}{2} \gg 1$$

So V_{eq2} can be neglected in the determination of the equivalent input noise at Y node. To complete the evaluation, the noise V_{I3} has to be considered, and its contribution at Y node V_{eq3} has to be taken into account. This can be done as considering the fig 4c, here voltage transfer function between Y and X nodes is obtained as:

$$V_X = -\frac{H_1(f)H_2(f)}{1-H_1(f)H_2(f)}V_Y$$

Following the same approach, the equivalent scheme shown in figure 4d is considered, from the circuit we have:

$$V_X = -\frac{H_1(f)H_2(f)}{1-H_1(f)H_2(f)}V_Y + \frac{H_1(f)H_2(f)}{1-H_1(f)H_2(f)}d'$$

$$d' = 0 \Rightarrow \overline{V}_{eq3}^2 = 0$$

This means that the inverter related to Z node does not give noise contributions at Y node, then it can be deduced:

$$\overline{V_Y^2} = \overline{V_{eq1}^2} + \overline{V_{eq2}^2} + \overline{V_{eq3}^2} + \overline{V_{eq4}^2}$$

$$4\gamma kT\frac{1}{gm_2}(2+2\frac{gm_4}{gm_2}) + 2(A_{f2}+A_{f4})\frac{1}{gm_2^2 f}$$

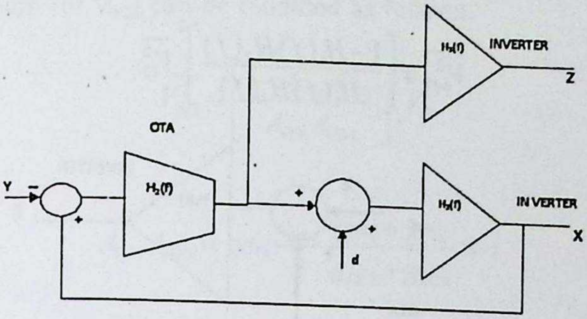

Fig 4a: CCII block scheme modified topology

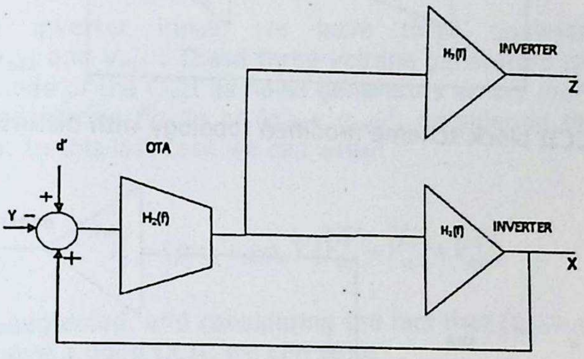

Fig 4b : CCII block scheme modified topology with disturb at $H_2(f)$ input transferred to Y node.

To complete the evaluation of the current conveyer noise sources, the equivalent current noise at X node has to be calculated. The approach is exactly the same used for the Y node noise estimation. The equivalent noise at X is evaluated through the circuit shown in fig 4e. Following the same approach as used in previous computations, the equivalent noise at X node originated by noise of $H_3(f)$ inverter can be evaluated as follows:

$$d' = \sqrt{\overline{V_{eq3}^2}};$$

$$V_z = -\frac{H_1(f)H_3(f)}{1-H_1(f)H_3(f)}V_Y + \frac{H_1(f)H_2(f)H_3(f)}{1-H_1(f)H_3(f)}d'$$

$$\frac{H_1(f)H_2(f)H_3(f)}{1-H_1(f)H_3(f)}d' = H_3(f)d \Rightarrow d' = \frac{H_1(f)H_2(f)}{1-H_1(f)H_3(f)}d$$

Which implies after squaring :

$$\overline{V_{eq3}^2} = \left[\frac{1-H_1(f)H_2(f)}{H_1(f)H_3(f)}\right]^2 \overline{V_{I3}^2}$$

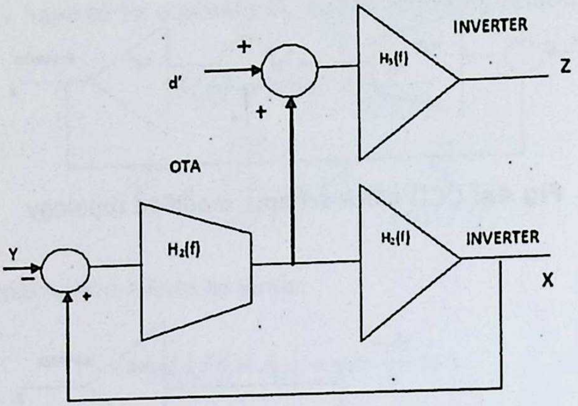
INVERTER
+
d'
H₃(f)
Z
+
OTA
H₂(f)
H₂(f)
INVERTER
Y
−
+
X

Fig 4c: CCII block scheme modified topology with disturb at $H_3(f)$

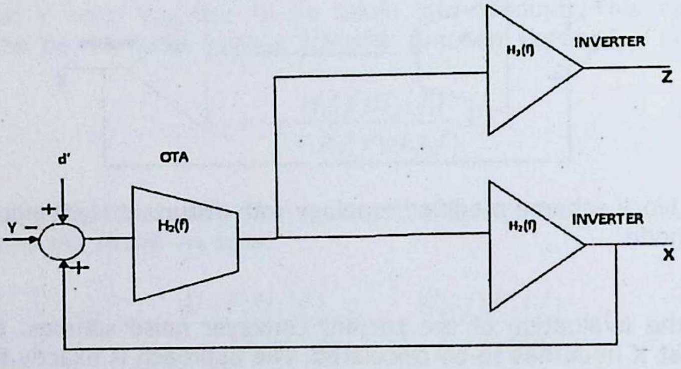
H₃(f)
INVERTER
Z
d'
OTA
+
Y −
H₂(f)
H₂(f)
INVERTER
+
X

Fig 4d: CCII block scheme modified topology with disturb at $H_3(f)$ input transferred to Y node

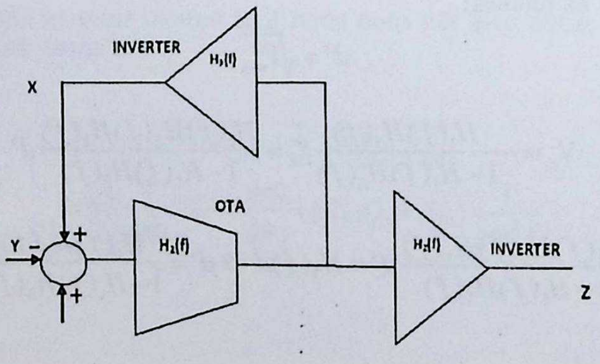
INVERTER
H₃(f)
X
OTA
Y −
+
H₁(f)
H₂(f)
INVERTER
+
Z

Fig 4e: CCII block scheme modified topology for Y node noise estimation

Since we are not considering high frequencies noise evaluation, each transfer function $H_1(f)$ in previous computations can be approximated by its low frequency value A_{VOI}. Expression for V_{eq3} can be modified as follows:

$$\overline{V_{eq3}^2} \approx \left[\frac{1-A_{VO1}A_{VO2}}{A_{VO1}A_{VO2}}\right]^2 \overline{V_{I3}^2}$$

$$A_{VO1}A_{VO2} = gm_2 \frac{r_{DS2}}{2} \frac{gm_5 + gm_6}{g_{DS5} + g_{DS6}} \gg 1$$

$$\Rightarrow \left[\frac{1-A_{VO1}A_{VO2}}{A_{VO1}A_{VO2}}\right]^2 \approx 1 \Rightarrow \overline{V_{eq3}^2} \approx \overline{V_{I3}^2}$$

Finally at $H_2(f)$ inverter input, we have three equivalent voltage noise generators, V_{eq1}, V_{eq2} and V_{eq3} . These three voltage generators can be transferred to the output i.e. X node of the CCII as noise generators simply multiplying their values by $(g_{m1}+ g_{m1})^2$ considering fig 5a or $(g_{m5}+ g_{m6})^2$, considering the current conveyer proposed in fig 2a. In this last case we can write:

$$\overline{i_X^2} = (gm_5 + gm_6)^2 (\overline{V_{eq1}^2} + \overline{V_{eq2}^2} + \overline{V_{eq3}^2})$$

Since V_{eq1} can be neglected, and considering the fact that $(g_{m5}+ g_{m6})$ has to be equal to $(g_{m6}+ g_{m7})$ to have a good CCII, we can write

$$\overline{i_X^2} = (gm_5 + gm_6)^2 (\overline{V_{I1}^2} + \overline{V_{I2}^2})$$

$$= 4\gamma kT(gm_5 + gm_6 + gm_7 + gm_8) + (A_{f5} + A_{f6} + A_{f7} + A_{f8})\frac{1}{f}$$

Finally a model for the noisy current conveyer can be drawn, as shown in fig 5b. The two equivalent noise sources are given by following expressions:

$$\overline{V_X^2} = 4\gamma kT \frac{1}{gm_2}(2 + 2\frac{gm_4}{gm_6}) + 2(A_{f2} + A_{f4})\frac{1}{gm_2^2}\frac{1}{f}$$

$$\overline{i_X^2} = 4\gamma kT(gm_5 + gm_6 + gm_7 + gm_8) + (A_{f5} + A_{f6} + A_{f7} + A_{f})\frac{1}{f}$$

From the theoretical analysis, it is possible to see that noise is directly affected by transistor operating points by means of γ parameter.

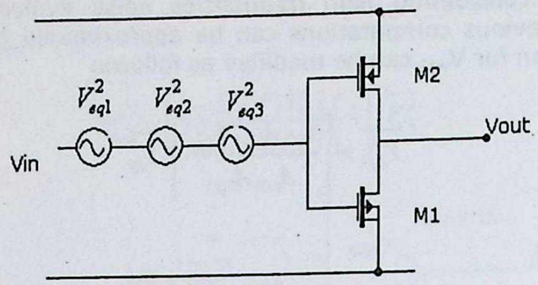

Fig 5a: Equivalent noise generators at $H_2(f)$ inverter input

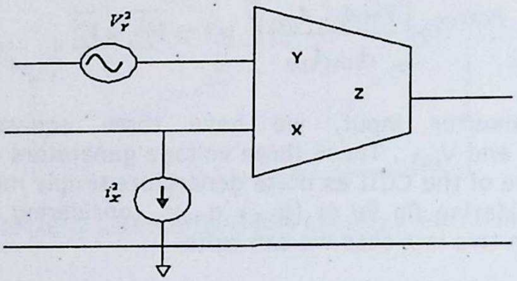

Fig 5b: Complete equivalent model for noisy CCII .

5.CONCLUSION

The Paper presents a different approach to noise analysis on CCII topology, based firstly on the noise determination of each block and then on the analysis of CCII overall noise, considering the connections as shown in different sub blocks of CCII. The theoretical analysis shows that noise is directly affected by transistor operating points by means of γ parameter.

6.ACKNOWLEDGEMENT

The authors are thankful to Maj. General K. K. Ohri, AVSM (Retd.) Pro Vice Chancellor, AUUP, Lucknow Campus, Prof. S. T. H. Abidi (Director, ASET), Brig. Umesh K. Chopra (Director, AIIT, & Dy. Director, ASET) and Prof O P Singh (Head of Department) for their cooperation, motivation and suggestive guidance.

REFERENCES

1. Allen and Holberg, D.R. "CMOS analog circuit design", New York: Holt, Rinehart and Winston, Inc. 1987.
2. Allen,P.E. and Holberg,D.R. "CMOS analog circuit design", New York: Oxford University Press,2002.

3. Arbel,A.F.(1995). "Comparison between the noises Performance of current-mode and voltage-mode amplifiers," *Analog Integrated Circuits and Signal Processing*, Vol. 7: 221-242, May 1995.

4. Bruun,E. Analysis of the noise characteristics of CMOS current conveyers. *Analog Integrated Circuits and Signal Processing*. Nr. 12; 1997; pp 71-78.

5. Ferri,G., De Laurentiis,P., Amico,A.D. and Stochino,G. Low voltage design. Electronics World, September 1999; pp 714-722.

6. Ferri,G. and Guerrini,N.(2001). Low-voltage low power current conveyers: designs and applications. *Alta Freqenza*. Nr 4; Vol 48:405-409.

7. Ferri,G., De Larentiis,P. and Stochino,G. Current conveyer II. Electronics World, April 2001; pp.300-302.

8. Ferri, G., De Larentiis,P. and Stochino,G. Current conveyer II. Electronics World, May 2001; pp379-381.

9. Hooge, F.N.(1994)."1/*f* noise sources," *IEEE transactions on Electron Device*, Vol. 41, (No. 11): 1926-1935, November 1994.

10. Kurashina,T., Ogawa, S. and Watanabe,K. A high performance class AB current conveyer. Proceedings of the IEEE International Conference on Electronic Circuits and Systems, 1998. Lisboa, Portugal.

11. Kwok K. Hung, Ping K. KO, Chenming Hu, and Yiu C.Cheng. "A Unified Model for the Flicker Noise in Metal-Oxide-Semiconductor Field-Effect 41 Transistors," *IEEE Transactions on Electron Devices*, Vol. 37 (No. 3): 654-665, March 1990.

12. Piovaccari,A., Graffi,S. and Masetti,G. A low voltage low power CMOS current conveyer. Proceedings of the European Conference on Circuit, Theory and Design, 1995.

13. Sedra,A.S. and Smith,K.C.(1970). "A second generation current conveyor and its application" *IEEE trans. Circuit theory*, Vol.ct-17 :132-134, Feb.1970.

14. Sedra,A.S., Roberts, G.W. and Gohh, F.(1990). "Current conveyor. History, progress and new results," *IEE Proceedings Part G: Electronic circuits and Systems*, Vol. 137:78-87 1990.

15. Serdijin,W.A., Vander Woerd,A.C., Kuenen,J.C. Low-voltage low-power analog integrated circuits. Kluwer Academic Publishers, Boston 1995.

16. Thoumazou,C., Lidgey,F.J. and Haigh,D.G. " Analog Integrated Circuits: The current mode approach "IEEE circuit and systems series 2(books) 1993.

17. Van Vliet, K.M.(1958)."Noise in Semiconductors and Photoconductors," *Proceedings of the IRE*, Vol.46(No. 6): 1004 – 1018, June, 1958.

Bulletin of Pure and Applied Sciences
Vol. 32 D (Physics) Issue (No.1) 2013:P.37-41
www.bpas.in

TROTTER DECOMPOSITION AND A SERIES EXPANSION OF THE PARTITION FUNCTION FOR HUND'S EXCHANGE COUPLING IN A QUANTUM MONTE CARLO ALGORITHM

Seema Priyadarshini
Department of Math, Rajendra College Chapra, J.P. University, Chapra, (Bihar), India.

Rajiv Mishra
Department of Math, Rajendra College Chapra, J.P. University Chapra, (Bihar), India

Kumari Ruchi
Deptt. of Physics, S.M. College, Hajipur, Vaishali ,(Bihar),India.

Shashi Shekhar
Department of Math, ABS College Lalganj, Vaishali, (Bihar), India.

Sanjay Kumar Singh
Deptt. of Physics, R.J.S. College, Dighwara, Saran, (Bihar), India.

Gyandeo Prasad Tiwari
Department of Physics, Rajendra College Chapra, Saran, (Bihar), India.

Received on 25 April 2013: Accepted on 20 May 2013

ABSTRACT

We have studied numerically exact auxiliary field quantum Monte Carlo scheme for the spin and orbital rotational invariant Hamiltonian by combining series expansion and Trotter decomposition. We have used algorithm to solve the dynamical field theory equations. We have employed Boltzmann operator with respect to the total interaction. The method significantly relaxes the sign problem and allows in principle for more than two orbitals. The computational effort increases with the perturbation orders appearing in the Mote Carlo samples. The order become very large in multiorbital systems. To remove this difficulty we have used the Hirsch-Fye quantum Monte Carlo and parturbation series expansion quantum Monte Carlo methods. This algorithm enabled us not only to handle three or more orbitals but also to reach much stronger coupling than in Hirsch-Fye quantum Monte Carlo calculations, even for the two orbital Hubbard model.

Key words : Quantum Monte Carlo scheme, Expansion and Trotter decomposition, Boltzmann operator ,Mote Carlo samples, Hirsch-Fye quantum Monte Carlo calculations.

INTRODUCTION

Arita and Held (2005) studied multiorbital Mott-Hubbard transition by dynamical mean field theory, showing that the correct symmetry of the exchange coupling is essential in close to and at the Mott-Hubbard transition. Anisimov *et al* (1997) reported that local density approximation and dynamical mean field theory allowed for calculating strong correlations in materials from first principles and it had become most active fields for research in Mathematical Physics. Caffarel *et al* (1994) and Hirsch and Fye (1986) showed that for multiorbital models, the exact diagonalization and Monte Carlo method are widely used for nonparturbative impurity solutions. They showed that both exact diagonalization and Hirsch-Fye quantum Monte Carlo methods have their pros and cons and are favorable in different situations. Han(2004) and Sakai *et al* (2004) studied the transformation with a real and discrete auxiliary field for the terms in two-orbital systems. S-wave super conductivity and orbital-selective Mott transition have been investigated with their transformation. It is still difficult to treat more than two orbitals because the exponentials of $\hat{Hj}$ is not equal to the product of the exponentials of the distinct two orbital parts $\hat{Hj}^{mm'}$. So it is not possible to decouple $\hat{Hj}$ for three or more orbitals by the simple product by two orbital parts. Rombouts *et al* (1999) first proposed the auxiliary field quantum Monte Carlo method based on perturbation series expansion for electron systems. Blankenbecler *et al* (1987) reported that Rowboats etal applied parturbation series expansion to the finite size single-orbital Hubbard model and succeeded in obtaining results without time discretization errors with less computational time than the conventional, Trotter decomposition algorithm. Rostov *et al* (2005) used a different algorithm to explain series expansion by the partition function for obtaining dynamical mean field theory equations. To remove previously found difficulties we have used a combination of Hirsch-Fye quantum Mote Carlo method and perturbation series expansion quantum Mote Carlo methods and satisfactory results were found. Obtained results were good in comparison to previous results.

METHODS AND MATERIALS

We have used Trotter-series-expansion method. We first applied the algorithm to study ferromagnetism in the two orbital Hubbard model within the dynamical mean field theory. We started with the series expansion of the Boltzmann factor for continuous time. We have performed this only for Hĵ i.e.

$$e^{Y-B\hat{H}} = e^{-B}(\hat{H}o\hat{H}u) + Y - B\hat{H}_J - e^{-B}(\hat{H}o\hat{H}u) + \sum_{k=1}^{\infty}\int_0^1 dt_k \ldots$$

$$\int_0^{t_2} dt_1 \prod_{i=k}[e^{t_i B(\hat{H}o+\hat{H}u)} \times (Y - B\hat{H}_J)e^{t_i B(\hat{H}o+\hat{H}u)} e^{-B(\hat{H}o+\hat{H}u)} \ldots\ldots\ldots\ldots\ldots\ldots(i)$$

Where Boltzmann factor have been shifted by a constant Y for $B\hat{H}_J$

We can show that

$$\sum_{S_1,\dots\dots,S_L}^{0,1} F(k;S_1,S_2,\dots\dots\dots,S_L)\prod_{i=1}^{L}\{e^{-\Delta T(\hat{H}o+\hat{H}u)}\hat{X}s_i\}+O(\Delta T)\dots\dots\dots\dots\dots\dots\dots\dots(ii)$$

Where F is a positive weight factor,

$$K=\sum_{i=1}^{L} Si \quad \text{and} \quad \hat{X}o=1\,.$$

We have replaced those terms having consecutive $\hat{X}_1$ by proximate terms including only one $\hat{X}_1$'s per imaginary time interval. We have separated out $\hat{H}u$ using Trotter decomposition as

$$e^{-\Delta T(\hat{H}o+\hat{H}u)}=e^{-\Delta T\hat{H}o}e^{-\Delta T\hat{H}u}+O(\Delta T^2)\dots\dots\dots\dots\dots\dots\dots\dots\dots\dots(iii)$$

Which is similar to Hirsch-Fye quantum Monte Carlo method.

RESULT AND DISCUSSION

Graph(1) shows a typical distribution N_k of the order of perturbation K contributing in the Monte Carlo Simulation for n=1.9, the imaginary time B=8, the interorbital U'=4, the Hund's coupling J=0.2. The resulting algorithm has a peak in the distribution residing at much lower K than for the perturbation series expansion quantum Monte Carlo approach. In present method we have used the expansion only with respect to $\hat{Hj}$, while the perturbation series expansion quantum Monte Carlo method expands with respect to the total interaction $\hat{H}u+\hat{Hj}$. In actual calculation the weight is virtually zero above a certain order K max. The maximum order in the distribution is $K_{max} \approx 100$ for the perturbation series expansion quantum Monte Carlo method while $K_{max} \approx 15$ is much lower in our quantum Mote Carlo method. Here we have used imaginary time interval L to be greater than 100. The smaller value of L reduces the computational effort in quantum Monte Carlo simulations. Graph (2) shows the computable regions for our quantum Monte Carlo method when $\hat{Hj}$ is included. It is seen from graph (2) that a much wider parameter region becomes computable in our algorithm than in the Hirsch-Fye quantum Monte Carlo method. We see that $\hat{Hj}$ is the source of negative weights appear L times for every simple in the Hirsch-Fye quantum for every sample in the Hirsch-Fye quantum method. But in our result we have only k such terms an average. When $J \leq 0.2$, we can get five to ten times lower temperatures. We also found that to obtain a region as computable when the average sign is greater than 0.01 .

CONCLUSION

In this work we have found that when combined Trotter decomposition and series expansion of the portion function for Hund's exchange coupling in a quantum Monte Carlo algorithm is used for multiorbital systems then there are rotational symmetries. These results are not found in conventional methods. The correct symmetry of the exchange coupling is essential for spin and orbited motion in the Mott-Hubbard transition. For correlation effects in multiorbital systems, the dynamical mean field theory is most successful method which has been used in our work for realistic calculations. Our results have great importance for the preservation of SU(2) symmetry. The tight binding parameters have also been used for calculation from the local density approximation. The self energy was obtained from Dyson's equation and the Green's function was calculated by averaging over quantum Mote Carlo samples. For this purpose we have used hyperbolic lattice with band width W=2. The results obtained were in good agreement with previously obtained results. From the graph(1) and (2) it is clear that our results were better than previous results.

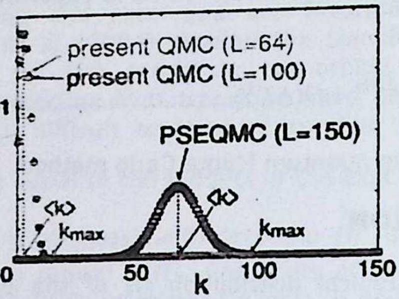

Graph : 1 - The distribution K_L of the order of perturbation k for the two-orbital Hubbard model with n=1.9, □=8, U'=4, J=0.2 obtained with the present algorithm (L=64 or 100) and with the PSEQMC algorithm (L=150)

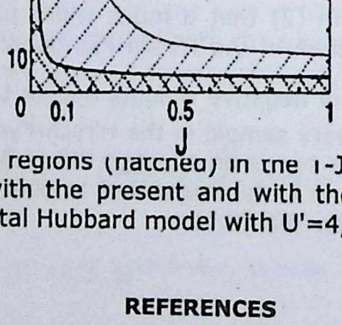

Graph : 2 - Computable regions (hatched) in the T-J parameter space that can be computed with the present and with the Hirsch-Fye QMC method for the two-orbital Hubbard model with U'=4, W=2.

REFERENCES

1. Arita, R. and Held, K. (2005). *Phys. Rev*. B. 72: 201102 (R).

2. Anisimov, V.I. *et al* (1997). *J. Phys. Condens Matter*, 9: 7359.

3. Blankenbecler, R. *et al* (1981). *Phys. Rev.* D, 24: 2278.

4. Caffarel, M. *et al* (1994). *Phys. Rev. Lett.* 72: 1545.

5. Han, E. (2004). *Phys. Rev.* B, 70: 054513.

6. Hirsch, J.E. and Fye, R.M. (1986). *Phys. Rev. Lett.* 56:2521.

7. Rombouts, S.M.A. *et al* (1999), *Phys. Rev. Lett.* 82, 4155.

8. Rubstov. A.N. *et al* (2005), *Phys. Rev.* B, 72: 035122.

9. Sakai, S. *et al* (2004). *Phys. Rev.* B. 70: 172504

Bulletin of Pure and Applied Sciences
Vol. 32 D (Physics) Issue (No.1) 2013:P.43-50
www.bpas.in

ELECTRONIC SPECTRA AND STRUCTURE OF CARBON DIOXIDE AND NITROUS OXIDE BY RINDO-CI METHOD

K. K. Karun,
Department of Physics, S. G. S. M. College, Sheikhpura (Bihar)

G. Chandra,
Department of Physics, T. N. B. College, Bhagalpur(Bihar)

B. K. Singh,
University Department of Physics, T. M. B. University, Bhagalpur(Bihar)

Received on 28 April 2013: Accepted on 30 May 2013

ABSTRACT

The electronic spectra and structure of carbon dioxide and nitrous oxide have been studied by RINDO-CI method. First the equilibrium geometries of the molecules have been calculated and these equilibrium geometries are used to predict the other properties. The calculated ground and excited state properties along with S-T splitting and Rydberg transitions are compared with experimental values. The results are in a good agreement with experimental values.

Key words: Electronic spectra, Rydberg transition, Equilibrium geometries, RINDO-CI, Ionization potential, Excited states.

INTRODUCTION

Molecular structures and electronic spectra of oxides have been calculated by several workers by different methods. Recently geometric and electronic structures of oxides like MoO_3 and MoO_2 have been calculated by Scanlon *et al* (2010) using the generalized gradient approximation density functional theory. Karun *et al* (2012) calculated the ground and excited state properties of HNO_2, CH3NO2 and $C_2H_3NO_2$ using RINDO-CI method and found good agreement with experimental result. In the present work we have used RINDO-CI method (Singh and Haque 1977) to carbon dioxide and nitrous oxide which show significant biological activities contribute to pollution of the atmosphere.

The theoretical studies on the electronic spectrum of carbon dioxide have also been done by several workers in past years (Tripathy 1981,Herzberg 967,Mc Curdy and Mc Koy 1974, England *et al* 1977,England Ermler 1979) .Nitrous oxide though having the same number of electrons as Carbon dioxide does absorb in the near ultraviolet region unlike that of carbon dioxide. The absorption spectrum of nitrous oxide has been studied by various workers (Sponer and Bonner 1940,Zelikoff *et al* 1953,Tanaka *et al* 1960,Astoin 1957) . The triplet state of nitrous oxide has also been studied by Kupermann *et al* (1978) in its electron impact spectrum. But the experimental observations are not found in the close resemblance with these theoretical studies. To remove the anomalies we have applied the RINDO-CI method in the present study.

METHOD

RINDO-CI method (Singh and Haque 1977) has been used to calculate the optimized geometries of these molecules. The calculated geometries have been used for the further prediction of ground and excited state properties of these molecules. The ground state geometry of carbon dioxide has been taken from Sutten (1969) and that of nitrous oxide from Mclean and Yoshimina (1967). The details are listed in table-1.

Table- 1: The Geometry of the Molecules
(Bond length in Å and bond angles in degrees)

Molecule	Geometry		
	Reported	**Reference**	**Present calculated**
CO_2	C-O = 1.16Å	c	1.13Å
	∠OCO = 90°		87°
N_2O	N-N = 1.125Å	d	1.118Å
	N-N = 1.185Å		1.192Å

C: Ref.[14], d: Ref. [15]

RESULTS AND DISCUSSION:

Charge Distribution: The net charge distributions in nitro-molecules are shown in fig-1. The calculation shows that in both the molecules the central carbon or nitrogen atoms are positively charged, while the other two oxygen or nitrogen atoms on either side of central atom are negatively charged.

Fig – 1: Net Charge Distribution in N_2O and CO_2

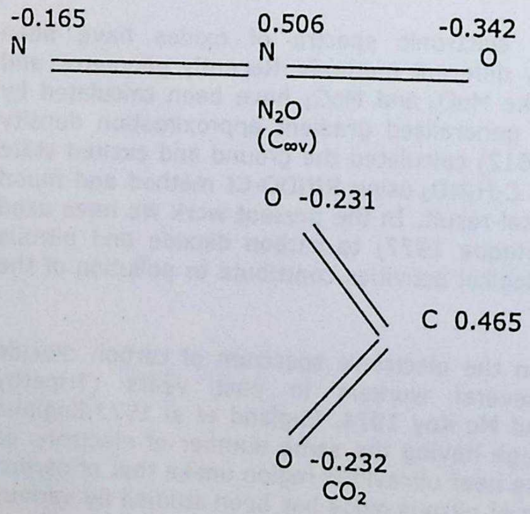

IONISATION POTENTIALS:

The Koopman's theorem ionization potentials (IP) along with symmetries of the corresponding orbitals are tabulated in table-2. This table also includes the experimental values obtained from the different sources (Rabalais *et al* 1969,Turner *et al* 1970).

The calculated IP's of carbon dioxide and nitrous oxide are somewhat lower than the experimentally observed values. RINDO-CI method predicts that in CO_2 and N_2O, a σ-electron is removed before a π-electron. This feature is found to be in line with experimental observation. Our calculated values for first ionization potentials are in better agreement than calculated by others where disagreement is of the order of about 2 eV.

Table-2 :The Lowest Ionization Potentials of CO_2 and N_2O (in eV)

Molecule	Exptl. value c	Theoretical value	
		RINDO-CI	
	I.P.	I.P.	Symm.
CO_2 (C_{2v})	13.78	12.88	$B_1(\sigma_n)$
	17.59	13.57	$B_2(\pi_n)$
	18.25	16.23	$B_1(\sigma)$
	19.40	16.85	$B_2(\pi_n)$
		20.44	$B_1(\sigma)$
		35.02	$B_1'(\sigma_n)$
N_2O ($C_{\infty v}$)	12.89	12.66	$A_1(\sigma_n)$
	16.38	12.82	$A_2(\pi_n)$
	18.23	16.03	$A_1(\sigma)$
	20.11	16.75	$A_1(\sigma)$
		16.98	$A_2(\pi)$
		21.46	$A_1(\sigma_n)$
		35.59	$A_1(\sigma)$

c: Ref. [17]

ELECTRONIC SPECTRA:

The electronic spectra predicted by RINDO-CI for carbon dioxide and nitrous oxide have been tabulated in table-3 and table-4. Table-3 contains the S-S transition whereas table-4 contains S-T transitions. Our calculations offer a better description of the excited states of these molecules along with Rydberg series and singlet-triplet splitting.

(i) Carbon dioxide (CO_2) :

The lowest energy S-S transition of carbon dioxide calculated by RINDO-CI method is predicted at 2.13 eV with oscillator strength $f = 5x10^{-3}$. This is assigned as $n \rightarrow \sigma^*$ transition and is entirely a valence shell type.This is followed by another $n \rightarrow \sigma^*$ transition at 3.48 eV and seems to be degenerate with the first. This is followed by a $n \rightarrow \pi^*$ which is predicted to lie at 3.96 eV.

All the three transitions lie in the range of observed bands of carbon dioxide in the region 2.38-3.54 eV.

The weak bands at 4.78 eV (f = $1x10^{-4}$) and at 6.23eV (f = $4x10^{-3}$) are assigned as n→π* and σ→σ* transitions respectively. These bands however correspond to the observed bands of Rabalais et al [18], with difference that the intensities of these bands are greater by the order of 10 and10^2 respectively. A transition at 6.56 eV is assigned as n→σ* transitions which is moderately intense band (f = 0.05). Taking into consideration of its intensity and position, the band should be assigned as σ→σ* transition and correlates to the experimentally observed band at 6.53 eV reported by Rabalais *et al* (1971).

RINDO-CI method predicted two bands at 8.21 and 9.12 eV as σ→σ* transition in the spectrum of CO_2. The former of these, is intense (f = 0.12) than the latter (f = 0.01). Both the transitions are of intravalence type since they possess same contributions from Rydberg character also.

The first Rydberg band appears at 9.58 eV with 95 per cent Rydberg character. This is assigned as n→σ_R* and implies a quantum defect (δ) as 0.90. This involves the excitation of lone pair electron to (^3S_c + ^3S_o) MO with ^3S_c, AO having largest contribution. This forms the first member of Rydberg *ns* series. This is in good agreement with the experimentally observed band at 9.31 eV with δ = 0.95 [38]. The second member of this series appears at 9.82 eV which is more intense (f = 0.02) than the first. This implies δ value of 0.88. This series is terminated by an intravalence n→σ* transition at an energy of 10.01 eV.

The band predicted at 10.23 eV with 95 percent Rydberg character assigned as n→σ_R* transition. This implies a quantum defect (δ) of 0.58. Thus this corresponds to the first member of Rydberg *np* series. The originating MO of this band is a lone pair MO and terminates to (^3X_c + ^3X_c) MO.The second member of this series at 10.38 eV with 99 per cent Rydberg contribution implies a (δ) value 0.55. However, we find that the members of this series show diffuse nature of spectrum. This series is also terminated by an intravalence transition at energy 10.83 eV which is very weak and assumes 6 per cent Rydberg character.

A weak band at 10.98 eV is assigned as n→σ_R* transition and involves 99 per cent Rydberg character. The corresponding quantum defect (δ) is 0.18recognisable value of Rydberg *nd* series. This is followed by other closely spaced bands of the same series.

The band predicted at 11.95 eV is assigned as σ→σ* transition which is most intense band (f = 0.52) of the spectrum. This may correspond to the experimentally observed valence band at 11.08 eV (${}^{1}\sum_{4}^{+} \leftarrow {}^{1}\sum_{g}^{+}$) reorted by Rabalais *et al* (1969).

The lowest energy transition in the S→T excitation is a n→σ* predicted at 1.12 eV. The corresponding S-T splitting is of 1.11 eV. The next is a π→σ* transition with S-T split of 0.32 eV. The Singlet-triplet transition predicted at 4034 eV lies 0.40 eVbelow the corresponding S-S transition. All these transitions are entirely valence shell type.

Table-3: The lowest singlet-singlet transition in CO_2 and N_2O

Molecule	Exptl. Value		RINDO-CI (Present)			% Rydberg character		
	ΔE	F	ΔE	f	Symm.	C	N+O	T
CO_2 (C_{2v})	3.25^b		2.13	5×10^{-3}	$B_1(n\rightarrow\sigma^*)$	0	0	0
	4.00^b		3.48	0.00	$B_2(n\rightarrow\sigma^*)$	0	0	0
	6.53^b	1×10^{-5}	3.96	0.00	$A_2(\pi\rightarrow\pi^*)$	0	0	0
	8.41^f	6.2×10^{-3}	4.78	1×10^{-4}	$A_1(\pi\rightarrow\pi^*)$	0	0	0
	9.31^f	7.5×10^{-3}	6.23	4×10^{-3}	$B_1(\sigma\rightarrow\sigma^*)$	0	0	0
	11.8^f	0.12	6.56	0.05	$A_1(\sigma_n\rightarrow\sigma^*)$	0	0	0
			7.82	0.01	$A_1(\pi\rightarrow\pi^*)$	0	0	0
			8.21	0.12	$A_1(\sigma\rightarrow\sigma^*)$	1	0	1
			9.12	0.01	$B_1(\sigma\rightarrow\sigma^*)$	0	4	4
			9.58	0.00	$B_1(n\rightarrow\sigma_R^*)$	90	5	95
			9.82	0.02	$A_1(n\rightarrow\sigma_R^*)$	0	10	10
			10.01	0.00	$A_2(\sigma\rightarrow\sigma^*)$	0	3	3
			10.23	0.00	$A_1(n\rightarrow\sigma_R^*)$	90	5	95
			10.38	0.00	$A_2(\sigma\rightarrow\sigma_R^*)$	96	3	99
			10.83	0.00	$A_1(\sigma\rightarrow\sigma^*)$	0	6	6
			10.98	0.00	$B_1(n\rightarrow\sigma_R^*)$	5	94	99
			11.95	0.52	$A_1(\sigma\rightarrow\sigma^*)$	0	0	0
N_2O ($C_{\infty v}$)	4.54^f	5×10^{-6}	3.23	0.00	$A_1(n\rightarrow\pi^*)$		0	0
	6.81^f	1.4×10^{-3}	3.36	0.00	$A_1(n\rightarrow\sigma^*)$		0	0
	8.52^f	7.2×10^{-3}	3.85	0.00	$A_2(n\rightarrow\sigma^*)$		0	0
	9.66^f	0.36	4.92	0.00	$A_2(n\rightarrow\sigma^*)$		0	0
			6.66	0.11	$A_1(\pi\rightarrow\pi^*)$		0	0
			9.01	0.00	$A_1(\sigma\rightarrow\sigma^*)$	0	0	0
			9.21	0.00	$A_1(n\rightarrow\sigma_R^*)$		98	98
			9.38	0.00	$A_2(\pi\rightarrow\sigma_R^*)$		80	80
			9.45	0.01	$A_1(\sigma\rightarrow\sigma^*)$		4	4
			9.62	0.00	$A_1(\sigma\rightarrow\sigma_R^*)$		99	99
			9.78	0.00	$A_1(n\rightarrow\sigma_R^*)$		98	98
			9.82	0.00	$A_2(\pi\rightarrow\sigma_R^*)$		100	100
			10.25	0.00	$A_2(\pi_n\rightarrow\sigma_R^*)$		95	95
			10.43	0.00	$A_1(n\rightarrow\sigma_R^*)$		100	100
			13.35	0.12	$A_1(\sigma\rightarrow\sigma_R^*)$		0	0

b: Ref.[3], f: Ref.(Armstrong *et al* 1968)

Table-4: The lowest singlet-triplet transitions in CO_2 and N_2O

Molecule	Exptl.		RINDO-CI (Present)					
						% Rydberg character		
	ΔE	S-T split	ΔE	S-T split	Symm.	C	N+O	T
CO_2	4.89[d]		1.12	1.11	$B_1(n \rightarrow \sigma^*)$	0	0	0
			1.86	0.32	$B_2(\pi \rightarrow \sigma^*)$	0	0	0
			3.22	1.41	$B_1(\sigma \rightarrow \sigma^*)$	0	0	0
			4.34	0.40	$B_2(\pi \rightarrow \pi^*)$	0	0	0
			4.85	0.36	$A_1(\pi \rightarrow \pi^*)$	0	0	0
N_2O	4.28[d]	5.38	2.85	1.18	$A_1(n \rightarrow \sigma^*)$		0	0
			3.46	2.22	$A_1(\pi \rightarrow \pi^*)$		0	0
			3.78	0.35	$A_2(\pi \rightarrow \pi^*)$		0	0
			4.46	0.45	$A_1(n \rightarrow \sigma^*)$		0	0

d: Ref. (Armstrong *et al* 1968)

(ii) Nitrous Oxide (N_2O) :

The RINDO-CI method predicts a valence shell very weak (f = 0.00) $n \rightarrow \pi^*$ transition as the lowest energy S-T transition at 3.23 eV. This is followed by a $n \rightarrow \sigma^*$ transition predicted at 3.36 eV. An intervening $\pi \rightarrow \sigma^*$ transition in nitrous oxide occurs at 3.85 eV is very weak (f = 0.00). The orbital of departure and the orbital of arrival for this band are completely of π-type. This calculation is in good agreement with the experimental observation ((Armstrong *et al* 1968) of this band at 4.54 eV (${}^1\Sigma^- \leftarrow {}^1\Sigma^+$).

The other $\pi \rightarrow \pi^*$ transition predicted to lie at 6.66 eV. This is an intense band (f = 0.11) and has appreciable mixing with a $n \rightarrow \sigma^*$ configuration. This may correspond to the experimentally observed band [18] at 6.81 eV (${}^1\Delta \leftarrow {}^1\Sigma^+$) with low intensity ($f = 1.4 \times 10^{-3}$).

The RINDO-CI method predicts a very weak (f = 0.00) valence $\sigma \rightarrow \sigma^*$ transition at 9.01 eV. This corresponds to the experimentally observed sharp but weak band at 1455 Å (8.52 eV). This band also demarcates the three Rydberg series at higher energy side.

The first transition with 98 per cent Rydberg character appears at energy 9.21 eV above the ground state. The corresponding quantum defect (δ) is 0.98. Thus this forms the first member of the Rydberg *ns* series. This is $n \rightarrow \sigma_R^*$ and involves the excitation of lone pair electron to the (${}^3S_N + {}^3S_N + {}^3S_O$) MO with ${}^3S_{N_2}$ having the largest AO coefficient. This is followed by a number of closely spaced bands with 80 per cent Rydberg character up to 9.82 eV all belonging to the same series.

The Rydberg *np* series starts at 10.25 eV. The first member of this series is a $\pi_n \rightarrow \sigma_R{}^*$ transition with 95 per cent Rydberg character. This implies a quantum defect $\delta = 0.49$. This is followed by rather closely spaced transitions which involve mainly the excitation of (n) electron to various combinations of Rydberg *p* orbitals.

The lowest S-T, 3(n→π), transition is predicted at 2.85 eV. The corresponding S-T splitting is 1.18 eV. The next S-T transition is a π→π* with S-T splitting equal to 2.22 eV. This is in fair agreement with experiment. The next is π→σ* transition at 3.78 eV with 0.35 eV as the corresponding splitting.

At higher energy side, the next intense band of the spectrum is calculated at 13.35 eV (f – 0.12). This is a σ→σ* transition and correspond well with the prediction of such valence band in CO_2 also.

REFERENCES

1. Armstrong, A.P., Bertus, B. and Mc Glynn, S.P. (1968). *Spectrs. Lett.* **11**:43
2. Astoin, N. (1957). *J. Rech. Cent. Nat. Rech. Sci* No. **38**:1
3. Eland, J.H.D. (1970). *Phil. Trans. Roy. Soc. London* **268A**:87
4. England, W.B., and Ermler, Wc (1979). *J. Chem. Phys.* , **70**: 1711
5. England, W.B., Yeager, D. and Wahl, A.C. (1977). *J. Chem. Phys.* , **66**: 2820
6. Herzberg, H. (1967). "Molecular spectra and Molecular structure.,**Vol. III**, Electronic spectra and Electronic structure of PolyatomicMolecules" D.Van Nastrand, Princeton. N.J.P. 623
7. Karun, K., Chandra, G. and Singh B.K. (2012). *Bulletin of Pure and Applied Sciences*,**31D** (1):41-50
8. Kuppermann, A., Erucholz, R.P. (1978). *J. Chem. Phys.* **68**:775
9. Mc Curdy Jr., C.W. and Mc Koy, V. (1974). *J. Chem. Phys.* **61**: 2820
10. Mclean, A.D. and Yashimina, M. (1967). 'Tables of linear molecules wave functions' I.B.M. san Jose Calif.
11. Rabalais, J.W., Mc Donald, J.M., Scherr, V. and Mc Glynn, S.P. (1971). *Chem Rev.* **71**: 73.
12. Rabalais, J.W., Mc Donald J.R. and Mc Glynn, S.P. (1969). *J. Chem. Phys.* **51**:5103
13. Scanlon, David O., Watson, Graeme W., Payne, D. J., Atkinson, J. R., Egdell, R.G. and Law, D.S.L. (2010). *J. Phys. Chem.* C, **114** (10):4636-4645
14. Singh, A.N. and Haque, W. (1977). *J. Phys.* **518**:218
15. Sponer, H. and Bonner, L.G. (1940). *J. Chem. Phys.* , **8**: 33
16. Sutten, L.E. (1969). "Tables of Inter atomic Distances and Configuration in Molecules and Ions" The Chemical Soc. London supplement.

17. Tanaka, Y., Jursa, A.S. and Le.Blance, F.J. (1960). *J. Chem. Phys.* , **32**: 1205

18. Tripathy, S.K. (1986). Ph.D. Thesis, Magadh University, Bodh Gaya

19. Turner, D.W., Baker, C., Baker, A.D. and Brundle, C.R. (1970). "Photoelectron spectroscopy" , John Wiley and Sons, New York

20. Zelikoff, M., Watanabe, K. and Inn., E.C.Y. (1953). *J. Chem. Phys.* , **21**: 1643

Bulletin of Pure and Applied Sciences
Vol. 32 D (Physics) Issue (No.1) 2013:P. 51-58
www.bpas.in

COMPARISON OF PROPERTIES AND MICROSTRUCTURE OF A356 - B4C NANO COMPOSITES, PRODUCED BY TWO METHODS OF CASTING VORTEX AND SEMI-SOLID CASTING

Meghdad Khademian[1], Ali Alizde, Hamidreza Baharvandi and Hasan Majidi
Materials and Manufacturing Technologies Complexes,
Malek Ashtar University, Terhran, Iran

Received on 30 April 2013: Accepted on 30 May 2013

ABSTRACT

In the present study, A1-B4C nanocomposite was produced using the methods of casting vortex and semi-solid casting. Boron carbide particles with an average diameter of 65 nm with the amount of 3 wt%, was added to the melted alloy of A356. In the method of Casting Vortex, boron carbide particles were added to the melted aluminum at 850 C° in 15 min and then casting was performed. In the semi-solid Casting method, temperature first rose to 700 C° when particles were mixing and then temperature was reduced to 608 C° within 15 min and then casting was done. Results show that tensile strength of the segments produced by semi-solid Casting method is 201 MPa which shows a 12% increase in strength compared to the segments produced by Casting Vortex with tensile strength of 178 MPA.

Keywords: Boron carbide, Aluminum matrix composites, Casting Vortex,Semi-solid Casting, Ultimate tensile strength.

1.INTRODUCTION

Vortex Casting is one of the methods used for producing metal matrix composites. This method is highly acceptable and efficient due to the simplicity of the process, repeatability and cost. However one of the problems with this method is the possible weakening of the ceramic particles by melted metal that leads to the creation of agglomeration and undesirable properties in the segments.

Semi-solid casting is another method of producing metal matrix composites. Mixing of boosting particles in the metal matrix in semi-solid state, and then performing the casting process is called semi-solid casting process.

---

[1] - Corresponding author: Meghdad Khademian
meghdadkhademian@yahoo.com m_khademyan@yahoo.com

This method is based on the theory of reduction of the viscosity of the fluid produced by shear stress in it, due to the conversion of the grains' morphology from dendritic to spherical. This means that by stirring the melt, fluidity increases (Sajjadi and Ezatpour,2012).

In addition to increasing the wettability of particles, this method prevents them from moving into the slag or from being deposited. Semi-solid casting is performed through Semisolid – Liquid and Semisolid – Semisolid methods. In the first method particles are mixed in the matrix in semi-solid state and then they are poured in the molten state with the increase in the temperature and in the second method, particle mixing and pouring both are performed in the semisolid state (Akhlaghi *et al* 2004).

Boron carbide is the hardest substance in the world after diamond and cubic boron nitride. This substance has a gray to black color and has a rhombohedral needle crystal structure or a hexagonal plate structure (With 1983). According to this fact that this substance has the lowest density among the Ultra-hard materials, which is a density of about 2.52 gr/cm^3 and its high refractory and no reduction in its strength and stiffness in the temperatures up to about 1300 °c, and good resistance to corrosion and chemical attacks and its reasonable price, it is increasingly used in the metal matrix composites (Rao,1995 ; Therenot 1990).

In the present study, in order to achieve a good composite of optimal values of volume percent, particles' shape, time and temperature of mixing, repetition of stirrer rounds, shape and angle of stirrer, and other effective variables that have already been studied by researchers, after extraction, articles and references were utilized, to provide a fair comparison between the composite segments produced using the two mentioned methods in the same conditions.

2.EXPERIMENTAL ACTIVITIES

In this study, the A356 alloy having the composition reported in Table (1) was used as metal matrix composites.

Table 1: Chemical composition of A-356 aluminum alloy

Elements	Al	Si	Fe	Cu	Mg	Mn	Zn	Ti	Ni
Wt%	91.77	7	.20	0.20	.38	0.10	.10	.20	.05

Casting system consists of three main sections of oven, stirrer and mold. Propeller of stirrer is made of graphite with vane angle of 45 degrees. Steel casting mold was designed in the form of rectangular cube for the preparation of the four cylindrical samples with dimensions of 15 cm and diameter of 3 cm.

Increase in the wettability of ceramic particles was done using the molted aluminum particles, by means of pure aluminum powder with the average grain size of +100 mμ and weight ratio of aluminum powder to boron carbide powder of 2, using planetary mechanical mill in the alcohol ethanol environment, at 300 r.p.m and in the turnaround time of 20 minutes, in reversible state of the machine.

After considering the amount of veneered aluminum over the powder, the amount of 3 Wt% of boron carbide powder with average particle size of 65 nm was calculated and put into the melt. Figure (1) shows the image taken of the boron carbide particles using TEM microscope.

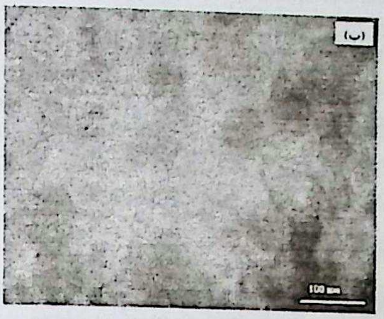

Figure 1- Image taken from boron carbide particles by TEM microscope

In order to manufacture segments using Casting Vortex method, particles were mixed in the melt, using stirrer, in 850 c° for 15 minutes and then casting operation was performed.

In the production of segments by semi-solid casting method, after the oven reached the temperature of 700 C˚, and at the same time of mixing particles by stirrer, the temperature dropped to 608 C˚ and then casting was done in the metal mold. The operation takes about 15 minutes. When mixing the particles, graphitic stirrer was placed inside the oven and crucible such that the distance between it and the crucible bottom was 1/3 of the total height of the crucible. Stirring speed at all stages was considered constant and equal to 300 r.p.m.

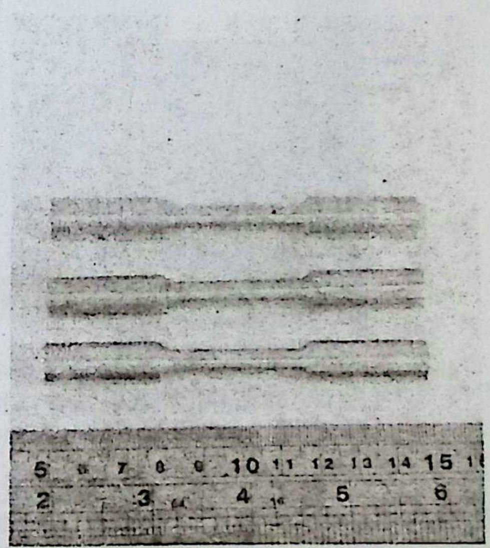

Figure- 2 – Segments prepared for tensile strength test.

To determine the tensile strength of the segments made in the machine, the tensile testing of German Zweck company was used, with the maximum error of 0.05, for all samples' tensile strength measurement. This error rate could have little effect on the results. Three samples per each pouring were prepared for tensile test, based on E8-ASTM standard (American Society for Testing Materials,1994). Figure 2 displays the images of three samples prepared for tensile test.

In order to prepare samples to see microstructures, after sanding and polishing of segments, etching operation was performed using a solution of 5 volume percent of Hf acid (Jeng and Yang,1995). The scanning electron microscope (SEM) of XL 30 model, made in Dutch company of Philips, was used to observe the microstructure.

3.RESULTS AND DISCUSSION

As you can see in figure 3, due to the type of production of segments in semi-solid state and mixing of boosting particles, meshing of composite segments in semi-solid method is mostly seen in the form of circle.

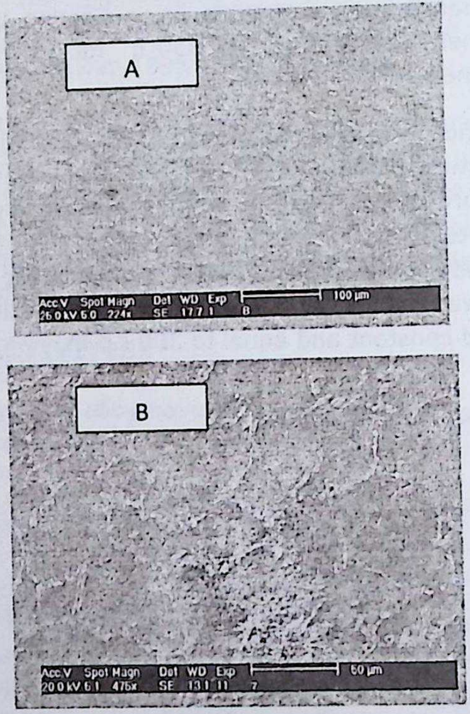
A
Acc.V Spot Magn Det WD Exp 100 µm
25.0 kV 5.0 224x SE 17.7 1 B
B
Acc.V Spot Magn Det WD Exp 50 µm
20.0 kV 6.1 475x SE 13.1 11 7

Figure- 3 – Images of meshing of segments in casting vortex in figure (A) and semi-solid in figure (B).

Meanwhile, due to casting in lower temperatures i.e. about 608 c°, distribution and size of pores improves in the semi-solid method (Rohatgi and Rajan

2007). Based on the density calculations, segment A356 has the proposity level of 1.14% without the reinforced particles produced by semi-solid and vortex methods, and its proposity level with boron carbide particles, in semi-solid method is 2.0242%, and in vortex method is 2.052%.

On the comparison of the distribution of agglomeration particles in the two methods, it can be said that, since the matrix aluminum is pasty, there is a mechanical conflict with the semi-solid metal due to the incorporation between the agglomerate particles, which results in a dramatic reduction in the amount and size of agglomerates. Furthermore, the semi-solid property of the metal prevents easy movement of boron carbide particles into the slag (Ghahremainian and Niroumand 2008; Aigbodion 2007).

Reduction in the amount and size of pores, decrease in the concentration of particles in form of agglomeration, better distribution of particles, and reduction in the amount of adverse reactions due to mixing of particles and melt at lower temperatures, results in improved mechanical properties of produced composites by semi-solid method compared with vortex method (Hashim and Looney 2006). In figures (4) and (5), the ultimate strength and hardness of segments produced by semi-solid and vortex casting methods, is displayed. According to the diagram, the ultimate tensile strength of the segment 356A without boosting particles is 105 MPa, and with boron carbide particles using vortex method is 178 MPa, and for semi-solid method is 201 MPa.

Furthermore, composite segments produced by casting vortex method have hardness of 61 HBN, but hardness of the segments produced by the semi-solid casting method is 68 HBN.

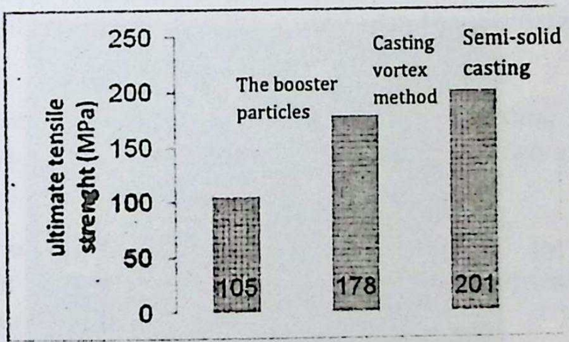

Figure- 4 – the ultimate tensile strength of segments produced by the methods of semi-solid and vortex casting.

3.1 Evaluation of fracture surfaces

In figure 6, the images of fracture surfaces of samples produced by the two methods of semi-solid and vortex casting are displayed.

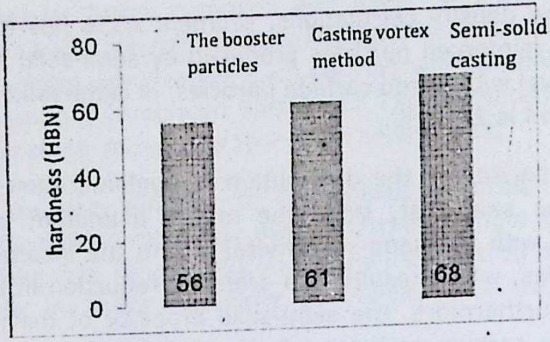

Figure- 5 – Hardness of segments produced by the methods of semi-solid and vortex casting.

Basically, 3 mechanisms are introduced when examining the fracture mode of composite segments. In this process, either the crack is formed on the booster particles, and then grows, or it is formed at the interface of the matrix and booster, and then grows, or the crack may start in the matrix and then grow.

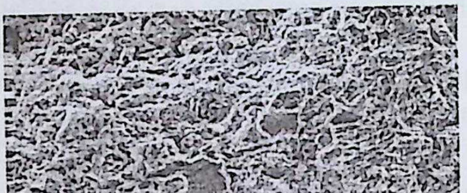
Acc V Spot Magn Det WD Exp
30.0 kV 4.6 100x SE 8.4 2 rdx
200 µm
Acc V Spot Magn Det WD Exp
30.0 kV 4.5 100x SE 7.7 1 ml
200 µm

Figure- 6 - Comparison of fracture surfaces of composite segments manufactured by casting vortex method in Figure A, and semi-solid method in Figure B.

By observing the soft fracture surface, it becomes clear that the crack is formed on the booster particles, and for this reason, the remaining particles of booster phase can be observed when examining the fracture surface.

However, in brittle fracture, we face with a sudden fracture and the absence of the necking phenomenon, and the fracture surface is relatively smooth and has cleavage. Usually in this type of fracture, cracks grow from the porosities. Therefore, more porosity, results in the increase in tendency to brittle fracture in the composites [(Zong and Derby 1996,Syu and Ghose 1994,Christman and Needleman 1989,Yulong and Ramesha 2004).

When examining the fracture surface of the segments manufactured by the two methods due to reduced porosity and their shrink in size, as shown in Figure (7), and noting that the porosity is the starting point of brittle fracture, it is observable that in the composite segments manufactured by the semi-solid method, despite of their brittleness, the segments are softer than the segments made by the vortex method. As seen in the figure below, the amount of the Cleavage Planes at the fracture surface of the segments produced by semi-solid method has decreased and there are more river places indicating that the fracture type is moving from brittle to soft mode.

4.CONCLUSIONS

1- Aluminum alloy A356 was successfully reinforced by boron carbide particles and A1-B4C composite was produced using the two methods of vortex and semi-solid casting.

2- The ultimate tensile strength of the segment produced by semi-solid casting is 201 MPa, which represents an increase of 12%, when compared with the segment manufactured by casting vortex with the ultimate tensile strength of 178 MPa.

3- Hardness of the segment produced by semi-solid casting method is 68 HBN, while hardness of the segment manufactured by casting vortex method is 61 HBN.

4- The amount of porosity of the segment produced by semi-solid casting method is less than the amount of porosity of the segment manufactured by casting vortex method.

5- Fracture of the segments manufactured by casting vortex is more brittle than fracture of the segments produced by semi-solid casting method.

REFERENCES

1. Sajjadi, S. and Ezatpour,H.R.(2012). " Comparison of fabricated by stir and compo-casting processes", *Materials and Design*, Vol. 34: 111–106.

2. Akhlaghi,F., Lajevardi,A. and Maghanaki, H.M.(2004)." Effects of casting temperature on the microstructure and wear resistance of compocast A356/SiCp composites: a comparison between SS and SL routes", *Materials Processing Technology* ,Vol. 65:155–156.

3. With, G.D.(1983)m"Note on the Temperature Dependence of Hardness of Boron Carbide ", *Less Common Met*, Vol. 95:133-138.

4. Rao, B.V.S.S. "Synthesis of High Purity Boron Carbide Powder", Universities Press, India, 1995.pp.82-87

5. Therenot ,F.(1990). "Boron Carbide-A Comprehensive Review", *J. Euro. Soc.* Vol.6, PP. 205-225, 1990.

6. American Society for Testing Materials, "Standard Test Method of Tension Testing Wrought and Cast Aluminum and Magnesium Alloy products - B557", Handbook of ASTM Standards, Vol. 3, pp. 91, 1994.

7. Jeng, S.M. and Yang,M.(1995)." Processing and high temperature deformation of metal-matrix composites", *Materials Science and Engineering* , Vol. 191:49-59.

8. Rohatgi, P.K. and Rajan, D.(2007)."Fabrication and characterisation of Al–7Si–0.35Mg /fly ash metal matrix composites processed by different stir casting routes", *Composites Science and Technology*, Vol. 67:3369–3377.

9. Ghahremainian, M. and Niroumand, B.(2008). "Compocasting of an Al-Si-SiCp composite using powder injection method", *Solid state Phenomena*, Vol. 65:175-180.

10. Aigbodion,V.S.(2007)."Effects of silicon carbide reinforcement on microstructure and properties of cast Al–Si–Fe/SiC particulate composites", *Materials Science and Engineering*, Vol. 447:355-360.

11. Hashim,M. and Looney,L.(2006). "Particle distribution in cast metal matrix composites", *Journal of Materials Processing Technology*, Vol. 123:251-257.

12. Zong,B.Y. and Derby,B.J.(1996). "Comparison of the plastic deformation and failure of A359/SiC and 6061- T6/Al2O3 metal matrix composites under dynamic tension", *Material Science and Technology*, Vol. 131:297-301.

13. Syu,G.C. and Ghosh,A.K.(1994). "The effect of temperature on the fracture mechanism in 2014A1/15 vol. %Al2O3 composite", Materials Science and Engineering, Vol. 184:27-33.

14. Christman, T. and Needleman,A.(1989). "Effect of fibre debonding in a whisker-reinforced metal", *Materials Science and Engineering*, Vol. 107: 49-51.

15. Yulong,L. and Ramesha,K.T.(2004). "The infiltration of B-SiC in porous Alumina compacts in a microwave field", *Materials Science and Engineering*, Vol.33: 5-12.

Bulletin of Pure and Applied Sciences

Volume 32-D- Physics
Issue No.2 (July-December)
2013

Central Library
Gurukul Kangri University
Hardwar-249404 (U.A.)

A Peer Reviewed Journal

This publication is included in Abstracted/Indexed coverage of ProQuest , Indian Science Abstract, Indian citation index. etc

Url : www.bpas.in

Bulletin of Pure and Applied Sciences

Volume 32 D (Physics), Issue (No.2) January-June, 2013

EDITORIAL BOARD

Convenor (Hon.) : Prof. Durga P. Ojha, *FRSC (UK)*
*Professor,*School of Physics, Sambalpur University, Jyoti Vihar-768 019,Sambalpur, Orissa, India
E-mail: durga_ojha@hotmail.com

MEMBERS

Prof. R. N. P. Choudhary Dept. of Physics IIT Kharagpur(WB) (INDIA)	Prof. Florentin Smarandache University of New Mexico Gallup NM 87301 USA	Prof. A. K. Deb Dept. of Physics University of Chittagong Chittagong Bangladesh
Prof. V. R. K. Murthy Dept. of Physics IIT Chennai (INDIA)	Prof. Dmitri Rabounski Sirenevi boulevard 69-1-65, Moscow 105484, Russia.	Prof. Sarabettin EREL Dept. of Physics University of Kirikale (INDIA)
Prof. Madan jee Dept of Physics B.R.A. Bihar University Muzaffarpur (Bihar) (INDIA)	Prof. H.O. Boyo Dept. of Applied Physics Fukuoka University Nanakuma, Joham-ku Fukuoka Japan	Prof. M.C.Rao Dept. of Physics Andhra Loyola College Vijayawada (A.P.) 520 008 (INDIA)
Prof. B. Hanumanaiah Dept. of Physics IIT Bangalore (INDIA)	Prof. A. O. Boyo, Dept. of Physics, Lagos State University Ojo Lagos State Nigeria	Dr. D. K. Dwivedi Reader in Physics Dept of Applied Sciences M.M.M. Engineering College Gorakhpur
Prof. Rajnikant Head P.G. Dept of Physics University of Jammu Jammu Tawi (J & K)	Prof. C. Y. Lo Applied and Pure Research Institute Nashua NH 03060,USA	Prof. R.Jeevan Kumar Dept. of Physics S.K. University Anantapur (A.P.) (INDIA)
Prof. S.H. Pawar Dept. of Physics Shivaji University Kolhapur (INDIA)	Prof. Bekir GURBULAK Ataturk University Fizik Bolumu, 25240 ERZYRUM TURKEY	Prof. Lalan Jha Dept. of Physics L.N. Mithila University Darbhanga (INDIA)
Prof. S.C. Mehrotra Dept. of Physics Dr. B.A.M. University Aurangabad (INDIA)	Prof. S. Umapathy School of Physics Madurai Kamaraj University, Madurai (INDIA)	Prof. S.K. Narayandass Dept. of Physics Bharathiar University Coimbatore (INDIA)

(Research papers may be submitted through the above Professors)

Bulletin of Pure & Applied Sciences is devoted to the international advancement of organized knowledge on all aspects of Science. It provides a forum for comments by publishing original research contributions, scientific survey, case studies, book review and letter to the Editor-in-Chief.

Bulletin of Pure & Applied Sciences is issued six monthly, i.e. June and December of every year. The Editor-in-Chief/Managing Editor/Editorial Board etc. assumes no responsibility for the statements and opinions advanced by the contributors. The editorial staff in its work of examining papers, received for possible publication is assisted, in an honorary capacity, by a large number of distinguished scientist working in various parts of the world.

Bulletin of Pure & Applied Science is copy-righted. Manuscripts published in the Bulletin should not be reproduced without the written permission of the Editor-in-Chief.

Annual Subscription Rate

Print version INDIA) Rs. 1000 U.S. $ 60 U.K. £ 30 (www.bpas.in)
Online version (contact www.indianjournals.com)

Bulletin of Pure and Applied Sciences
Vol. 32 D (Physics) Issue (No.2) 2013:P. 59-65
www.bpas.in

FABRICATION AND ANALYSIS OF ELECTRICAL BEHAVIOUR OF CARBON NANOWIRES BY FOCUSED ION BEAM INDUCED DEPOSITION TECHNIQUE

Sudhanshu Srivastava[1] **and K. K. Verma**[1]
[1]Department of Physics and Electronics, Dr. R. M. L. Avadh University,
Faizabad (UP)-224001, India
Email: kkverma23@gmail.com

Received on 08 July 2013: Accepted on 29 November 2013

ABSTRACT

Present paper reports the fabrication of carbon nanowires on SiO_2 substrate using focused ion beam induced deposition and their electrical transport property studies. I-V characteristics of the nanowires have been investigated. The resistivities of the carbon nanowires fabricated by FIB are found to be more than that of the bulk crystalline graphite and nearly equal to bulk amorphous carbon. An increment in the resistivity has been explained on the basis of carbon allotropes. I-V characteristics of the nanowires fabricated in parallel combinations confirm the validation of resistance addition laws.

Keywords: FIBID,Carbon Nanowire,Electrical Behaviour,SEM and EDS.

INTRODUCTION

Now a days Focused ion beam (FIB) assisted fabrication process has become important in manufacturing and development of prototype nano / micro sensors[1,2], actuators[3], micro and nano-electro-mechanical systems (MEMS and NEMS)[4,5] and biological applications[6]. FIB / FEB fabricated structures can also be used as functional building blocks for various nano-optoelectronic devices[7] and are destined to play important role in futuristic nano / micro systems. One of the important applications of FIB is to provide electrical contacts for structures of nano regime to the macro world[8]. Keeping in view this fact the properties of these nanowires itself need to be investigated. There are a variety of techniques for the fabrication of nanowires[9] like ion beam irradiation of MWCNTs[10],ethanol catalytic combustion process[11,12],microwave plasma enhanced CVD[13] and IBID[14,15,].Keeping in view this, in the present work emphasis has been done to fabricate carbon nanowires by most effective technique of FIB using Nova Nanolab (FIB) System installed at IIT, Kanpur.

EXPERIMENTAL WORK

In the present work, Naphthalene ($C_{10}H_8$) precursor reservoir was used for carbon deposition. The aforesaid reservoir was connected to the vacuum chamber of FIB system by means of a nozzle along with field emission Ga^+ ion source, high resolution (7 nm) ion optics, high resolution milling and e-beam patterning, scanning electron microscope (SEM) with energy dispersive spectroscopy (EDS) facilities. In the present experiment focused ion beam with energy ranging from 10 KeV to 30 KeV and beam currents ranging from 0.3 pA to 100 pA have been utilized. Firstly, a 500 nm thick SiO_2 layer was grown on Si substrate by wet oxidation for proper electrical insulation and then deposition of 100 nm gold using an I-shaped mask, having two square holes of dimension 1 mm x 1 mm connected with a line of width 200 µm was deposited.Gold film of thickness 100 nm was thermally evaporated at a rate of 1 Å/sec on SiO_2/Si substrate through above pre-designed mask to obtain the structure as depicted in figure 1(a). The pressure inside the chamber was maintained at 2 $\times 10^{-6}$ mbar or less during the evaporation. The gold deposited SiO_2 sample was annealed in the atmosphere at temperature of 500^0C for 30 minutes to improve the adhesion of the gold film. The gold pads were connected to the Keithley 6430 source meter and the sample was mounted inside the FIB chamber. Then the isolation of gold macro contacts was done by ion milling.These steps are shown in the figure below.

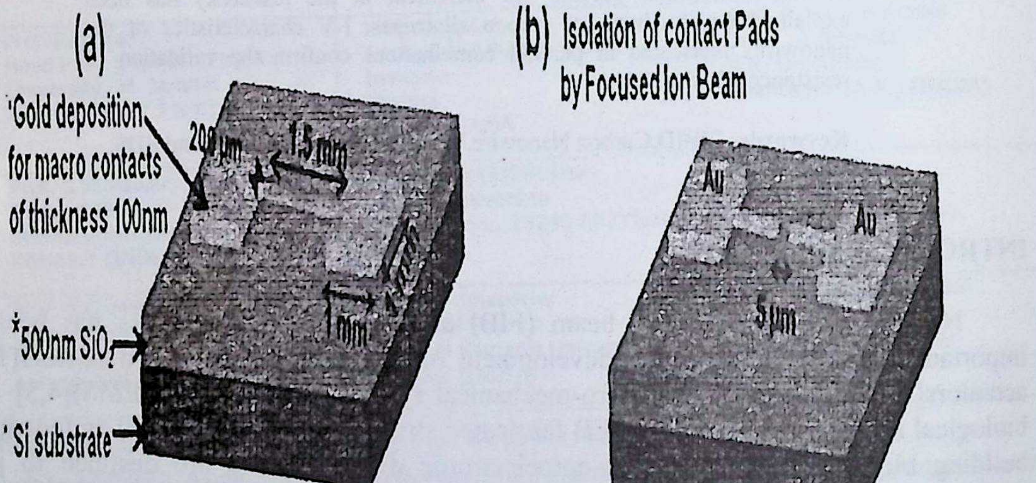
(a)
Gold deposition for macro contacts of thickness 100nm
200 µm
1.5 mm
1 mm
1 mm
*500nm SiO_2
Si substrate
(b) Isolation of contact Pads by Focused Ion Beam
Au
Au
5 µm

Figure.1

The precursor temperature was set to 30°C to achieve good equilibrium condition. The other parameters that affect the deposition results are deposition rate, which is a combination of the local gas flux and Beam current, Scan area (pattern size), Scan speed (dwell time per pixel and beam overlap).

The experimental setup is shown in fig. 2.

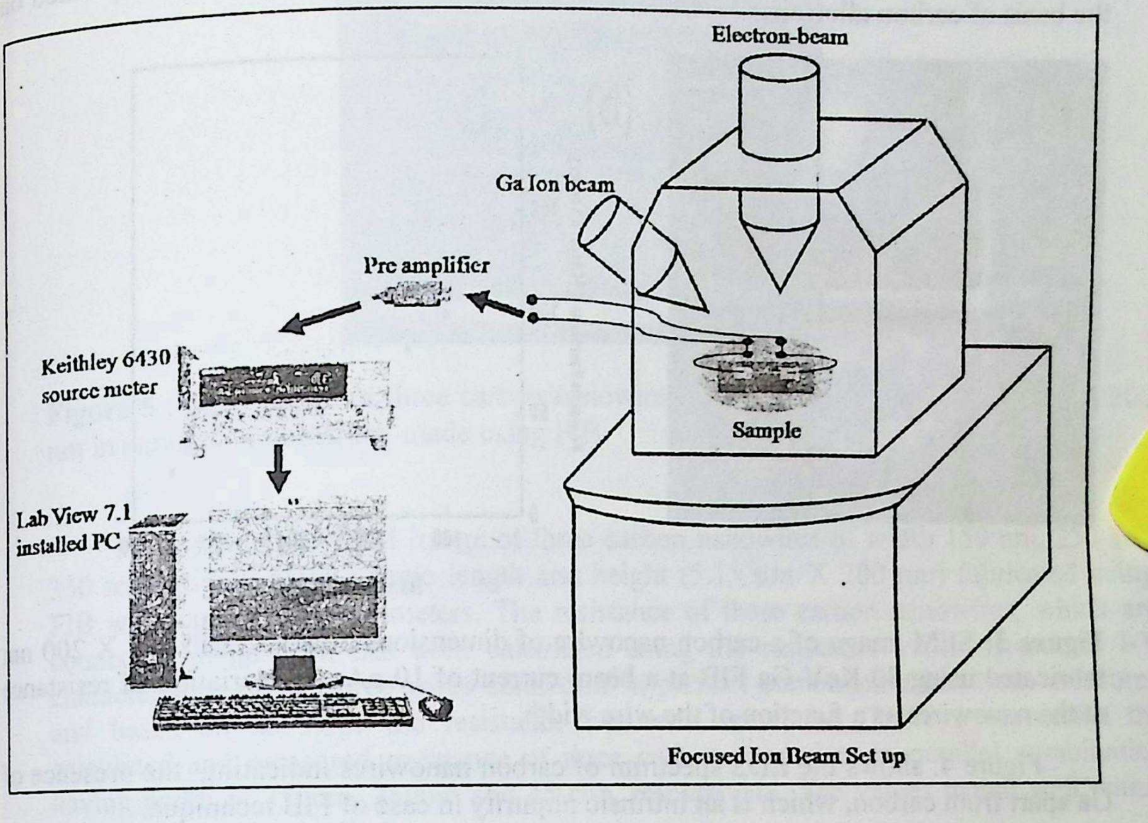

Figure-2: Schematic diagram of the experimental set up.

Keithley's remote source meter model 6430 was utilized for the resistivity measurements. All the measurements were performed at room temperature (293 K) and at chamber pressure of less than 5 X 10^{-6} mbar. The gold line connecting the pads was milled 5.15μm wide in the middle using FIB to isolate the macro pads as shown in fig. 1 (b). In the present investigation carbon nanowires having length in the range of 4–8 μm and width between 50 nm to 450 nm in Parallel combinations were fabricated. I-V characteristics of these nanowires have been studied. The surface morphology was done by SEM and composition was done EDS.

RESULTS AND DISCUSSION

I-V characteristics of 50nm X 5.15 μm X 200 nm Carbon nanowires with the width ranging form 50 nm to 450 nm as shown in fig.3(a) have been studied. The resistances of these nanowires have been calculated using the slope of the I-V curve. Fig.3(b) shows the variation of resistance of the nanowires as a function of the wire width. The resistance 'R' is found to be inversely proportional to the nanowire width 'w'. The behavior is similar as that of the bulk material. The resistivity of the Carbon nanowires has been calculated which turns out to be ~337.93 ohm-µ meter. The measured resistivity value is much larger than the bulk carbon (Graphite) resistivity ~0.3-6.0 x 10^{-6} ohms-meter. An increase in the resistivity value of the FIB fabricated nanostructures can be explained on the basis of carbon allotropes.

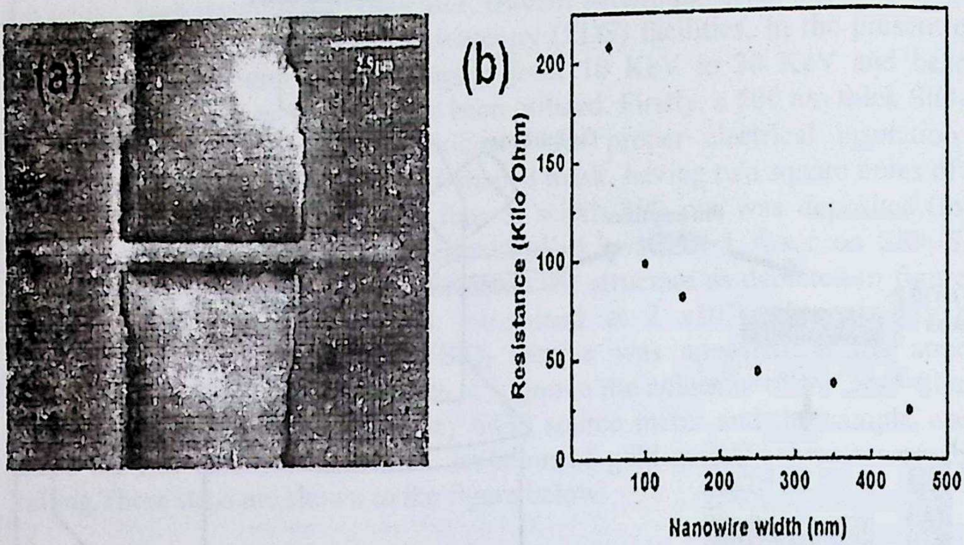

Figure 3: SEM image of a carbon nanowire of dimensions 50nm X 5.15 µm X 200 nm fabricated using 30 KeV Ga FIB at a beam current of 10 pA. (b) Variation of resistance of the nanowires as a function of the wire width.

Figure 4. shows the EDS spectrum of carbon nanowires indicating the presence of Ga apart from carbon, which is an intrinsic impurity in case of FIB technique.

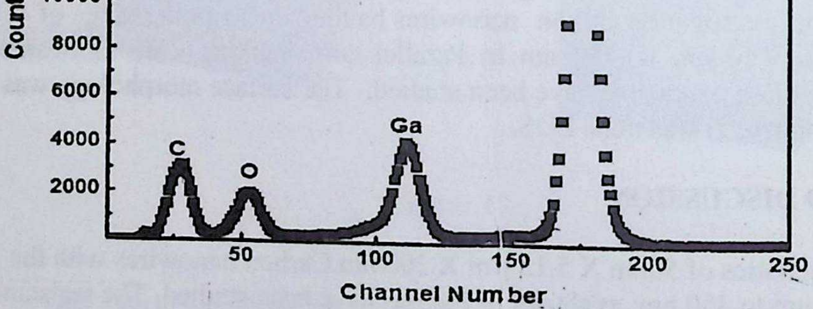

Figure-4: EDS spectrum of carbon nanowire indicating the presence of Ga.

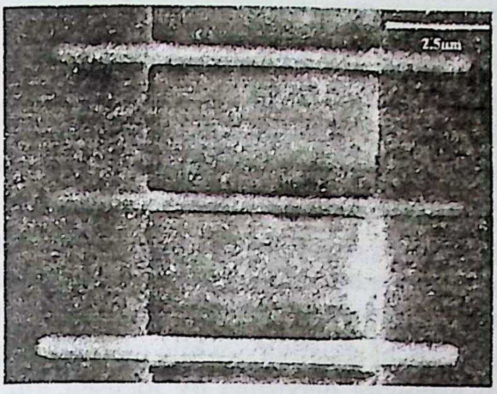

Figure 5 : SEM image of three carbon nanowires of dimensions 50nm x 5.15 μm x 200 nm in parallel combination made using FIB.

Fig.5 shows the SEM image of three carbon nanowires of width 150 nm, 250 and 350 respectively having same length and height (5.15 μm X 200 nm) fabricated using FIB with same beam parameters. The resistance of these carbon nanowires, which are connected in parallel, has been calculated using the resistance value measured. I-V characteristics of the three wires connected in parallel combination has been measured and based on its slope the resistance has been calculated. Table 1 represents the calculated and measured resistance of three carbon nanowires in parallel combination having width of 250nm, 350nm and 450nm, respectively. The values match well within the experimental error limit.

Table 1: Calculated and measured resistance of carbon nanowires in parallel combination having width of 150nm,250nm and 350 nm, respectively.

C nanowires width (nm)	**Resistance single wire (kΩ)**	**Resistance of parallel wires**	
		Calculated Value (kΩ)	**Measured Value (kΩ)**
150	81.60	16.66	17.8
250	43.8		
350	37.5		

CONCLUSION

Carbon nanowires have been fabricated on SiO_2 substrate using FIB and their electrical behaviour have been studied. The resistivity of the material of FIB fabricated nanowires are found to be more than that of the bulk material. An increase in the resistivity value of the FIB fabricated nanostructures can be explained on the basis of carbon allotropes. Carbon has many allotropes like diamond, graphene, graphite and amorphous carbon. In diamond the carbon atoms are bonded together in a tetrahedral lattice arrangement while in a graphite and graphene the carbon atoms are bonded in sheets of hexagonal lattice and single sheet of hexagonal lattice respectively. Because of arrangements of carbon atoms in diamond and graphite their physical and electrical properties vary widely for example diamond is crystalline structure and hardest naturally-occurring material known, while graphite is soft enough to form a streak on paper. Diamond has a very high electrical resistivity, while graphite is a very good conductor. In the same way the carbon nanowire deposited by focused ion beam is amorphous and because of that the resistivity will be higher than graphite. It has also been shown that the nanowires fabricated in parallel combinations confirm the validation of resistance addition laws in nano regime.

Thus it can be said that Carbon nanowires are very resistive (KΩ) and because of this, these are suitable only for reducing charging of samples and as a protective layers for TEM sample preparation.

ACKNOWLEDGEMENTS

We thank the staff of the Ion Beam Laboratory at IIT Kanpur for their assistance. We acknowledge Indian Institute of Technology Kanpur for procurement of the FIB system. Discussions with Dr.R.K.Tiwari (Dr.RML Avadh University, Faizabad), Dr.Anchal Srivastava,(BHU), Dr.R.K.Sinha(CSIR) and Prof.R.K.Shukla, (University of Lucknow) is highly acknowledged.

REFERENCES

1. Khizroev,S., Hijazi, Y., Chomko, R., Mukherjee,S. Chantrell, R., Wu, X., Carley, R. and Litvinov,D.(2005). "FIB- fabricated nanoscale magnetoresistive", *Appl. Phys. Lett.* **86**: 42502 (2005).

2. Masao Nagase, Kenichiro Nakamatsu, Sinji Matsui, Hideo Namatsu, Hiroshi Yamaguchi, (2006)."Carbon Multiprobe on a Si Cantilever for Pseudo-Metal-Oxide-Semiconductor Field-Effect-Transistor". *Jpn. J. Appl. Phys.*, Vol. 45: 2009(2006).

3. Kometani, T., Morita, K.., Watanabe, T. , Hoshino, K.. Kondo, K., Kanda, Y., Haruyama, T., Kaito, J., Fujita, M., Ishida, Y., Ochiai and Shinji Matsui, (2004)"Nanomanipulator and Actuator Fabrication on Glass capillary by Focused-Ion-Beam Chemical vapor Deposition", *J. Vac. Sci. Technol.* B 22: 257-263 (2004).

4. Sattron,F.P.,Kubena,R.L.,McNulty,H.H., Joyce,R.J..,and Vajo, J.(1998). "*Microelectromechanical tunneling sensor fabrication and post-processing characterization using focused ion beams*", *J. Vac. Sci. Tecnol.* B 16(1998): 2449-2454.

5. Ben Assayag,G., Gierak, J., Hamet,J.F., . Prouteau,C., Flament,S., Dolabdjian,C', Gire,F., Lesquey,E., Gunther, G., Dubuc,C., Bloyet,D., Robbes, D.(1995).*"In situ processing of high-T_c YBaCuO superconducting devices by focused ion beam micromachining at low temperature", J. Vac. Sci. Technol*. B 13(6): 2772-2776(1995).

6. Hoshino, A., Ozasa, R., Kometani, T., Suzuki, S., Matsui and Mabuchi,K.(2006). "*Development of a Regeneration-type Neural Interface: A micro tube Guide for Axon Growth of Neuronal cells Fabricated using Focused-ion-beam Chemical vapor Deposition", J. Vac. Sci. Technol*. B 24(6): 2538-2543, (2006).

7. Shizhuo, Yin,(1999). "*Fabrication of high-aspect-ratio submicron-to-nanometer range microstructures in $LiNbO_3$ for the next generation of integrated optoelectronic devices by focused ion beams (FIB)", Microwave and optical technology letters*, 22: 396-398 (1999).

8. Vila, F. Harnandez-Ramirez, J., Rodriguez, O., Casals, A., Romano_Rodriguez,J. R. and Morante, M Abid. (2006). "*Fabrication of Metallic contacts to nano-meter-sized materials using a focused ion beam (FIB)", Material Science and Engineering*, C 26:1063-1066

9. Heath,J.R. and LeGouse,F.K.(1993) "*A liquid solution synthesis of single crystal germanium quantum wires", Chem. Phys. Lett*. **208:** 263(1993)

10. Z. Ni, Q. Li, L. Yan, J. Gong and D. Zhu, March (2008*). "Fabrication of carbon nanowires by ion beam for irradiation of MWCNT", Diamond & Related Materials*, Vol.17, issue 3: 365-371.

11. Kiuchi,M., Matsui,S. and Isono,Y.(2008). "*The piezoresistance effect of FIB-deposited carbon nanowires under severe strain", Journal of micromechanics and microengineering*, (2008), Vol.18, Issue 6. pp10.

12. J. Cheng, J., Xiao-ping Zon, Fei Li, Hong-dan Zhang, and Peng-sei REN (June 2006), "*Effect of catalyst precursor on Carbon nanowires by using ethanol catalytic combustion technique*", *Transactions of Nonferrous Metals Society of China*, Vol.16, supplement 1: s385-s387.

13. Kun-Hon Lio and Jhy-Ming Ting,(2004), *"Effets of Ni-catalyst characteristics on the growth of cabon nanowires", Carbon*, Vol.42, Issue 3:509-519.

14. Gamo, K.,Takakura, N. Samoto,N. Shimizu,R. and Namba, S."*Ion beam Assisted Deposition of Metal Organic Films Using Focused Ion Beams", Jpn. J. Appl. Phys.*, Part 2**23**: L293(1984).

15. Wagner, J. P. Levin, J. L. Mauer, P. G. Blauner, S.J. Kirch, and P. Longo (1990), "X-ray mask repair with Focused Ion Beams*",Journal Vac.Sc.Technol*.B.81557

Bulletin of Pure and Applied Sciences
Vol. 32 D (Physics) Issue (No.2) 2013:P. 67-80
www.bpas.in

AN EXPERIMENTAL AND NUMERICAL STUDY OF VORTEX GENERATORS ON THE FLOW PATTERN AND THE AERODYNAMIC COEFFICIENTS

Morteza Alipanah and Ali Zahmatkesh[1]
University of Applied Science and Technology, Sari, P.O. Box 4814975344, Iran
Islamic Azad University of Sari, Sari, P.O. Box 561, Iran

Received on 16 August 2013: Accepted on 22 November 2013

ABSTRACT

This study deals with the experimental and numerical investigation of the effect of vortex generators on the flow pattern on the upper surface of a model of an airliner wing as well as its aerodynamic coefficients. Wing section airfoil is NACA 65-210. The vortex generators used have zero and 15 degrees position angles to flow direction. The experimental tests include detection of flow patterns on the wing's upper surface using Taft, and measurement of lift and drag forces. Fluent software and Reynolds stress model have been used for the numerical analysis of the flow. The studies have been performed in the free stream velocity of 30 meters per second, which corresponds to 265,000 Reynolds and in the angle of attack of 2 - to 20 degrees. Experimental and numerical results show that adding vortex generators to the wing increases the maximum lift coefficient and exhaustion angle of attack and decreases the drag force. Also the maximum lift and minimum drag forces belong to the wing with vortex generators with the yawing angle of 15 degrees. At low angles of attack (before exhaustion) there was a good agreement between the numerical and experimental data, but at high angles of attack (after exhaustion and separation of the flow), due to the complexity of the separation problem, the fluent software is not sufficiently accurate.

Keywords: Vortex generators, Flow pattern, Aerodynamic coefficients, Velocity.

INTRODUCTION

Reduction of drag force has always been of interest to scholars and aerospac scientists, automotive industry, designers of buildings, towers, bridges, etc. In all case the end was to decrease the drag force, by the use of new samples and tricks. Since th first flight was made by the Wright brothers, it was to design the outward shape of th plane so that to produce the lowest possible drag forces in order to use the least thrust t push it forward. Then with increasing advances in science, various strategies wer proposed in this regard. One of the factors that produce drag forces is the separation c the flow from the surface of objects. There are different ways to prevent boundary laye

---

[1] - corresponding author: zahmatkeshali209@yahoo.com

separation in the plane and engineering applications. Some of these devices need an additional power which is produced by propulsion, to perform its task; these devices are called Active. Some devices are passive. i.e. they do not need additional power to perform their tasks. According to a general rule, in straight horizontal flights, in which passive control devices are not required, the drag force will increase if there are such devices. To control boundary flow for active devices, we can use the methods of suction, blowing, mobile surface, magneto dynamics, electro dynamics, jet induced turbulence, feedback control systems binary boundary layer, and for passive devices vertex generators, wing fence, leading edge strake and saw-tooth leading edge can be used. Most of the active saw non-12 teeth boundary layer control devices produce vortexes in different ways. In the back oriented wings, due to the tendency of the flow to move towards the tip of the wing and exhaustion in the wing tip, passive devices are usually used to control the flow. One of the usual devices to control the flow on the surface of the back oriented wings, are vortex generators (figure 1).

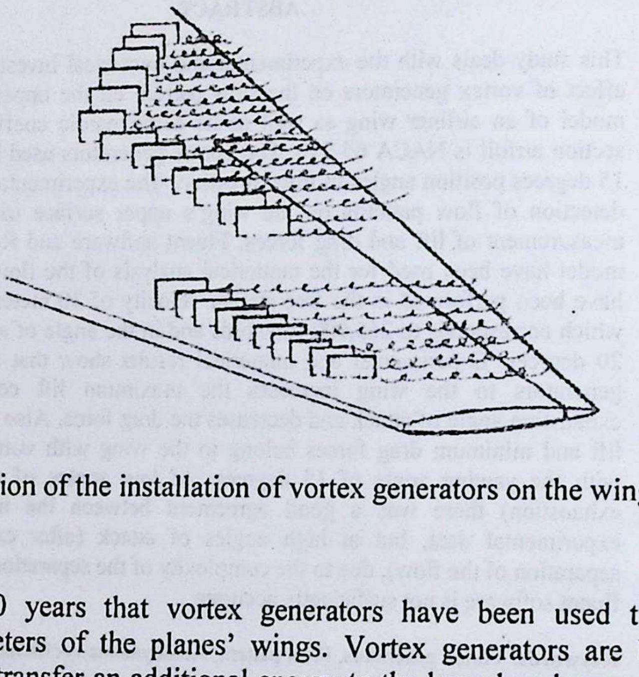

Figure 1: Illustration of the installation of vortex generators on the wing surface [1].

For more 50 years that vortex generators have been used to improve the aerodynamic parameters of the planes' wings. Vortex generators are boundary layer control devices that transfer an additional energy to the boundary layer adverse pressure gradient, which is separating from the surface. These devices are usually small, triangular or rectangular plates which are installed on the wing surface and in front of the flow. They act like a small wing with low aspect ratio and the flow passing from their tip creates a vortex flow in the direction of the wing's chord and this flow transfers much kinetic energy into the boundary layer. This devices delay the flow separation on the wing of an airplane, at high angles. It is obvious that delaying flow separation makes drag force decrease. These devices also increase the maximum lift coefficient so that the aircraft can land on the ground, in low speeds [2]. Vortex generators were studied for the first time in 1960 by Taylor and Bruynes, in NASA [3]. Control of the turbulent boundary layer flow separation, using very small vortex generators was studied by John

C. Lin [4]. This study includes the expansion of the flow field induced by vortex generators and their application to increase the amount of maximum lift force.

His fundamental research revealed that using very small vortex generators is the most effective way to decrease flow separation in turbulent boundary layers. These studies have been performed on a high-lift airfoil, at Reynolds numbers and near flight Reynolds numbers. The main advantages of this type of vortex generators, besides effectively controlling the flow separation, are their simplicity and low drag. The results of this study show using very small vortex generators, leads to a significant decrease in the separation of the flow passing through the flap. Other advantages of using these devices are 10% increase in lift force, 50% decrease in the drag force and 100% increase in the lift to drag ratio [4]. Examination of vortex generators as a new high-lift device in airliners has been performed by Melin *et.al* [5]. They used experimental and numerical methods to simulate the aerodynamic behavior of an airliner wing that is equipped with deployable vortex generators.

Geometry studied in this paper consists of a simple row of small triangular wings which are installed on the upper surface airfoils, near the leading edge. The experimental results of wind tunnel tests show an increase of 0/3 in the maximum lift coefficient and a slight increase in the drag coefficient and exhaustion characteristics [5]. To prevent exhaustion in an airfoil, Simon A. Prince et.al utilized air-jet passive vortex generators. In this study the empirical and numerical examination of an example of a flow control system of an air jet vortex generator has been performed, to delay or eliminate the separation of the boundary layer of the leading edge followed by exhaustion of a Naka 23012 airfoil model. The results of the study show that the use of passive air jet vortex generators effectively delays leading edge flow separation and exhaustion to higher angles of attack and significantly decreases the amount of drag force, without the need to the input energy [6]. Evaluation of the flow on the engine's position and controlling the flow on the wing using vortex generators in a high-lift configuration has been done by Yuzuru Yokokawa *et.al.* [7] In this study the effect of the vortex generator installed in the position of the engine, on the aerodynamic performance of a commercial aircraft with a high-lift configuration near the maximum lift has been empirically examined. In this study, the interaction of the flows between the engine and main wing has been observed using wind tunnel test and numerical methods, then by the use of Genetic Algorithms the optimal location of vortex generators has been specified through Kriging model and experimental tests. The results showed that the longitudinal vortices induced by the generator control the flow separated near the engine position and its tips [7].

Design and analysis of vortex generators for a hybrid electrical vehicle model has been performed by Johari Bin Ismail [8]. This study deals with the design and analysis of the vortex generators at the end part of the rear of a Proton hybrid electrical vehicle, using the Computational Fluid Dynamics methods. These vortex generators are in the form of a row of triangular-shaped blades which are installed on the end part of the vehicle roof. The aim of this study was to determine the percentage of drag force reduction when vortex generators are used in speeds from 60 to 120 km/h. In this study the amount of drag force has been calculated using finite element methods and the output of Computational Fluid Dynamics. The results showed that using vortex generators reduces the drag force in the amount of 6.61%. Natálie Součková et al. studied the control of boundary layer flow separation in flap airfoils using small vortex generators [9].

The study includes experimental and numerical investigations on six-series airfoils. First using numerical simulation of the flow, using fluent software on the airfoils, location of the flow separation and thickness of the airfoils boundary layer is determined, and then according to the results the vortex generators have been designed. In experimental studies using detection by Taft, the effect of the vortex generators on the flow on the airfoil surface has been examined [9]. Numerical study of the effect of the passive vortex generator in controlling the flow has been performed by Florian von Stillfried [10]. In this study a vortex generator statistical model which is developed by the Swedish Defense Research Agency, has been numerically examined. Using this statistical method there is no need to the complete calculation of the three-dimensional geometry of vortex generators in a Computational Fluid Dynamics mesh generation. Using this statistical model reduces the calculation costs and increases the speed of information processing [10]. Todd R. Quackenbush et.al. studied the development of deployable vortex generators and tested them, using memory alloy actuators [11]. This study deals with the design, construction, and practical demonstration of Pop Up Vortex Generators. Results of the wind tunnel tests on a full-scale wing with a row of this type of vortex generators show that the use of these tools significantly reduces flow separation and increases lift force as well as lift to drag ratio in airliners [11]. L. J Souverein has studied the effect of air jet vortex generators on shock wave boundary layer interaction [12]. In this study the effect of the upstream Injection of the continuous flow of air has been empirically studied by air-jet vortex generators in interaction with shock wave turbulent boundary layer. This test is performed on the Mach number of 23. The PIV measurement system is used to investigate the effect of the air jet vortex generators on the topology of the boundary layer of upstream flow, and on the distance and dynamic characteristics of injection, and hot wire is used to study the unsteady characteristics of the reflection shock wave. The results show that vortex generators can reduce the length and height of the separation bubble and increase the frequency range of the reflected shock wave energy by approximately 50% [12].

TEST EQUIPMENT

All the experiments were conducted in a subsonic wind tunnel. In these experiments, wind tunnel, model, A/D board, six-component balance and a computer for receiving, recording and processing of the data have been used.

Model

All the studies were performed on an airliner wing model. This wing model has a leading edge sweepback angle of 17 degrees, trailing edge sweepback angle of zero degree and aspect ratio of 3.17. The wing Span is 37.4 cm and its root chord is 14.6 cm. The airfoil of the wing's cross section is a 10 percent six-series airfoils of NACA 65-210 (figure 2) [16-17]. The wing has no twist.

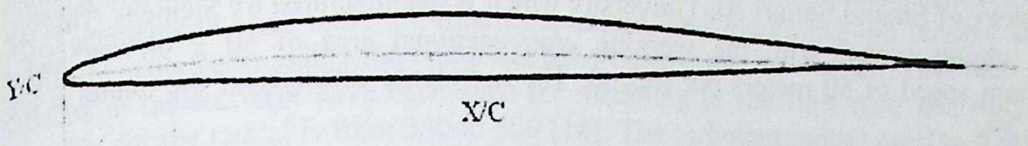

Figure 2: The NACA 65-210 airfoil used in the wing's cross section.

Vortex generators

In the experiments two types of vortex generators with lengths of 0.6 cm and height of 0.2 cm have been used. These vortex generators, which are made in the shape of a flat plate with zero and 15 degrees yawing angle, are mounted with the distance of 10% of mean chord from the leading edge (figures 3).

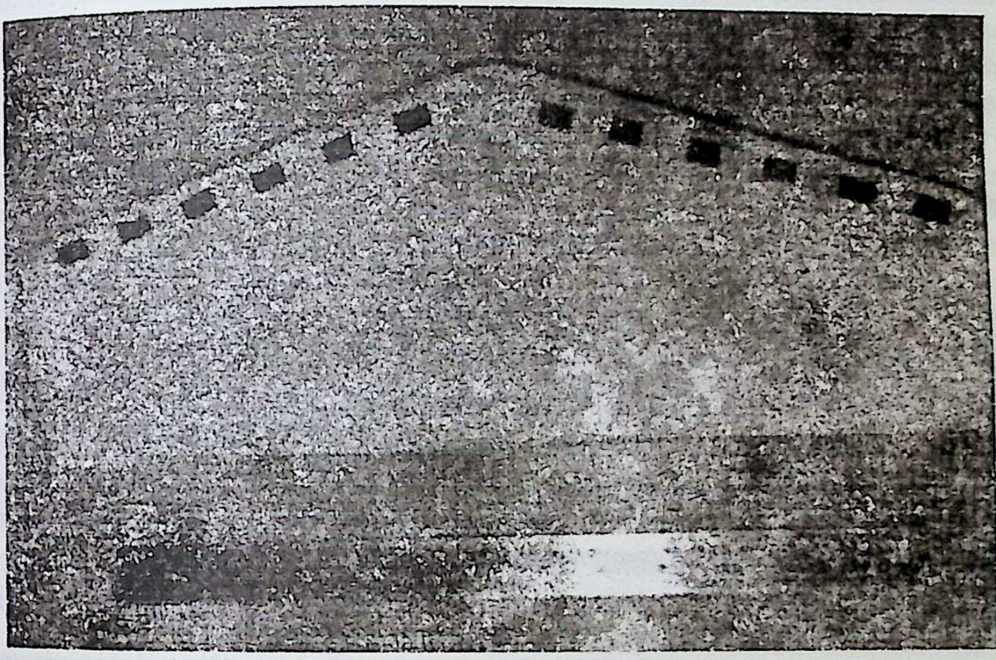

Figure 3: A view of the experimental model with vortex generator with yawing angle of zero degrees

The information on the vortex generators, which is based on the figure 4, is given in the following table:

Table 1: Geometric information about the vortex generators

Vortex generator	*Mounting angle (Deg)*	*Position along the chord (cm)*	*Length (cm)*	*Height (cm)*
The first type	Zero	3.74	0.6	0.2
The second type	15	3.74	0.6	0.2

Wind tunnel

The experiments have been carries out in the subsonic wind tunnel of the aerodynamics Laboratory of Shahid Sattari Air University which is manufactured by Siemens. This is a closed circuit tunnel with the working cross-sectional area of 50 x 96 cm^2 and a maximum speed of 50 meters per second. The turbulence intensity of the tunnel is less than 0.2%.

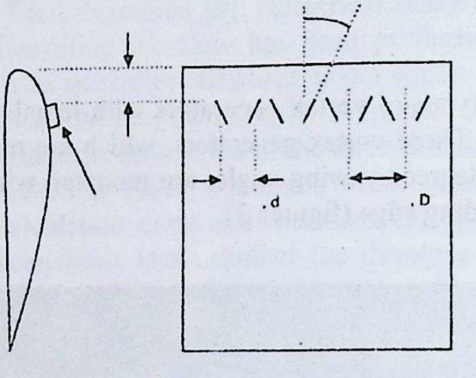

Figure 4: Introduction of the various parameters of vortex generators forms

PROCEDURES

All the experiments have been carried out at the speed of $V\infty = 30\ m/\ s$ which corresponds to the Reynolds number of $Re = 2.65\times 10^5$. The experiments have been performed at the angles of attack of 2 degrees to 20 degrees with steps of 2 degrees. The experiments conducted include the detection of the flow patterns on the upper surface of the wing using Taft, and measurement of the aerodynamic forces of lift and drag. First the wing exhaustion was determined using detection of the flow at different angles of attack and in the next step the vortex generators were installed in places where the wing exhaustion occurs. Then forces are measured using the balancing machine, and its output is received and transferred to the computer by the use of A/D board.

Numerical Simulation

Numerical analysis of the flow around the wing without and with the vortex generators is done by the fluent software version 6.2.0. The model used for analysis by the fluent software is made using the modeling software of Gambit version 2.4. The software tools are used to produce a computational grid for numerical calculation. Reynolds has been considered equal to 265,000 and the boundary layer thickness is assumed to be 0.5 cm. After doing some studies, the organization mesh was used for the model's mesh generation. Since the flow behavior faces more changes in the leading edge and the vortex generators' connection areas, special mesh generator with more elements is used in the surrounding areas. In this area, the total volume of the computational grid is divided into smaller volumes and the organization's B network is built on these volumes. In order to have an appropriate computational grid, the number of volume elements was increased to approximately 950,000 and a computer with two processors was used to implement the program. It should be noted that there is no need to increase the number of volume elements to have more accurate calculations, and increasing the number of the volume elements surrounding the body, does not change the results. The Standard Wall Functions in the software have been used for modeling of the flow near the wall. The value of y_* for the model is from 350 to 500 [18]. The turbulent model used to solve the flow equations, is of the type of Reynolds stress model. Compared with different turbulence models k –ε, this turbulent model is more complete in predicting flow physics and solving turbulent equations. In this way, there will be an acceptable continuity between the flow momentum equations and flow turbulence parameters, and finally the prediction of the flow physics is done more accurately. In order to calculate other parameters of the flow, perfect gas equations have been used and Sutherland method was used for viscosity of the flow. In the numerical calculation using this method, the convergence of the residues is done very slowly, and in order to accelerate it, it is better to use easier methods such as k-ε, to guess initial values, and to do the rest of calculations by the Reynolds stress model. Since in this method the relationship between momentum equations and the values of turbulent variables is highly accurate, so the convergence of the equations' solutions would lead to more problems than other methods such as standard $k-\varepsilon$ or RNG, and it is necessary to make some changes in the experimental values of the software, during the process of numerical calculations [19-20]. For the numerical simulation of the flow, the boundary conditions of pressure and Mach number of the flow are applied to a finite volume, and equations are solved using the implicit continuous method in flow field. In addition to having proper adjustment with the flow pattern, use of these boundary conditions leads to faster convergence of the residuals. Another factor affecting the convergence of residuals' values is the extension of the control volume to the model, and the control volume should be large enough. For this purpose, according to the model size and width, control volume is considered about 25 to 30 times the length of the model.

RESULTS

The results of the study are presented in the two forms of numerical and experimental results.

a-Experimental results

As it is shown in the figures, for the wings with narrow liquidity ratio of about 0.6 (Narrow liquidity ratio of the wing), exhaustion starts from the end part of the wing, and with increasing angle of attack, this area also increases and covers more area of the wing surface. This type of prediction, is done regardless of the type of the airfoils comprising the wing and other parameters such as torsion angle of the wing, location of the wing in the aircraft, and accessories such as wing tip's flap, aileron and the like which can affect the aerodynamic behavior of the wing and change the process and location of its separation. The flow conditions, flow's turbulence or slowness and Reynolds can also affect the angle of attack of the separation and the speed of exhaustion's expansion. Diagnosis of the mechanism of exhaustion in a three-dimensional wing is important in design and layout of different elements on the surface of the wing like ailerons, flap, and consolidation of structural components such as Rib and Spars and the wing skin. Care must be taken in designing a wing. Control surfaces especially ailerons should be placed in positions so that they maintain their effectiveness and efficiency in the maximum efficiency of the angle of attack, and even after the complete exhaustion of the wing, they should remain applicable; because for getting out of the exhaustion conditions and returning to flight conditions, applying control surfaces, especially ailerons is inevitable. In addition, structural design of the wing should be done in a way that in all aerodynamic situations arising, there would be a proper structural confidence margin.

Comparing these figures with the figures of single wing and combination of wing with vortex generators with yawing angle of zero degree, we can conclude that vortex generators with yawing angle of 15 degrees, delay the flow separation on the wing surface to a greater extent and the wing would be effective to higher angles of attack.

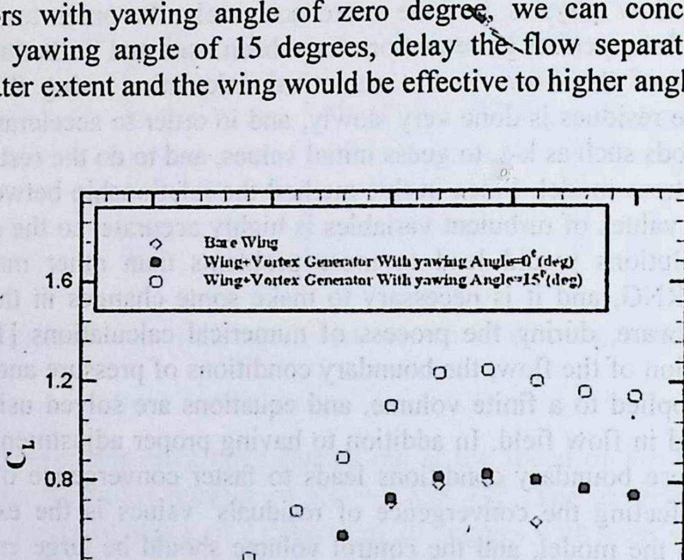

Figure 5- Lift coefficient changes based on the angle of attack

Lift coefficient changes for different conditions of the single wing and wing with vortex generators with yawing angle of zero and 15 degrees are illustrated in the figure 5. As you can see in the figure, lift coefficient increases with increasing the angle of attack. Since the model used has curvature, so there is non-zero lift in the angle of attack of zero degree. Maximum lift occurs at the angle of attack of about 14 degrees which is the angle of attack in exhaustion, and after this angle of attack, flow separation occurs and because of the wing's exhaustion, lift coefficient decreases. Installing the vortex generators on the wing delays the flow separation on the wing surface and changes the wing exhaustion pattern and increases the value of lift coefficient. The maximum lift coefficient occurs when vortex generators with yawing angle of 15 degrees are mounted on the wing, which indicates at this yawing angle, stronger vortexes are produced on the wing. The present figure confirms the results of detection of the flow patterns on the upper surface of the wing. As you can see in the figure, lift coefficient in the single wing has suddenly started to decline after the angle of attack of exhaustion; so these results also confirm the existence of the separation bubble. Therefore this wing model has leading edge exhaustion. In this type of exhaustion, lift coefficient experiences a sharp and sudden decrease after the angle of attack of exhaustion (according to reference [13]). As you can see after installing vortex generators, flow separation moves towards the flow's downstream point on the wing surface and flow separates from the wing's leading edge instead of trailing edge and separation pattern becomes similar to the trailing edge exhaustion (lift coefficient decreases slowly, with the increase of the angle of attack). Adding vortex generators with yawing angle of zero degree, does not change the slope of lift coefficient to the single wing and only increases the value of maximum lift coefficient, which is in accordance with the results of reference [26]. But for vortex generators with yawing angles of 15 degrees, both the slope of lift according to the angle of attack and the value of *CLMax* will rise dramatically.

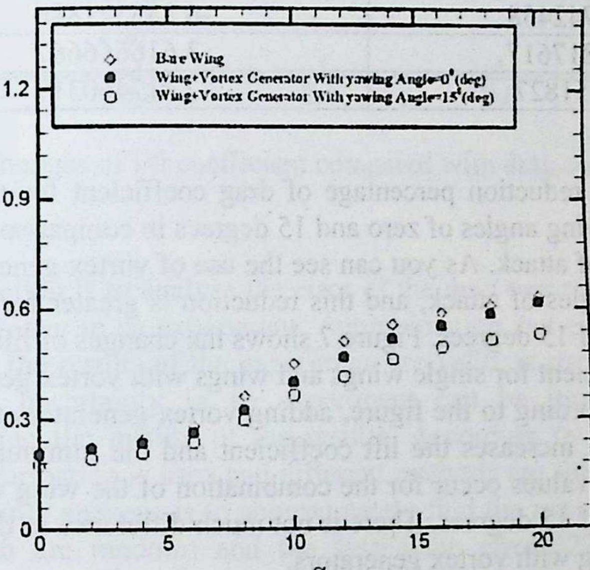

Figure 6- Drag coefficient changes based on the angle of attack

Figure 6 shows the drag coefficient changes based on the angle of attack for the single wing and the wing with vortex generators with yawing angles of zero and 15 degrees. As you can see in the figure, drag coefficient increases with the increase of the angle of attack. After the wing model becomes exhausted (at the leading edge of about 14 degrees) because of the flow separation from the wing surface, a sudden increase in the value of drag occurs. After installing vortex generators on the wing surface and producing vortex flow, since the additional energy is added to the boundary layer, flow separation is delayed and drag coefficient at all angles of attack decreases. It is also seen in the figure that the minimum drag value occurs in the case that a vortex generator with yawing angle of 15 degrees is mounted on the wing surface.

Table 2: Percentage of the reduction in drag coefficient due to the use of vortex generators with different yawing angles.

Reduction percentage of drag coefficient of wings with VG with angle of 15 degrees	Reduction percentage of drag coefficient of wings with VG with angle of zero degrees	Angle of attack
-19.88475111	-4.691358025	-2
-19.75058716	-6.28440367	0
-11.011565	-0.772727273	2
-15.11183498	-3.29218107	4
-16.35074769	-5	6
-16.57258237	-11.01928375	8
-20.0063171	-12.33766234	10
-19.85967954	-8.660035108	12
-15.80388752	-6.329113924	14
-16.63742458	-6.885521886	16
-14.30817617	-3.616666667	18
-16.3151827	-2.317460317	20

Table 2 shows the reduction percentage of drag coefficient for the wings with vortex generators with yawing angles of zero and 15 degrees in comparison with the single wing at different angles of attack. As you can see the use of vortex generators has reduced the drag force at all angles of attack, and this reduction is greater for the vortex generators with yawing angle of 15 degrees. Figure 7 shows the changes of lift coefficient compared with the drag coefficient for single wings and wings with vortex generators with different yawing angles. According to the figure, adding vortex generators to the wing, decreases drag coefficient and increases the lift coefficient and the minimum drag force and the maximum lift force values occur for the combination of the wing with vortex generators with yawing angle of 15 degrees. There is not much difference in the value of *CD* for the single wing and wing with vortex generators.

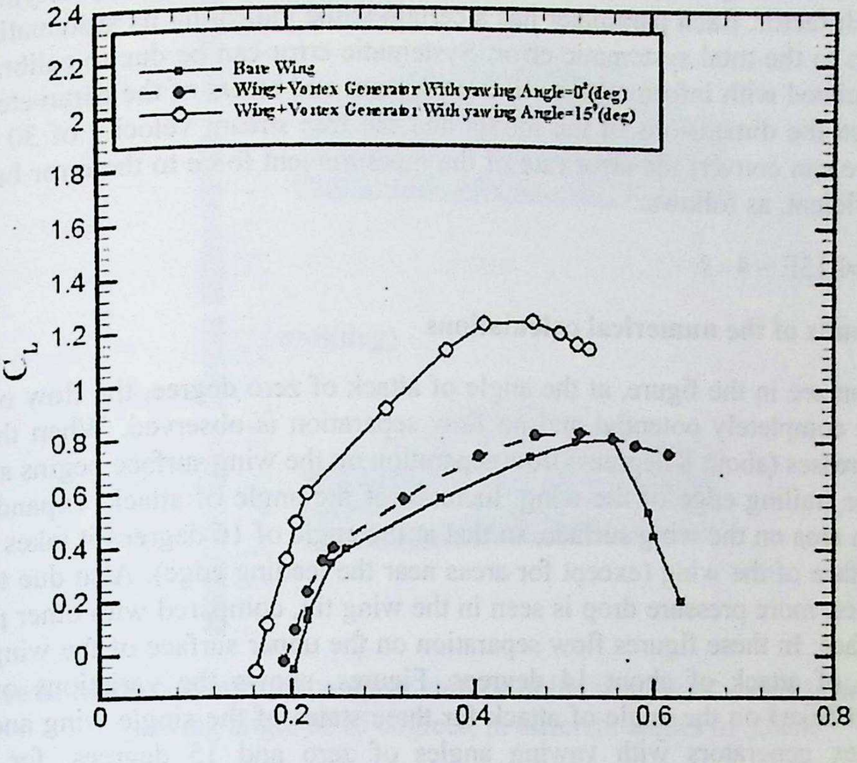

Figure 7: Changes of lift coefficient compared with drag coefficient

Uncertainty of the answers

The purpose of this section is to analyze the error of the drag force measurement. There are various sources of error in an experiment. Approximation and estimation of the rate of this error to ensure the results of the experiment are valid, is part of the experiment. The measurement of uncertainty in an experiment can be introduced during the experiment to determine the quality of the results. According to the purpose of the experiment, certain information is used and different methods are followed. The ultimate purpose of the uncertainty analysis is to approximately find the maximum parameters of Precision error (which are random) and the systematic error [27]. Considering the combination of these two parameters we can determine the ultimate experiment errors and the uncertainty of the results.

Precision error is usually estimated using data obtained from experiment's results. This type of error is concerned with the reproducibility of the answers, and is obtained based on statistical mathematics. The differences in responses observed in the experiments, which are due to unexpected changes in the conditions of the experiments, are recorded. Using statistical calculations, the approximate variance of the data obtained from the experiment can be considered as the equivalent of the Precision error. Systematic error is the error of the components used in the experiment and is not related to the answers obtained by repeating the experiment. The main characteristic of systematic error is detection and confirmation of the results used for each parameter that determines the general range of the ultimate answers' uncertainty. Systematic error approximation is done by determining the parameters used in the measurements and specifying the error rate of each factor. Each parameter has a certain value indicating its systematic error and contributes to the total systematic error. Systematic error can be due to calibration error, error associated with information collecting system and errors of the parameters together [28]. Given the dimensions of the model and the free stream velocity of 30 meters per second, we can convert the error rate of the measurement force to the error based on the drag coefficient, as follows:

$$C_D = C_D \pm 4.15\mathrm{E}-4$$

b-The results of the numerical calculations

As you can see in the figure, at the angle of attack of zero degree, the flow on the wing surface is completely potential and no flow separation is observed. When the angle of attack increases (about 8 degrees) flow separation on the wing surface begins and extends toward the trailing edge of the wing. Increase of the angle of attack, expands the flow separation area on the wing surface, so that at the angle of 16 degrees it takes almost the entire surface of the wing (except for areas near the leading edge). Also due to the wing tip vortexes, more pressure drop is seen in the wing tip, compared with other parts of the wing surface. In these figures flow separation on the upper surface of the wing occurs at the angle of attack of about 14 degrees. Figures, shows the variations of the drag coefficient based on the angle of attack for three states of the single wing and the wing with vortex generators with yawing angles of zero and 15 degrees, for numerical calculations. According to this figure, before the angle of attack of about 10 degrees, the minimum drag value belongs to the wing with vortex generators with yawing angle of 15 degrees which is in accordance with the results of the experimental data, and at higher angles of attack, due to lack of proper performance of the fluent software in the wing exhaustion areas, the minimum drag value belongs to the wing with vortex generators with yawing angle of zero degree, that shows this software is unable in modeling the flow at its separation areas.

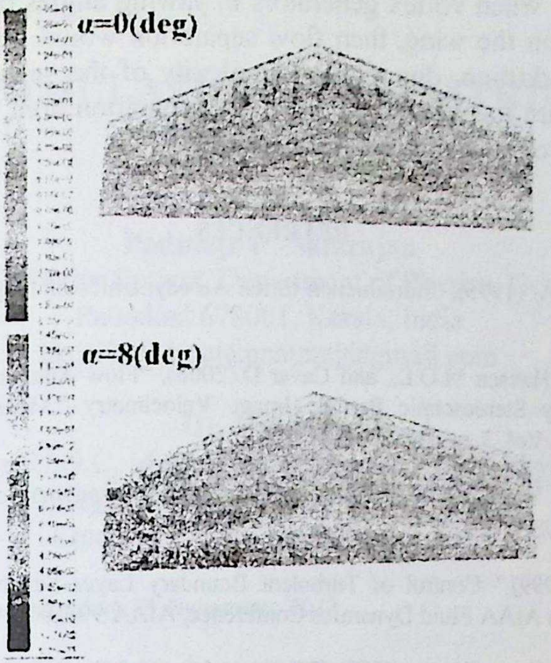

Figure 8: Mach contour on the upper surface of the wing with vortex generators with yawing angle of 15 degrees, at different angles of attack

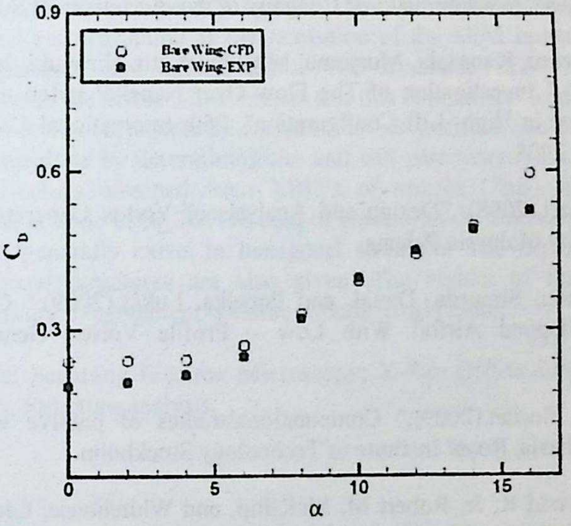

Figure 9: Comparison of the drag coefficient changes with respect to the angle of attack, for experimental and numerical data of the single wing

CONCLUSION

The results of the experiments and numerical calculations suggest that adding vortex generators to the wing delays the flow separation on the wing surface, due to adding a kinetic energy to the boundary layer which is separating from the body surface.

It was also found that when vortex generators in yawing angles other than angle of zero degree, are mounted on the wing, then flow separation would occur later and at higher angles of attack. In addition, due to the complexity of the separation process and the fluent software's failure to work properly on the separation area, this software can only be used for the angles of attack before the exhaustion.

REFRENCES

1. Talay Theodore A. (1975), "Introduction to the Aerodynamics of Flight", NASA SP-367, pp.47-49.

2. Velte C.M., and Hansen M.O.L., and Cavar D.(2008), "Flow Analysis of Vortex Generators on Wing Section by Stereoscopic Particle Image Velocimetry Measurements", *Environmental Research Letters*, Vol. 3, no. 015006, pp. 1-11.

3. Kuethe A.R, and Yen Chow C. (1986),"Foundations of Aerodynamics", Fourth ed., John Wiley and Sons Press, USA.

4. Lin, John C. (1999)," Control of Turbulent Boundary Layer Separation Using Micro Vortex Generators", 30th AIAA Fluid Dynamics Conference, AIAA 99-3404.

5. Melin, Tomas, Crippa, Simone, Holly, Martin and Smid, Miroslav,(2006)," Investigating Active Vortex Generators as a Novel High Lift Device", 25th International Congress of the Aeronautical Sciences, ICAS 2006.

6. Prince, Simon A, Khodagolian, Vahik, Singh, Chrisminder, Moir, Sunil and Kokkalis, Anastasios,(2008)," Aerodynamic Stall Suppression on Aerofoil Section Using Passive Air Jet Vortex generators",26th International Congress of the Aeronautical Sciences, ICAS 2008.

7. Yokokawa, Yuzuru, Kanazaki, Muryama, MitsuhiroKato, Hiroyuki, Ito, Takeshi and Yamamoto, Kazuomi.(2008)," Investigation of The Flow Over Nacelle/ pylon and WingControlled With a Vortex Generator in High- Lift Configuration", 26th International Congress of The Aeronautical Sciences, ICAS 2008.

8. Bin Ismail, Johari.(2008), "Design and Analysis of Vortex Generator for a HEV Model", B.S Thesis, University Malaysia Pahang.

9. Součková, Natálie, Šimurda, David, and Popelka, Lukáš.(2009)," Control of Boundary Layer Separationon Flapped Airfoil With Low – Profile Vortex Generator", Colloquium Fluid Dynamics.

10. Von Stillfried, Florian.(2009)," Computationalstudies of passive vortex generators for flow control", PhD Thesis, Royal Institute of Technology Stockholm.

11. Quackenbush, Todd R, Jr, Robert M. McKillip, and Whitehouse, Glen R.(2010)." Development and Testing of Deployable Vortex Generators Using SMA Actuation", 8th AIAA Applied Aerodynamics Conference, AIAA 2010-4686.

12. Souverein, L. J., and Debie`ve, J. F.(2010), " Effect of air jet vortex generators on a shock wave boundarylayer interaction", *Experimental Fluids journal*, pp1053-1064

Bulletin of Pure and Applied Sciences
Vol. 32 D (Physics) Issue (No.2) 2013:P. 81-94
www.bpas.in

COMPUTER SIMULATION OF SEM STRUCTURES OF THIN FILMS

Padmaja P Natarajan
Project Fellow, U.G.C. Major Project, Department of Physics, Govt. Victoria College,
Palakkad 678001, Kerala, India
Email: padmaja.pnataraj@gmail.com

Dr. V. Geetha
Principal Investigator, U.G.C. Major Project, Department Of Physics, Govt. Victoria
College, Palakkad 678001, Kerala, India
Email:geethavishnu22@yahoo.com

Received on 20 July 2013: Accepted on 29 November 2013

ABSTRACT

Current methods for reconstructing surface topography from SEM images are either not suitable at nanometer scales, restricted to simple shapes described by a limited number of parameters or involve time consuming steps. We describe a computer simulation (using C-programming) whereby an initial surface is iteratively updated. This simulation performs a two dimensional reconstruction at the resolution of the SEM images for both high temperature and ageing cases. The simulated SEM images are compared with the actual SEM images and this comparison leads to further refinement of the reconstructed surface. Further justifications of simulated structure are done by determining the unit cell parameters (h k l) with the help of d-values obtained from XRD's of sample (ZnS), and thereby comparison is done using JCPDS data of zinc sulphide.It revealed that zinc sulphide.It generally exists in hexagonal structure. The explanations for non-hexagonal structures are also given .The results of the computer simulations are in agreement with the experimental results.

Keywords: Scanning Electron Microscopy; X-Ray Diffraction; Computer simulation; Structure analysis.

1: INTRODUCTION

ZnS is a semiconductor with a wide band gap, which makes it suitable as a transparent material in the visible region. They exist mainly in two forms, an α–phase (hexagonal wurtzite structure) and β-phase (cubic sphalerite structure) [22] and this dualism is often a salient example of polymorphism. Out of these two phases, its β-phase is more stable at standard temperature and pressure (STP).It is the sample chosen for our study because it is easily available and good quality thin films can be produced. Zinc Sulphide was successfully deposited on the glass substrate by chemical deposition method with the help of Successive Ionic Layer Adsorption and Reaction (SILAR). This technique involves multiple dipping of a substrate in cationic and anionic precursors. Between every immersion it is rinsed in distilled water or ion exchanged water.

The structure of the films is ascertained by x-ray diffraction (XRD) method. From XRD patterns of ZnS, Hexagonal structures were investigated and it was seen that no good peaks were obtained in Rhombohedral or Cubical structure. From this, it was clear that ZnS generally exist in Hexagonal structure. In order to establish this, SEM patterns of corresponding thin films were taken. It revealed that sphalerite structures are transient in nature and most of the ZnS observed are of wurtzite structure. In order to justify this, we made use of computer simulation method.

In the present paper, regeneration of surface topography from SEM micrographs with specified resolutions (for ageing & high temperature cases) are done using computer simulation method and the results are correlated using JCPDS (Joint Committee on Powder Diffraction Standards) data. The simulation of films can give an idea of how to rearrange the defects and vacancies on it, that may be useful in nanotechnology

2: SCANNING ELECTRON MICROSCOPY

Scanning Electron Microscopy (SEM) [7,17,5] opens the possibility to image surfaces and cross- sections with a high resolution (~2-5 nm) and high depth of field. It is a versatile tool with a stepless magnification range of 20 to 200,000 and it allows fast switching from one sample to the next. In combination with X-Ray Spectroscopy (EDX (Energy-Dispersive X-ray)), the SEM is the ideal tool for failure analysis as it combines microscopic visualization with local chemical analysis. On cross-sections it can be used for precise measurement of thin film thickness within the nanometer to millimeter range and after deposition of a thin conductive coating even insulating samples can be investigated.

The scanning electron microscope (SEM) uses a focused beam of high-energy electrons to generate a variety of signals at the surface of solid specimens. The signals that derive from electron-sample interactions reveal information about the sample including external morphology (texture), chemical composition, and crystalline structure and orientation of materials making up the sample. In most applications, data are collected over a selected area of surface of the sample, and a 2-dimentional image is generated that displays spatial variations in these properties. Areas ranging from approximately 1 cm to 5 microns in width can be imaged in a scanning mode using conventional SEM techniques. The SEM is also capable of performing analyses of selected point locations on the sample; this approach is especially useful in qualitatively or semi-quantitatively determining chemical compositions (using EDS (Electronic Data Systems)), crystalline structure, and crystal orientations (using EBSD (Electron probe Micro Analyzer). The design and function of the SEM is very similar to the EPMA (Electron probe Micro Analyzer) and considerable overlap in capabilities exists between the two instruments [2,19]. With the help of scanning electron microscope, the micrographs of the sample with specified resolution are taken and for further structural analysis XRDs of that particular sample are taken.

3: X-RAY DIFFRACTION

X-Ray Diffraction (XRD) [1,4,14] is a versatile technique for investigating the structure of crystalline materials. In addition to identifying crystallographic phases it is possible to measure grain sizes, textures and internal stresses. For these investigations not only planar but also curved surfaces are suitable. XRD can also provide information on unit cell dimensions. The analyzed material is finely ground, homogenized and average bulk composition is determined.

XRD is most widely used for the identification of unknown crystalline materials. Other applications include:

- Characterization of crystalline materials
- Determination of unit cell dimensions
- Determination of crystal structures
- Measurement of sample purity
- Identification of fine-grained minerals such as clays and mixed clays that are difficult to determine optically.

In x-ray diffractometers, the x-rays generated are collimated and directed onto the sample. As the sample & detector are rotated, intensity of the reflected x-rays is recorded. When the geometry of the incident x-rays impinging the sample satisfies the Bragg equation, constructive interference occurs and a peak in intensity occurs. A detector records and processes this x-ray signal and converts the signal to a count rate which is then output to a device such as a printer or computer monitor [16,20].

A peak in intensity occurs when the mineral contains lattice planes with d-spacings appropriate to diffract x-rays at that value of θ. Results are presented as peak positions at 2θ and x-ray count (intensity) in the form of an X-Y plot. The d-spacing of each peak is then obtained by solution of Bragg equation for the appropriate value of λ.

From analysis of XRDs & SEM, it was found that the sample (ZnS) mostly exists in hexagonal structure with crystallographic axes, $a=b \neq c$, $\alpha=\beta=\gamma \neq 90°$ [9] .In addition to these hexagonal structures, there exists several other structures such as Rhombohedral, Cubic etc. It may be due to overlapping of adjacent planes, orientation of planes, existence of Zinc Oxide without ionization etc. The white coloration may be due to precipitation of Zinc as sulphides [6].

Our main aim is to simulate the SEM micrograph structures with specified resolution using C-programming. For this, we first go through an introduction to computer simulation and then we will give the explanations.

4: COMPUTER SIMULATION

Computer simulation [8,21] is an analysis technique suitable for modeling and analyzing complex, dynamic systems. Computer simulation programs generate data describing systems operating characteristics for a time period of interest. Computer simulation of random phenomena has become an indispensable tool in modern scientific investigations. Computer simulations vary from computer programs that run a few minutes, to network-based groups of computers running for hours, to ongoing simulations that run for days.

The scale of events being simulated by computer simulations has far exceeded anything possible (or perhaps even imaginable) using traditional paper-and-pencil mathematical modeling. The most significant feature of a simulation is that it allows scientists to imitate one process by another process. "Process" here refers solely to a temporal sequence of states of a system. Given the observation that processes are dealt with by all sorts of scientists, it is apparent that simulations prove to be a powerful inter-disciplinarily acknowledged tool. Accordingly, simulations are best suited to investigate the various research strategies in different sciences more carefully [10].

Why use computer simulation?

A computer simulation is valuable in many respects. It can be used:

a) To provide counterexamples to proposed theorems
b) To build intuition by experimenting with random numbers
c) To lend evidence to a conjecture

A typical dictionary definition from The Oxford English Dictionary describes simulation as:

"The technique of imitating the behavior of some situation or system (Economic, Mechanical etc.) by means of an analogous model, situation, or apparatus, either to gain information more conveniently or to train personnel."

Paul Fishwick, a specialist in simulation techniques, in his book "Simulation model design and execution"1, describes computer simulation as:

"*.. the discipline of designing a model of an actual or theoretical physical system, executing the model on a digital computer and analyzing the execution output.*"

From the educational perspective, Diana Laurillard in "Rethinking University Teaching" states:

"*A computer-based simulation is a program that embodies some aspect of the world, allows the user to make inputs to the model, and displays the results.*"

From the educational perspective Laurillard would set a level below which a simulation ceases to be useful. She says:

"Simulations are useful in representing complex relations. There would be little point, for example, in simulating a model of an aspect of the economy, such as `increasing inflation leads to increasing unemployment` as the relationship is simple enough to understand from the description alone."

Using C-programming, simulation work is done in order to reconstruct the surface topology from SEM images with specified resolutions. The computer simulated structures were enlarged view of the micrographs obtained within a certain micrometers (µm).The program I&II (not given here gives the output at higher temperature and ageing respectively and are compared below

The computer algorithms, programs and outputs are shown below:

ALGORITHM FOR PROGRAM I

i. Specify the (x,y) coordinates of the six vertices namely (x1,y1),(x2,y2),(x3,y3),(x4,y4),(x5,y5),(x6,y6).
ii. Initialize graphics mode.
iii. Set the line style, background and foreground color using corresponding functions.
iv. Accept the number of iterations 'i' from the user.
v. Pass the values of the six coordinates (x1,y1),(x2,y2),(x3,y3),(x4,y4),(x5,y5),(x6,y6) to a sub function..
vi. Draw six line segments joining (x1,y1),(x2,y2),(x3,y3),(x4,y4),(x5,y5),(x6,y6) so as to form a hexagonal structure.
vii. Repeat the steps (i), (iii), (v) with different integer values in order to construct the actual form of the SEM micrograph structure.

ALGORITHM FOR PROGRAM II

i. Initialize graphics mode.
ii. Set the line style, background & foreground colors using corresponding functions.
iii. Specify the (x,y) coordinates of the six vertices namely (x1,y1),(x2,y2),(x3,y3),(x4,y4),(x5,y5),(x6,y6).
iv. Draw six line segments joining (x1,y1),(x2,y2),(x3,y3),(x4,y4),(x5,y5),(x6,y6) so as to form a hexagonal structure.
v. Repeat steps (iii), (iv) with different integer values in order to construct the actual form of the SEM micrograph structure.

5.OUTPUT FOR HIGHER TEMPERATURE (WITH DIP & EXDIP (60, 10))

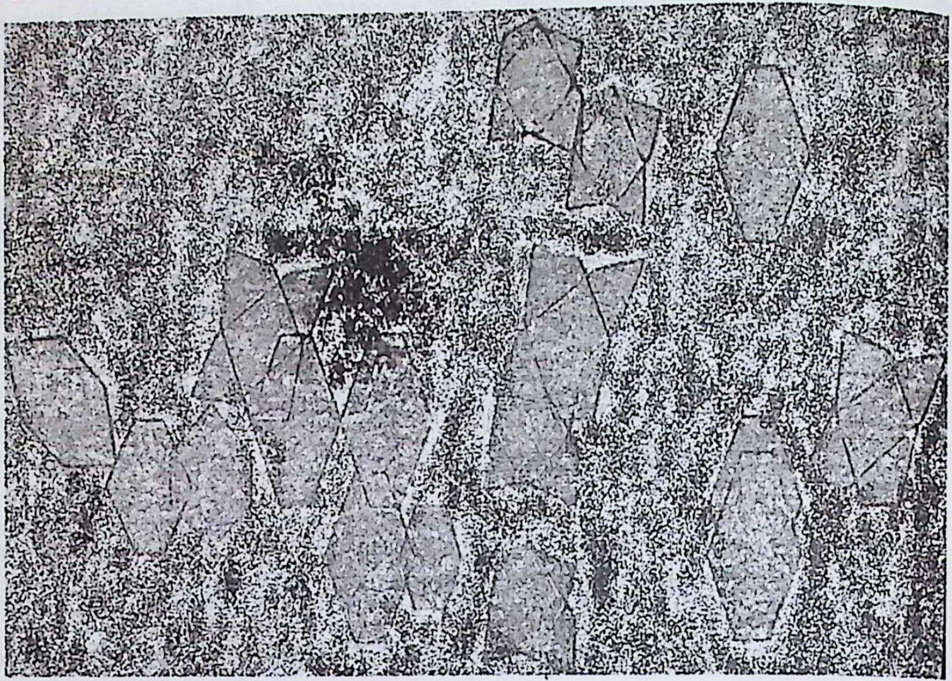

FIGURE 1: ENLARGED VIEW OF SIMULATED SEM STRUCTURE OF HIGHER TEMPERATURE (WITH DIP & EXDIP (60,10))

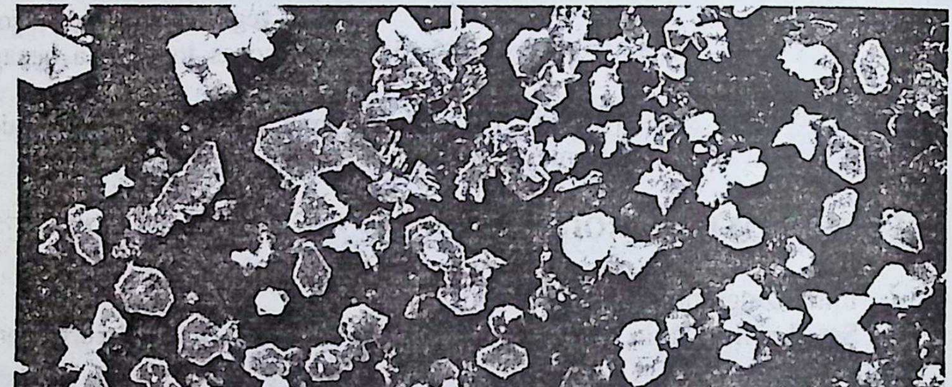

FIGURE 2: SEM STRUCTURE OF HIGHER TEMPERATURE (WITH DIP & EXDIP (60,10))

OUTPUT FOR HIGHER TEMPERATURE (WITH DIP & EXDIP (60,5)).

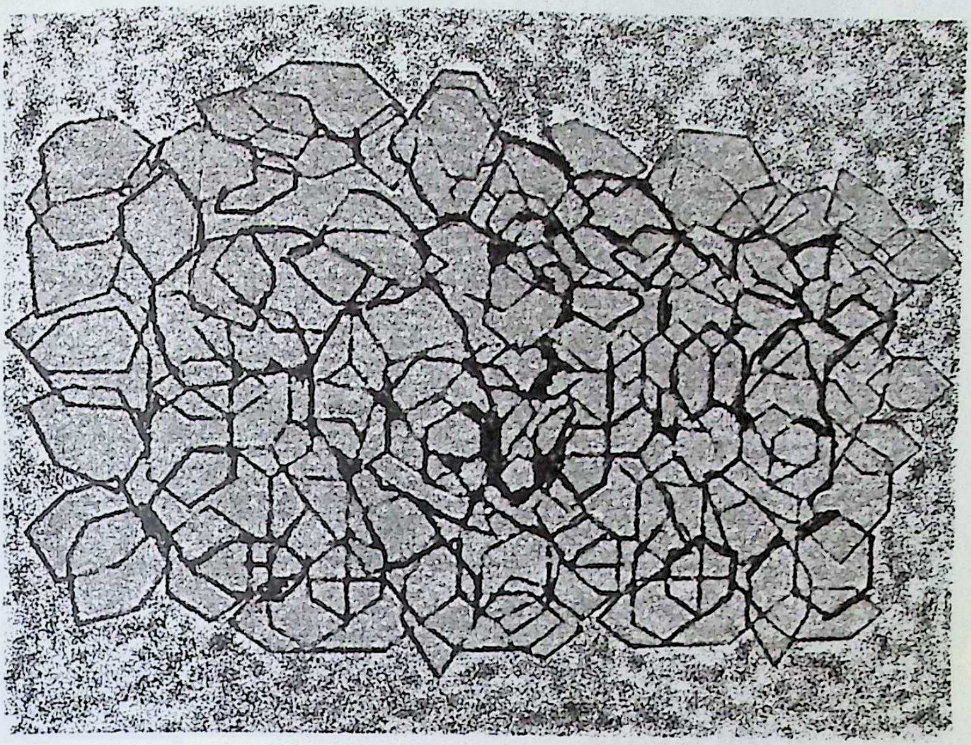

FIGURE 3: ENLARGED VIEW OF SIMULATED SEM STRUCTURE OF HIGHER TEMPERATURE (WITH DIP & EXDIP (60,5))

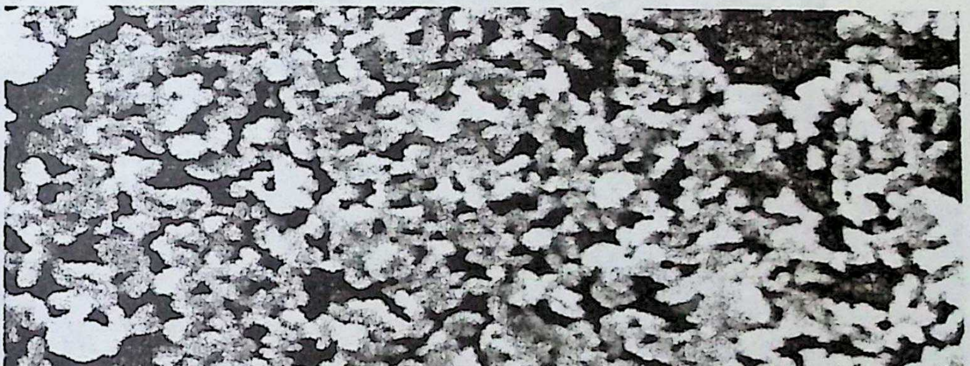

FIGURE 4: SEM STRUCTURE OF HIGHER TEMPERATURE (WITH DIP & EXDIP (60,5))

OUTPUT FOR SEM STRUCTURE AFTER AGEING OF 43 DAYS

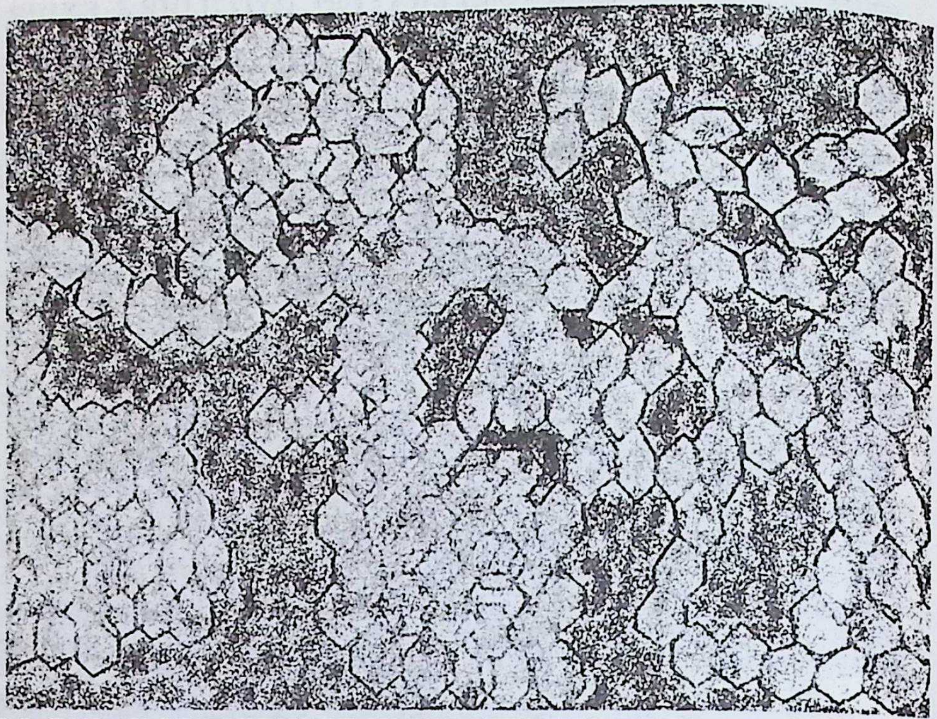

FIGURE 5: ENLARGED VIEW OF SIMULATED SEM STRUCTURE FOR AGEING AFTER 43 DAYS

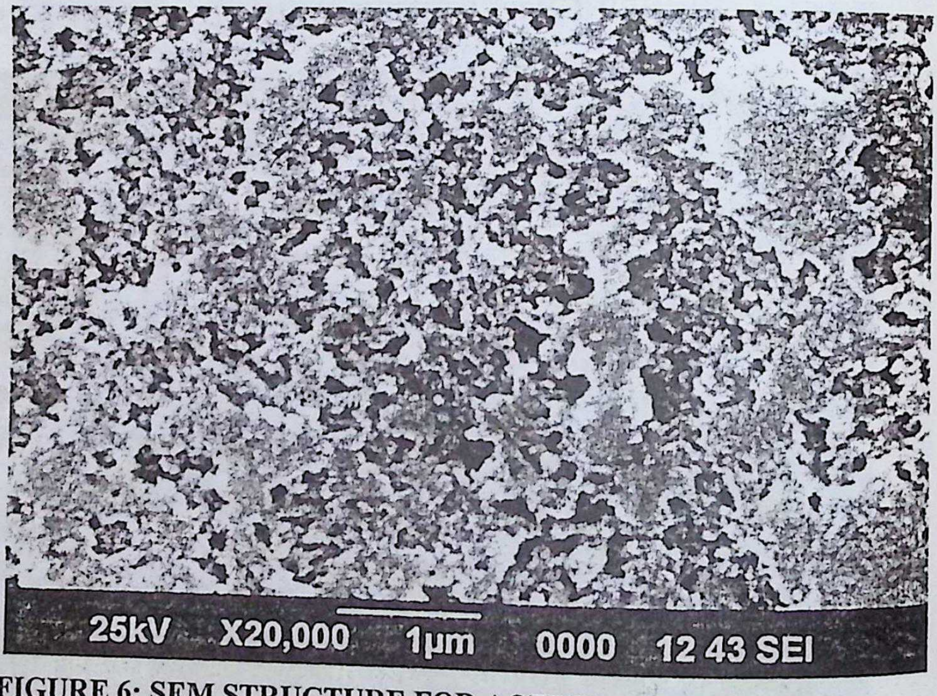

FIGURE 6: SEM STRUCTURE FOR AGEING AFTER 43 DAYS

Similarly programs were done for ageing after 40 days, 45 days, 100 days & the corresponding outputs are shown below:

OUTPUT FOR SEM STRUCTURE AFTER AGEING OF 40 DAYS

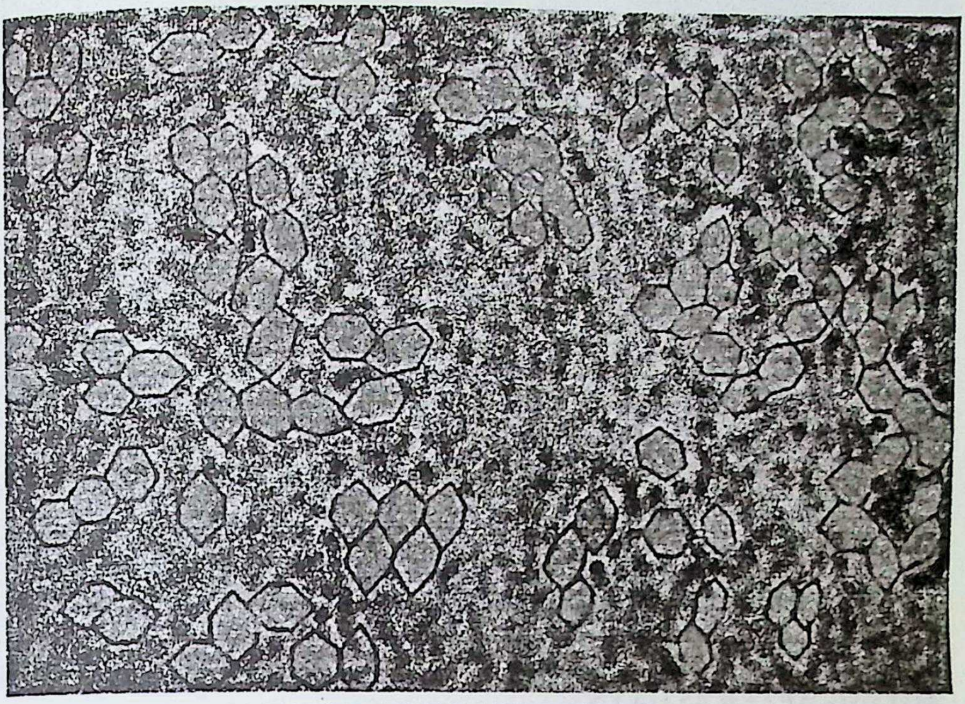

FIGURE 7: ENLARGED VIEW OF SIMULATED SEM STRUCTURE FOR AGEING AFTER 40 DAYS

25kV X20,000 1μm 0000 12 43 SEI

FIGURE 8: SEM STRUCTURE FOR AGEING AFTER 40 DAYS

OUTPUT FOR SEM STRUCTURE AFTER AGEING OF 45 DAYS

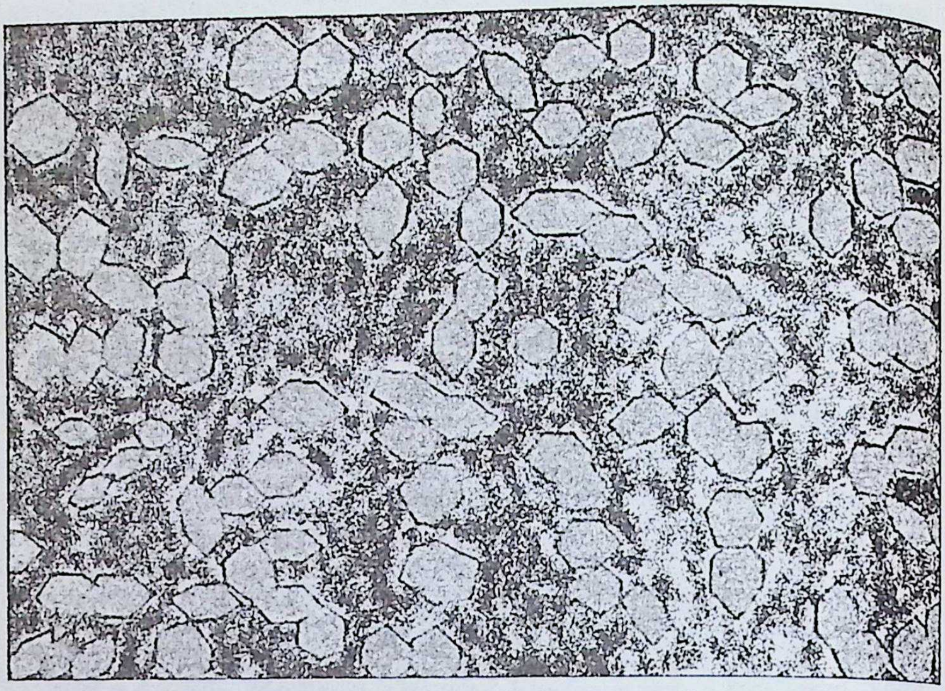

FIGURE 9: ENLARGED VIEW OF SIMULATED SEM STRUCTURE FOR AGEING AFTER 45 DAYS

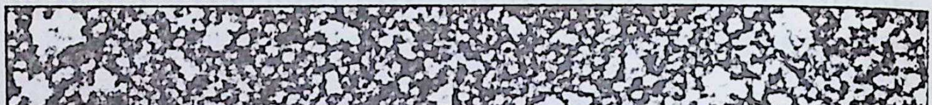
25kV X20,000 1µm 0000 12 43 SEI

FIGURE 10: SEM STRUCTURE FOR AGEING AFTER 45 DAYS

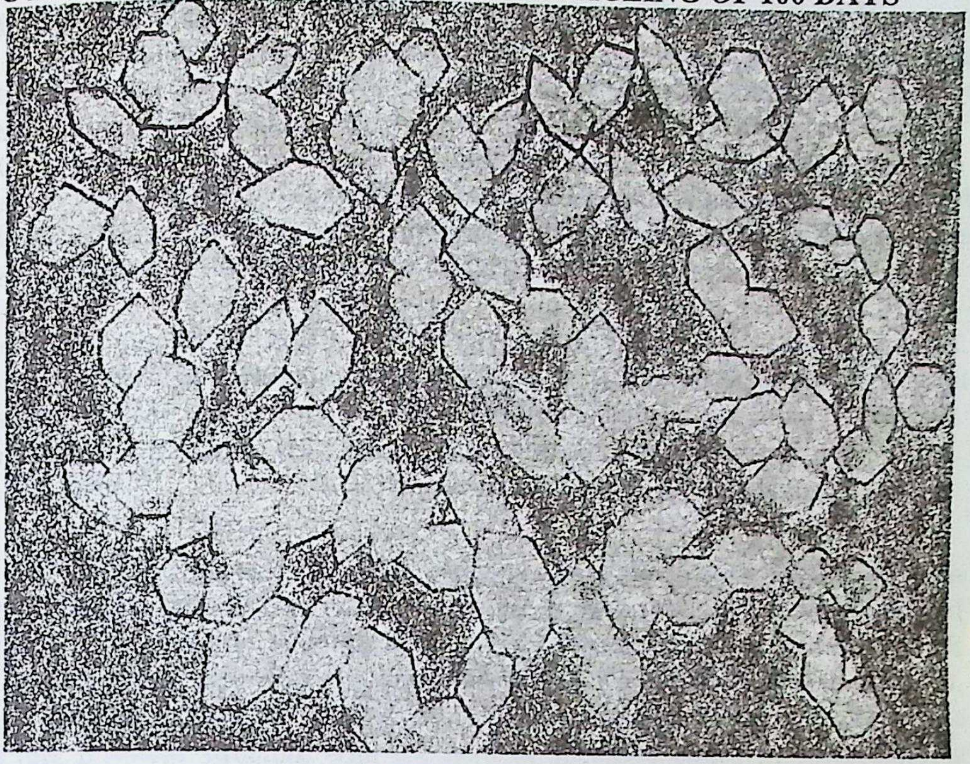

OUTPUT FOR SEM STRUCTURE AFTER AGEING OF 100 DAYS

FIGURE 11: ENLARGED VIEW OF SIMULATED SEM STRUCTURE FOR AGEING AFTER 100 DAYS

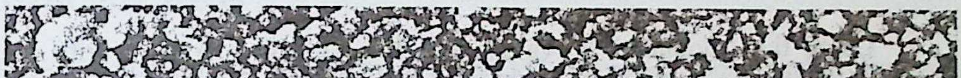
20kV
X15,000
1µm
0000
10 46 SEI

FIGURE 12: SEM STRUCTURE FOR AGEING AFTER 100 DAYS

6: OUTPUT ANALYSIS

With reference to the SEM structure, computer simulation work was done in order to regenerate the topography of SEM structures for both ageing and high temperature cases. From SEM micrograph, it was clear that most of the zinc sulphide exists in wurtzite structure (i.e.; hexagonal). So, efforts were made to reconstruct the 2-dimensional hexagonal structure satisfying the condition, $a=b \neq c$, $\alpha=\beta=\gamma \neq 90°$ (condition for hexagonal crystal structure).But, further observations of SEM micrograph revealed that there were structures other than hexagonal. So, such structures i.e. Rhombohedral, Cubic etc. were also reconstructed by computer simulation method. This process is carried out for two cases: (i) Ageing & (ii) High temperature.

To compare the obtained 2-D hexagonal structure, we took help of XRD plots. From XRD plots, the d-value corresponding to good hexagonal peaks were taken [15,13]. Assuming h, k values (since it is 2-D structure) for each simulated structures with $a=b \neq c$, we found the value for 'l' using the expression,[3,18]

$$\frac{1}{d_{hkl}^2} = \frac{4}{3}\left(\frac{h^2 + hk + k^2}{a^2}\right) + \frac{l^2}{c^2} \ldots\ldots\ldots\ldots\ldots\ldots\ldots (1)$$

With ***C=1.633 a***

Where

d_{hkl} is the inter planar spacing
h, k, l are the crystallographic axes
a, b, c are the sides of hexagonal structure

Using the calculated 'l' value, the (h k l) values for wurtzite structure were compared with the JCPDS data [11,12]. The results were in agreement with the experimental results. Similarly, this is carried out for many structures of both ageing & high temperature cases.

Another observation was made on change in the crystallographic axes, which resulted in size variation of hexagonal structures. It may be due to orientation of hexagonal structures during temperature changes. The existence of non-hexagonal structures may be due to overlapping of two or more hexagonal structures. Other possibilities may be presence of zinc as a whole or its oxides, which may result in Cubic or Rhombohedral structure. White, yellow colorations were also observed in the simulated structures, it may be due to precipitation in form of sulphides. However, there were some white spots in the SEM patterns that might be colloidal particles sedimentation mixed with ZnS.

By observing the simulated structure for high temperature case, it was also noticed that in structure [figure caption (60, 5)], the structures were in cluster form. It may be due to transformation tending from amorphous to crystalline nature. While in structure [figure caption (60, 10)], the hexagonal structure (wurtzite) was clearly observed. It can be established from theoretical concept that the dipping time plays an important role in formation of crystalline films & hence it shows a transformation from amorphous to crystalline nature during temperature variations, the collisions of the cations in the solution among themselves and with the substrate increases, which leads to more alignment on the glass slide.

In simulated structure of ageing also, this type of clusters were observed (SEM structure of 40 days, 43 days etc.). But in SEM structure of 45 days & 100 days, the clusters were transformed into hexagonal structures.

Finally, from the observations made from simulated SEM micrograph structures, it was obvious that simulated structures were in agreement with theoretical and experimental results.

7: CONCLUSIONS

From the above studies, it was clear that computer simulation of random phenomena has become an indispensable tool in modern scientific investigations. It can be considered as a powerful tool for providing solutions to many unanswered questions in various fields of applied science. They also find application in diverse fields like physical sciences, biological sciences and chemical industry. By using computer simulations, it is possible to generate any physical structure with the help of specified codes in corresponding computer languages. After structure generation, comparisons can also be made using theoretical means.

8: ACKNOWLEDGEMENT

We express our sincere thanks towards U.G.C. for providing financial assistance in carrying out the project. We are also thankful to the Department of Physics, Govt. Victoria College, Palakkad for all their support.

REFERENCES

1. Bish, D.L. and Post, J.E., editors. (1989). Modern Powder Diffraction. *Reviews in Mineralogy*. Vol. 20. Mineralogical Society of America.
2. Clarke, A. R. (2002). Microscopy techniques for materials science. CRC Press (electronic resource) Crystallography and Minerals Arranged by Crystal Form, Web mineral.
3. Cullity, B. D.(1978). Elements of X-ray diffraction. 2nd ed. Addison-Wesley. Reading. Mass.
4. Egerton, R. F. (2005). Physical principles of electron microscopy : an introduction to TEM, SEM, and AEM. Springer, 202.
5. Feng, H. J.Ye, and R.F.W. Pease(2005)."Reconstruction of pattern images from scanning electron microscope Images," *J. Vac. Sci. Technol*. B 23:3080 (2005).
6. Goldstein. J. .(2003). Scanning electron microscopy and x-ray microanalysis. Kluwer Academic/Plenum Publishers, 689 p.

7. Hartmann, S.(1996). The World as a Process: Simulations in the Natural and Social Sciences, in: R. Hegselmann et al. (eds.), *Modelling and Simulation in the Social Sciences from the Philosophy of Science Point of View*, Theory and Decision Library. Dordrecht: Kluwer 1996, 77–100.

8. Hurlbut, Cornelius S. and Klein, Cornelis, (1985). *Manual of Mineralogy*, 20th ed., pp. 78 - 89, ISBN 0-471-80580-7

9. James J. Nutaro(2010). *Building Software for Simulation: Theory and Algorithms, with Applications in C++*. Wiley, 2010.

10. Joint Committee on Powder Diffraction Standards (JCPDS), International Centre for Diffraction Data, Swarthmore, PA (1995), card no. 36-1450.

11. Joint Committee on Powder Diffraction Standards (JCPDS), International Centre for Diffraction Data, Swarthmore, PA (1995), card no. 39-0354.

12. Kasi S. R, y' Lifshitz, J. W. Rabalais, and W. Eckstein.(1990).*Phys. Rev*. B 41. 468 (1990).

13. Klug. H. P. and L. E. Alexander. (1974). X-ray diffraction procedures for polycrystalline and amorphous materials. 2nd ed. Wiley, New York.

14. Moller W, D. Bouchier, O. Burat, and V. Stambouli,(1991). *Surf. Coat. Technol*. 45,73 (1991).

15. Moore, D. M. and R. C. Reynolds, Jr. (1997). X-Ray diffraction and the identification and analysis of clay minerals. 2nd Ed. Oxford University Press, New York.

16. Reimer, L. (1998). Scanning electron microscopy: physics of image formation and microanalysis. Springer, 527 p.

17. SEM/EDX webpage from Indiana University - Purdue University Fort Wayne

18. Seeger A., "Surface Reconstruction from AFM and SEM Images". Ph.D. Thesis, University of North Carolina,2004.

19. Villarrubia J.S., "Algorithms for Scanned Probe Microscope Image Simulation, Surface Reconstruction, and Tip Estimation." *Journal of Research of the National Institute of Standards and Technology* 102(4),1997, pp. 425-454

20. Winsberg E., *Science in the Age of Computer Simulation*. Chicago: University of Chicago Press, 2010.

21. Wyckoff , R.W.C., Crystal Structure, Vol.1, Wiley, New York, 1963, p.108.

Bulletin of Pure and Applied Sciences
Vol. 32 D (Physics) Issue (No.2) 2013:P. 95-98
www.bpas.in

TRANSPOT COEFFICIENT OF SILICON BASED QUANTUM WELL AND CALCULATION OF ENERGY LOSS RATE

Aparajita,
University Deptt. of Physics, B.R.A. Bihar University, Muzaffarpur,Bihar, India.
Amita Sharma
Department of Physics, R.D.S. College, Muzaffarpur, Bihar India.
Sippy Kumari
University Deptt. of Physics, B.R.A. Bihar University, Muzaffarpur,Bihar, India.

Received on 18 August2013: Accepted on 29 November 2013

ABSTRACT

We have studied the temperature dependent transport co-efficient of Silicon based quantum wells. In our study energy dissipation power by non equilibrium carriers, and phonon-drag thermo power were taken in out in n-type Silicon inversion layers. It was found that under the Bloch-Gruniesen regime of electron scattering obeyed simple power dependence on temperature. We found that for the change of the observed temperature dependence is the dielectric of the particular structure. The structure contains a conductive channel close to quantum well. This type of channel is due to gate electrode in inversion layer. The same situation is found in heavily doped region in modulation doped Silicon. It was observed that there is changes in screening of the electron-phonon interaction for phonons having wave length close to the distance between the quantum well and the channel. It was found that deformation potential has a complex form due to degeneracy of the hole at the top of the valance bond.

Key words : Transport coefficient, quantum well, phonon drag, modulation, inversion layer

INTRODUCTION

Gantmakher and Levinson (1987) [1] explained various transport properties of bulk semiconductors. They are also applicable in the case of nanostructures.

Xie et al (1986)[2] and Song et al (1997)[3] measured low temperature carrier transport coefficient of Silicon based quantum wells. Prus et al (2002)[4] studied screened deformation potential dependences for temperature around and below 1k. Glavin et al (2005)[5] observed that such dependences appeared for Piezo electric interaction which is not possible for Silicon for Silicon based structures. Sergeev et al (2005) [6] reported that they are relative with the role of disorder phonon confinement.

Pekar et al (1966)[7] showed mechanism of electron-phonon interaction. Ma et al (1991)[8] determined the energy loss rate of two dimensional carriers by the following eqn. $P=F(Te) - F(T_{eat})$. Ando et al (1982)[9] determined screening factor for the case of near surface and thin film scattering and Sirenko et al (1997)[10] formed the analysis. In our study we have successfully studied the transport properties of Silicon based quantum well.

METHOD

Quantum well was placed in the vicinity of a conductive region, then screening of the electron small wave vector phonon interaction become independent on the wave vector and changed the temperature dependence of the transport parameters. The study was made under the Bloch-Gruniesen regime of electron scattering. The corresponding exponent depended on the mechanism of electron-phonon interaction. The screened deformation potential was found. Temperature dependence in the dielectric environment for the particular structure were studied. The case of heavily doped region in modulation doped Silicon of quantum wells were taken into account.

RESULTS AND DISCUSSION

The model used for study was not rigorous for electrons in Silicon inversion layer. This simplified model allowed accounting in a qualitative way the cross over in the temperature dependence of transport parameters. It was found that the transport coefficients are proportional to some power of temperature. The screening factor was determined. The two dimension carriers experienced perturbation. All quantities were assumed to obey plane-wave dependence in the x, y plane, the perturbation of the charge dependence was expressed by

$$\delta n = X^2(z)\, M\Pi$$

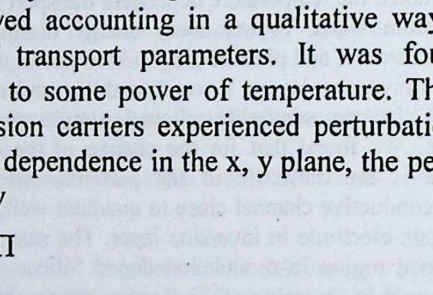

Graph 1. : Schematics of the structure.

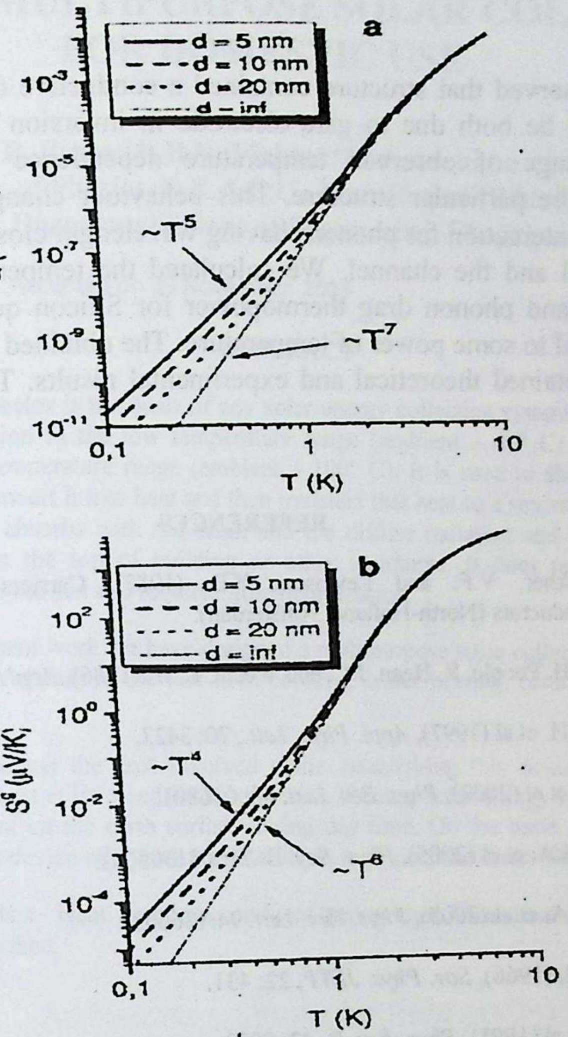

Graph 2. : Temperature dependence of the power loss (a) and phonon-drag thermopower (b) QW with different values of spacer thickness d.

where X is the envelope wave function of two dimensional carriers, M is the electron-phonon interaction form factor and II is the polarization function. It was observed that channel can be due to gate electrode in the case of inversion layer. The same is found in a heavily doped region in modulation doped Silicon quantum wells, which changed the screening of the electron-phonon interaction for phonons whose wavelength was close to the distance between the quantum well and the channel. Graph (1) shows that carriers are confined in quantum walls. Graph (2) shows dependence of the power loss, and phonon drag thermopower for Silicon doped p-type quantum well with different values of spacer thickness.

CONCLUSION

It was observed that structure contained a conductive channel close to quantum well channel can be both due to gate electrode in inversion layer and heavily doped region. The change of observed temperature dependence was due the dielectric environment of the particular structure. This behaviour changed the screening of the electron-phonon interaction for phonons having wavelength close to the distance between the quantum well and the channel. We calculated the temperature dependence of the energy loss rate and phonon drag thermopower for Silicon quantum wells and it was found proportional to some power of temperature. The obtained results were compared to the previously obtained theoretical and experimental results. They were found in good agreement.

REFERENCES

1. Gantmakher, V.F. and Levinson, Y.B. (1987), Carriers scattering in metals and semiconductors (North-Holland, Amsterdan).
2. Xie , Y.H. People. R, Bean, J.C. and Wecht, K.W. (1986), *Appl. Phys. Lett.* 49:283.
3. Song, S.H. et al (1997), *Appl. Phys. Lett.*, 70: 3422.
4. Prus, O. et al (2002), *Phys. Rev. Lett.* 88: 016801.
5. Glavin, B.A. et al (2005), *Phys. Rev*. B. 71: 081305(R).
6. Sergeev, A. et al (2005), *Phys. Rev. Lett.* 94:136602.
7. Pekar. S.I. (1966), *Sov. Phys. JETP*, 22: 431.
8. Ma, Y. et al (1991), *Phys. Rev*. B, 43: 9033.
9. Ando, T. et al (1982), *Rev. Mod. Phys*. 20:1993.
10. Sirenko, Yu. M. et al, (1997), *Phys. Rev*. B, 56: 15770.

Bulletin of Pure and Applied Sciences
Vol. 32 D (Physics) Issue (No.2) 2013:P. 99-103
www.bpas.in

DESIGN OF MULTIPURPOSE SOLAR COLLECTORS FOR DOMESTIC USE

B. Prasad*, B.N. Mahtoand Archana**
*Deptt. of Physics, B.R.A.B.U., Muzaffarpur (Bihar), India.
**Deptt. of Physics, Bhagalpur College of Engineering, Bhagalpur (Bihar), India

Received on 17August 2013: Accepted on 30 November 2013

ABSTRACT

Solar Collector is the heart of any solar energy collection system designed for operation in the low temperature range (ambient – 60° C) or in the medium temperature range (ambient – 100° C). It is used to absorb solar energy, convert it into heat and then transfers that heat to a stream of liquid or gas. It absorbs both the beam and the diffuse radiation and is usually planted on the top of building or other structures. It does not require tracking of the sun and requires little maintenance.

In the present work we have designed a multipurpose solar collector which is used for domestic use that is in cooking, water heating, candle making etc.

In this process the cost involved while establishing this device and no recurring cost is involved in the operation because solar energy is available in abundant on the earth surface during day time. On the basis of study it seems that device will work successfully n multipurpose domestic use

Key words : Heat exchange, ambient temperature, heat loss coefficient, glazing surface.

INTRODUCTION

A solar collector usually consists of the following components:-

(i) Glazing, which is a sheets of glass or some other diathermanous (radiation transmitting) material as shown in fig. 2
(ii) Tubes fins or passages for conducting or directing the heat transfer fluid from the inlet to the outlet.
(iii) Absorber plate which may be flat.
(iv) Header or manifolds, to admit and discharge the fluid.
(v) Insulation, which minimizes heat loss from the back and sides of the collector.
(vi) Casing, which surrounds the various, components and protects them from dust, moisture etc. The complete view of the collector is shown in fig. (1)

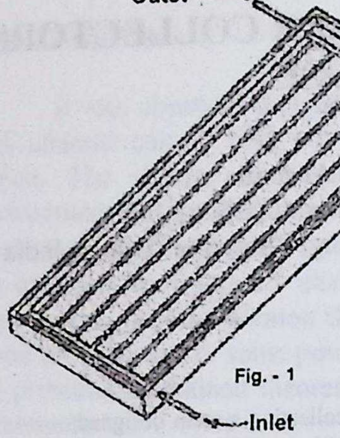

Fig. - 1

Complete View of Collector

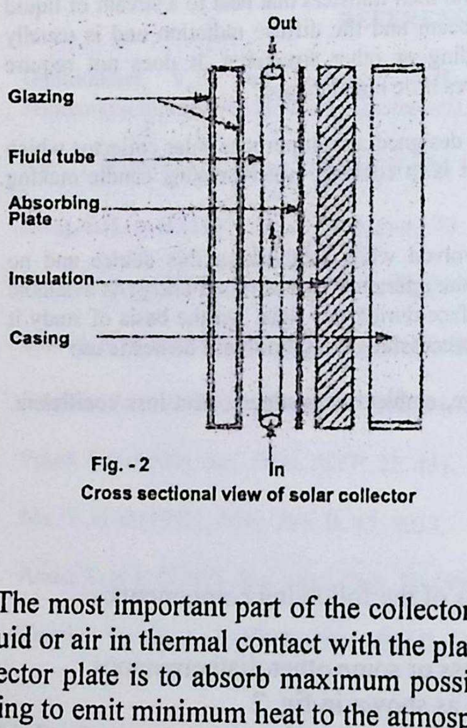

Fig. - 2

Cross sectional view of solar collector

The most important part of the collector is the absorber plate along with the pipe pass liquid or air in thermal contact with the plate to transfer heat from it. The function of the collector plate is to absorb maximum possible solar radiation incident on it through the glazing to emit minimum heat to the atmosphere and down ward, through the back of the casing and to transfer the retained heat to the fluid. Materials generally used for collector plates, in decreasing order of cost and conductance are copper, aluminium and steel. The surface coating of the plate should be such that it has high absortivity and poor emissivity for the required temperature range. Selective surface are particularly important when the collector surface temperature is much higher than the ambient air temperature. For domestic water heating system the plate is normally painted black. The energy absorbed by the plate is extracted by circulating a fluid, through a network of tubes in good thermal contact with the plate. The bottom and sides of the collector are covered with insulation to reduce the conductive heat loss. The collector is placed inclined at a suitable angle to receive the maximum solar radiation.

CALCULATION

In steady – state condition, the rate of energy absorbed by plate per unit area should be equal to the sum of the rate of the useful energy ($\dot{q}_u$) transferred to the fluid and the rate of energy lost ($\dot{q}_L$) per unit area by the plate to the surrounding. Thus

$$\dot{q}_{ab} = \dot{q}_L + \dot{q}_u \quad \text{---------} \quad (1)$$

Where $\dot{q}_{ab} = (\tau_0\alpha_0)\, I(t)$;

And $\dot{q}_L = U_L \quad (T_p - T_a)$

Equation (1) can be rewritten as

$$\dot{q}_u = (\tau_0\alpha_0)\, I(t) - U_L \quad (T_p - T_a) \quad \text{--------} \quad (2)$$

Further

Efficiency,

$$\eta_i = \frac{\dot{q}_u}{I(t)} = \tau_0\alpha_0 - U_L \frac{Tp - Ta}{I(t)} \quad \text{--------} \quad (3)$$

पुस्तकालय
132146
गुरुकुल कांगड़ी विश्वविद्यालय

Where τ_0 and α_0 is the transitivity and absorptive of the glazing surface, respectively. $I(t)$ is the incident solar radiation in the plane of absorber (W/m^2), T_p and T_a are the plate and ambient temperature (°C) respectively and U_L is the heat loss coefficient for collector (W/m$^{2\circ}$C).As shown in Fig.(3),

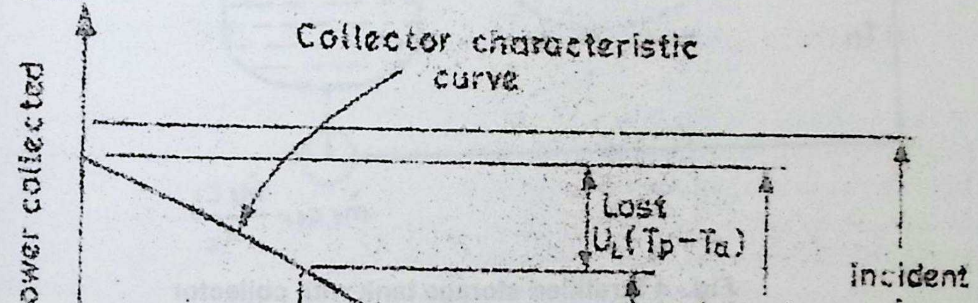

Temperature of plate above ambient

Fig. - 3

The useful energy decreases with increasing temperature difference. The thermal loss to the surrounding is an important factor in the determination of performance of a collector, the higher the losses the lower is the useful energy ouput and heat loss depends upon (T_p - T_a). Hence, for different ranges of temperature difference, different types of collectors have been designed to minimize $\dot{q}_L$ and optimize $\dot{q}_u$, as attempts to decrease $\dot{q}_L$ and decreases $\dot{q}_{ab}$.

Uses:

There are many domestic uses of solar collectors as for example.

(1) Water heating, (2) Air heating (3) drying (4) Candle making etc.

(1) Water or liquid heating –

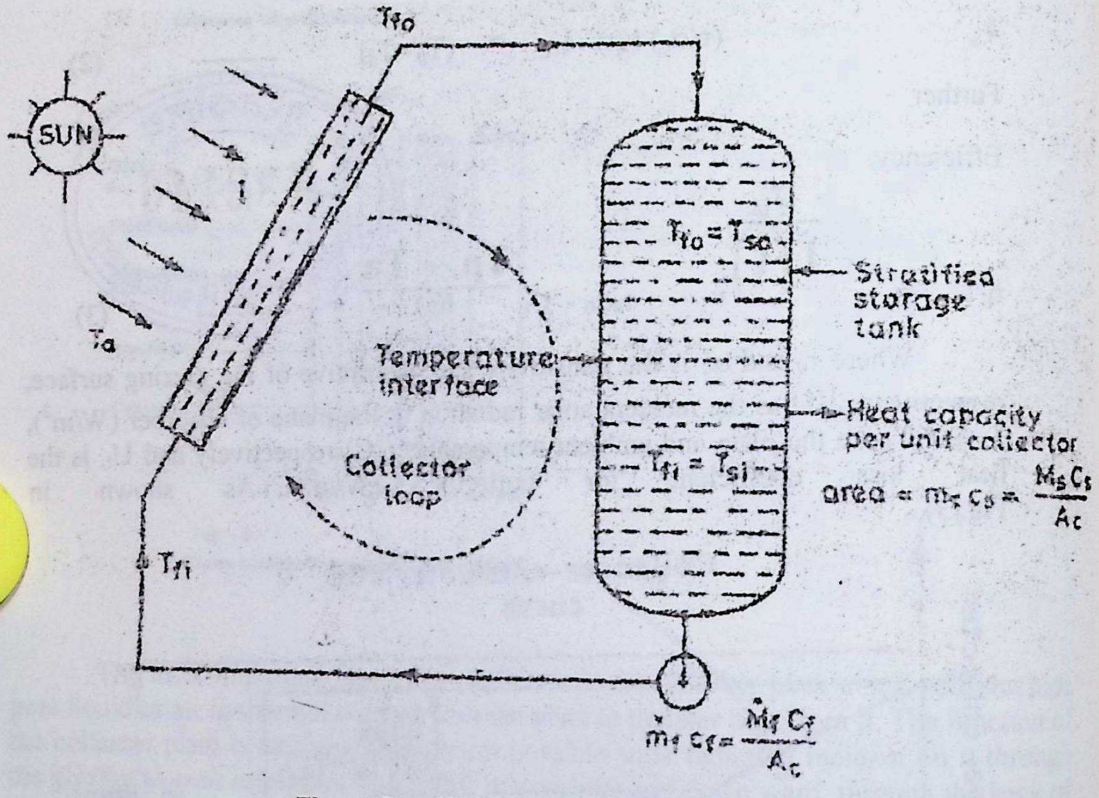
T_{fo}
SUN
T_a
$T_{fo} = T_{so}$
Stratified storage tank
Temperature interface
Heat capacity per unit collector area = $m_s C_s = \frac{M_s C_s}{A_c}$
Collector loop
$T_{fi} = T_{si}$
T_{fi}
$\dot{m}_f C_f = \frac{\dot{M}_f C_f}{A_c}$

Fig.- 4 Stratified storage tank with collector

The schematic diagram of water or liquid heating shown in the Fig. 4 below.

CONCLUSION

In this process the cost is involved which establishing this device and no recurring costs is involved in operating this system because solar energy is available in abundant on the earth during day time.

The drawback of this procedure is that during night time it cannot be operated because there is no solar radiation available on the earth surface during night time.

REFERENCES

1. Gunnewiek, L.H., Brundrett, E. and Hollands, K.G.T. (1996) Flow distribution in unglazed transpired plate solar air heaters of large area, *solar energy*, 58:227.
2. Karim, M. A. And Hawlader, M.N.A. (2006). Performance investigation of flat-plate V-Corrugated and finned air collectors, *energy*, 31:452.
3. Mohammad, A.A. (1997). High efficiency solar air heater, *Solar energy*, 60:71.
4. Nayak, J.K. and Amar, E.H. (2000). Experimental and theoretical evolution of dynamic test procedures for solar flat-plate collectors, *solar energy* 69:337.

Bulletin of Pure and Applied Sciences
Vol. 32 D (Physics) Issue (No.2) 2013:P. 105-125
www.bpas.in

ERROR MODELING ON CNC MACHINE TOOL FOR GEOMETRIC, THERMAL AND LOAD ERRORS

Ahmad Afsari and Mohammad Vahdani
Mechanic Department, Islamic Azad University, Shiraz Branch, Shiraz, Iran
Email:vahdani260@gmail.com

Received on 16August 2013: Accepted on 30 November2013

ABSTRACT

High precision in manufacture is an advantage in the recent competitive market. High precision makes a demand for a reduction in the errors of CNC machine tools. For this purpose, it is useful to develop a greater understanding of errors in machine tool drives. This research presents the geometric, thermal and load errors commonly encountered on CNC machine tools. Many researches have been extended which enable a good understanding of the interaction between these errors, various details of design and the dynamic behaviour of driven systems. this research uses the classical eigenvalue method for finding the natural frequencies and other dynamic characteristics of systems to include viscous damping effects using a generalised eigenvalue approach. A development of this modelling method gives the sensitivity of the system to changes in stiffness and damping characteristics. which is an aid in deciding the most convenient remedy to vibration problems which may occur in service. In addition, a strategy for compensation of some of these errors has been devised.

Keywords: Error modeling, CNC machine tool, for geometric, thermal and load errors

1- INTRODUCTION

Most manufactured products are an assembly of many parts. It is highly desirable that these parts are made to the highest standards of accuracy. Workpiece accuracy is influenced by the environment in which a machine tool operates, the way it is used and errors associated with the machine itself. In order to achieve the desired levels of accuracy the errors associated with machine tools must be reduced to the lowest practicable level. Errors in machine tools can be grouped under three main categories geometric, thermal and load (Aomori, 2000)[1].

In the operation of a machine tool, one or more machine tool drives are needed to move the tool relative to the workpiece. If the required motion is linear, the motion is generated by a screw mechanism in which the rotational motion of a screw is transferred to linear motion of the nut. For machines with above 3 m travel, rack and pinion drives are often employed (Bryan, 1990)[2].

Linear motors are sometimes employed for smaller machines, but screws remain the most widely used mechanisms. In most modern machine tools, the control of the motion of its various parts is by means of motor-driven mechanisms governed by an electronic controller (Holroyd, 2001)[4].

The controller receives signals from transducers placed at suitable locations on the machine which enable the position and speed of the different parts to be determined. It uses this information, together with a set of instructions known as a part program, to determine how the machine should operate to produce the desired shape in the workpiece (Jan, 1992). A typical machine tool drive therefore consists of an electronic controller, an electric motor, a drive mechanism and transducers or encoders which provide feedback signals to the controller.

Modern control systems use digital technology and so errors in the drive system can arise due to the sampling and quantisation involved in converting analogue signals into digital form. Errors such as interpolation and servo up-date errors can also be generated while converting the digital output to the analogue signal used to drive the motor.

- Two strategies can be deployed to improve the accuracy of a machine, viz: error avoidance – this approach minimises errors through better machine design, construction and control of the machine's environment (Blake, 1995)[3].
- Error compensation – this approach seeks to compensate for errors which cannot be eliminated. The assumption is made that many errors are repeatable and predictable. A model of the machine's behaviour can therefore be made which describes the machine tool and which can be validated experimentally.

The aims of this research therefore are:

- To prepare a mathematical model of a ballscrew which takes into account the geometric, thermal and load errors commonly encountered on CNC machine tools and
- To devise strategies and algorithms for the correction of these errors.
- The objectives of the research can be listed as follows:
  Starting from a basic understanding of the behaviour of a ballscrew, to outline the relevant static elastic theory, dynamic elastic theory and the theory of thermal modelling.
- To develop further the dynamic theory by examining the continuous matter approach including wave solutions and the discrete matter (or "lumped mass") approach with its matrix solutions.
- To extend the classical eigenvalue method for finding the natural frequencies and other dynamic characteristics of ballscrew systems and to include viscous damping effects using a generalised eigenvalue approach. This will give estimates of not only the natural frequencies, but also the damping coefficient of each predicted vibration mode (Frank and Ruech, 1999)[5]. The sensitivity of the system to changes in stiffness and damping characteristics will also be derived.

- To devise a method of modelling a ballscrew driven mechanical system with a moving nut whose configuration changes with time.
- To develop a means of compiling a mathematical model which includes non linear phenomena such as backlash and Coulomb friction as well as time dependent stiffness and damping characteristics.
- To apply the new approach to the axial and torsional behaviour of the screw with a view to predicting the position error of the ballscrew nut.
- To apply the new approach to the transverse behaviour with a view to predicting the vibration characteristics of the screw.
- To develop the mechanical model in such a way that the energy dissipative mechanisms give a prediction of heat inputs for a model of the thermal behaviour.
- To develop a model to predict the thermal behaviour of a ballscrew system
- To consider the feasibility of cooling parts of the ballscrew system with a view to reducing thermal errors.
- To compare the simulated results of the models with data measured from the test rig and other relevant experimental data that is in the public domain or within the University internal reports.

2- MATERIAL AND METHODS

A ballscrew drive system is made up of several mechanical components, see Figure 1. These are solid bodies made of materials which deform elastically under applied forces. They also have the property of resisting changes in their state of motion which is known as inertia.

The system also includes an electric motor governed by a controller. In order to model the mechanical parts it is necessary first to set up equations of motion which are based on the laws of physics to which such mechanical components are subject. These are the laws of elasticity first enunciated by Hooke and the laws of motion formulated by Newton. There are several ways that these laws can be applied to mechanical systems in order to investigate their dynamic properties.

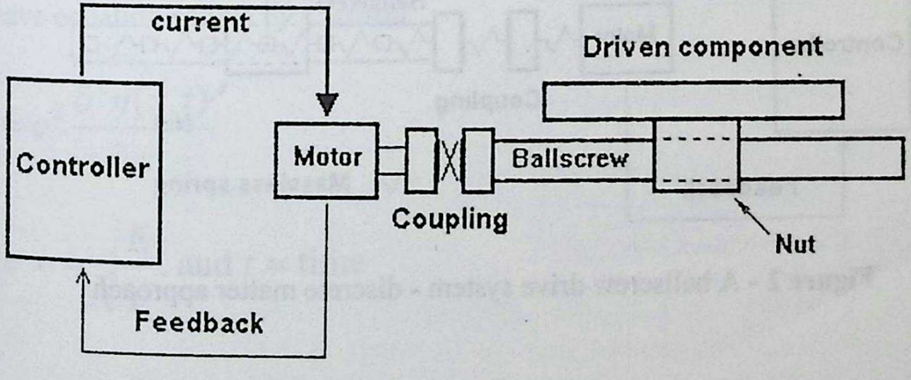

Figure 1 - A feed drive system

In this investigation work has been done under four broad headings

1. a hybrid modelling approach,
2. a wave theory approach,
3. a generalised eigenvalue approach and
4. the moving mass models.

There are two ways of looking at the bodies of which a mechanical system is made. One is the "continuous matter" approach and the other is the "discrete matter" or "lumped mass" approach.

In the "continuous matter" approach the mass is considered to be distributed throughout the volume occupied by the body in a smooth manner, so that at any point in the body a mass per unit volume (density) ñ can be defined. The elastic properties of the material are defined by its elastic moduli, which are the stress required to produce a unit strain. The equation of motion of such an arbitrarily small volume is derived which normally gives rise to a partial differential equation. The solution of such an equation often is a set of waves (Wang et al., 1996)[10].

The **"discrete matter" approach** can involve modelling the mechanical system under consideration as a set of "lumped masses" and springs, see Figure 2. In other words the mass or inertia in the system has to be considered to act at a set of discrete points in a multidimensional space. These point masses are connected by a set of "springs" in which the stiffness of the system is considered to act. The points at which the masses are considered to act are commonly called **nodes** and the springs which connect them **elements**. The discrete matter approach is in essence a finite element method. Therefore the behaviour of the system can be represented by a finite number of differential equations which are derived by considering the equations of motion of each element of the system. The solutions of such sets of differential equations lend themselves naturally to matrix methods.

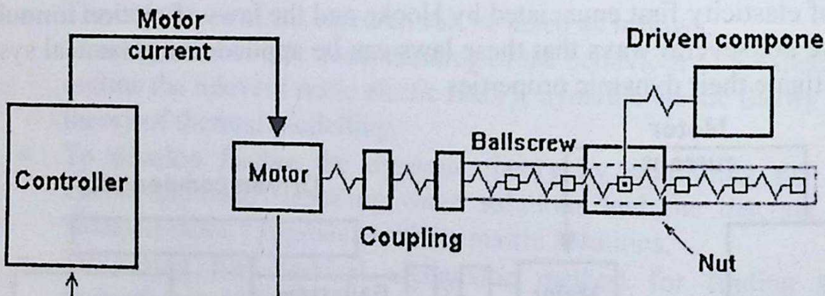

Figure 2 - A ballscrew drive system - discrete matter approach

2-1-Continuous matter approach – wave solutions

The analysis of dynamic systems using a continuous matter approach gives rise to differential equations. These can be sub-divided into **homogeneous quations,** where some function based on the partial derivatives of the variables involved (one or more spatial dimensions and time) is equal to zero, and **inhomogeneous** or **non-homogenous equations** where the function involving derivatives equals a function of time which in general is non-zero. In a mechanical system, this latter function expresses the external forces on the system and is commonly known as the "forcing term". Solving the homogeneous equation with the appropriate boundary conditions gives an indication of how a system will behave after it has been set in motion and then subject to no further force.

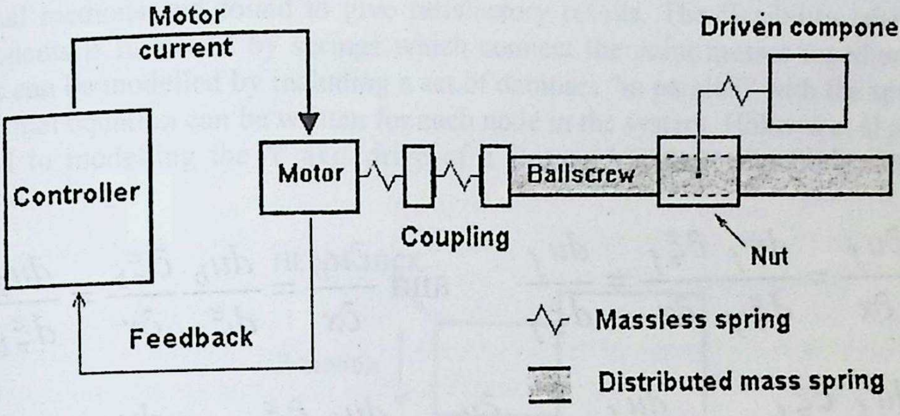

Figure 3 - A ballscrew drive system - continuous matter approach

The ballscrew has to transmit thrust loads and torsional loads (torque) as the nut is driven along the screw. Motion in the axial direction is the simplest to model mathematically and so it was considered first (Figure 3).

Considering a shaft with cross sectional area A, made from a material with density ρ and Young's modulus E, which lies along the x axis. Let u represent the axial motion of a small element at a point x along the axis. It can be shown that this motion is governed by a wave equation shown by Coulson:

$$\frac{\partial^2 u}{\partial t^2} = c^2 \frac{\partial^2 u(x,t)}{\partial x^2}$$

where $c = \sqrt{\frac{E}{\rho}}$, and $t =$ time

The general solution is a superposition of a wave u_f travelling forwards with a velocity c and a wave u_b travelling backwards with the same speed

$$u(x,t) = u_f(x - ct) + u_b(x + ct)$$

Torsional movement of a shaft with a shear modulus of G is represented by a similar set of equations summarised by De Silva where:-

$$c = \sqrt{\frac{G}{\rho}}$$

Considering the axial strain of the shaft at any point along its length, the axial tension T is given by

$$T = EA\frac{\partial u}{\partial x}$$

Introducing the dummy variables

$$\frac{\partial u_f}{\partial x} = \frac{du_f}{d\xi_f}\frac{\partial \xi_f}{\partial x} = \frac{du_f}{d\xi_f} \quad \text{and} \quad \frac{\partial u_b}{\partial x} = \frac{du_b}{d\xi_b}\frac{\partial \xi_b}{\partial x} = \frac{du_b}{d\xi_b}$$

$$\frac{\partial u_f}{\partial t} = \frac{du_f}{d\xi_f}\frac{\partial \xi_f}{\partial t} = -c\frac{du_f}{d\xi_f} \quad \text{and} \quad \frac{\partial u_b}{\partial t} = \frac{du_b}{d\xi_b}\frac{\partial \xi_b}{\partial t} = c\frac{du_b}{d\xi_b}$$

from which it follows that

$$T = \frac{EA}{c}\left(-\frac{\partial u_f}{\partial t} + \frac{\partial u_b}{\partial t}\right)$$

It was therefore decided to design an element based on velocity waves to model the behavior of the screw.

To test this element, a simple system consisting of two masses *m1* and *m2* connected by such an element was constructed using Simulink. The first mass could be subject to an external force, *Fe*. A viscous damper parallel to the spring was included to prevent the system going into a state of perpetual oscillation.

Lumped mass approach – matrix solutions

The "discrete matter" approach entails representing the behaviour of the system at a finite set of nodes by an equation of motion for each node. The mass of such systems can be represented by a consistent mass matrix M_e defined by:-

$$M^e = \int \rho N^T N . dv$$

where ρ is the density, N is a matrix representing the shape of the system and v is the volume.

This can be simplified by using direct lumping, that is modelling the mechanical components as a set of "lumped masses" in which the mass or inertia in the system acts at the nodes. This simplification entails significant computational advantages in calculations which use the inverse of the mass matrix M-1. The approach has been tested against classical methods and found to give satisfactory results. The flexibility inherent in the components is modelled by springs which connect the point masses together. Damping effects can be modelled by including a set of dampers "in parallel" with the springs and a differential equation can be written for each node in the system. Holroyd et al applied this method to modelling the Y axis drive of a Beaver VC35 CNC milling machine, see Figure 4.

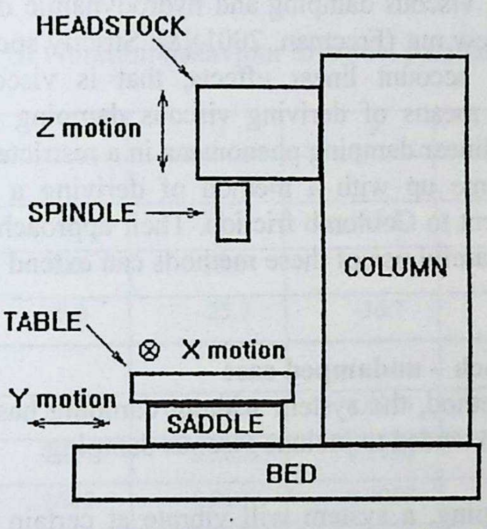

Figure 4 - Beaver VC35 CNC milling machine

This fixed vertical column CNC milling machine has a saddle which moves towards and away from the column in the Y direction, carrying a table which moves sideways in front of the column in the X direction. Z motion is achieved by moving the spindle up and down on the front face of the column. The drive for the Y direction consists of a DC electric motor which drives a ballscrew via a belt drive, the ballscrew then drives the saddle.

2-2- Dynamic model – a generalised eigenvalue approach

The amplitude of the vibration response of an electro-mechanical system to various stimuli is determined to a large extent by the level of damping. Damping can take several forms (viscous, hysteresis, friction etc.), but only viscous damping is a linear phenomenon and therefore amenable to simple mathematical analysis. The response of damped systems can be studied by a "forced damped" approach (White et al., 2001)[10] in which various stimuli (for example out-of-balance forces) can be applied to a system. A picture can be built up of the vibration characteristics of the system by applying such forces at a variety of frequencies.

It has been thought useful to extend the eigenvalue method so an attempt has been made to determine the damped natural frequencies with their associated modes using a generalized eigenvalue method. This avoids having to analyse the system with a variety of stimuli over a possibly extended frequency range. The method of approach adopted here is to seek to understand the vibration characteristics of a system in two stages:

- to determine the natural frequencies and modes of vibration which would be expected if there were no damping
- to investigate how damping modifies this behaviour.

Using the MATLAB/Simulink approach it is possible to model "damping" in the form of Coulomb friction, viscous damping and hydrodynamic drag, and also to model the backlash in the ballscrew nut (Freeman, 2001)[8]. Strictly speaking the method used here can only take into account linear effects, that is viscous damping. Various researchers have devised means of deriving viscous damping coefficients which are equivalent to various non-linear damping phenomena in a restricted set of circumstances. Tan and Rogers have come up with a method of deriving a coefficient of viscous damping which is equivalent to Coulomb friction. Their approach can also be applied to other forms of damping. Careful use of these methods can extend the scope to which this approach is applicable.

2-3-An eigenvalue approach – undamped case

In order to develop the method, the system without damping has been considered first, then the method has been extended to include viscous damping.

If there is no damping, a system will vibrate at certain frequencies with little stimulus (Fraser et al., 1998)[5]. A **natural frequency** of a system is a frequency at which such free vibration takes place.

A vibration **mode** is a characteristic pattern assumed by a system in which the motion of every particle is simple harmonic with the same frequency. The **mode shape** can be represented by plotting on a graph the relative amplitude of the different points taking part in the vibration mode. The mode shape gives an idea of where in the system the greatest vibratory activity may be seen.

A common approach to determining the undamped natural frequencies and mode shapes is the eigenvalue method (Chen, 1996)[6].

To use this method it is necessary to model the mechanical system under consideration as a set of "lumped masses" and springs. In other words the mass or inertia in the system has to be considered to act at a set of discrete points in some sort of space. These point masses are connected to one another by a set of "springs" in which the stiffness of the system is considered to act. The behaviour of such a system can be represented by a finite number of differential equations which are derived by considering the equations of motion of each element of the system. These equations can be solved to give the natural frequencies and the mode shapes as will be shown later.

The eigenvectors are arbitrary to one scalar factor; therefore only their relative values are determined and the absolute value can be any desired value. For the purposes of presentation, the eigenvectors are normalised such that the sum of the squares of their absolute values equals one. Also because the ball-screw ratio *R* is so small (0. 0015915 m/rad) for the studied case, any mode shape selected for plotting is set to equivalent ball-screw rotation before plotting. This drive model was incorporated into the MATLAB software. The resulting program calculates the eigenvalues and eigenvectors and orders them in order of ascending natural frequency.

Table 1: The sensitivity of vibration behaviour to model parameters (Y-axis drive)

Mode	1	2	3	4	5
Nat. freq.					
Undamped, Hz	0.0	75.1	111.8	524.7	581.6
Damped, Hz	0.0	75.3	111.6	524.8	574.2
Damping, 1/sec	-0.0	-25.7	-36.7	-21.2	-491.8
δnf / δk					
- k_ms	NaN	0.0605	0.0274	0.0171	0.4002
- k_bl	NaN	0.2653	0.1396	0.0000	0.0978
- k_bs	NaN	0.0107	0.0036	0.4730	0.0145
- k_nut	NaN	0.0773	0.1601	0.0032	0.0000
- k_ax	NaN	0.0781	0.1698	0.0049	0.0001

The results of the sample undamped natural frequency analysis are presented in Table 1. The Y-axis represents the normalised vibration amplitude. The nodes or masses are laid out along the X-axis in the order that they are included in the mass matrix. Thus the point at x = 1 represents the torsional motion of the motor, the point at x = 2 represents the torsional motion of the driving pulley, that at x = 3 the torsional motion of the driven pulley and those at x = 4 to 11 the torsional motion of the points along the ballscrew in increasing distance from the driven pulley. The point at x = 12 represents the axial motion of the point at the ballscrew centre at the position along the ballscrew where the nut is considered to be, and the point at x = 13 represents the axial motion of the table to which the ballscrew nut is attached. This information is summarised in the left-hand box on Figure 4.9.

The results of the analysis were compared with measured data taken from the milling machine drive operated by a controller. The controller is set up to ensure that the motion of the motor follows a pre-determined pattern. This has the effect of restraining the vibratory motion of the motor. In order to simulate this restraining effect, the inertia of the motor in the model was increased by a factor of 1000. The first mode is, as expected, the "roll mode" at 0 Hz. The second mode, predicted for the resonance frequency of 75 Hz for the Y-axis drive, involves the driven pulley, ball-screw and load bouncing against the motor and driving pulley. The third mode corresponding to 112 Hz involves mainly axial movement. The fourth and fifth modes are quite high in our frequency range for experimental measurement of 1 - 600 Hz. In order to prove the method, MATLAB program "natf_tr1", which uses the eigenvalue approach was produced which gave natural frequencies and mode shapes for the case of free vibration of the ballscrew,. These were compared with the standard results given by Harris. It was found that the predicted natural frequencies were very sensitive to the number of elements used and only gave results close to those standard results in the case where a large number of elements was used. The first two modes are, as expected, the "tilt modes" at 0 Hz and are not included on the mode shape plot.

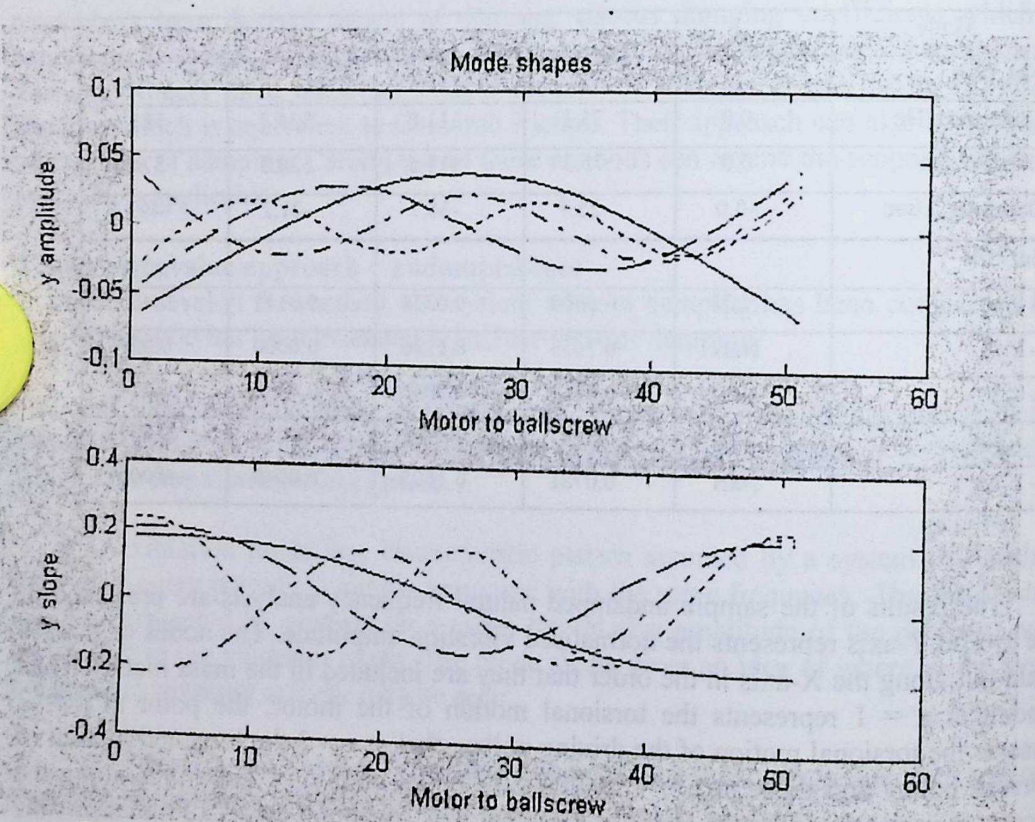

Figure 5 - *Natf_tr1.m – Natural frequency and modes shapes – free-free*

By including an extremely large mass element it is possible to provide a "pinned" restraint and by including a large tilt inertia as well it is possible to model a "built-in" restraint. Using such methods it was possible to model a cantilever beam which also gave results that compared well with the standard results when a large number of elements was used. Comparisons between natural frequencies predicted by the models (M rows). The mode shapes are illustrated in Figures 5.

2-4-A generalised eigenvalue approach – damped case

a) *Theoretical treatment of the linear dissipative effects*

Viscous damping gives rise to a force that is proportional to the relative velocity of two parts of a system. Therefore viscous damping has a linear effect and fits in readily with linear differential equations. It can be introduced deliberately as in the case of a hydraulic damper or "shock absorber" in a vehicle suspension, or it might occur naturally as the result of the dissipative properties of the component's material.

A **damped natural frequency** of a system can be understood as a frequency of free vibration, that is, it is a frequency at which a system will vibrate after some stimulus with the amplitude of the vibrations dying away with time. A vibration **mode** is a characteristic pattern assumed by a system in which the motion of every particle is simple harmonic with the same frequency.

The **mode shape** of a damped mode can be represented by plotting on a graph or graphs the relative amplitude of the different points taking part in the vibration mode. Phase changes of other than ±180° are expected to occur in the case of a damped mode so the mode shape has to be represented by two sets of numbers. The mode shape shows where in the system the greatest vibratory activity may be seen.

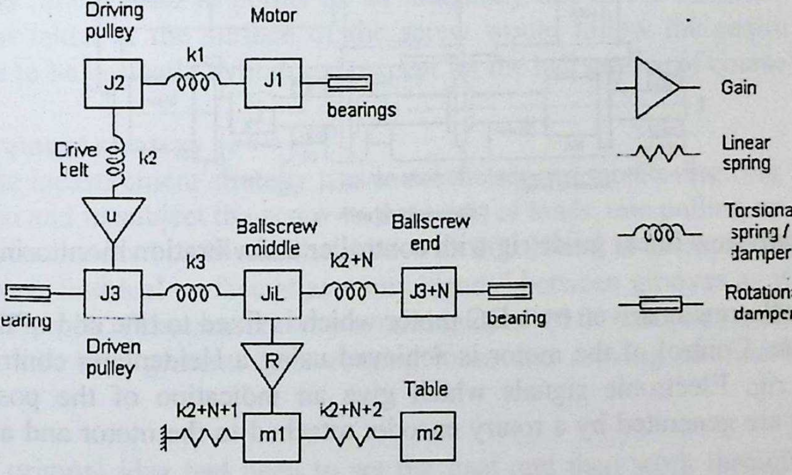
Driving pulley
Motor
k1
J2
J1
bearings
Drive belt
k2
u
Ballscrew middle
Ballscrew end
k3
k2+N
bearing
J3
JiL
J3+N
bearing
Driven pulley
R
Table
k2+N+1
k2+N+2
m1
m2
Gain
Linear spring
Torsional spring / damper
Rotational damper

Figure 6 - Model of the mechanical transmission of the CNC machine tool axis drive considering viscous damping

The eigenvalues come in conjugate pairs in the case that the mode is sub-critically damped, (when a sudden application of an external force gives rise to oscillations that die away), therefore a lightly damped model might have up to *N*+5 pairs. The imaginary part is the natural frequency in radians per second and the real part is the coefficient of damping. In order to represent a positive coefficient of damping the real part of the eigenvalue should be negative. If the mode is critically damped or over-critically damped, all the solutions will be real. This means that there is not an oscillatory response to a step input. There are two real "solutions" for each mass element. Since the sub-critical natural frequencies come in conjugate pairs, a sense of mathematical tidiness suggests that the two real solutions also be grouped together. At this stage it is not understood how to pair them up as two solutions of one "mode". (Figure 6).

3- RESULT AND DISCUSSION

The experimental verification of the dynamic model has been undertaken using the linear guideway rig. This consists of a cast iron milling machine base with a cast iron saddle carried on two linear guideways. The saddle is driven by a ballscrew mounted in the base. The ballscrew nut is attached to the underside of the saddle by a set of screws. The ballscrew itself is held between two sets of angular contact ball bearings. Each bearing set is mounted in a bearing housing into which the outer races of two bearings have been pressed. The inner races are a sliding fit on the ballscrew and are held in place by a locking nut. The degree of preload applied to a bearing set is determined by the torque applied to the locking nut with an upper limit being reached when the axial gap between the inner races has been closed (Figure 7).

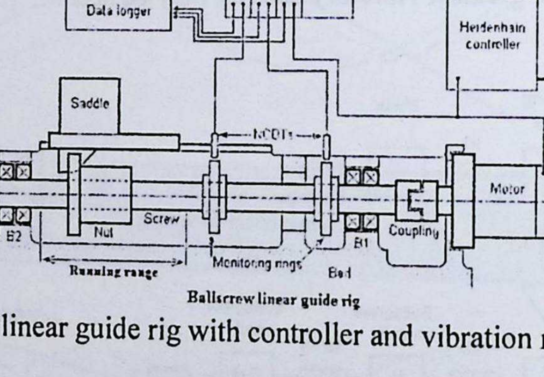

Figure 7 – Ballscrew linear guide rig with controller and vibration monitoring equipment

The ballscrew is driven by a DC motor which is fixed to one end of the base via a mounting plate. Control of the motor is achieved using a Heidenhain controller located close to the rig. Electronic signals which give an indication of the position of the ballscrew nut are generated by a rotary encoder attached to the motor and are fed to the controller.

Since the ballscrew is manufactured to a good standard of precision, and since the ballscrew is limited to a speed of 2500 rpm (40 m/min nut speed), it is not expected that this particular screw should generate high levels of vibration by itself. Other applications involving long ballscrews may do so, it is hoped that the mathematical models developed in this Research will be of help in designing or helping to diagnose problems with such systems.

But in order to demonstrate the model's ability to predict levels of transverse vibration it is necessary to subject the screw to artificially high levels of vibration excitation. It is also necessary to measure the vibration produced.

3-1-Static measurements

The support stiffness of the bearings has a significant influence on the dynamic behavior of the ballscrew. Data given by bearing manufacturers are often "typical" and do not cover the range in which values of particular bearings can lie. Also the stiffness offered to the screw by the bearings also includes that of the support structure, in this case the rig base, bearing housings etc. It was therefore decided to try to derive the bearing support stiffness from the deflected shape of the screw under a known set of forces.

3-2-Preliminary considerations

To get a feel for the order of magnitude of the deflections likely to be encountered consider the case of a cylindrical bar supported at each end. Neglecting the ballscrew nut, the clamping rings, the monitoring rings and half of the flexible coupling between the ballscrew and the drive motor, the ballscrew can be represented approximately by a hollow cylindrical bar of length l = 1.182 m, the distance between the bearing pack centres. The maximum deflection of the ballscrew under its own weight should be between 20 and 100 μm. The total weight of the ballscrew using this simple model is:

$$W = \frac{\pi}{4} \times (0.03796^2 - 0.010^2) \times 1.182 \times 7860 \times 9.80665 = 95.95 \text{ N}$$

The deflections predicted by simple beam theory and those predicted by the moving mass model refer to points on an imaginary line at the centre of the screw. A measurement taken at the surface of the screw would follow the centre if the screw surface were to be perfectly cylindrical (except for the ball groove of course).

3-3-Measurement strategy

Therefore the measurement strategy was to set the second monitoring ring in a particular axial position and to subject the screw to three sets of loads, one pulling up with a load of 20 N, the second with 110 N and the third with 200 N and to measure the deflection of the ballscrew cylindrical surface at as many "lands" between grooves as were accessible to the NCDT probe. (The reason why a minimum of 20 N load was maintained was to prevent the link arrangement from coming loose and moving as measurements were under way.)

The original idea had been to set the load and then work through all the axial positions in turn to get a deflection curve, move on to the next load, take another set of deflection readings and so on. However it became clear that the readings were subject to a significant drift of values with time.

3-4-Measurement results

The results are summarised in Table 2. The data for Position 1 is plotted on Figure 8.

The results are processed in the case of each loading position by first subtracting the data in the colunns obtained from a 110 N pull from data in the columns obtained from a 20 N pull and then subtracting the 200 N data from the 110 N data. The result is a set of data which gives the effect of pulling with a force of 90 N in zero gravitational field. (This is because the effect of gravity, the self weight forces, are the same in all cases, as are the geometrical errors.) A MATLAB function, "funcs_2_dat" has been written which does this. Figures 8 and 9 show this process applied to the results for Position 1.

The next stage is to formulate a model which predicts the behaviour of the ballscrew. The final stage is to extract by an optimisation process the support stiffness which gives a predicted behaviour closest to the observed behaviour.

Table 2 – Static measurements – Raw data

	Position 1			Position 2			Position 3		
Land	20 N	110 N	200 N	20 N	110 N	200 N	20 N	110 N	200 N
1	5.527	5.236	5.046	5.451	4.960	4.471	5.361	5.254	5.148
2	5.541	5.296	5.048	5.465	4.961	4.461	5.469	5.354	5.244
3	5.559	5.302	5.045	5.471	4.956	4.438	5.478	5.364	5.249
4	5.580	5.317	5.053	5.485	4.964	4.439	5.505	5.389	5.272
5	5.572	5.303	5.029	5.485	4.955	4.421	5.494	5.374	5.253
6	5.557	5.278	5.004	5.469	4.925	4.381	5.478	5.355	5.231
7	5.553	5.270	4.939	5.455	4.901	4.353	5.465	5.338	5.210
8	5.535	5.247	4.958	5.435	4.879	4.328	5.456	5.325	5.195
9	5.522	5.227	4.937	5.427	4.866	4.306	5.448	5.317	5.183
10	5.514	5.219	4.919	5.421	4.857	4.291	5.437	5.304	5.168
11	5.531	5.228	4.923	5.433	4.865	4.298	5.426	5.289	5.152
12	5.456	5.148	4.841	5.365	4.797	4.231	5.392	5.251	5.116
13	5.410	5.099	4.797	5.317	4.750	4.184	5.332	5.190	5.049
14	5.394	5.080	4.766				5.315	5.175	5.032
15	5.384	5.068	4.754				5.305	5.161	5.015
16	5.341	5.026	4.711				5.270	5.124	4.978
17	5.149	4.832	4.511				5.084	4.935	4.786
18	5.166	4.843	4.527				5.081	4.933	4.785
19	5.160	4.848	4.531				5.093	4.945	4.798
20	5.146	4.834	4.523				5.065	4.920	4.772
21	5.150	4.841	4.535				5.057	4.911	4.764
22	5.127	4.823	4.517				5.039	4.893	4.747

3-5-Dynamic measurements – nut in fixed position

During these measurements the ballscrew nut was detached from the saddle and clamped in position near to the tail end of the ballscrew as in the case of the static measurements.

Two monitoring rings were fitted to the screw, one as close as possible to the drive end bearing. The other monitoring ring was fitted between the column support bridge and the ballscrew nut and was used to carry the eccentric weights used to apply radial force excitation to the ballscrew. In the case of this second ring it was possible to fit it in a variety of positions.

Deflection of the ballscrew was measured by mounting an NCDT close to each monitoring ring. The probe for the second NCDT was held by bracketry carried on a magnetic clamp attached to the bed slide. The probe for the NCDT closest to the drive end bearing was held on a mounting plate which was bonded to the bed. 8.2.2 Measurement strategy Therefore the measurement strategy was to set the second monitoring ring in a particular axial position and to subject the screw to two sets of out-of balance loading, one with the eccentric weights applied and one without. The maximum load was fixed by running the screw with the out-of-balance weights fitted at a speed which gave rise to vibration levels which appeared to an experienced operator of the rig to be at the upper end of the tolerable range. Using this speed as a maximum four other speeds were determined so as to give 20%, 40%, 60% and 80% of the dynamic force applied at the maximum speed.

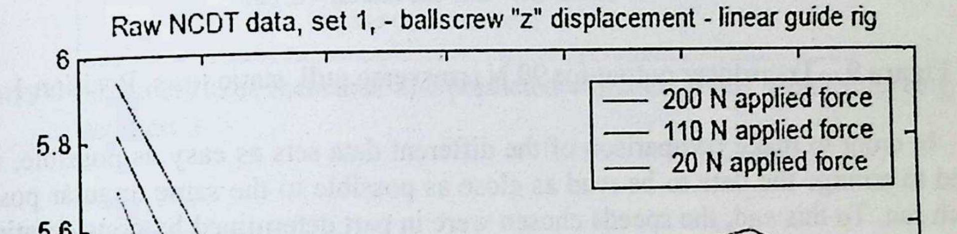

Figure 8 – Raw data, static tests, Position 1

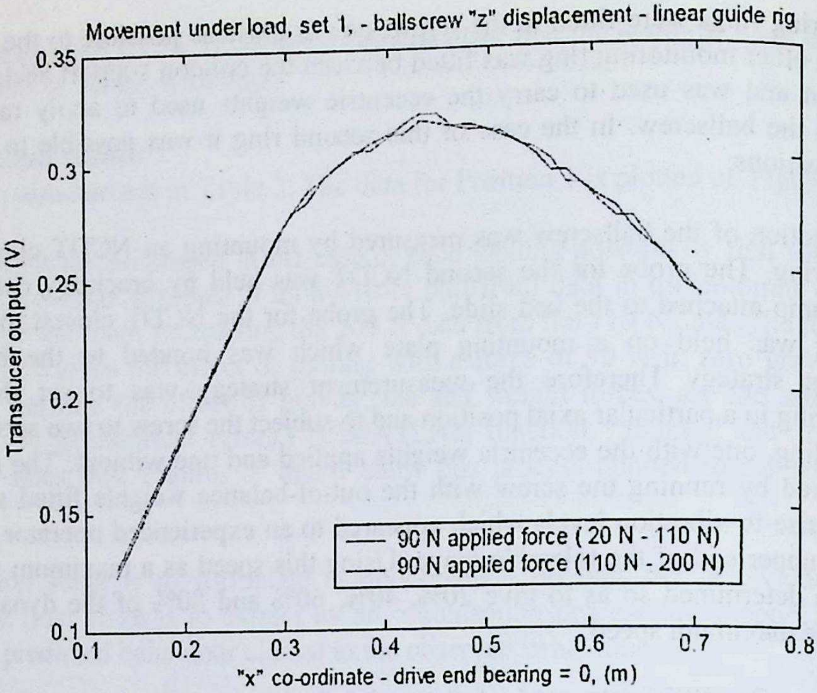

Figure 9 – Transducer output for 90 N transverse pull, static tests, Position 1.

In order to make comparison of the different data sets as easy as possible, it was decided to arrange the data to be read as close as possible to the same angular positions for each run. To this end, the speeds chosen were in part determined by considerations of which sampling times could be set most conveniently in the configuration file of the Data Logger.

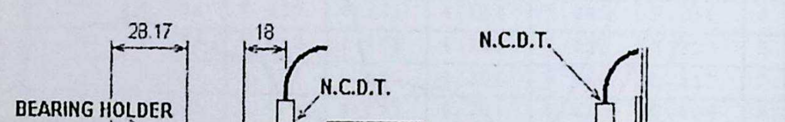
28.17
18
N.C.D.T.
N.C.D.T.
BEARING HOLDER
BEARING
X
"X" MOTION
16 PITCH
10
15
B1
17.06
110
33.56
79.22
BED

Figure 10.- Dimension X in the dynamic tests

Three loading positions were used. These were such that Dimension X (see Figure 10) was 410 mm, 235 mm and 60 mm respectively.

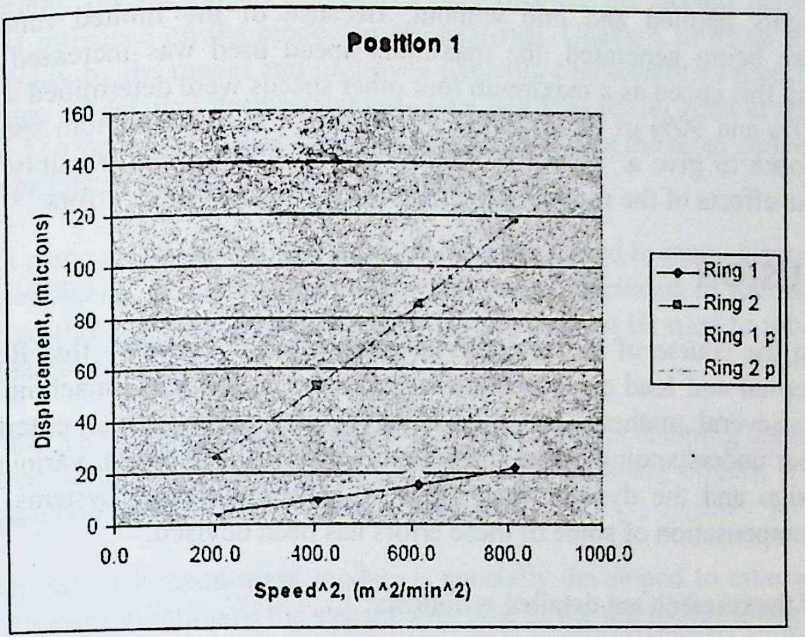

Figure 11 – Comparison of measured and predicted vibration levels Monitoring ring position 3

3-6-Measurement results

For each test, the raw data recorded by the data logger was a time series of the vertical displacement of the monitoring rings as sensed by the NCDT's, and the angular position of the screw as seen by the drive motor's rotary encoder. The data recorded at the "full speed" of the run was extracted and plotted as a function of angular position, and an average of ring surface vertical position as a function of angle was formed. This was done both with and without excitation weights. The difference between the two plots was taken, thus giving the effect of the weights alone. This curve was Fourier analysed to extract the shaft order amplitude, which is the one caused by out-of-balance excitation. Grouping these values by monitoring ring position enables a graph to be plotted of observed amplitude versus speed for each position.

3-7-Dynamic measurements – nut moving along screw

After taking the measurements with the ballscrew nut clamped close to the non-drive end bearing, the clamps were removed and the nut was re-attached to the saddle. As for the "fixed nut" measurements, two monitoring rings were fitted to the screw, one as close as possible to the drive end bearing, the other being fitted between the column support bridge and the ballscrew nut and was used to carry the eccentric weights used to apply radial force excitation to the ballscrew. In the case of this second ring it was possible to fit it in a variety of positions.

3-8-Measurement strategy

Therefore the measurement strategy was to set the second monitoring ring in a particular axial position and to subject the screw to two sets of out-of balance loading, one with the eccentric weights applied and one without. Because of the limited time at which vibrations were being generated, the maximum speed used was increased to 40 000 mm/min. Using this speed as a maximum four other speeds were determined so as to give 40%, 60%, 80% and 90% of the dynamic force applied at the maximum speed. A final speed was chosen to give a "slow roll" the results of which might possibly be used to subtract out the effects of the runout of the monitoring ring and other errors.

4- CONCLUSION

During the course of the programme of research covered by this Research the geometric, thermal and load errors commonly encountered on CNC machine tools have been studied. Several mathematical models have been developed or extended which enable a deeper understanding of the interaction between these errors, various details of ballscrew design and the dynamic behaviour of ballscrew driven systems. Further, a strategy for compensation of some of these errors has been devised.

The results of the research are detailed as follows:

- The static elastic theory relevant to ballscrew machine tool drives has been brought together to form a group of formulae useful for estimating the static stiffness characteristics of such systems.
- The relevant dynamic elastic theory and the theory of thermal modelling have been applied to develop a detailed understanding of the behaviour of a ballscrew driven system. A set of working models have been assembled which cover the dynamic and thermal aspects of ballscrew behaviour.

- The continuous matter approach to the dynamics of a ballscrew using wave solutions was developed. Although this succeeded in giving satisfactory results for the case of axial and torsional behaviour, it did not prove to be a useful method for dealing with transverse vibratory behaviour.

- Several models based on the discrete matter or "lumped mass" approach were devised. Using matrix solutions, three useful models were developed as follows.

- The first of these models extends the classical eigenvalue method for finding the natural frequencies and other dynamic characteristics of ballscrew systems to include viscous damping effects by using a generalised eigenvalue approach. This not only gives estimates of the natural frequencies, but also the damping coefficient of each predicted vibration mode. This feature enables many of the natural frequencies predicted by standard undamped natural frequency analyses to be dismissed as being of little consequence to the vibratory behaviour of the system and is a useful contribution to knowledge in this field.

A development of this modelling method gives the sensitivity of the system to changes in stiffness and damping characteristics. When a mode of vibration is considered to be potentially detrimental to a system's performance, the design parameters which have greatest influence on the mode can be identified. Changes in these parameters can be tested quickly by the model and improved dynamic characteristics found before going on to the stage of detailed design changes. This is a tool useful both at the preliminary design stage of a ballscrew system, and for helping to decide the most convenient remedy to vibration problems which may occur in service.

With some modification, the approach can be applied to many electro-mechanical systems. Specifically, the controller parameters can be included in the model giving a means of investigating how changes in such parameters can be used to modify the drive system's behaviour.

By using a suitable means of deriving a set of viscous damping coefficients which are equivalent, in defined circumstances, to non-linear damping effects, it is possible to extend this method to include non-linear behaviour.

• The second set of lumped-mass models is specially developed to take account of the changes in the configuration of the system with time as the nut moves along the screw.

These deal only with the axial and torsional degrees of freedom of the system, which have the most direct impact on the response of a ballscrew driven system. A special difficulty arises when the position of the nut does not coincide with a node in the model. Using a "simple" approach to connecting the nut with the screw gave rise to a response that was dependent on the structure of the model. This problem has been successfully addressed by using a "massless node" as the connection point. Implementation of this approach entailed the development of an algorithm based on sophisticated matrix algebra, which has succeeded in advancing knowledge by giving a seamless dynamic response.

• These models can predict the position error of the ballscrew nut.

• The third set of models includes the transverse degrees of freedom as well as the axial and torsional ones. These give a means of predicting the vibration amplitudes which might be expected as a system "runs through" a natural frequency, either because the system parameters change as the nut moves along the screw or because the speed of the screw is changing.

• The second and third sets of models include the non-linear phenomena of backlash and Coulomb friction as well as time dependent stiffness and damping characteristics.

Both of these models are capable of being extended to include other non-linear phenomena, such as stiffness which is dependent on the state of strain (e.g. Hertzian contact stiffness characteristics) and drag terms which are dependent on the square of the speed.

• The three groups of lumped mass models all include features which calculate the energy converted to heat by all the energy dissipative mechanisms in the model. The Engineering Control and Machine Performance Group at the University have already produced a model which predicts the thermal behaviour of a ballscrew system. This model has been validated experimentally. The heat output from a dynamic model has been shown to correlate well with the heat levels used in this proven thermal model. Therefore dynamic models and a suitably adapted thermal model, used together, could be used to predict the thermal behaviour of a ballscrew system.

REFERENCES

1. Aomori H., "Metal cutting machine tools, Japan", Industry Sector Analysis, U. S. Department of Commerce - National Trade Data Bank, November 3, 2000.

2. Bryan J., (Lawrence Livermore Nat. Lab.), "International status of thermal error research". *Annals of the CIRP*, Vol. 39, N2, P645-656, 1990.

3. Blake M. D., "Investigation into load effects on machine tool accuracy". MPhil research, University of Huddersfield, 1995.

4. Holroyd G., Pislaru C. and Ford D. G., Identification of damping elements in a CNC machine tool drive. In Proceedings of 5th International Conference on *Laser Technology, Machine Tool, CMM and Robot Performance* LAMDAMAP 2001 (Ed. WIT Press), Birmingham, UK, July 2001, pp. 289-299.

5. Frank A., Ruech F., "Thermal behaviour of position measurement systems: linear transducer - rotary encoder", Proc. EUSPEN Conf., Bremen, Germany, 31st May 4th June 1999, pp124-127

6. Chen J. S., "A study of thermally induced machine tool errors in real cutting conditions". *International Journal of Machine Tools and Manufacture*, Vol. 36/12, pp. 1401-1411, 1996.

7. Wang Y., Zhang G., Moon K. S., Sutherland J. W., "Compensation for the thermal error of a multi-axis machining center", *Journal of Materials Processing Technology*, Vol. 75, pp. 45-53, 1998

8. Fraser S., Attia M. H., Osman M. O. M., "Modelling, identification and control of thermal deformation of machine tool structures, part 1: concept of generalized modelling", *Transactions of the ASME, Journal of Manufacturing Science and Engineering*, Vol. 120, pp. 623-631, August 1998

9. Jan H.-K., Chu C. N., Liu C. R., "A configuration independent error model of machine tools: hyperpatch model and metrology pallet", *Robotics and Computer-Integrated Manufacturing*, Vol. 9/3, pp. 201-210, 1992

10. White A. J., Postlethwaite S. R., Ford D. G., "A general purpose thermal error compensation system for CNC machine tools", LAMDAMAP 2001, University of Huddersfield, UK, pp. 3-13.

11. Freeman J. M., White A. and Ford D. G, "Ball-screw thermal errors – a finite element simulation for on-line estimation", LAMDAMAP 2001, Precision Engineering Research Group, The School of Engineering, University of Huddersfield, England, pp 269-278.

Bulletin of Pure and Applied Sciences
Vol. 32 D (Physics) Issue (No.2) 2013:P. 127-130
www.bpas.in

TRANSMISSION OF HOLES BY A MULTIBAND-MULTICHANNEL MODEL

Ravi Anjan
Department of Physics, Rajendra College Chapra, J.P.U., Saran, Bihar, India.
Rekha Singh
University Deptt. of Physics, B.R.A. Bihar University Muzaffarpur, Bihar, India.
Kumari Ruchi
Department of Physics, S.M. College, Hajipur, Vaishali, Bihar, India.
Satyendra Kumar Singh
Department of Chemistry, A.B.S. College, Lalganj, Bihar, India.
Shashi Sekhar
Department of Math, A.B.S. College Lalganj, Bihar, India.
Rakesh Kumar Ranjan
Department of Physics, J.P. University Chapra, Saran, Bihar, India.

Received on 18August 2013: Accepted on 28 November 2013

ABSTRACT

We have studied transmission of holes by a multiband-multichannel model. We combined the effective Hamiltonians of the k-p approach with the multichannel transfer matrix approach. We have shown that using an orthonormal basis derived from quadratic eigen value problem, the important flux conservation requirement was rigorously satisfied. For calculation of transport properties of multichannel-multilayered systems, we employed the finite periodic systems theory. The transmission amplitudes matix, which like the scattering matix contains entire information on the scattering process described by the model Hamiltonian. By obtaining transmission amplitudes one can easily determine transmission coefficients, and specific transport properties such as the channel interference characteristics and global quantities such as the Landauer conductance as function of the incoming Fermi energy and the heterostructure parameters. We studied all amplitudes of heavy and light holes at the same time. This study has benefit of identifying inter and intra-band hole transitions.

Key words : Transmission, Multiband, multichannel, Hamiltonian, Matrix, Eigenvalue, Transport, Scattering, Landauer, Heterostructure.

INTRODUCTION

Payne (1986) studied that the weakly coupled multimode electron tunneling ca be properly described within a one dimensional approximation. Morifuji and Hamaguch (1995) reported that multimode problems have been considered with relative success i the framework of tight-binding approximations for valence bands and the k-p approach Carlo et al (1998) showed it for valence and conduction band mixing. In the tight binding and k-p approaches, some effective Hamiltonian are built on and eventually, the solutions described within the envalope function approximation. Kumar et al (1997) reported that even though these solutions are multicomponent wave functions to determine transmission coefficients. Wannier and Wigner functions (1987) and Ando et al (1987) performed one dimensional transfer matrix for the study of transmission of holes. Kane (1969) explained that in general the strongly mixed non parabolic bands is not capable for our problem. Sanchez et al (1995) showed that besides this it is also usual, after block diagonalizing to work in reduced Hilbet spaces, which taken separately do not fulfill all the physical symmetries of the whole Hilbert space. Broido and Sham (1985) presented several transmission coefficient results exhibiting among other features the mixing of light holes and heavy holes.

METHOD

We have used the quadratic eigenvalue problem method and the multichannel transfer matrix technique. We developed an approach to study multichannel-multiband transport properties through multilayered systems. To solve the second order differential equation associated to N-fold Kohn-Luttinger type Hamiltoniana and to obtain the momentum eigen values we followed the quadratic eigen value problems method employed by Tisseur and Meerbergen. We studied hole transport properties through III-V semiconductor heterostructures described by Kohn-Luttinger model.

RESULTS AND DISCUSSION

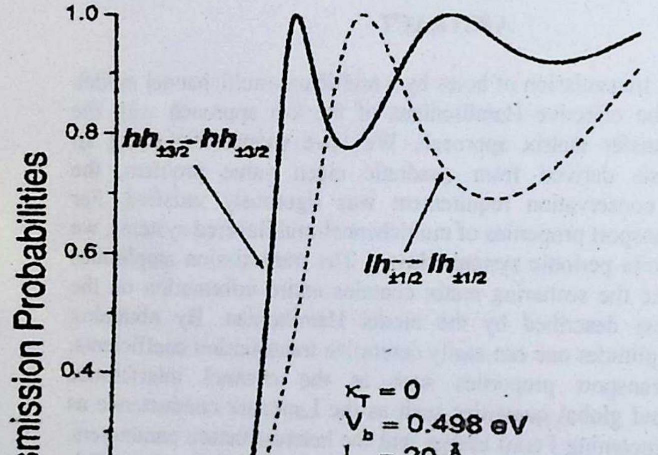

Graph 1. :- Transmission probabilities as function of the incident-particles energy for the heterostructure GaAs-cladding layer.

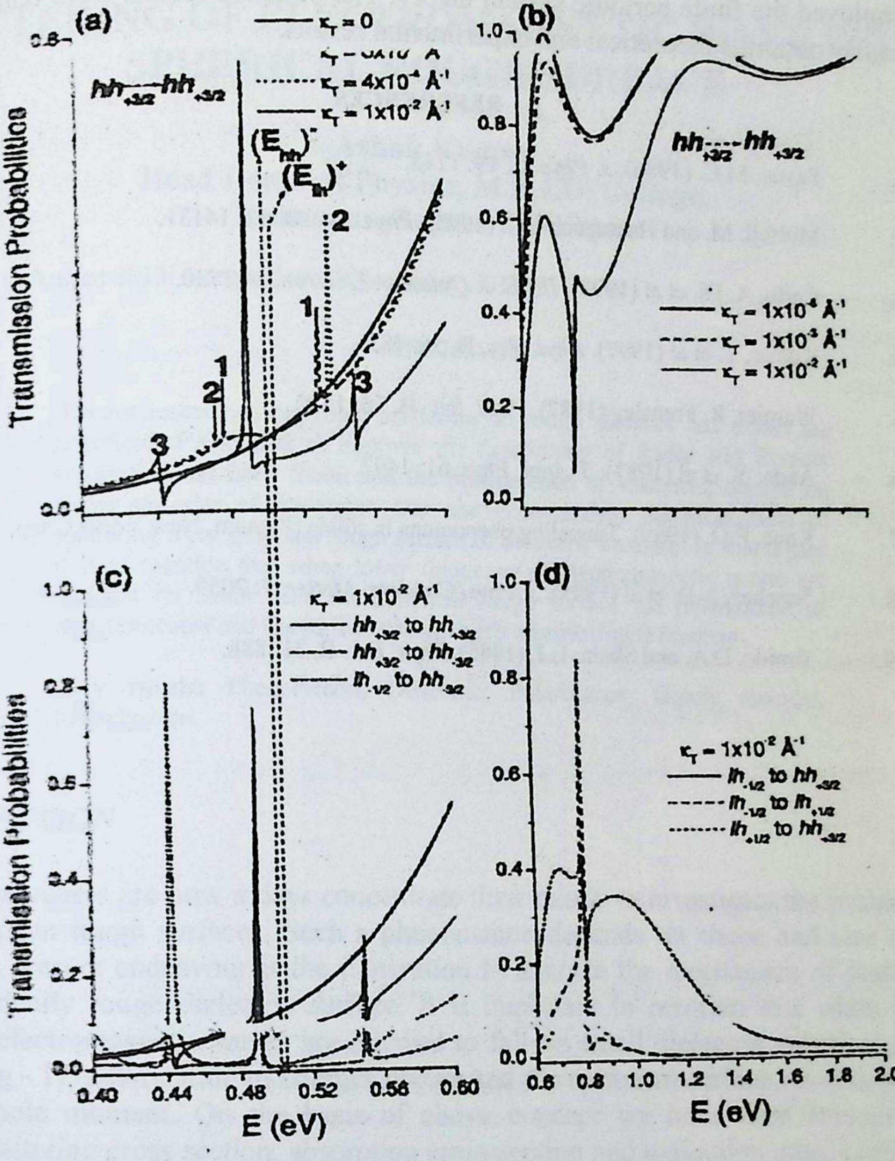

Graph 2. :- Transmission coefficients as functions of the incoming energy.

CONCLUSION

We have calculated transmission amplitudes for incoming and out going propagating modes. We have studied hole tunneling through single barrier and multiple-barrier semiconductor heterostructures. We observed that one component flux description for a transport process characterized by mixed multicomponent flux is unreliable. We considered all the propagating modes jointly and simultaneously and a multicomponent description of transmission amplitudes was carried out in a natural way. We combined the effective Hamiltonians of the k-p approach with the multichannel transfer matrix approach. For calculation of transport properties of multichannel multilayered systems, we employed the finite periodic system theory. The obtained results were compared with previously obtained theoretical and experimental results.

REFERENCES

1. Payne, M.C. (1986). *J. Phys.* C, 19: 1145.
2. Moifuji. M. and Hamaguchi., C. (1995). *Phys. Rev.* B, 52: 14131.
3. Carlo, A. Di. et al (1998). *IEEE. J. Quantum Electron*, 34:1730.
4. Kumar, T. et al (1997). *Phys. Rev.* B, 56: 4836.
5. Warnier, R. Frensley (1987), *Phys. Rev.* B, 36: 1570.
6. Ando, Y. et al (1987). *J. Appl. Phys.* 61: 1497.
7. Kane, E.O. (1969). Tunneling phenomena in solids (Plenum, New York) Chap. 1.
8. Sanchez, A.D. et al (1995). *J. Phys. Condens. Matter*, 7: 2059.
9. Broido. D.A. and Sham. L.J. (1985). *Phys. Rev.* B, 31: 888.

Bulletin of Pure and Applied Sciences
Vol. 32 D (Physics) Issue (No.2) 2013:P. 131-139
www.bpas.in

SCATTERING OF ELECTROMAGNETIC WAVE FROM SPHERICAL ROUGH SURFACE

Ashok Kumar
Head Deptt. of Physics, M.R.J.D. College,
Bishnupur, Begusarai (Bihar)

Received on 08August 2013: Accepted on 25 November 2013

ABSTRACT

Recent researches regarding scattering on rough surfaces has drawn the attention of scientists to improve the functioning of Radar and Remote sensing. It has been found that the phenomenon of scattering depend on shape and size of the target. Our aim is to analyse the mechanism of scattering from spherical rough surface of dielectric medium. In this regard it is to mention that when lower frequency of electromagnetic waves are incident on small dielectric spherical rough surface the polarization of charges occurs and the surface possess a net electric dipole moment.

Key words: Phenomenon, Dielectric, Polarization, Dipole moment, Investigation.

INTRODUCTION

Researchers are now a days concentrate their minds to investigate the problem of scattering from rough surfaces. Such a phenomenon depends on shape and size of the target. Out present endeavour is the motivation to analyze the mechanism of scattering from spherically rough dielectric surface. It is important to mention that when lower frequency electromagnetic waves are allowed to fall on small dielectric spherical rough surface (Fig.- 1), polarization of charges occurs and the spherical surface possesses a net electric dipole moment. On the basis of above concept we have here attempted to evaluate scattering cross section, absorption cross-section and extinction cross-section of a spherical dielectric rough surface.

DEVELOPMENT OF THEORY

If $\vec{E}_i$ is the incident electric field and $\vec{E}_s$ the scattered electric field then total electric field produced by a source in presence of dielectric medium is given by

$$\vec{E} = \vec{E}_i + \vec{E}_s \qquad \ldots(1)$$

The current density $\vec{J}$ is given as

$$\vec{J} = j\,\omega\,(\in_r - \in_0)\,\vec{E} \qquad \ldots(2)$$

Where $\in$ is the complex permittivity of dielectric material, which may be obtained from relation

$$\in = \left(\in_r - j \frac{\sigma}{\omega \in_0} \right) \in_0 \qquad \ldots(3)$$

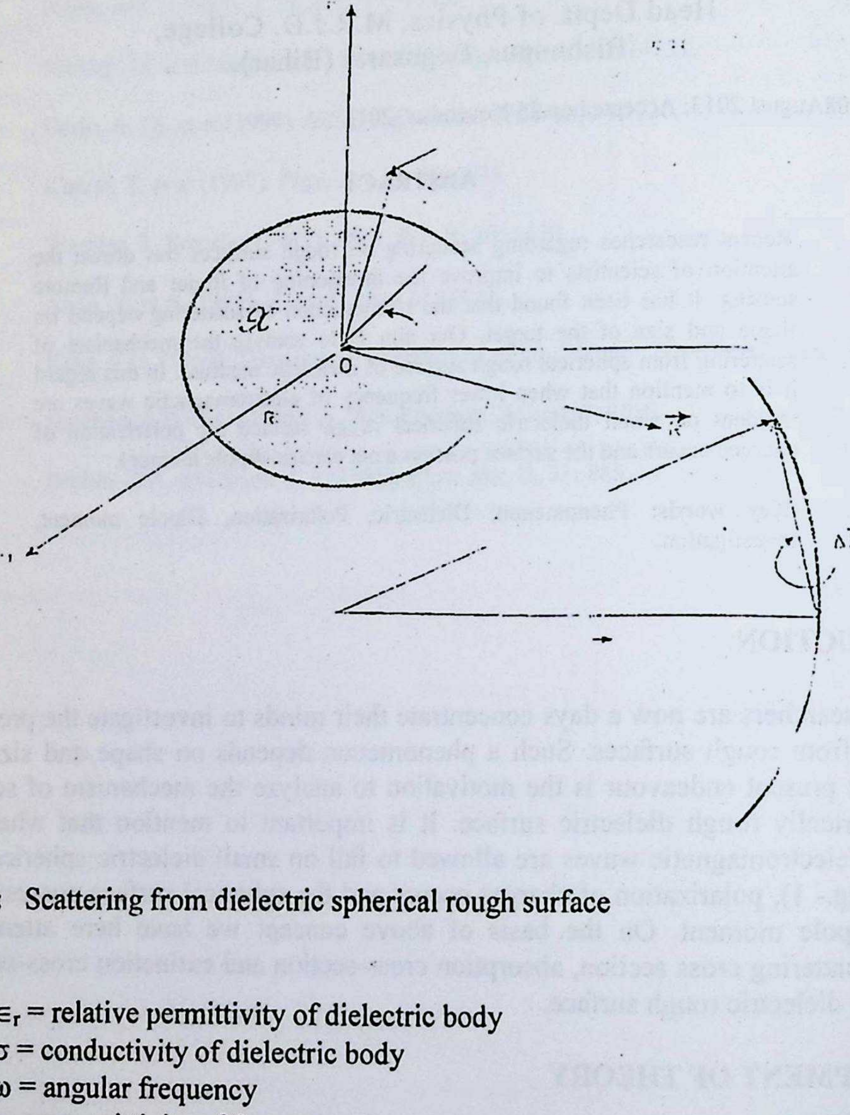

Fig.- 1 : Scattering from dielectric spherical rough surface

Where

$\in_r$ = relative permittivity of dielectric body
σ = conductivity of dielectric body
ω = angular frequency
$\in_0$ = permittivity of free space

Thus combining equation (1) and (2) we find

$$\bar{J} = j\,\omega\,(\in - \in_0)\,\vec{E}_i + \vec{E}_s \qquad \ldots(4)$$

Thus the scattered field $\vec{E}_s$ produced by current density $\bar{J}$ can be written as

$$\vec{E}_s = -\Delta\,\phi - j\,\omega\,\vec{A} \qquad \ldots(5)$$

where ϕ is scalar electric potential and $\vec{A}$ is the vector potential. Equation (5) may be modified as

$$\vec{E}_s = \frac{-j\omega\,\mu_0}{4\pi} \iiint_v \vec{J}\,G\,dv - \frac{\Delta}{4\pi \in_0} \iiint_v \vec{J}\,G\,dv \qquad \ldots(6)$$

Where G is the Green's function

$$G = \frac{e^{-jkR}}{R}$$

where

$$R = \sqrt{(x-x')^2 + (y-y')^2 + (z-z')^2}$$

$$K = \frac{2\pi}{\gamma}$$

λ = wavelength

The charge density ρ associated with current density $\vec{J}$ can exist only on the surface of the body hence inside homogeneous dielectric body has the relation

$$\vec{\nabla}\vec{J} = \vec{\nabla} \cdot \vec{E} = 0$$

Thus the second term in equation (6) can be replaced by surface integral of charge density as

$$\rho = \frac{1}{j\omega}\left(\vec{n} \cdot \vec{J}\right) \qquad \ldots(7)$$

$\vec{n}$ is the unit outward normal vector. The value of scattered field $\vec{E}_s$ can be obtained by combining equation (6) in (7)

$$\vec{E}_s = -\frac{-j\omega\,\mu_0}{4\pi} \iiint \vec{J}\,G\,dv - \frac{\vec{\nabla}}{j\omega\,\pi \in_0} \iiint \left(\vec{n} - \vec{J}\right) G\,ds \qquad \ldots(8)$$

Hence it is clear from equation (8) that the value of scattered field $\vec{E}_s$ can be obtained when the value of $\vec{J}$ is known. Let us consider a small spherical dielectric body whose size is less than a wavelegth. The field will be scattered in and near the dielectric body.

Thus the uniform electric field $\vec{E}$ inside the dielectric body due to incident electric field $\vec{E}_s$ can be given as

$$\vec{E} = \frac{3}{\in_r + 2} \qquad \vec{E}_i = \frac{3}{\in_r + 2}\,\vec{E}_i\,\hat{e} \qquad \ldots(9)$$

Combining equation (2) and (8) we have,

$$\vec{J} = \left[j\omega\left(\in - \in_0\right)\right] \frac{3}{\in_r + 2}\ \vec{E}_i\, \hat{e} \qquad \ldots(10)$$

Substituting value of $\vec{J}$ from equation (10) in equation (8) we have

$$\vec{E}_s = \frac{-j\omega\, \mu_0}{4\pi} \iiint \vec{J}\, G\, dv\ \left[j\omega\left(\in - \in_0\right)\right] \frac{3}{\in_r + 2}\ \vec{E}_i\, \hat{e}$$

$$\frac{\vec{\nabla}}{j\omega\, \pi \in_0} \left(\iint G ds\right) \left(\vec{n} - \vec{J}\right) \left[j\omega\left(\in - \in_0\right)\right] \frac{3}{\in_r + 2}\ \vec{E}_i\, \hat{e} \qquad \ldots(11)$$

Thus the scattered power may be given as

$$\text{P} = \frac{\frac{1}{2}\,|\,E_s\,|^2}{\eta_0} \qquad \ldots(12)$$

where η_0 is the impedance of free space hence the scattering cross section of rough surfaces may be obtained as

$$\sigma \int_c = \frac{P_s}{P_i} \qquad \ldots(13)$$

The inside power P_i is given as

$$\text{P}_\text{i} = \frac{|\,E_s\,|^2}{2\eta_0} \qquad \ldots(14)$$

Putting the value of $\vec{E}_s$ in equation (12) we get

$$\text{P}_\text{s} = \frac{1}{2\eta_0} \left[\frac{j\omega\, \mu_0}{4\pi} \left[\iiint\ G\ dv\right] \left[j\omega\left(\in - \in_0\right)\right] \frac{3}{\in_r + 2}\ \vec{E}_i\, \hat{e}\right.$$

$$\left. -\frac{\vec{\nabla}}{j\omega\, \pi \in_0} \left(\iint G ds\right) \vec{n}\ - \left[j\omega\left(\in - \in_0\right)\right] \frac{3}{\in_r + 2} \vec{E}_i \hat{e}\right]^2 \qquad \ldots(15)$$

The value of σ_{sc} will be modified as

$$\sigma_{sc} = \left| \begin{array}{l} \dfrac{1}{2\eta_0} \dfrac{j\omega\,\mu_0}{4\pi} \left[\iiint G\,dv \right] \left[j\omega\left(\in - \in_0\right) \right] \dfrac{3}{\in_r + 2} \vec{E}_i \hat{e} \\ - \dfrac{\vec{\nabla}}{j\omega\,\pi \in_0} \left(\iint G ds \right) \vec{n} \left[j\omega\left(\in - \in_0\right) \right] \dfrac{3}{\in_r + 2} \vec{E}_i \hat{e} \end{array} \right|^2 ds \qquad \text{...(16)}$$

The value of scattering cross section (σ_{sc}) in dB may be given as

$$\sigma_{sc} = 10\log \left| \begin{array}{l} \dfrac{1}{2\eta_0} \dfrac{-j\omega\,\mu_0}{4\pi} \left[\iiint G\,dv \right] \left[j\omega\left(\in - \in_0\right) \right] \dfrac{3}{\in_r + 2} \vec{E}_i \hat{e} \\ - \dfrac{\vec{\nabla}}{j\omega\,\pi \in_0} \left(\iint G ds \right) \vec{n} \left[j\omega\left(\in - \in_0\right) \right] \dfrac{3}{\in_r + 2} \vec{E}_i \hat{e} \end{array} \right|^2 dB \qquad \text{...(17)}$$

The absorption cross section (σ_{abs}) defined

$$P_{abs} / P_i$$

where P_{abs} is the observed power and P_i the incident power

$$P_i = \frac{\frac{1}{2} | E_0 |^2}{\eta_0}$$

The time over observed power given by the relation

$$\begin{aligned} P_{abs} &= \frac{1}{2} \text{Re} \int_0^a \int_0^{2\pi} \int_0^{\pi} E\ j^* \,\text{P} r^2 \sin\theta\, d\phi \\ &= 2/3\, \pi\, a^3\, \text{Re}\, E\, j^*\, \rho \\ &= \sigma\, \pi\, a3\, k_0\, y_0 \left| \frac{\in - 1}{\in + 2} \right|^2 \frac{\in_2 \left| E_0^2 \right|}{\left(\in_1 - 1\right)^2 + E_2^2} \end{aligned} \qquad \text{...(18)}$$

Dividing the equation (8) by incident power density we can obtain the absorption cross section

$$\sigma_{abs} = \frac{P_{abs}}{P_i} = 12\pi\, a3\, (k_0\, a) \left| \frac{\in - 1}{\in + 2} \right|^2 \frac{\in_2}{\left(\in_1 - 1\right) + \in_2^2} \qquad \text{...(19)}$$

The absorption cross section is taken in dB is given as

$$\sigma_{abs} = 10 \log \left|\frac{P_{abs}}{P_i}\right| \text{dB}$$

$$= 2 \log \left| 12\pi \text{ a3 } (k_0 \text{ a}) \left|\frac{\in -1}{\in +2}\right|^2 \frac{\in_2}{(\in_1 -1)^2 + \in_2^2} \right| \text{dB} \qquad \ldots(20)$$

The extinction cross section (σ_{ext})

$$\sigma_{ext} = \sigma_{sc} + \sigma_{abs}$$

$$= \left| \begin{matrix} \dfrac{1}{2\eta_0} \dfrac{-j\omega\,\mu_0}{4\pi} \left[\iiint G\,dv\right] \left[j\omega\,(\in - \in_0)\right] \dfrac{3}{\in_r +2} \vec{E}_i \hat{e} \\ -\dfrac{\vec{\nabla}}{j\omega\,\pi \in_0} \left(\iint G ds\right) \vec{n} \left[j\omega\,(\in - \in_0)\right] \dfrac{3}{\in_r +2} \vec{E}_i \hat{e} \end{matrix} \right|^2 ds$$

$$+ 12\pi \text{ a3 } (k_0 \text{ a}) \left|\frac{\in -1}{\in +2}\right|^2 \frac{\in_2}{(\in_1 -1)^2 + E_2^2} \qquad \ldots(21)$$

Numerical values of σ_{sc}, σ_{abs} and σ_{ext} have been calculated as function of frequency with the help of equation (16), (19) and (21). The data so obtained are shown in the form of graphs in Fig. 2, 3 & 4.

DISCUSSION OF RESULTS

Calculation have been made with the help of equation (16), (19) and (21) for scattering cross section absorption cross section and extinction cross section respectively. Calculated σ_{sc}, σ_{abs} and σ_{ext} are shown in Fig. – 2, 3 and 4. These cross sections generally increase with the increasing frequency. In lower range of frequency there absorption cross section has appreciable value but scattering cross section is significantly lower. Hence at lower frequency the absorption cross section dominate over extinction cross section, which is in accordance with real scattering which depend on fourth power of $(2\pi a/\lambda)$. At lower frequency the scattered power will be very weak resulting low scattering cross section with increase in frequency the scattering cross section and extinction cross section also increase.

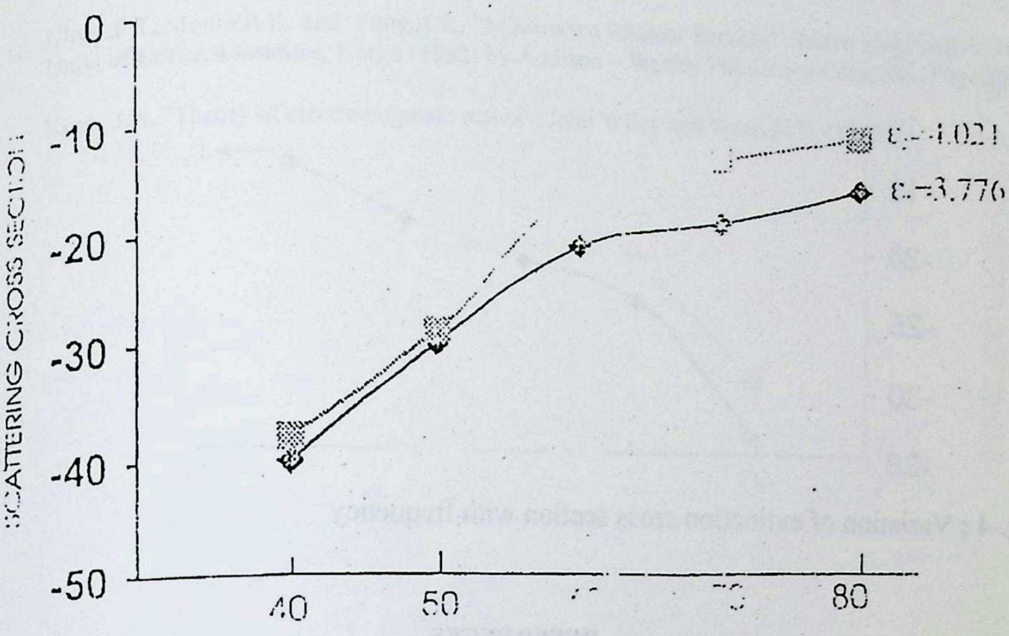

Fig.-2 : Variation of scattering cross section with frequency

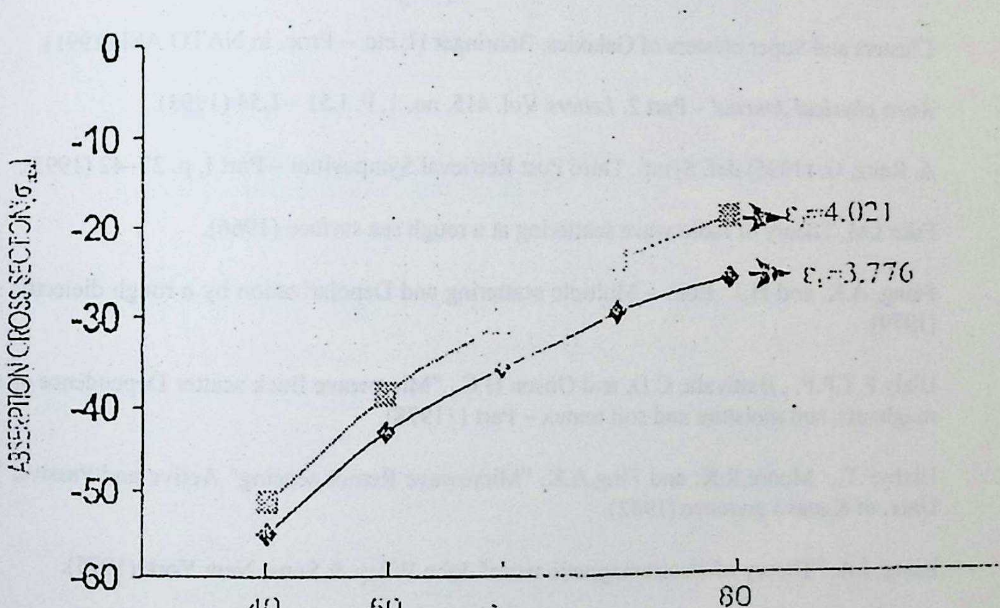

Fig.-3 : Variation of obserption cross section with frequency

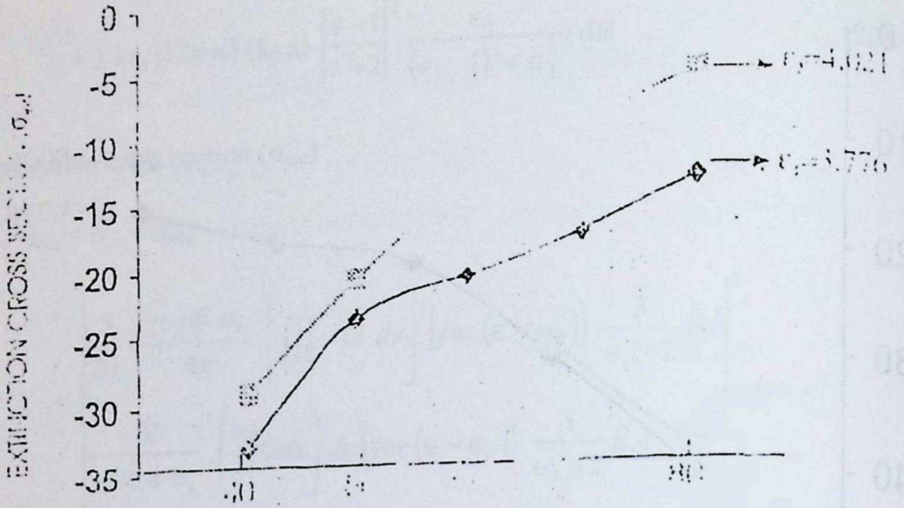

Fig.-4 : Variation of extinction cross section with frequency

REFERENCES

1. Faber, S.M., Primack, J.R., and Rees, M.J., *Nature* – 311, 517 (1984).

2. Clusters and Super clusters of Galaxies, Bohringer H, etc. – Proc. in NATO ASI (1991).

3. *Astro physical Journal* – Part 2. *Letters* Vol. 415, no. 1, P. L51 – L54 (1993).

4. A. Reitz, G. (1995) def. Symp. Third Post Retrieval Symposium – Part I, p. 37–42 (1995).

5. Fuks I.M. Theory of radio wave scattering at a rough sea surface (1966).

6. Fiang, A.K. and H.J. Eom – Multiple scattering and Depolarization by a rough dielectric surface (1979).

7. Ulaly F.T.P.P. , Battivala, C.D. and Obson H.C., "Microwave Back scatter Dependence on surface roughness, soil moisture and soil tentux – Part I (1978).

8. UlabyF.T., Moore,R.K. and Fing,A.K. "Microwave Remot sensing" Active and Passive, Vol. II, Univ. of Kanas Lawrence (1982).

9. Kong, J.A. "Theory of electromagnetic wave" John Wiley & Sons, New York (1975).

10. Fuks, I.M. (1966). "Theory of radio wave scattering at a rough sea surface". Soviet Radio Physics, pp. 976 – 997. Russian transl. Appears with some volume and number in (1969).

11. Fung, A.K. and Eom,H.J. (1979)."Multiple scattering and depolarization by a rough dielectric surface". *J. Fronklin Institute*, 285:125–133.

12. Fung, A.K. and Fom,H.J. (1979) "Multiple scattering and depolarization by a randomly rough Kirchhoff surface", Remote sensing Lab. TR 369 – 4 Univ. of Konas, Lawrence, Konus.

13. Uloby, F.T.P.P., Baltivola and Dobson,M.C. (1978), "Microwave backscatter dependence on surface roughness, Soil moisture and soil texture", Part 1 vegetation – covered soil, *IEEE Trans. Geo Sci. Electr. GE* – 16: 286 – 295.

14. Uloby,F.T.,Moore,R.K. and Fung,A.K. "Microwave Remote Sensing" Active and Passive Vol. II Univ. of Konas, Lawrence, Konas (1982) by Addison – Wesley Publishing Company, Page 933.

15. Kong, J.A. "Theory of electromagnetic waves", John Wiley and Sons. N.Y. (1975).

Bulletin of Pure and Applied Sciences
Vol. 32 D (Physics) Issue (No.2) 2013:P. 141-146
www.bpas.in

A FIRST PRINCIPLE STUDY OF ELECTRONIC AND STRUCTURAL PROPERTIES OF INDIUM ARSENIDE(INAS)

Vrishali Joshi
Department of Physics,Govt. P. G. College, Guna (M.P.)
Email:vrivin@gmail.com

Received on 18 August 2013: Accepted on 30 November 2013

ABSTRACT

The operating characteristics of electronic and opto-electronic devices depend not only on material engineering at a practical level, it also demands clear understanding of the properties of materials and the fundamental science behind these properties. Owing to their technological significance, it is important to know different properties of these semiconductor compounds. Theoretical investigations as well as experimental research is therefore of vital interest to all those working in this area of research.In the present paper we have studied the electronic properties of ZB InAs, a binary semiconductor.The calculations are performed using the FP-LAPW approach plus local orbitals within the framework of density functional theory (DFT)

Key Words: Wien2k code, DFT(Density functional Theory),FP-LAPW, density of states (DOS) ,elastic moduli.

INTRODUCTION

Indium Arsenide is a narrow band gap semiconductor with a band gap of 0.35 eV. This makes InAs a useful material for devices targeted at very high speed (and low power) electronics and Infrared optoelectronics. Since there are no measured properties of InAs in the wurtzite phase, the choice of an ab- initio method is highly appropriate because it does not require any previous knowledge of the material parameters and allows one to predict numerous properties ranging from the equilibrium lattice constant to the band structure. The ground-state electronic structure of solids is well described by density-functional theory (DFT). There are several methods to find solutions for exchange correlation functional. We have chosen one which includes modifications in the calculations of GGA approximation.They have studied structural,electronic and optical properties of InxGa1-x-As alloys (Sudhirkumar et al 2008)[5],The electronic band structure of InN,InAs and INSb compounds was studied(Rezek Mohammad et a 2008)[3]. these researchers have investigated the elastic properties of zinc blende iii- compounds under pressure effects using FP-LAPW+localculations(A.Bouhemadou et a 2009)[1], Modified atomic scattering amplitudes and size effects on the 002 and 22 electron structure factors of multiple Ga1-xInxAs/GaAs quantum wells were studied by ii-vi common cation semicondutors ternary alloys was performed(Nacir tit et al 2010)[4]. Some researchers have calculated band structure engineering and vacancy induced metallicity at the GaAs-AlAs interface(M.Upadhyay et al 2011)[7],First-principle investigations of structural, electronic, elastic and magnetic properties of Ga1-x MnxP and In1-x MnxP were made by researchers(A. Djedid et al 2013)[2].

COMPUTATIONAL TECHNIQUE

We use the first-principle method to compute total energy for ZB- InAs under hydrostatic pressure. Hydrostatic pressure is achieved by resizing the volume of the unit cell. The calculations are performed using the FP-LAPW approach plus local orbitals within the framework of density functional theory (DFT) as implemented in the Wien2k code. Thus the equilibrium lattice constants of ZB-InAs compound is determined by the minimization of the total energy with respect to the volume of the unit cell. Corresponding to minima of the total energy versus unit cell volume, in both the cases, pressure is assumed to be zero.

In the calculations for ZB-InAs we use two atoms per primitive cell, where In is considered at (0,0,0) and As at (¼,¼,¼) position. In order to decide optimum number of k-points plots between total energy and number of k-points were drawn. On the basis of the convergence of the total energy we use 1000 k-points for the ZB structure within Brillion zone. The k-points sets used in the calculations are based on a 10x10x10divisions of the reciprocal unit cells that results into 45 equivalent k-points due to symmetry in InAs.

RESULTS AND DISCUSSION

Structural properties

In this study, the exchange-correlation potential functional, under GGA approach, are employed to characterize the atomic behavior in cubic phase ZB- under ambient condition. Figure1show the calculated energy-volume curves for ZB-InAs. For the plot seven points were calculated. The calculated values of lattice constants along with their available experimental and earlier reported values are listed in table. In comparison with the experimental values, error in the lattice constant of ZB-InAs is 3%. In the calculation of bulk modulus the error in comparison with its average experimental values is 15% for ZB-InAs. The amount of errors show that the reported results are acceptable and hence other predictions can be forecasted on the basis of computational results.

From figure 1 it is clear that the total energy per formula unit of the ZB phase is -16288.82 Ryd corresponding to equilibrium lattice constant.

The curves in figure 1 were obtained by calculating the total energy at seven different volumes around equilibrium of InP in ZB phase and by fitting the calculated values to the Murnaghan equation of state.

Table 1: Basic parameters for structural and electronic properties in ZB-InAs phase.

stant	6.058	**Expt**
	6.18	**[PW]**
nd gap Eg (eV)		
	0.36	Expt
	0.35	[PW]
ulus B(GPa)	64	Expt
	58	Expt.
	49.64	[PW]
ı ıs B'	1.58	LDA
	4.65	[PW]
nstants(GPa)		.
	101.1 56.1 45.6	Theo

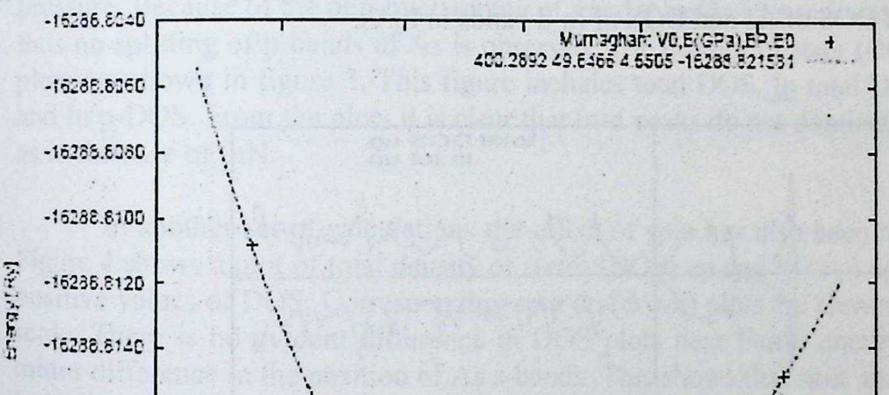

Figure 1: Total energy versus lattice volume plot due to Murnaghan fit. At the minima of the plot pressure is considered to be zero and corresponding lattice parameter corresponds to the theoretical constant.

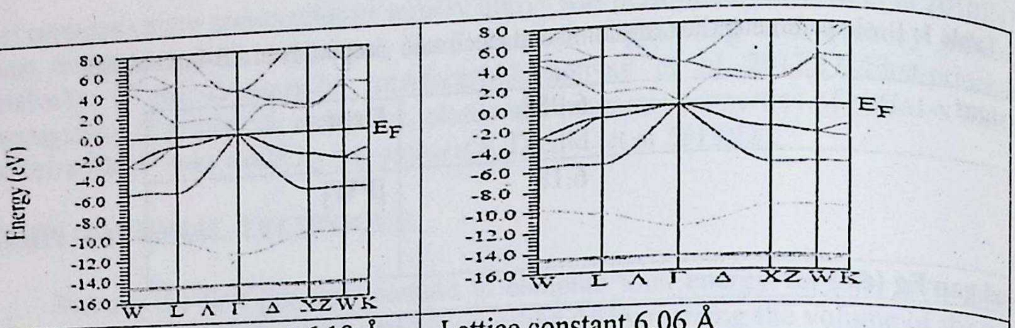

Lattice constant 6.18 Å
(Theoretical value)
Energy band gap 0.2 eV

Lattice constant 6.06 Å
(Experimental value)
Energy band gap 0.35 eV

Figure2: Band structure of ZB-InAs corresponding to two different lattice constants

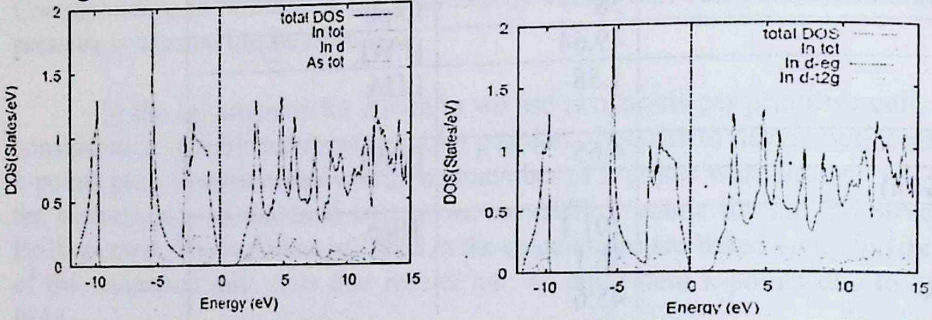

Figure 3 : Density of states (DOS) versus energy (in eV) for total DOS of InAs, total DOS of In, total DOS of As and DOS of In-d bands in InAs.

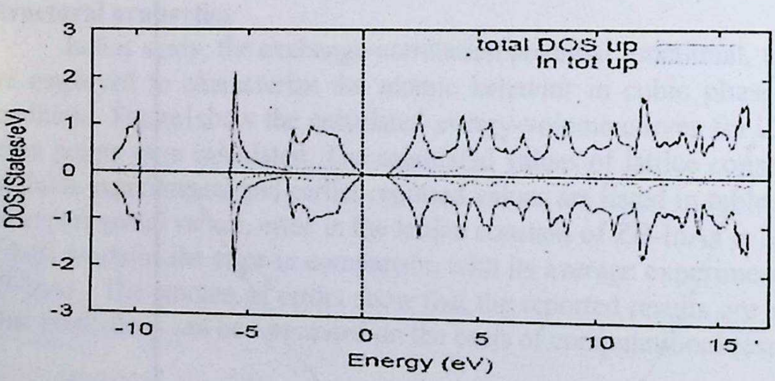

Figure 4 : Density of states (DOS) versus energy (in eV) for total DOS of InAs and total DOS of In corresponding to spin up and spin down modes.

From the Murnaghan fit of the total energy versus unit cell volume the bulk modulus B, its derivative B′ and pressure corresponding to various values of volume are calculated using relations given in previous chapter. The calculated values of bulk modulus are in good agreement with earlier reported results as listed in table .

Elastic properties

In this section we investigate the high-pressure behavior of the elastic moduli fo cubic InAs. Elastic constants are one of the important technological properties of solids They determine the behavior of materials under sufficient small loading because of the fact that the elasticity of simple crystals is a local property. Elastic constants are calculated corresponding to theoretical values of lattice constant. Difference between earlier reported C11 and present value is 3%, C12 differs by 15% and C44 is 10% or higher side. This is due to the fact that our calculated values of elastic constants are or higher side corresponding to theoretical lattice constant which is about 3% more than experimental value.

Electronic properties

Table 1 comprises detailed information about InAs. It also includes experimental values of band gap in ZB-phase of InAs. In present study, corresponding to experimental values of lattice constant, the calculated value of direct band gap for ZB-InAs is obtained as 0.35eV. It is comparable with the values reported in literature (table). From the band structure plots, shown in figure 2, it is evident that energy band gap increases with the increase in pressure, i.e., with the decrease in lattice parameter.

In the plot of band structure three bands near valance band are p-bands of As while next band in the series is corresponding to As s-band. Next group of bands are due to 4d-electrons in In. In this case too, contrary to InN, the valley of s-band of arsenide does not overlap the d-band of In. Depth of these bands decreases with the increase in pressure. Because of the non-overlapping of s and d bands interaction does not take place, thus no splitting of p-bands of As is observed. The density of state (DOS) versus energy plots are shown in figure 3. This figure includes total DOS, In total DOS, As total DOS and In p-DOS. From the plots it is clear that In-d peaks do not dominate over other peaks as in the case of InN.

In another set of calculations the effect of spin has also been taken into account. Figure 4 shows a plot of total density of states (DOS) up and In total up corresponding to positive values of DOS. Corresponding spin dn (down) plots are shown on negative DOS scale. There is no evident difference in DOS plots near Fermi energy level but a very minor difference in the position of As s-bands. This shows that spin magnetic moment of InAs is zero and there is no difference between-spin up (majority carrier) and spin down (minority carrier) concentration.

CONCLUSION

From the present study it is clear that energy band gap in InAs increases with the increase in pressure hence decrease in lattice constant. Experimental values of energy band gap may be justified corresponding to different pressure under which material is being synthesized. In the case of InAs- DOS plots it is clear that 4d- electrons have no dominating effect over other band electrons. Also, InAs is free from spin effect, i.e., majority and minority carriers are almost equal in number.

REFERENCES

1. Bouhemadou, A., Khenata,R., Kharoubi, M., Seddik, T. and Al-Douri .Ẏ.(2009). *Computational Materials Science* 45, 474-479
2. Djedid, A., Doumi, B., Méçabih, S. and Abbar, B.(2013).*Journal of Materials Science* ,0022-2461,1573-4803.
3. Mohammad, R., Katircioglu, S. and Musa, E.(2008). *J. Mater. Sci.* Vol. 43: 2935-2946.
4. Nacir, T., Noureddine, A. and Reshak, A. (2010).*Journal of electronic materials*, 39, 178.
5. Sudhir, K, Tarun, K.,Maurya, S. and Auluck, S.(2008).*Japanese Journal of Applied Physics* 47: 5417-5419.
6. Titantah, J., Lamoen, D., Schowalter, M. and Rosenauer, A.(2009).*Journal of Applied Physics* 105: 084310.
7. Upadhya, M., Nazir, S. and Schwigenschogl, U. (2011). *Appl. Phys. Lett.*99: 123501.

Bulletin of Pure and Applied Sciences
Vol. 32 D (Physics) Issue (No.2) 2013:P. 147-157
www.bpas.in

WIRELESS SENSOR NETWORK SIMULATOR TO STUDY ROUTING PROTOCOLS

Mojgan Eivazzadeh Kalejahi
Department of Computer Engineering, Osku Branch, Islamic Azad University, Osku, Iran
Email: eyvazzade@iauosku.ac.ir

Received on 18August 2013: Accepted on 30 November 2013

ABSTRACT

Wireless sensor networks are applied in many applications. The routing protocols that are developed for sensor networks must be energy efficient and scalable. It is necessary to perform a detailed analysis of sensor networks for understanding of the performance of them. Network simulators can inform us about the performance and behavior of these protocols on various network topologies. This research considers simulation of routing protocols at Sensor Networks Research Laboratory. Sensor Simulator is a discrete event simulation framework for sensor networks built over OMNeT++. This framework allows the user to debug and test software for distributed sensor networks. This research implements a comparative study on Directed Diffusion Routing Protocol on both ns2 and Sensor Simulator.

Keywords: Simulations Optimized Broadcast Protocols, Sensor Networks, Wireless Sensor Networks.

1-INTRODUCTION

A Sensor Node consists of one or more sensing elements (motion, temperatu pressure, etc.), a battery, and low power radio trans-receiver, microprocessor and limi memory, mobilizer (optional), a position finding system. An important aspect of su networks is that the nodes are unattended, have limited energy and the network topolo is unknown. Many design challenges that arise in sensor networks are due to the limi resources they have and their deployment in hostile environments.

Sensor nodes are deployed in environments where it is impractical or infeasi for humans to interact or monitor them. These unattended nodes may have effect on t efficiency of many military and civil applications such as target field imaging, distribut computing, intrusion detection, security and tactical surveillance, inventory contr disaster management and detecting ambient conditions. Some applications requ sensors to be small in size and have short transmission ranges to reduce the chances detection. These size constraints cause further constraints on CPU speed, amount memory, RF bandwidth and battery lifetime. Hence efficient communication techni are essential for increasing the lifetime and quality of data collection and decreasing the communication latency of such wireless devices [1].

Unlike the mobile ad hoc networks, sensor nodes are most likely to be stationary for the entire period of their lifetime. Even though the sensor nodes are fixed, the topology of the network can change. During periods of low activity, nodes may go to inactive sleep state, to conserve energy. When some nodes run out of battery power and die, new nodes may be added to the network. Although all nodes are initially equipped with equal energy, some nodes may experience higher activity as result of region they are located in. Communication pattern is intermittent and sensor applications are data-centric in nature. An important property of sensor networks is the need of the sensors to reliably disseminate the data to the sink or the base station within a time interval that allows the user or controller application to respond to the information in a timely manner, as out of date information is of no use and may lead to disastrous results. Another important attribute is the scalability to the change in network size, node density and topology. Sensor networks are very dense as compared to mobile ad hoc and wired networks. This arises from the fact that the sensing range is lesser than the communication range and hence more nodes are needed to achieve sufficient sensing coverage. Sensor nodes are required to be resistant to failures and attacks.

The current work is focused to study the performance and behavior of these routing protocols on various network topologies. The report begins with an introduction to Wireless Sensor Networks and the importance of routing protocols in various Sensor Network Applications. Section 2 gives an overview on the existing simulators and a brief description of OMNeT++ Framework. Section 3 gives an overview on the design of Sensor Simulator Architecture and how various protocols can be added at different layers without much dependency. Section 4 gives an overview on Optimized Flooding Protocol and its implementation in the Simulator.

2- LITERATURE REVIEW

Network simulators are very important for analyzing various protocols designed for a network (wired or wireless) and its necessity is very well known in the field of research. Especially, the research challenges in wireless sensor networks brought many open issues to network designers. The techniques used for analyzing the performance of any wireless networks are physical measurement, analytical methods and computer simulation. The constraints imposed on sensor networks, such as energy limitation, fault tolerance make the algorithms for sensor networks to be quite complex and usually defy analytical methods that have been fairly effective for traditional networks. And physical measurement is not possible because of the unsolved research problems in the field of sensor networks. Hence computer simulations appear to be the only feasible approach than anything else [2].

This extension might be easy for traditional networks but not for sensor networks where the protocols are not very dominant and it is very unlikely that a single algorithm will be optimal under various circumstances. Also various simulation studies show that the memory utilization of ns2 is very high and increases for very large simulations. Since the application areas in sensor networks require many number of sensor nodes in a sensor field, the simulations in ns2 take lot of memory. Also another disadvantage posed by ns2 comes from its open source nature. The documentation is often limited and out of date with the current release of the simulator. The problems can be solved with the help of dynamic news groups and going through the source code. Also, the consistency of code is lacking as it is developed by many users. There are no tools describe simulation scenarios and analyze or visualize simulation trace files. The tools for ns2 are written with scripting languages. The lack of generalized analysis tools may lead to different people measuring different values for the same metric names [3].

OPNET modeler is another popular commercial platform for network modeling and simulation which allows the design and study of communication networks, devices, protocols, and applications with unmatched flexibility and scalability. This is used by many prestigious technology organizations to accelerate the research and development process. OPNET Modeler is based on a series of hierarchical editors that directly parallel the structure of real networks, equipment, and protocols. The wireless model uses a stage pipeline to determine connectivity and propagation among nodes. Modeler's object oriented modeling and hierarchical editors mirror the structure of actual networks and network components [4]. The difficulty with OPNET Modeler is to build the state machine for each level of the protocol stack. It is difficult to abstract such a state machine starting from a pseudo-coded algorithm. But state machines are the most practical input for discrete simulators. Hence, it is possible to reuse a lot of existing components (MAC layer, transceivers, links, etc.) improving the deployment process. But on the other hand, any new feature must be described as a finite state machine which can be difficult to debug, extend and validate [5]. Also it is commercial and is not available for public which becomes the biggest disadvantage for working on it. J-Sim is an open-source, component based network simulation environment developed entirely in Java by Ohio State University (initially and later by University of Illinois). This along with the autonomous component architecture makes it a truly platform-neutral, extensible, and reusable environment. The Sensor Network Framework developed in J-Sim provides an object-oriented definition for target, sensor and sink nodes; sensor and wireless communication channels; and physical media such as seismic channels, mobility model and power model [6]. The simulation analysis described in [7] show that the execution speed of J-Sim is less compared to many other simulators and this happens because of its implementation in JAVA. But the memory consumption of HSim is less compared to others and this advantage comes from its garbage collectors. GloMoSim developed initially at UCLA Computing Laboratory, is a scalable simulation environment for wireless and wired networks systems developed. It is designed using the parallel discrete-event simulation capability provided by a C-based parallel simulation language. It currently supports protocols for purely wireless networks and is built using a layered approach. Standard APIs are used between the different layers and allow the rapid integration of models developed at different layers by users. The difficulty with GloMoSim was to describe a simple application that bypasses most OSI layers. The bypass of the protocol stack is not obvious to achieve as most applications usually lie on top of it. The architecture is also not very flexible compared to other simulators.

3- ARCHITECTURE OF SENSOR SIMULATOR

The goal of the framework provided by Sensor Networking Research Laboratory [8] is to reduce the interdependence between modules and increase the reusability. The development of the simulator was done in such a way that the above goal is achieved. Though many students were working in the project, certain coding practices were followed. The following section gives the architecture of Sensor Simulator and a description on the various modules implemented. The architecture closely models a Sensor Network scenario [8] which can be represented by the high-level representation shown below in Figure 1. The sensor model can be represented by the Sensor Node model and the Power model.

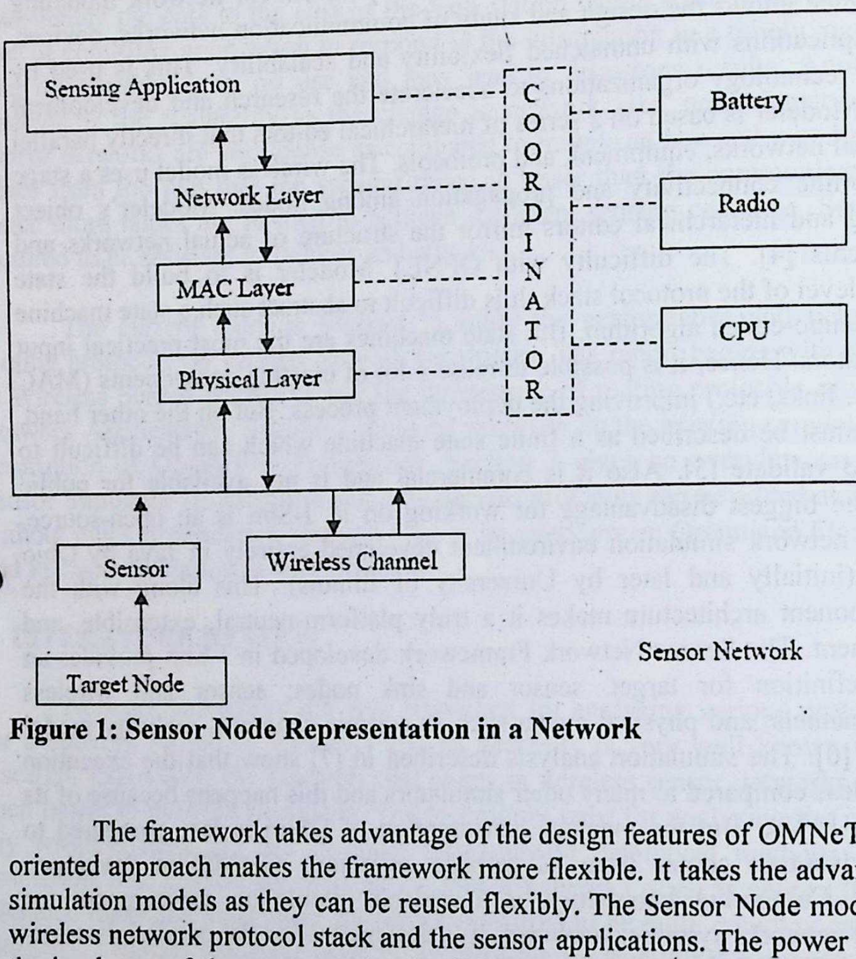

Figure 1: Sensor Node Representation in a Network

The framework takes advantage of the design features of OMNeT++. The object – oriented approach makes the framework more flexible. It takes the advantage of modular simulation models as they can be reused flexibly. The Sensor Node model represents the wireless network protocol stack and the sensor applications. The power model represents the hardware of the sensor node: the CPU, Sensor and RF transceiver. The two models act in parallel and achieve the task assigned to a sensor node. The state of the hardware model is changed based on the operation carried out by the software model of a Sensor Node. The power model in a Sensor Node is hardware abstraction of sensor node. This interacts with sensor node model to estimate the power usage. The power model comprises of a single energy source and many consumers. The battery module is a provider with finite amount of energy. The consumers are radio, CPU and other sensing devices that maybe added to the device as illustrated in Figure 1. The dashed connections between the CoOrdinator module to all other modules represent the direct communication between it to others. And the arrowed lines represent the gate connections between modules. Consumers report their power usage change to the energy source (battery) and the energy source updates the energy.

The simulator is designed in the form of a layered architecture and the communication between the different layers and modules are accomplished through message passing [9]. The implementation has a hierarchical structure where in the code is divided into base classes and sample classes. Any layer has a base class definition which is a derived class from LayerBase. LayerBase defines the properties of any layer in the protocol stack. It defines the gate connections and the required parameters that are needed for any layer.

The base class derived from LayerBase has the properties for that particular layer. The sample classes derived from the base class has the implementation needed by users. Hence a user has to derive his class from the base class for his protocol at a particular layer. In this way, all the protocols in samples directory are independent of each other and can also be used collectively. These details are explained in the following section for all the layers. The following section also describes the different modules of the framework.

Common directory has CoOrdinator, packets structures for Network and Mac layer and other constants and attributes used for simulation. This directory is derived by all other directories of the samples directory. TargetBase class is the base class that represents the Target Node. It has the base class functionalities that are essential for any target node which includes the position of the target node, its id, its speed etc. TargetNodeSimple extends the TargetBase and has the functional implementation of any target node. Any target node module maintains gate connection with the sensor channel. The simple class generates the stimuli and passes the message to the sensor channel.

The SensorNode module describes the behavior of a sensor node in the simulation. It is a compound module with different layers of the protocol stack as its submodules. The SensorNode module definition and the class represent all the components of the sensor node.

One of the features that the SensorSimulator incorporates in a sensor node module description is the addition of a coordinator module that acts as an interface between all the other sub-modules or layers in a sensor node. As such, the Coordinator Module has the functionalities that coordinate the activities of the hardware and the software modules in a sensor node. The module has to be extended with an added functionality for accessing the properties of the newly added hardware modules or consumers. It has reference to all the layers of a sensor node and all the layers in the sensor node may access the Coordinator. Hence with the help of this coordinator module, any layer may access and update the properties of the other layer. When there is any transmission or reception of a packet, the physical layer has to inform the battery about the decrease in its energy accordingly. This is not done directly between physical layer module and the battery module but is done through the coordinator. Hence physical layer module indicates the coordinator module and this in turn indicates the battery module. The important advantage of this feature is that the individual layers need not have a reference to each of the implementations of a layer. It can have reference only to this coordinator module.

3- COMPARATIVE STUDY ON DIRECTED DIFFUSION

The initial version of Sensor Simulator is verified by making comparisons with ns2. The performance of the simulator is tested in terms of execution speed and memory consumption. This is done by implementing Directed Diffusion routing protocol with a similar setup as that of ns2. The implementation details are maintained same in both of them. The reason to choose Directed Diffusion was that it being a very well known and useful protocol implementation for a new simulator. The comparisons with a protocol that is under research will help further study on it.

Directed Diffusion is a new data dissemination paradigm for sensor networks and is data centric. Data generated by the nodes have attribute value pairs. Interests are generated by nodes for the named data and the data matching the interest is drawn down towards that node [10]. Intermediate nodes cache, or transform the data.

The details of the protocol are as follows: The nodes that generate queries are called subscriber nodes and generate queries at a regular interval. The subscriber node initially generates beacon messages and gets the information about neighbors from beacon replies and then forwards the query. Each node follows this procedure and use Geographic Routing to forward the query to the region. If a node in the path does not have any neighbors or all its neighbors are away from the region, then it sends a message to its parent node that it is a dead-end. The parent node on updating the cost of the unreachable node, forwards the query in an alternate route towards the region. In the specified region, the interest is recursively flooded. The interest cache is maintained at each of the nodes in the path with its gradient of interest to each of the neighbors. The nodes in the region that have the specified properties of the interest send out data. These nodes are referred to as Publishers [8].

The data is marked as Exploratory to reinforce the path that was taken by the interest. On receiving the data marked as Exploratory by the subscriber, positive reinforcement message is sent out by the Subscriber node. Each node on path forwards this message thus reinforcing the path to the region. When the node reinforces a path, its cost to the region is known and this cost is sent back to its source node, which updates the cost information of that node to the particular region of interest. Thus the path with the highest cost is always maintained, reinforcing the route. The data from the region follow the path established by the reinforced messages. The nodes in the region send out data at the rate that is specified in the query. Data caching is implemented in intermediate nodes and so the data requested by different subscribers from the same region maybe satisfied by the common node in the path thus reducing the traffic and redundant messages. The data marked as exploratory are sent to identify better paths and reinforce at regular intervals. Also the neighbor- updating procedure phase is carried out, i.e. at regular intervals the beacon messages are broadcast and beacon-reply messages are sent by neighbors thus maintaining latest neighbor information [8].

4-IMPLEMENTION OF RAW

As discussed in the introduction Section that sensor networks are energy constraint, energy efficient communication techniques are very critical for increasing the lifetime of sensor nodes. Hence the design of a good power management protocol for wireless sensor networks needs to consider the following attributes; energy efficiency and scalability to the change in network size, node density and topology whereas latency, fairness and bandwidth, which are generally the primary concerns in traditional wireless voice and data networks, are secondary in sensor networks.

The Random Asynchronous Wakeup (RAW), a power management scheme is explicitly designed for wireless sensor networks [18], focusing on the above discussed issues. With reduced energy consumption, the protocol achieves good scalability and low latency. This is achieved by reducing idle listening; by making the sensors operate at very low-duty cycle modes. And a low duty cycle increases latency and reduces throughput.

RAW uses the concept of Stateless Nondeterministic Geographic Forwarding (SNGF) [19]. The Protocol consists of two schemes; routing based on forwarding sets and random wakeup scheme. The routing protocol is designed to take advantage of the fact that sensor networks are densely deployed. Unlike conventional routing protocols, a packet can be forwarded to any of the several paths existing between the source and destination nodes, where the path lengths of these paths are comparable to the shortest path. The Random Wakeup Scheme allows a node to be active during a randomly chosen fixed interval in each time frame.

4-1- The Protocol

Each sensor gets up periodically, transmits a beacon message indicating that it is ready to receive or forward a message. It waits for duration tx for a reply. If it gets an RTS from any of its neighbor in that duration, it receives the message and extends the duration of its idle time. Then it checks if it can forward the message to any of its neighbor. If no neighbor in the forwarding set is awake it waits until a neighbor is awake.

Then it forwards the message to that node and goes to sleep again. Time axis is divided into fixed-length time frames of length *T*. Let Tsetup be the time taken by a sensor to send a beacon message once it is awake and receive a reply consisting of it neighbor information. tx is the duration that the sensor waits for an RTS.

4-2-Receive Transmit

A sensor in this state performs the tasks of receiving and transmitting packets. It should be observed that a sensor will be awake until it could forward the packet, after which it goes back to Ready to Receive state.

4-3-Performance of RAW

The performance of the protocol is verified on a standard network simulator ns2. Various scenarios were tested with MAC 802.11 at the MAC Layer with a simple Propagation Model. The simulations were carried on a 5RX5R network with a density of 6 nodes per RXR region and hence 150 nodes. The transmission radius can be varied accordingly for different network topologies. The model parameters and limits on transmission bit rates and energy ratings are set according to Crossbow MICA2 sensor nodes [10]. Nodes were deployed randomly in the rectangular region. The energy consumption for switching the radio from idle to sleep modes and vice versa is assumed to be negligible and hence not considered. The raw available bandwidth for each node is set to 1Mbps. The functionality of 802.11 is changed accordingly so that the node will be able to withstand sleep and idle schedules.

The simulations shown in Figure 2 are for a network of 150 nodes with a schedule period *Ti* being 0.5sec. There were 10 source nodes that generate packets at a date rate of 1-5 packets/sec and the performance is tested when there are one and two destination nodes. It is observed that for a fixed density and with an increase in traffic, the awake time of the nodes does not vary much with the average latency being increased considerably. This can be seen in Figure 3.

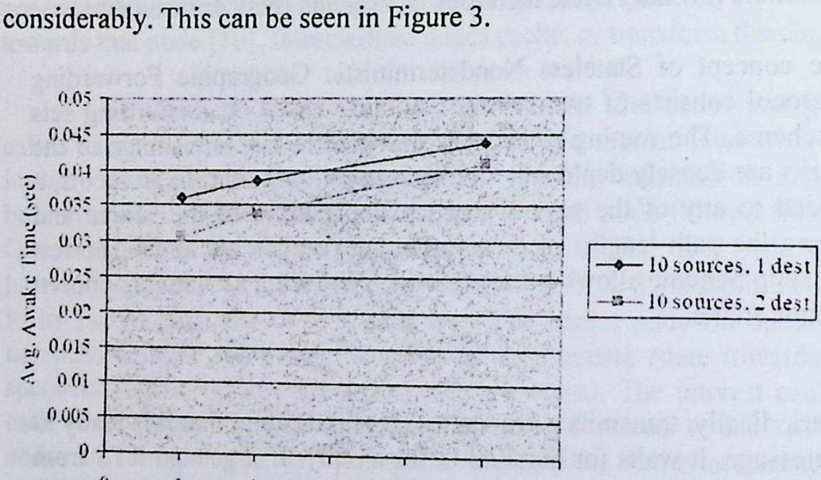

Figure 2. Effect of Awake Time of Nodes with Traffic

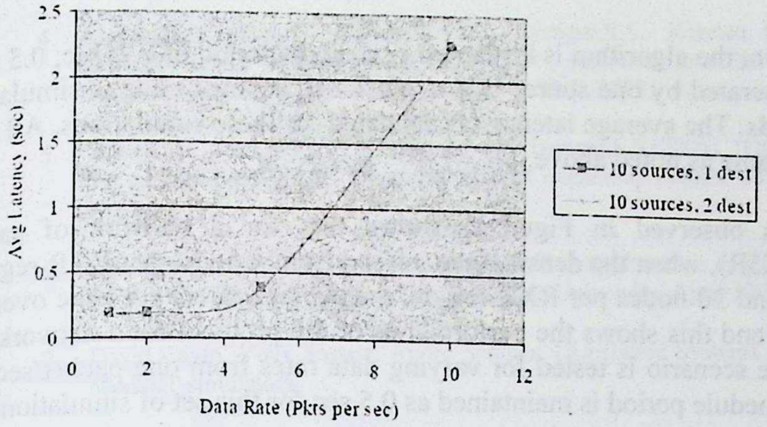

Figure 3. Effect on Latency with Traffic

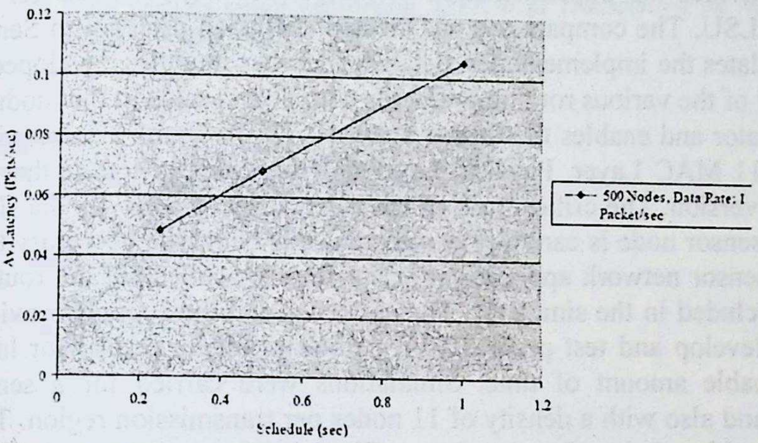

Figure 4. Effect of Schedule Period on the performance of protocol

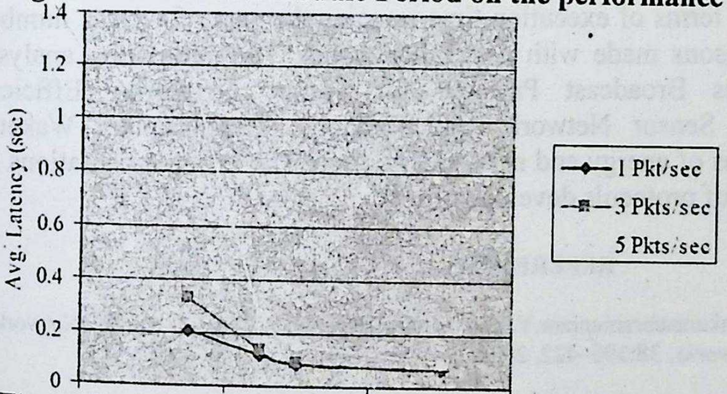

Figure 5. Performance of the protocol for various densities.

The performance of the protocol is also seen when the schedule period changes. As seen in Figure 4, for a network size of 5RX5R with 500 nodes, density being

20 nodes per RXR region, the algorithm is tested for a schedule period of 0.25sec, 0.5 sec and 1.0 sec. Data is generated by one source at a rate of one packet/sec and is simulated for 50 simulation seconds. The average latency is calculated for these simulations. All the parameters remain the same as noted above.

The simulations observed in **Figure 5** shows that for a network of same rectangular region (5RX5R), when the density is increased from 4 nodes per RXR region to 10 nodes, 12 nodes and 20 nodes per RXR region, the average latency for the overall simulation is decreased and this shows the performance of the protocol for a network of very large densities. The scenario is tested for varying data rates from one packet/sec to five packets/sec. The schedule period is maintained as 0.5 sec for this set of simulations.

5- CONCLUSION

This research provides the implementation of various routing protocols for the Simulator developed at LSU. The comparisons of Directed Diffusion protocol in Sensor Simulator with ns2 validates the implementation details of various modules developed in the simulator. The study of the various routing protocols with 802.11 adds to the modules developed for the simulator and enables the further analysis. This research also provides enxtensions to the 802.11 MAC Layer, Physical Layer and the Energy Module that are developed in the initial version. The critical task of the MAC layer to consider the sleep and idle switching of a sensor node is carefully designed as this being the necessary task for a sensor node in a sensor network application. Script files for collecting the routing protocol statistics are included in the simulator. The simulator and the support provided makes it very easy to develop and test protocols very fast and obtain results for large simulations at a reasonable amount of time. Simulations were carried for a sensor network of 2000 nodes and also with a density of 11 nodes per transmission region. This shows the scalability achieved by the simulator. The simulations show that the performance of simulator in terms of execution time remains the same for large number of nodes also. The comparisons made with ns2 validate this. The simulation analysis shows that the algorithms Broadcast Protocol for Sensor Networks, Efficient Coordination Protocol for Sensor Networks and Random Asynchronous Wakeup Protocol are efficient in terms of energy and network life time. These implementations in the simulator expand the set of protocols developed for it.

REFERENCES

1. Akyildiz,I.F., Su, W., Sankarasubramaniam,Y. and Cayirci ,E. (2002).Wireless Sensor Networks: A Survey. *Computer Networks*, 38:393–422, 2002.

2. Chen, G., J. Branch, M. J. Pflug, L. Zhu and B. Szymanski (2004). SENSE: A Sensor Network Simulator. Advances in Pervasive Computing and Networking. B. Szymanksi and B. Yener, Springer: 249-267.

3. Ahmed Sobeih, Wei-Peng Chen, Jennifer C. Hou, Lu-Chuan Kung, Ning Li, Hyuk Lim, Hung-Ying Tyan, and Honghai Zhang, J-Sim: A Simulation and Emulation Environment for Wireless Sensor Networks.

4. Mallanda, C., Suri,A., Kunchakarra,V., Iyengar,S.S., Kannan, R., and . Durresi,A. Simulating Wireless Sensor Networks with OMNeT++ , submitted to IEEE Transactions on Computers.,A. Tannenbaum. Computer Networks. Prentice Hall, 2002.

5. Durresi,A.,. Paruchuri,V., Kannan,R. and Iyengar,S.S.(2005). "Optimized Broadcast Protocol for Sensor Networks, *IEEE Transactions on Computers*, Volume 54, Issue 8, August 2005: 1013 - 1024.

6. Dommety,G. and Jain,R.. Potential networking applications of global positioning systems (GPS). Tech. Rep. TR-24, CS Dept., The Ohio State University, April 1996

7. David Cavin, Yoav Sasson, Andre Schiper, Distributed Systems Laboratory, On the accuracy of MANET simulators

8. David M. Nicol, Dartmouth College, Comparison of Network Simulators Revisited, May 20, 2002.

9. Intanagonwiwat,C., Govindan,R. Estrin, D., Heidemann, J. and Silva,F.(2003). Directed diffusion for wireless sensor networking. *IEEE/ACM Transactions on Networking*, 1(1): 2–16, February 2003.

Bulletin of Pure and Applied Sciences
Vol. 32 D (Physics) Issue (No.2) 2013:P. 159-164
www.bpas.in

PHOTONIC CRYSTAL IN ELECTRICAL ENGINEERING

Shiv Ranjan Kumar
Deptt. of Physics
Govt. Polytechnic, Muzaffarpur (Bihar)

Received on 18 August 2013: Accepted on 30 November 2013

ABSTRACT

Photonic Crystal (PhC) based devices are being increasingly used in multifunctional, compact devices in integrated optical communication systems. They provide excellent controllability of light, yet maintaining the small size required for miniaturization. The band gap properties of PhCs and their typical applications in optical waveguide have been considered. Novel PhC based application such as nonlinear switching and tapers are considered and simulation results are shown using the accurte time-domain numerical method based on Finite Difference Time Domain (FDTD) scheme. The suitability of these devices for novel applications is discussed and evaluated.

Keywords: Band gap engineering, photonic crystal, optical waveguide.

INTRODUCTION

Photonic crystals (PhCs) are relatively recent, flexible and competent tools that control the propagation of light in optical media by allowing the light to propagate over a desired range of frequencies. These are artificial, periodic dielectric structures prohibiting light propagation in certain frequencies: this range of frequencies is called as the photonic band gap (PBG). Today, almost two decades after their appearance, PhCs are being widely used for design of various optical circuit elements such as waveguides, cavities, tapers, power splitters filters etc. These devices can be realized by deliberately introducing defects in the otherwise periodic crystal. The defect can be either point-or line-type. Cavities and waveguides can be created by point defects and line defects respectively. The light, that falls in the stopband, can be allowed to guide or confine within the sharp bends, cavities or line defects that causes the propagation of light in a controlled manner. The PhCs, as an extended application, can also be used as switching elements due to the presence of the band gap as these band gaps can be shifted from one position to the other by using nonlinearity of the material involved in making the PhC. These nonlinear PhCs are periodic structures whose optical response depends on the intensity of optical field that propagates through the crystal. They can provide novel and improved optical functionalities that cannot be obtained by using linear PhCs. The PhC taper is another application of great significance in integrated optics. A waveguide taper is used to transform the modal size from an optical fiber to an optical chip or vice versa. Conventional waveguide tapers are not efficient and introduce losses. PhC tapers, on the other hand, provide much better functionality and hence are the potential candidates that n be used for low loss coupling between chip-to-fiber in opto-electronic integrated rcuits.

We have investigated the properties of nonlinear switches and also tapers based n PhCs, as examples out of numerous such devices that can be realized using PhCs, for lustration. We have found the band gap for linear photonic crystal and also the band ructure for the linear photonic crystal with defect. We have also carried out a detailed ystematic analysis of the effect of the material parameters on the movement of the band ap which can be helpful to understand the suitability of the photonic crystal as switching evice. The analysis of various butt- coupled (non-tapered) waveguides has also been one and the improvement in the transmission characteristics while moving from the utt-coupled to the taper configuration has also been studied. A plane wave expansion ethod PWE along with the Finite Difference Time Domain (FDTD) scheme has been sed for the simulations.

hotonic crystal structure and bandgap calculation Method:

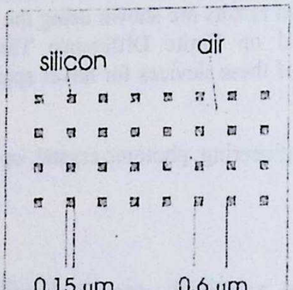

Fig.-1 Two-dimensional photonic crystal composed of square silicon rods in air.

We have considered a crystal as shown in Fig. 1, consisting of a square lattice of licon rods in air, having a lattice constant of 600 nm. The rods have a 150 x 150 nm uare cross- section and a refractive index of 3.4 (assumed constant in the wavelength egion of interest around λ =1550 nm). For a very similar structure a bandgap is known exist around λ =1.5 μm for TE polarization (i.e. E-field parallel to the rods, erpendicular to the calculation window).

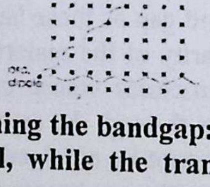

ig.-2 Configuration for determining the bandgap: a dipole radiator is positioned at he left-hand side of the crystal, while the transmission is determined along a ertical line at the right-hand side.

A straightforward method for determining the bandgap is to calculate the ransmission of a broad-band electromagnetic signal through the crystal for all directions n the reduced Brillouin zone. For that purpose, a 2-dimensional finite difference time domain (FDTD) scheme is used. As shown in Fig. 2, a finite crystal of 8 rods width is defined. To the left of this, a dipole is oscillating at a central frequency corresponding to a wavelength of 1.5 μm; it is modulated with a pulse that is short enough (50fs) that the resulting electromagnetic wave contains all wavelengths in the bandgap. This dipole will radiate in all directions. Taking the time-domain Fourier transform of the transmitted field at the right hand side of the crystal for a range of propagation angles between 0 and 45^0 covering the reduced Brillouin zone of the square lattice, yelds the transmitted amplitude for a sufficiently wide wavelength range around the bandgap.

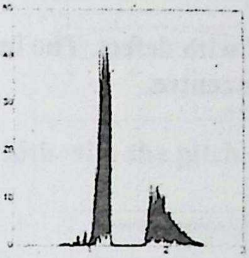

Fig.-3 Superposition of the transmission amplitudes across all relevant angles.

Fig. 3 shows a superposition of the graphs of the transmitted amplitude versus the wavelength, fro 100 uniformly distributed propagation angles between 0 and 45^0. In the wavelength range from ≈ 1.3-$1.7\,\mu$m, the transmission is nearly zero for all directions, revealing the photonic bandgap.

Although other methods which use a single unit cell for the band-structure calculation, are more accurate, this method is fast and gives a good approximation of the total bandgap of the crystal, similar to the bandgap for the similar structure studied in.

SIMULATION RESULTS AND DISCUSSION:

For illustration of functionality, a PhC consisting of an array of dielectric rods with a square lattice is considered, where the dielectric rods with an initial radius of r =0.18*a* (*a* =1 μm) are embedded in a silicon (n=3.4) background, a and n being the lattice constant of the photonic crystal and the refractive index of dielectric rods. For this uniform structure, the band gap is found to be in range 0.304 ($1/\lambda$) to 0.444 ($1/\lambda$) for TE mode, as shown in Fig.-4.

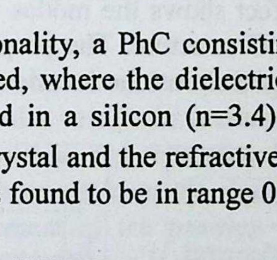

Fig.-4 Photonic band gap for a uniform (without defect) PhC structure. The shaded area represents the band gap.

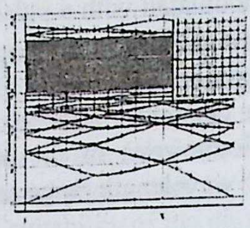

Fig.-5 Photonic band gap PhC with defect. The inset shows the layout for the PhC with a defect introduced in the centre.

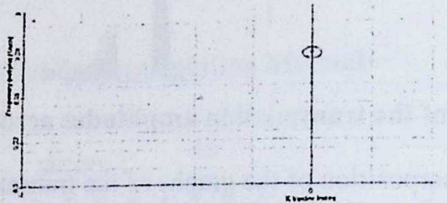

Fig.-6 The location of the defect mode.

A defect has been created in the above structure: Fig.5 shows the band structure when the point defect is created in the structure. The inset in Fig.5 shows a schematic representation of the PhC layout with defect: i.e. one rod missing at the centre. As expected, the band diagram with defect shows the modes within the band gap obtained for the usual (i.e. without defect) PhC structure. The propagation can take place in the range 0.387 ($1/\lambda$) to 0.389 ($1/\lambda$) Fig. 6 shows the location of the defect mode inside the band gap.

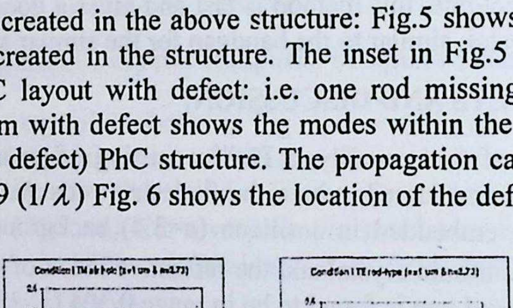

Fig.-7 Variation of band gap centre and width with radius of air holes/rod for TM and TE cases.

The dynamics of the band gap under varying conditions, a simple PhC lattice is designed consisting of an air-hole PC slab, and also another lattice with material rods, with 2r/a=0.64 in both cases and the material refractive index is chosen. The two configurations mentioned above (i.e. air-hole type and material-rod type, henceforth called as hole-type or rod-type PhC) are known to provide photonic band gaps for TM nd TE polarizations respectively. To investigate the dynamic shifting of the band gap nd also the change in the width of the band gap, we gradually and continuously change he value of radius, lattice constant and refractive index one at a time, keeping other arameters constant. Fig.7 shows the comparison of extent of band gap shifting and videning in TM and TE case respectively for varying radius of air holes/rods.

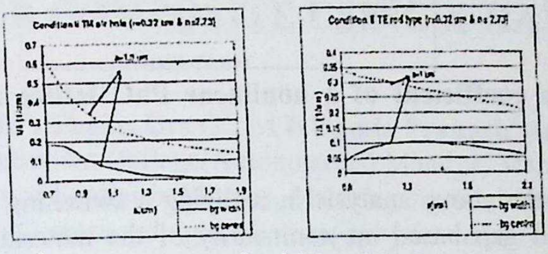

Fig.-8 Variation of band gap centre and width with the pitch of the lattice structure

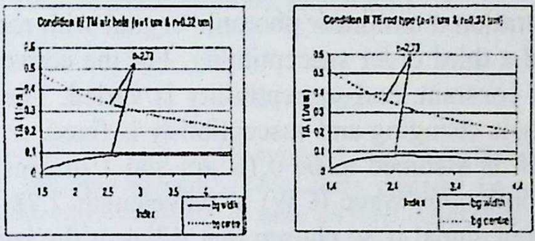

Fig.-9 Variation of band gap centre and width with refractive index of material for TM (index of background material varies) and TE (index of rods varies) cases.

Fig.8 and Fig.9 show the corresponding comparison for the shifting of the band gap central frequency and the width of the band gap as a function of the material parameters such as refractive index and geometrical parameters such as pitch for TE and TM modes.

It can be observed from the above results that for TM polarization (hole-type structure), an increasing radius of holes results in increase of the width upto a certain point where it reaches to maximum value, and thereafter it decrease. The movement of the centre of the gap can also be observed from the figures. An increase in the lattice constant results in downward movement of the position of band gap. However, with change in refractive index, no point of inflexion is observed in the plots within the given range of frequencies. For the TE case, a change in radius results in a movement of band gap that is opposite to the corresponding TM wave. This results because the effective refractive index of the PhC lattice changes in opposite direction in hole-type and rod-type structures with change in the radius. When lattice constant is varied, an increasing lattice constant results in the band gap width increase that reaches to a maximum value and then decreases. Similarly, a change in refractive index results in dynamic shifting of band gap.

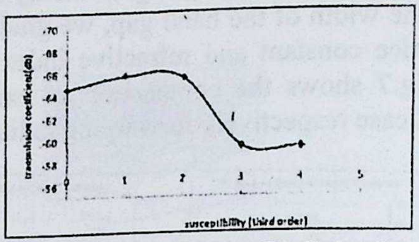

Fig.-10 Transmission coefficient of a nonlinear PhC lattice as a function of the nonlinearity

We have used the above analysis in realizing a switching element based on the movement of the band gap based on nonlnearity of the material involved. Nonlinear materials have been established to be potential candidates for ultrafast optical switching applications. For the analysis of photonic crystal device as switching element we have considered for illustration a nonlinear photonic crystal with rod type structure having the refractive index and a third order susceptibility. For the convenience the intensity of the input signal is kept constant, and susceptibility is varied. The similar effect is expected when input intensity is changing and susceptibility is fixed, as for any practical material. The radius and pitch is assumed to be 0.18 μm and 1 μm respectively. An input signal consisting of the continuous wave (CW) at wavelength 2.78 μm is being applied. The frequency of the input signal is so chosen that it lies at the band edge, and so that when the signal passes through the nonlinear lattice, it can affect a change in band structure resulting in self switching. Fig.10 shows the variation in output (transmission coefficient) as the susceptibility is being varied.

It can be clearly observed from the graph shown in Fig.10 that the transmission is increasing with increasing nonlinearity. This is due to the signal which, while passing through the lattice, evokes nonlinearity, resulting in movement of band gap which results in jumping of the signal frequency from inside of the band gap to the outside at a particular point. This principle can be used for fast optical switching, and results can be further explored.

REFERENCES

1. Yablonovitch, E., Inhibited Spontaneous Emission in Solid-State Physics and Electronics, *Physical Review Letters*, Vol. 58 (20), pp. 2059-2062,1987
2. Parker, G. and Charlton, M., Photonic crystals, *Physics World*, Vol. 13 (8), p. 29-34,2000.
3. Villeneuve, P.R. and Piche, M., Photonic Bandgaps in Periodic Dielectric Structures, *Progress in Quantum Electronics*, Vol. 18 (2), pp. 153-200, 1994.
4. Jin, J., *The Finite Element Method in Electromagnetics*, John Wiley &Sons, New York, 1993
5. Niceneco, B., *Easymesh quality mesh generator, wwwdinma.univ.Trieste.it/-nirftc/research/easymesh*, 2000.

Bulletin of Pure and Applied Sciences
Vol. 32 D (Physics) Issue (No.2) 2013:P. 165-174
www.bpas.in

CHARACTERIZATION OF HPMC/GLY: NA_2SO_4 POLYMER COMPOSITE USING X-RAY TECHNIQUE

H T Ananda[1], Thejas Urs G[2], M B Nanda Prakash[2] and R Somashekar[2]*
[1]Government College(Autonomous) Mandya, Mandya – 571401.
[2]Dept of Studies in Physics, Manasagangotri, Mysore – 570006.
*Corresponding Author: rs@physics.uni-mysore.ac.in

Received on 18 September 2013: Accepted on 30 November 2013

ABSTRACT

Water soluble polymer Hydroxypropyl methyl cellulose added with inorganic salt like Sodium sulphate were prepared by solution casting method. The characterization of these polymer composites are carried out for various concentration of Sodium Sulphate added and the changes encountered are reported. The Microstructural parameters of these polymer composites are evaluated using in-house programs and the changes in conductivity are compared with the XRD results. An attempt was done to sketch the radial distribution of these polymers using the pair correlation function which is evaluated using the XRD data obtained.

Key words: X-Ray Diffraction, Polymer Composites, Conductivity.

1. INTRODUCTION

Polymers have become an essential part of our everyday life. Nowadays conducting polymers are of great importance due to their incredible properties like easy fabrication, low cost, leak proof, biodegradability and good storage capacity. For this purpose we have chosen Hydroxy propylmethyl cellulose (HPMC) is a polysaccharide, prepared from cellulose, with methyl and hydroxyl groups that render the cellulose molecule hydrophobic and hence it acquires surface-active properties. HPMC is water soluble tasteless non-ionic derivative of cellulose, which has been accepted as food additives in Europe, inactive apthalmic preparations, oral capsules, suspension syrups, and eye drops [1-3]. The changes in microstructural parameters of edible polymer films of Hydroxypropyl methylcellulose with plasticizers such as glycerol(GLY) have been studied using wide angle X-ray scattering (WAXS) data and line profile analysis (LPA). Exponential function for the column length distribution has been used for the determination of microstructural parameters. The crystal imperfection parameters such as crystal size <N>, lattice strain %(g) and orientational parameters have been computed and correlated with the amount of plasticizers. The flexibility of the films is expected to increase due to decrease in the number of weak inter- and intramolecular hydrogen bonds with the addition of plasticizers. From these investigations it is also observed that there is an increase in unit cell volume with increase in the plasticizers in HPMC films indicating greater stability of the composites which are essential in packing industry. Sodium sulfate is an inorganic salt with a melting point of approximately 884 °C, a relative density of 2.7 g/cm3 at 20°C and a water solubility of 161 g/l at 20°C[6]. In the dry state it exists a white powder or white crystalline solid of formula Na_2SO_4, it has a bitter saline taste. Sodium sulfate is a chemical compound that can be found as a mineral in nature or derived from certain industrial processes as a byproduct. It has many commercial applications, and is classified as a non-toxic chemical under normal handling circumstances. Inspection of practically any bottle or package of soap or detergent product will reveal some form of sodium sulfate, and it is also used in other manufacturing industries such as paper and textiles. Sodium sulfate is still widely in use today, and should continue to be so for some time. Even though some manufacturing processes are phasing out use of the compound, other purposes are continuing to be found. Sodium sulfate's unique heat storage properties make it an ideal candidate for use in many future processes and products.

Hydroxypropyl methylcellulose and Sodium sulfate polymer composite films were investigated using X-ray technique to understand their micro- structural behavior. Conductivity and pair correlation studies of these polymer composites were done, which gives a good support in this characterization.

2. MATERIALS AND METHODS

2.1 Materials

Pure HPMC and various compositions of complexed films of HPMC with Sodium sulphate salt were prepared by solution cast method using double distilled water as solvent. Hydroxypropyl methylcellulose was purchased from (HPMCE15LV), Loba Chemicals India, and Sodium sulphate were purchased from S. D. fine chemicals India.

2.2 Preparation of Films

To prepare the polymer films, HPMC polymer was doped with inorganic salt Sodium sulphate. The completely soluble homogeneous solution was filtered through Whatmann No 41 filter paper and degassed. Then the clear solution of HPMC: Sodium sulphate was poured on to a clean and leveled glass plates to evaporate at room temperature for 5 days and peeled off from the glass plate. The final films were vacuum dried thoroughly and stored in desiccators to avoid the absorption of moisture. Sodium sulphate is hygroscopic in nature and the higher concentration of Sodium sulphate has got the tendency to absorb more moisturizer.

However HPMC: Sodium sulphate polymer composites prepared were found to be more brittle in nature. To overcome this, glycerol was used as plasticizer. The prepared polymer films are shown below in figure 1.

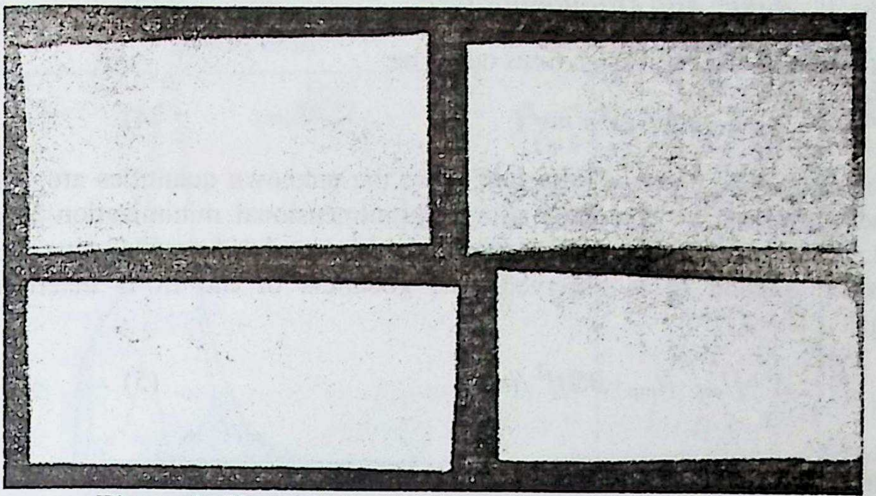

Figure 1: Photograph of polymer Composites prepared.

3. EXPERIMENTAL

3.1 X-ray Diffraction Measurements.

The X-Ray diffractograms (XRD) of the polymer samples were recorded using Rigaku Miniflex-II, X-Ray diffractometer (Japan) with Ni filtered, CuKα radiation of wavelength λ=1.5406 Å, with a graphite monocrhomator. The specifications used for the recordings were 30Kv, 15mA. The samples were scanned in the 2θ range 10-60° with a scanning speed and step size of 1°/min and 0.02 respectively.

3.1.1 Theory

Microstructural parameters such as crystal size(<N>) and lattice strain (g in %) are determined by employing Fourier method of Warren and Averbach and Warren[4-5]. The intensity of a profile in the direction joining the origin to centre of the reflection can be expanded in terms of Fourier cosine series:

$$I(s) = \sum A(n)\cos\{2\pi nd(s - s_0)\} \qquad (1)$$

Where the coefficients of the harmonics A(n) are function of the size of the crystallite and disorder of the lattice. Here, s is $sin(\theta)/\lambda$, n is the harmonic number and d is the lattice spacing. The Fourier coefficients can be expressed as;

$$A(n) = A_s(n) . A_d(n) \qquad (2)$$

An analytical expression for the size distribution yields an expression for crystallite size distribution as

$$A_s(n)= A(0)\ exp\{-\alpha(n-p)\}/(\alpha N) \qquad (3)$$

and for lattice strain, the expression turns out to be;

$$A_d(n)= exp\{-2\pi^2 n^2 mg^2\} \qquad (4)$$

Where m is the order of reflection, Here the unknown quantities are N,g,α and background which can be computed using multidimensional minimization SIMPLEX program-2. The experimental profile is matched with simulated profile using the above parameters till a good fit is observed. The goodness of the fit is determined by computing,

$$\Delta^2=[I_{cal}-(I_{exp}+BG)]^2\ /(npt) \qquad (5)$$

3.2 Conductivity measurements

The conductivity measurements of samples were determined by using HIOKI LCR-Hi tester 3532-50 (Japan) model available. Our samples were taken in the sample holder provided in the instrument. This instrument gives the transconductance (G) of the sample which is dependent of its thickness and the area.

The conductivity (σ) of the sample can be obtained by the relation,

$$\sigma=\frac{t\times G}{A} \qquad (6)$$

Where 't' is the thickness and 'A' is the area of the sample.

This instrument gives the transconductance values for different frequencies from 50Hz to 5MHz. The obtained transconductance values for various frequencies were evaluated to get the conductivity results for the same corresponding frequencies.

3.3 Pair Correlation studies

Pair Correlation or Radial distribution of materials can be obtained by Fourier transformation of the total structure factor that is measured in the X-Ray scattering equipments. The standard algorithm used to derive the pair correlation function is given below,

$$g(r)= 1+\frac{1}{2\Pi^2 r\rho_0}\int_0^\infty Q[S(Q)-1]\sin(Qr)dQ \qquad (7)$$

ρ_0 is the average number density of the samples, Q is the scattering vector. And S(Q) [illegible] I(Q). An in-house program has been written to analyze the X-ray powder patterns. It is available on request.

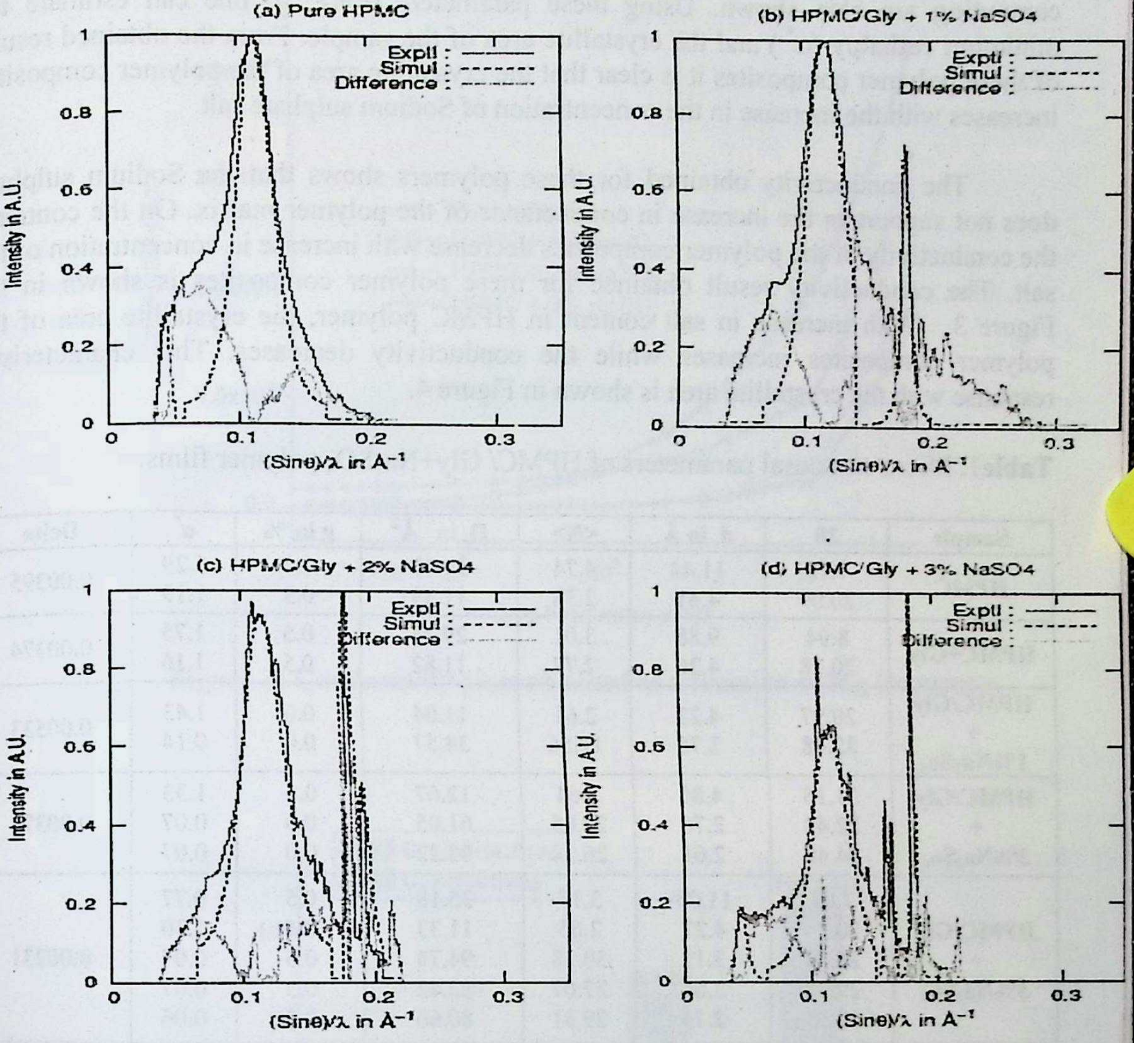

Figure 2: Whole Pattern Fitting of the Pure HPMC and HPMC: Sodium sulphate Composites.

4. RESULTS AND DISCUSSION

X-ray diffractograms for HPMC polymer films with Na_2SO_4 are given Figure 2. Whole pattern fitting method is quite useful for relative comparison of crystallite size and strain in a series of polymer composite films of various concentration of Na_2SO_4 in HPMC. The computed micro structural parameters of HPMC and HPMC:$_{Na2SO4}$ polymer composite are given in Table 1. The computed microcrystalline parameters like crystallite size <N>, lattice strain g in % and the standard deviation of these parameters while computing are also shown. Using these parameters (<N>, g) one can estimate the minimum enthalpy (α^*) and the crystallite area of the sample. From the obtained results of these polymer composites it is clear that the crystallite area of the polymer composites increases with the increase in the concentration of Sodium sulphate salt.

The conductivity obtained for these polymers shows that the Sodium sulphate does not support in the increase in conductance of the polymer matrix. On the contrary, the conductivity of the polymer composites decrease with increase in concentration of the salt. The conductivity result obtained for these polymer composites is shown in the Figure 3. With increase in salt content in HPMC polymer, the crystallite area of the polymer composites increases while the conductivity decreases. This characteristic response with the crystallite area is shown in Figure 4.

Table1. Micro structural parameters of HPMC/ Gly+Na_2SO_4 polymer films.

Sample	2θ	d in Å	<N>	D_s in $Å^2$	g in %	α^*	Delta
HPMC	7.72 20.09	11.44 4.41	4.74 2.58	54.22 11.39	0.5 0.5	1.29 1.19	0.00395
HPMC+Gly	8.94 20.78	9.88 4.26	3.01 2.77	29.74 11.82	0.5 0.5	1.75 1.16	0.00374
HPMC/Gly + 1%Na_2So_4	20.97 32.48	4.23 2.75	2.61 12.56	11.04 34.57	0.0 0.0	1.43 0.14	0.00533
HPMC/Gly + 2%Na_2So_4	21.16 32.48 34.48	4.80 2.76 2.61	2.64 22.05 26.14	12.67 61.05 68.22	0.5 0.0 0.0	1.33 0.07 0.07	0.00378
HPMC/Gly + 3%Na_2So_4	7.09 20.75 28.50 29.30 32.53	11.09 4.27 3.12 3.04 2.75	3.17 2.65 30.28 27.07 29.31	35.18 11.33 94.74 82.42 80.60	0.5 0.5 0.5 0.5 0.5	0.77 1.30 0.07 0.07 0.06	0.00231

Table 2. Conductivity results.

Sample	Conductivity10^{-7} S/cm	Crystallite area $Å^2$
HPMC	4.08	617.56
HPMC/Gly+1%Na_2SO_4	3.48	381.65
HPMC/Gly +2%Na_2SO_4	0.54	864.34
HPMC/Gly +3%Na_2SO_4	0.29	1073.40

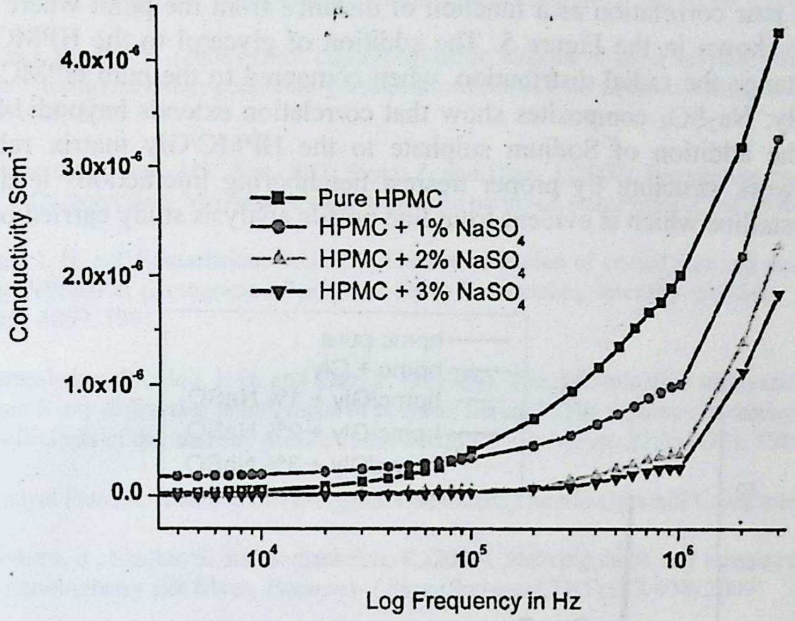

Figure 3: Conductivity plots obtained as a function of log frequency.

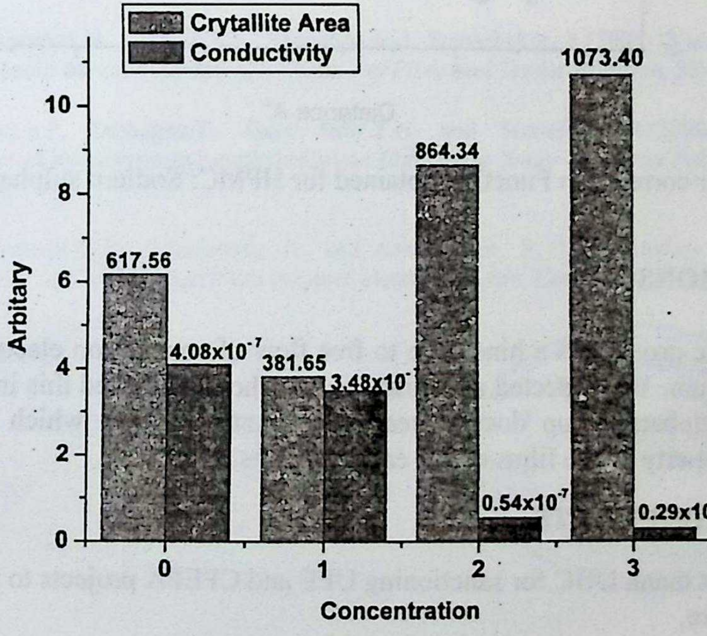

Figure 4: Characteristic behavior of crystallite area and conductivity.

The Pair Correlation Function obtained for these composites gives a supporting good comparative result in addition to the Microstructural parameters computed. The changes in the pair correlation as a function of distance from the point where X-ray hit the sample are shown in the Figure 5. The addition of glycerol to the HPMC polymer matrix does change the radial distribution, when compared to the pure HPMC polymer. The HPMC/Gly: Na_2SO_4 composites show that correlation extends beyond 14Å, which implies that the addition of Sodium sulphate to the HPMC/Gly matrix rebuilds the polymeric network structure by proper nearest neighboring interactions leading to an increase in crystalline which is evident from line profile analysis study carried out here.

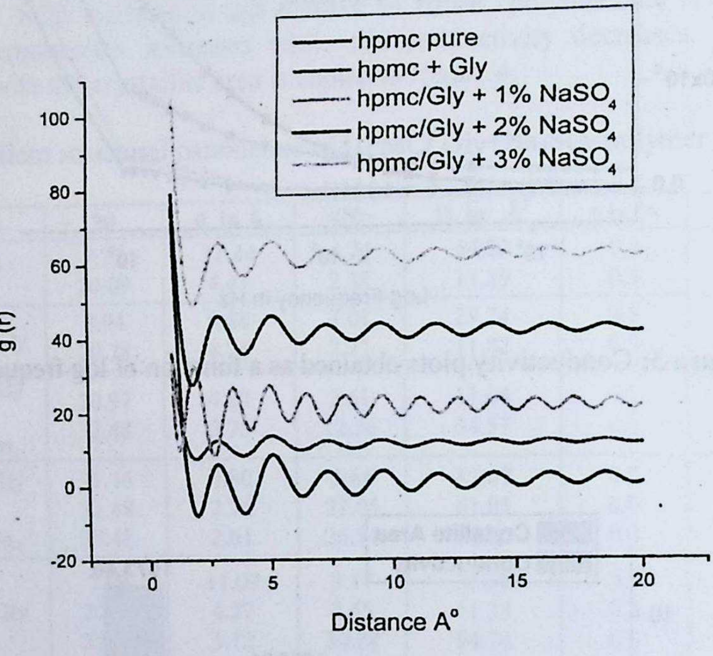

Figure 5: Pair correlation Function obtained for HPMC: Sodium sulphate Composites.

5. CONCLUSIONS

Sulphate group acts a hindrance to free flow of conduction electron in a polymer dielectric medium. We expected a contrary result when we started this investigation. The presence of sulphate group does increase the crystallite size, which do enhance the mechanical property of the films as per earlier reports.

ACKNOWLEDGEMENTS

Authors thank UGC for sanctioning UPE and CPEPA projects to the University of Mysore, Mysore.

CHARACTERIZATION OF HPMC/GLY: NA_2SO_4 POLYMER COMPOSITE USING X-RAY TECHNIQUE

REFERENCES

1. Wade, A., Weller. P.J. Handbook of Pharmaceutical Percipients, 2nd ed,pp. 229-232. 1994

2. Wang, L., Xu, Y. (2006) Graft copolymerization kinetics of ethyl acrylate onto hydroxylpropyl methylcellulose using potassium persulphate as initiator in aqueous medium. *Iran Polym J*, **15**: 467-475. 2006

3. Zhang, J.M., Gao, J.G., Sun, X.G., Peng, Z. and Diao, J.(2007). Preparation and characterization of TiO2/poly(St*co*- MAA) core/shell composite particles, *Iran Polym J*, **16**: 39-46. 2007

4. Hall, I. H. and Somashekar, R.(1991). The determination of crystal size and disorder from the X-ray diffraction photograph of polymer fibres 2. Modeling intensity profiles. *J Appl Cryst*. 24: 1051-1059, 1991

5. Somashekar, R., Hall, I. H. and Carr, P. D.(1989). The determination of crystal size and disorder from X-ray diffraction photographs of polymer fibres. 1. The accuracy of determination of Fourier coefficients of the intensity profile of a reflection. *J Appl Cryst*. 22:363-371, 1989

6. Pradyot Patnaik, Handbook of Inorganic Chemicals, The Mc-Grawhill Companies, 2002.

7. Divkara, S., Madhu, S. and Somashekar, R.(2009). Stacking faults and microstructural parameters in non-mulberry silk fibres. *Pramana-J.Phys,(Springer)*,73(5):927-938. 2009

8. Somashekar,R. and Somashekarappa.H.(1997). X-ray diffraction line-broadening analysis: paracrystalline model. *J. Appl.Cryst*,30(2).147-152. 1997

9. Divakara,S., Siddaraju,G.N. and Somashekar,R.(2010). Comparative study of natural and man-made polymers using whole powder pattern fitting technique. *Fibers and Polymers*,11(6):861 – 868. 2010

10. Somashekarappa,H., Mahesh,S.S., Sangappa and Somashekar, R.(2005). Variation of crystallite shape ellipsoid in non-mulberry silk fibers. *J of Fibre and Textile Research*. 30: 309 – 314. 2005

11. Parameswara,P. Demappa,T., Guru Row.T.N. and Somashekar,R.(2008). Microstructural parameters of hydroxypropyl-methylcellulose films using X-ray data. *Iran Polym J*. **17** (11): 821-829. 2008.

12. Nanda Prakash.M.B.. Manjunath, A. and Somashekar, R. (2013)Studies on AC electrical conductivity of $CdCl_2$ doped PVA polymer electrolyte. *Adv. Cond Matter Phys*. (Accepted) Vol-2013.

पुस्तकालय
132146
गुरुकुल कांगड़ी विश्वविद्यालय

Stock Verification-2024

.Sha
132146

GURUKUL KANGRI LIBRARY

	Signature	Date
Access No.		8.12.2016
Class No.		
Cat No.		
Tag etc.		
E.A.R.		
Recomm. by		
Data En by		10.12.2016
Checke		